Adham BEKHIT

NUMERICAL SIMULATION OF THE SHIP HULL HYDRODYNAMIC PERFORMANCE

SIMULAREA NUMERICĂ A PERFORMANȚELOR HIDRODINAMICE ALE CORPULUI NAVEI

- Teză de doctorat -

EDITURA FUNDAŢIEI UNIVERSITARE„*Dunărea de Jos*” – GALAŢI – 2023
ISBN 978-973-627-689-7

UNIVERSITATEA „DUNĂREA DE JOS” GALAȚI
Facultatea de Arhitectură Navală

Editura Fundaţiei Universitare „Dunărea de Jos” din Galaţi
este acreditată de CNCSIS

Referent științific:
Prof. univ. dr. ing. Florin Popescu

ISBN 978-973-627-689-7
Directorul editurii.
Prof. univ. Emerit dr. Cosma TUDOSE

www.editura.ugal.ro
editura@ugal.ro

Acknowledgments

I would like to express my endless gratitude and thanks for those who helped me and offered their unconditional support.

Special thanks to Dr. Thomas B.

This work was entirely submitted for the accordance of the PhD title, public defense was held on September 22nd, 2021, while the confirmation of the PhD title was granted based on the Ministry of Education order nr. 5999/30.12.2021.

Nomenclatures

S_L	Minimum oscillation value in simulation
S_U	Maximum oscillation value in simulation
T_e	Wave encounter period
U_P	General parameter uncertainty
δ_P	General parameter error
Δ_y	Distance of the first point from the solid wall
$\mathrm{CD}_{\mathrm{k}\omega}$	Cross-diffusion in the $K-\omega$ model.
g_i	Gravity vector
Ω_{ij}	Vorticity magnitude
C_F	Frictional Resistance coefficient
C_R	Residual Resistance coefficient
CF_∞	Value of fitted function in verification process
C_T	Total resistance coefficient
C_i	Correction factor
E_{av}	Average absolute error
F_S	Factor of safety
I_j	Unity vector whose components vanish, except for the component j
Q^*	Second invariant Q criterion
R_F	Frictional Resistance
R_R	Residual Resistance
R_G	Grid convergence ratio
R_T	Time step convergence ratio
R_T	Total resistance
R_i	Convergence ratio
S_C	Simulation benchmark
S_{ij}	Total stress tensor
U_{S_CN}	Corrected uncertainty
U_{V_c}	Corrected validation uncertainty
$\vec{U}$	Velocity vector
U_∞	Far field velocity
U_D	Data uncertainty
U_G	Grid uncertainty
U_I	Iteration uncertainty
U_S	Simulation uncertainty
U_{SM}	Modeling uncertainty
U_{SN}	Numerical uncertainty
U_T	Time step uncertainty
U_V	Validation uncertainty
U_{reqd}	Required level of uncertainty
c_i	Volume fraction for fluid i
f_e	Wave encounter frequency
f_w	Wave frequency
$\vec{n}$	Unit normal vector directed outward
p_∞	Far field pressure
p_G	Grid order of accuracy
p_T	Time step order of accuracy
p_a	Atmospheric pressure

p_i	Simulation order of accuracy
r_G	Grid refinement ratio
r_i	General verification ratio
y^+	Non-dimensional distance from the wall
γ_I	Wave initial phase angle
δ_D	Data error
δ_G	Grid error
δ_I	Iteration error
δ_{RE}^*	Richardson Extrapolation error
δ_S	Simulation error
δ_{SM}	Modeling error
δ_{SN}	Numerical error
δ_{SN}^*	Estimated value with sign and magnitude of the numerical error
δ_T	Time step error
δ_{ij}	Kronecker (delta) operator
ε_{av}	Average relative error
ζ_i	Incident wave height
ν_t	Turbulent eddy viscosity
ρ_a	Mass density of air
ρ_w	Mass density of water
σ_a	Tangential force on the free-surface in water
σ_w	Tangential force on the free-surface in water
τ_{ij}	Viscous stress tensor
τ_{ij}	Mean viscous stress tensor
Δp_γ	Pressure jump at the free-surface interface
Δx	Cell size in x-direction
Δy	Cell size in y-direction
Δz	Cell size in z-direction
A	Wave amplitude
A_0	Propeller disk area
A_E	Expanded blade area
B	Beam of the ship
C_{AW}	Added resistance in waves coefficient
C_B	Block coefficient
C_H	Heave force coefficient
C_M	Mid-ship section coefficient
C_M	Pitch moment coefficient
C_{Tcw}	Calm water total resistance coefficient
C_{Tw}	Total resistance coefficient in waves
D	Measured value in tank test
D	Depth of the ship
D_h	Propeller hub diameter
D_p	Propeller diameter
Fr	Froude number
He	Helicity
H_w	Wave height
J	Propeller advance coefficient
k	Wave number
K_Q	Propeller torque coefficient
K_T	Propeller thrust coefficient
LCB	Longitudinal center of buoyancy
L_{PP}	Length between perpendicular

L_{ref}	Reference length
M_i	General representation for grid density, i=1:n, finest grids i=1, coarsest grid i=n
$Ø$	Roll angle
$Ø_0$	Initial roll angle
$Ø_m$	mean decay roll value
Q	Propeller torque
RAO	Response Amplitude Operator
Re	Reynolds number
S	Simulation value computed based on CFD
S_0	Wetted surface area of the ship without appendages
SFC	Shear Force Correction
S_R	Wetted surface area of the rudder
T	Draft of the ship
T	Simulation time
T	Propeller thrust
T	Wave period
t	Simulation time
TF	Response Transfer Function
U	Ship Speed, axial flow velocity in x-direction
V	Axial flow velocity in y-direction
W	Axial flow velocity in x-direction
x_{CG}	Longitudinal position of C.O.G
Z	Number of propeller blades
z_{CG}	Vertical position of C.O.G
Δ	Ship displacement
$\Delta Ø$	Roll angle decrement
Δt	Simulation time step
ζ	Absolute free-surface elevation
λ	Wave length
ω	Specific dissipation rate of turbulent frequency
ω	Wave circular frequency
E	Absolute error
K	Kinetic energy
$P(t)$	Fourier transform parameter
S	Control surface in fluid governing equation
V	Control volume in fluid governing equation
c	Volume fraction coefficient
n	Propeller rotation rate
p	Pressure field
u	Fluid velocity in x-direction
v	Fluid velocity in y-direction
w	Fluid velocity in z-direction
$\mathcal{D}(\,)$	Divergence operator
∇	Volume of displacement
β	Modeling coefficient for k-ω turbulence model
γ	Surface tension
ε	Turbulent energy dissipation
$\varepsilon\%$	Relative error
μ	Viscosity
ρ	Mass density of fluid
σ	Sinkage
τ	Trim

Abbreviations

A.P.	Aft Perpendicular
ABKV	Aft-Body Keel Vortices
AIAA	American Institute of Aeronautics and Astronautics
ALE	Lagrangian-Eulerian
ASM	Algebraic Stress Model
AW	Active Wall
BEM	Boundary Element Method
BKV	Bilge Keel Vortices
BSV	Bottom-Shaft Vortices
CAD	Computer Aided Design
CFD	Computational Fluid Dynamic
CFL	Courant–Friedrichs–Lewy number
CMT	Circular Motion Test
CPU	Central Processing Unit
DARPA	Defense Advanced Research Projects Agency
DDES	Delayed Detached Eddy Simulation
DES	Detached Eddy Simulation
DHRL	Dynamic Hybrid RANS/LES
DNS	Direct Numerical Simulation
DOF	Degrees of Freedom
DTMB	David Taylor Model Basin
DTRC	David Taylor Research Center
DW	Disabled Wall
EASM	Explicit Algebraic Stress Model
EEDI	Energy Efficiency Design Index
EEO	Energy Efficiency Operational Indicator
EFD	Experimental Fluid Dynamic
ESD	Energy Saving Devices
F.P.	Forward Perpendicular
FBKV	Fore-Body Keel Vortices
G2K	Gothenburg 2000 Workshop on Computational Ship Hydrodynamics
GD	General Domain
GHG	Green-House Gases
HMRI	Hyundai Maritime Research Institute
HPC	High Performance Computing
HSVA	Hamburgische Schiffbau-Versuchsanstalt (Hamburg Ship Model Basin)
IDB	International Data Base
IDDES	Improved Delayed Detached Eddy Simulation
IIHR	Iowa Institute of Hydraulic Research
IMO	International Maritime Organization
INSEAN	Istituto Nazionale per Studi Ed Esperienze di Architettura Navale
ITTC	International Towing Tank Conference
JBC	Japan Bulk Carrier
KCS	KRISO Container Ship
KRISO	Korea Research Institute of Ships and Ocean Engineering
KVLCC	KRISO Very Large Crude Carrier
LBM	Lattice Boltzmann Method
LDV	Laser Doppler Velocimetry
LES	Large Eddy Simulation
LIF	Laser Induced Fluorescence

MAC	Marker-And-Cell
MARIN	Maritime Research Institute of Netherlands
MEPC	Marine Environment Protection Committee
MOERI	Maritime and Ocean Engineering Research Institute
NMRI	National Maritime Research Institute
NSE	Navier-Stokes Equations
NSWC	Naval Surface Warfare Center (Carderock Division)
NTNU	Norwegian University of Science and Technology
ONRT	Office of Naval Research Tumblehome
OU	Osaka University
PISO	Pressure-Implicit with Splitting of Operators
PIV	Particle Image Velocimetry
PMM	Planar Motion Mechanism
POW	Propeller Open Water
PTV	Particle Tracking Velocimetry
RANS	Reynolds-Averaged Navier-Stokes
RANSE	Reynolds-Averaged Navier-Stokes Equations
RAO	Response Amplitude Operator
RE	Richardson Extrapolation
RSM	Reynolds Stress Model
RTV	Rudder Tip Vortices
SDV	Sonar Dome vortices
SIMMAN	Workshop on Verification and Validation of Ship Manoeuvring Simulation Methods
SIMPLE	Semi-Implicit method for Pressure-Linked Equations
SPIV	Stereo Particle Image Velocimetry
SST k-ω	k-ω Shear Stress Transport turbulence model
SV	Shaft Vortices
TKE	Turbulent Kinetic Energy
URANSE	Unsteady Reynolds-Averaged Navier-Stokes Equations
VLM	Vortex Lattice Method
VOF	Volume Of Fluid

List of Figures

		Pg.
Figure 1.1	Classification of methods used in viscous computational hydrodynamics	8
Figure 1.2	The development of CFD in ship hydrodynamics	12
Figure 2.1	General CFD process	36
Figure 3.1	Sources of errors in CFD results	37
Figure 3.2	Geometrically similar grid for a simple cube configuration	47
Figure 3.3	Geometrically similar grids for the JBC ship model	48
Figure 4.1	JBC model geometry highlighting stern, fore, duct, propeller and rudder	50
Figure 4.2	Computational domain, dimensions and boundary conditions	51
Figure 4.3	Computational grid, showing: (a) JBC with ESD, (b) duct and strut, (c) free-surface refinement, (d) fore and (e) stern comparison between fine and coarse grids	53
Figure 4.4	Computed total resistance coefficient C_T with: (a) JBC w/o. ESD, (b) JBC w. ESD and (c) Richardson Extrapolation error	56
Figure 4.5	Computed free-surface at T=30 s, showing: (a) free-surface configuration, (b) mass fraction, (c) CFD vs. EFD for the free-surface topology, (d, e and f) CFD vs. EFD for wave profile at the hull, at distances y/L_{PP}=0.1043 and y/L_{PP} =0.19, respectively	57
Figure 4.6	PIV measuring sections	58
Figure 4.7	EFD and CFD results for the axial velocity contours computed at T=30s for ship without ESD at section S2 using different turbulence models	59
Figure 4.8	Section S4 EFD and CFD results for the axial velocity contours computed at T=30s for ship without ESD using different turbulence models	59
Figure 4.9	Section S7 EFD and CFD results for the axial velocity contours computed at T=30s for ship without ESD using different turbulence models	60
Figure 4.10	Comparison between the streamwise velocity contours measured and computed at T=30 s using EASM turbulence model for ship with ESD for sections S2, S4 and S7	60
Figure 4.11	Workshop data for the second invariant iso-surface Q^*=25 colored by helicity and the corresponding CFD results computed at T=30 s using EASM model	61
Figure 4.12	KVLCC2 model geometry highlighting propeller and rudder	62
Figure 4.13	Discretization grid for ship with; simplified rudder (left) and actual rudder (right)	64
Figure 4.14	Obtained results for ship without rudder: (a) Computed total resistance coefficient C_T compared to the EFD, (b) estimated error as a function of grid density	64

Figure 4.15	CFD results compared to EFD showing: (a) total resistance coefficient C_T (b) sinkage σ and (c) trim τ	65
Figure 4.16	Free-surface topology (left), and wave cuts at y/L_{pp}=-0.0964 and -0.1581(right)	66
Figure 4.17	CFD vs. EFD streamwise velocity contours at sections: x/L_{pp}=0.85 and 0.9825	66
Figure 4.18	Velocity and TKE contours in the wake	67
Figure 4.19	Second invariant iso-surface Q^*=25 colored by non-dimensional helicity	67
Figure 4.20	DTMB model geometry viewing: front, profile, bottom and rear	68
Figure 4.21	Computational grids showing: (a) Fine and coarse grids, (b) free-surface refinement and (c) a forward section	70
Figure 4.22	Total resistance results based on the grid density	71
Figure 4.23	Total resistance error computed for Fr=0.28 based on the wall treatment approach	72
Figure 4.24	Free-surface profile (left), and wave cuts at y/L_{pp}=0.082 and y/L_{pp}=0.172 (right)	73
Figure 4.25	CFD vs. EFD streamwise velocity contours at different sections	74
Figure 4.26	Discretization grid highlighting the appendages refinement	75
Figure 4.27	Resistance results for the fully appended ship and hull components individually	76
Figure 4.28	Free-surface profiles for bare and appended hull	77
Figure 4.29	Comparison between bare and appended hull for axial velocity contours (U) and Turbulent Kinetic Energy (TKE)	79
Figure 4.30	Second invariant iso-surface Q^*=10 colored by non-dimensional helicity bottom view: (a) Bare hull, (b) appended hull, and (c) appended hull profile	80
Figure 4.31	Ship model and the towing carriage arrangement	82
Figure 4.32	Free-surface topology at ship extremities during the test: bow (left), stern (right)	84
Figure 4.33	Extrapolated data of the UGAL – Model compared to INSEAN – Model	85
Figure 4.34	Wave pattern for active tank walls domain showing wave reflection at the wall	87
Figure 4.35	Wave elevation diagram: (a) general domain, (b) active walls domain	88
Figure 4.36	The numerically predicted against the measured free-surface profile at model extremities	88
Figure 5.1	Simulation domain dimensions and boundary conditions in *x-z* and *y-z* view	91
Figure 5.2	Discretization grids for the finest grid illustrating blades grid and refinement zone	92
Figure 5.3	Thrust coefficient K_T, torque coefficient K_Q and propeller open water efficiency η curves compared to EFD data	93
Figure 5.4	Pressure distribution on the suction and pressure sides of the propeller at different advance ratios J: a) J=0.7, a) J=0.5, a) J=0.3 and a) J=0.1	93

Figure 5.5	Axial flow velocity, pressure distribution, turbulent viscosity and TKE in the propeller wake for J=0.3 and J=0.6	94
Figure 5.6	Vortical structure of the wake flow computed at T=5 sec. for: (a) J=0.3, (b) J=0.6	95
Figure 5.7	Longitudinal cut in the vortical structure of the wake flow at J=0.6	95
Figure 5.8	Computational domain and boundary conditions for self-propulsion simulation	96
Figure 5.9	Sliding grid arrangement for JBC without ESD (left) and with ESD (right)	97
Figure 5.10	Grid arrangement for: actuator disk(left) and sliding grid (right) approches	98
Figure 5.11	CFD results for nominal (a and b) and effective (c and d) velocity contours computed for ship without and with ESD, respectively, using actuator disk method	100
Figure 5.12	Results interpolation to predict the propeller revolution rate	101
Figure 5.13	Comparison between the streamwise velocity contours measured and ship without ESD for sections S4 and S7	102
Figure 5.14	Comparison between the streamwise velocity contours for ship without ESD and the second invariant Q^*=50 for ship with and without rudder, computed using DES turbulence model	103
Figure 5.15	Mesh arrangement of the fine grid	105
Figure 5.16	Open water propeller performance curves CFD results against EFD data	106
Figure 5.17	Vorticity at J=0.2: (a) vector form, (b) magnitude, (c) trajectory and (d) vortex cores	106
Figure 5.18	Second invariant computed for J=0.2 based on different turbulence models for iso-surface=500	107
Figure 5.19	Flow characteristics computed for J=0.2 based on DDES turbulence model	107
Figure 5.20	Second invariant computed for J=0.4 based on different turbulence models for iso-surface=250	108
Figure 5.21	Flow characteristics computed for J=0.4 based on DDES turbulence model	108
Figure 5.22	Second invariant computed for J=0.6 based on different turbulence models for iso-surface=125	109
Figure 5.23	Flow characteristics computed for J=0.6 based on DDES turbulence model	109
Figure 5.24	Grid geometry for actuator disk approach (top) and fully discretized propeller (bottom) highlighting the propeller and rudder	111
Figure 5.25	Prediction of the self-propulsion point using interpolation method	112
Figure 5.26	Streamwise velocity contours comparison between CFD and EFD	113
Figure 5.27	Vortices formation in the wake showing the profile and bottom view	113
Figure 6.1	Domain geometry, dimensions and boundary conditions	117
Figure 6.2	Grid configuration showing: stern, bow, longitudinal section free-surface top view	118

Figure 6.3	Resistance C_T, Heave C_H and Pitch C_M coefficients compared to EFD	119
Figure 6.4	Grid resolution effect on the total resistance coefficient	120
Figure 6.5	Comparison between the time history of the total resistance based on wave steepness for *Ak* = 0.025, 0.050 and 0.075	120
Figure 6.6	Schematic diagram for the quartering wave instants corresponding to the encountering moment with the F.P. of the ship	121
Figure 6.7	Computed free-surface at four wave quarters compared EFD	121
Figure 6.8	Wave visualisation at the bow and stern of the ship for *Ak=0.075* at different encountering instants	122
Figure 6.9	Wave profile and mass fraction for *Ak=0.075* when the peak and trough encounter F.P., from left to right, respectively	122
Figure 6.10	Relative velocity contours at x/L_{PP}=0.935 and t t/T=0 compared to EFD	123
Figure 6.11	Streamwise velocity contours for different wave steepness	123
Figure 6.12	Total resistance coefficient C_{TW} computed based on grid convergence study for C1	126
Figure 6.13	Heave response computed based on the grid convergence study for C1	127
Figure 6.14	Pitch response computed based on the grid convergence study for C1	128
Figure 6.15	Added resistance in wave schematic representation	129
Figure 6.16	Unsteady signal of the total resistance time history at λ=1.0 L_{pp} and λ=1.25 L_{pp}	130
Figure 6.17	RAO for: (a) heave and (b) pitch compared to EFD data [87] at cases2~8	130
Figure 6.18	Relative wave elevation computed for free and fixed ship conditions	132
Figure 6.19	Free surface profile and mass fraction computed for case C11 at Fr=0.41	132
Figure 6.20	Hull wave interaction at t/T=0 and t/T=0.5	133
Figure 6.21	Relative velocity contours at x/L_{PP}=0.935 and t/T=0 compared to EFD	133
Figure 6.22	Axial velocity contours computed at equal distances Δx=0.1L_{pp}, and second invariant iso-surface=50 at a random momewnt during simulation	134
Figure 6.23	Vortices formation in wave at t/T=0 and 0.5 compared to calm water	133
Figure 6.24	Simulation domain and boundary conditions	136
Figure 6.25	Finest grid discretization, spotting: (a) 3D hull; (b): longitudinal section; (c,d): lateral section depicting the refinement boxes around the hull and bilge keels; (e): the free-surface refinement section top view	137
Figure 6.26	Time history for roll simulation at altered initial roll angles	139
Figure 6.27	Fitted decay curves for computed results compared to EFD data	140
Figure 6.28	Time history for roll decay based on: (a) grid & (b) time step convergence tests	141
Figure 6.29	Free-surface topology recorded in the second roll period at the four quarters in case of initial roll angle $Ø_0$=10 and Fr=0.28	142
Figure 6.30	Time history for roll decay curves corresponding to various ship speeds	143
Figure 6.31	Computed free-surface at the 6th roll for various ship speeds	143
Figure 6.32	Computed and measured velocity contours at x/L_{pp}=0.675 for the second roll period instances: (a) t/T=0.5; (b): t/T=0.75	144
Figure 6.33	Vortices formations during the roll period quarters showing: (a) ship bottom, (b, c) starboard port sides, respectively for t/T=0	145

Figure 6.34	(a): U contours, (b): TKE contours and (c): Q*=25 second invariant visualized at section x/L_{pp}=0.675 at 8 segments of the roll period	147
Figure A.1	Main components of the ship hydrodynamics computational methods	169
Figure A.2	Hierarchy of turbulence models based on physical modeling and computational cost	171
Figure A.3	Most popular turbulence models used in CFD applications	176
Figure A.4	Height function for a 2D open interface	179
Figure A.5	Interface representation using MAC method	180

List of Tables

		Pg.
Table 3.1	Geometrically similar grids parameters for a cube	47
Table 4.1	Principal particulars of ship and duct	50
Table 4.2	Boundary conditions for open boundaries and solid walls	52
Table 4.3	Computational grids	53
Table 4.4	C_T results computed at T=30s Compared to EFD data	54
Table 4.5	Sinkage and trim results computed at T=30s Compared to EFD data	54
Table 4.6	Grid convergence parameters for total ship resistance Coefficient C_T	55
Table 4.7	Validation data for total ship resistance Coefficient C_T	55
Table 4.8	Principal particulars of ship and rudder	62
Table 4.9	Computational cases and corresponding ship speed parameters	63
Table 4.10	Computational grids for ship with and without rudder	64
Table 4.11	Grid convergence parameters for total ship resistance Coefficient C_T	65
Table 4.12	DTMB ship models and full scale characteristics	69
Table 4.13	Computational cases and corresponding ship speed parameters	69
Table 4.14	Computational grids for ship based on the wall treatment modeling	70
Table 4.15	Verification and validation parameters for total ship resistance in the wall modeled case	71
Table 4.16	Sinkage and trim results	72
Table 4.17	Computational grids for ship based on the wall treatment modeling	75
Table 4.18	Total resistance computed for the appended hull and appendages drag force	75
Table 4.19	Total resistance coefficient C_T computed for the bare hull component compared to EFD data	76
Table 4.20	Sinkage and trim values computed for the fully appended hull compared to the measured value	77
Table 4.21	Test cases and corresponding ship speed parameters	81
Table 4.22	Measured total resistance and corresponding resistance coefficients	82
Table 4.23	Extrapolated data from the UGAL model to the INSEAN model scale	84
Table 4.24	Total resistance comparison between CFD and EFD results	86
Table 5.1	Principal characteristics and parameters of the JBC propeller	90
Table 5.2	POW simulation cases and flow parameters	91
Table 5.3	Computational grids	92
Table 5.4	Number of grid cells based on simulation conditions and grid density	97
Table 5.5	Self-propulsion results for ship with and without ESD based on actuator disk method	99
Table 5.6	Self-propulsion coefficient for ship with and without ESD using sliding grid method	101
Table 5.7	Self-propulsion results for ship with and without rudder	102
Table 5.8	Principal particulars of KVLCC2 E698 propeller model	104
Table 5.9	Computational grids for the self-propulsion simulation	110
Table 5.10	Thrust and torque coefficients computed using the actuator disk method compared to the EFD data extracted	111
Table 5.11	Interpolation of the propeller rotation based on resistance and thrust results	112
Table 6.1	Simulation conditions and corresponding wave parameters	117
Table 6.2	Computed versus measured C_T, C_H, C_M coefficients	119
Table 6.3	Simulation cases parameters and corresponding grid density	124

Table 6.4	Grid convergence parameter for the total resistance coefficient in wave $C_{Tw\text{-}G}$	126
Table 6.5	Time step convergence parameter for the total resistance coefficient in wave $C_{Tw\text{-}T}$	126
Table 6.6	Grid convergence parameter for the heave response	127
Table 6.7	Time step convergence parameter for the heave response	127
Table 6.8	Grid convergence parameter for the pitch response	128
Table 6.9	Time step convergence parameter for the pitch response	128
Table 6.10	Validation parameter for resistance in wave, heave and pitch in C1	129
Table 6.11	Added resistance in waves for cases C2~C8	130
Table 6.12	Heave and pitch responses in at different *Ak* from C9	131
Table 6.13	Grid arrangement for the grid convergence study	138
Table 6.14	Computed results for roll amplitudes compared to EFD data and corresponding average and mean values for decay fitting curves	140
Table 6.15	Grid convergence study parameters	141
Table 6.16	Time step convergence study parameters	141
Table 6.17	Results for validation test	141
Table 7.1	Ship performance contribution in the present study	154

Table of Contents

Acknowledgments i
Nomenclatures i
Abbreviations v
List of Figures vii
List of Tables xii
Table of Contents xiv
Chapter I 1
Introduction 1
1.1 Motivation 1
1.2 Background 2
1.3 Literature Review 4
1.3.1 Resistance 5
1.3.2 Propulsion 12
1.3.3 Seakeeping 16
1.3.4 Maneuvering 19
1.4 Scope and Objectives 20
1.5 Structure of the Book 22
Chapter II 25
Mathematical Model 25
2.1 Governing Equations 26
2.2 Turbulent Closure Equations 27
2.2.1 Menter Two-Equation Model $\boldsymbol{k-\omega}$ SST [110] 28
2.2.2 Explicit Algebraic Stress Model (EASM) [110] 29
2.3 Boundary Conditions 31
Solid Body (Ship Hull) 32
Free-Surface 32
Infinity 33
The Turbulence Model 33
2.4 CFD Process 34
Chapter III 37
Verification and Validation 37

3.1 Verification and Validation Concept 38
3.2 Verification Methodology 40
Iterative uncertainty and errors 41
Convergence uncertainty and errors 42
3.2.1 Generalized Richardson Extrapolation (RE) 43
3.2.2 Estimating Errors and Uncertainties with Correction Factor 44
3.2.3 Estimating Uncertainties with Factor of Safety 45
3.3 Validation Methodology 45
3.4 Unstructured Grid Generation for Verification and Validation Studies 46
Chapter IV 49
Ship Resistance Performance 49
4.1 Japan Bulk Carrier (JBC) 50
4.1.1 Analysis Conditions 51
4.1.2 Domain & Boundary Conditions 51
4.1.3 Computational Grids 52
4.1.4 Simulation Strategy 53
4.1.5 Resistance and Motion Results 54
4.1.6 Free-Surface Results 56
4.1.7 Local Flow Results 57
4.2 KRISO Very Large Crude Carrier (KVLCC2) 62
4.2.1 Analysis Conditions 63
4.2.2 Domain & Boundary Conditions 63
4.2.3 Computational Grids 63
4.2.4 Resistance and Motion Results 64
4.2.5 Free-Surface Results 66
4.2.6 Local Flow Results 66
4.3 David Taylor Model Basin (DTMB) Surface Combatant 68
4.3.1 Bare Hull Ship Model 69
4.3.1.1 Analysis Conditions 69
4.3.1.2 Domain & Boundary Conditions 69
4.3.1.3 Computational Grids 70
4.3.1.4 Resistance and Motion Results 70
4.3.1.5 Free-Surface Results 73

4.3.1.6 Local Flow Results 73
4.3.2 Appended Hull Ship Model 74
4.3.2.1 Analysis Conditions 74
4.3.2.2 Domain & Boundary Conditions 74
4.3.2.3 Computational Grids 74
4.3.2.4 Resistance and Motion Results 75
4.3.2.5 Free-Surface Results 77
4.3.2.6 Local Flow Results 77
4.3.3 Experimental Test 81
4.3.3.1 Experiment Setup 81
4.3.3.2 Resistance Measurements 82
4.3.3.3 Free-Surface Measurements 83
4.3.3.4 Measurements Validation 84
4.3.3.5 CFD Approach 85
Chapter V 89
Ship Propulsion Performance 89
5.1 Propulsion Performance of the JBC 90
5.1.1 Propulsion Performance in Open Water 90
5.1.1.1 Analysis Conditions 90
5.1.1.2 Domain & Boundary Conditions 91
5.1.1.3 Computational Grids 91
5.1.1.4 Simulation Strategy 92
5.1.1.5 Thrust and Torque Results 92
5.1.1.6 Wake Flow Analysis 94
5.1.2 Self-Propulsion Simulation 96
5.1.2.1 Analysis Conditions 96
5.1.2.2 Domain & Boundary Conditions 96
5.1.2.3 Computational Grids 97
5.1.2.4 Simulation Strategy 97
5.1.2.5 Self-Propulsion Results 98
5.2 Propulsion Performance of the KVLCC2 104
5.2.1 Propulsion Performance in Open Water 104
5.2.1.1 Analysis Conditions 104

5.2.1.2 Domain & Boundary Conditions 104
5.2.1.3 Computational Grids 105
5.2.1.4 Simulation Strategy 105
5.2.1.5 Thrust and Torque Results 105
5.2.1.6 Local Flow Results 106
5.2.2 Self-Propulsion Performance 110
5.2.2.1 Analysis Conditions 110
5.2.2.2 Domain & Boundary Conditions 110
5.2.2.3 Computational Grids 110
5.2.2.4 Simulation Strategy 110
5.2.2.5 Thrust and Torque Results 111
5.2.2.6 Local Flow Results 112
Chapter VI 115
Ship Seakeeping Performance 115
6.1 Seakeeping Performance in Regular Head Waves 116
6.1.1 Seakeeping in Wave Diffraction Condition 116
6.1.1.1 Analysis Conditions 116
6.1.1.2 Domain & Boundary Conditions 117
6.1.1.3 Computational Grids 118
6.1.1.4 Simulation Strategy 119
6.1.1.5 Resistance, Forces and Moments Results 119
6.1.1.6 Free-Surface Results 120
6.1.1.7 Local Flow prediction 123
6.1.2 Seakeeping in Wave Radiation Condition 124
6.1.2.1 Analysis Conditions 124
6.1.2.2 Domain & Boundary Conditions 125
6.1.2.3 Computational Grids 125
6.1.2.4 Simulation Strategy 125
6.1.2.5 Results 125
6.2 Roll Decay Performance in Calm water 136
6.2.1 Simulation Conditions 136
6.2.2 Domain & Boundary Conditions 136
6.2.3 Computational Grids 137

6.2.4 Simulation Strategy 138
6.2.5 Roll Motion Results 138
6.2.6 Free-Surface Analysis 141
6.2.7 Local Flow Analysis during Roll Damping 144
Chapter VII 149
Conclusions, Contributions and Recommendations 149
7.1 Concluding Remarks 150
For resistance performance 150
For propulsion performance 151
For Seakeeping performance 152
7.2 Personal Contributions 153
7.3 Recommendations and Future Perspectives 157
References 159
Appendix A 169
Numerical Methods used in Ship Hydrodynamics Applications 169
A.1. Physical Modeling 170
A.1.1 Flow Modeling 170
A.1.2 Turbulence Modeling 170
A.1.2.1 Direct Numerical Simulation (DNS) 171
A.1.2.2 Large Eddy Simulation (LES) 171
A.1.2.3 Hybrid RANS/LES (HRL) 172
A.1.2.4 Reynolds-Averaged Navier Stokes (RANS) 173
A.2 Numerical Modeling 176
A.2.1 Reference Frames 176
A.2.2 Spatial Discretization 176
A.2.3 Temporal Discretization 177
A.2.4 Grid Generation 178
A.2.5 Interface Modeling 178
A.2.6 Velocity-Pressure Coupling 181

Chapter I
Introduction

1.1 Motivation

Prediction of the ship hydrodynamic performance is of a major importance in modern ship design. Understanding all related problems of a moving ship, whether in calm water or in waves, is essential to enhance and optimize ship performance to meet the design challenges of the 21st century, especially from safety, economy and energy efficiency point of view. The continuous development in the maritime industry increases the demand for more complex geometries and rather intricate design requirements. A need of a robust, flexible and reliable tool to achieve a proper balance between design requirements and design constraints is significantly important.

The past three decades showed a considerable growth of interest in Computational Fluid Dynamic (CFD) as an alternative tool for experimental and empirical based approaches; not just on an academic base, but also for industrial purposes. This progress has reached the milestones of providing the first concept of simulation-based design with extensive capabilities for all ship hydrodynamics problems in both model and full-scale simulations. The broad availability of commercial software, as well as the recent techniques developed for CFD applications gave a proper definition of the physical phenomena, which resulted in higher level of accuracy and more realistic solutions. The currently used methods such as the free-surface modeling (capturing/tracking), turbulence modeling, sliding and overset grid techniques, six Degrees of Freedom (DOF) motions simulations, High Performance Computing (HPC) and automated optimization methods made it possible to cover, not just the main fields of ship hydrodynamics represented by the resistance, propulsion, seakeeping and maneuvering, but also more complicated scenarios such as the stability, capsizing, flooding and interaction between ships. Nevertheless, to increase the fidelity of the numerical results, a continuous improvement of the numerical methods, besides a systematic verification and validation procedures are absolutely necessary.

Following this remarkable success in CFD, especially in model scale simulations, the so-called Numerical Towing Tank (or Virtual Towing Tank) term has begun to impose alongside with classic experimental towing tanks. This technique is widely recognized nowadays, at the level of the most famous maritime organizations, such as the International Maritime Organization (IMO) and the International Towing Tank Conference (ITTC). The latter started recently to provide recommended practice and standardization procedures for CFD codes as it used to do for the Experimental Fluid Dynamic (EFD) since the day of its establishment. The results achieved in CFD are recently used by the IMO to provide new regulations for the assessment of minimum propulsion power to maintain maneuverability under adverse conditions [1]. Still, due to some complications regarding the numerical modeling of the nonlinear flow around the ship, which in some applications cannot avoid the use of approximations or simplified assumptions, and sometimes ignores less important phenomena, these simplifications may generate less accurate results or discrepancies between the CFD solutions and the EFD data or sea trials. Nevertheless, the continuous development in CFD codes associated with the huge development of the

computational power is expected to cover more areas of the hydrodynamics and provide more capabilities with fewer approximations.

Taking advantage of the aforementioned opportunities and merits of CFD, and taking into account the present level of accuracy of the numerical solutions, in this study extensive numerical simulations are performed on different types of ships, all aimed at investigating the possibilities of a unique CFD code to solve different ship hydrodynamic problems. The accuracy of the obtained solutions is rigorously investigated through a systematic verification and validation techniques. The global target of these numerical simulations is to predict, where applicable, the forces acting on the hull of the ship under investigation and the flow configurations around that hull, to provide a proper understanding of the physical phenomena and help finding engineering solutions for improving and optimizing the ship hydrodynamic performance in general.

1.2 Background

Ship hydrodynamics is by definition concerned with the flow around a given hull and the associated loads induced by the flow itself. Mainly, the attempt to solve a ship hydrodynamic problem is usually focused on calculating the global pressure and the three-dimensional velocity components, not only on the submerged part of the ship, but also in the immediate vicinity of it. The further step is to integrate the pressure to compute the forces and moments acting on the hull. Predicting ship hydrodynamic performance can conventionally be divided into four major areas of scientific interest: resistance, propulsion and powering, seakeeping and maneuvering. As mentioned above, any review of the state-of-the-art in the field reveals two different techniques employed to predict the hydrodynamic performance: experimental and theoretical based methods. The former uses experimental modeling of the physical problem, such as in towing tank and cavitation tunnel tests or full-scale trials, while the latter uses the theoretical-based approaches to either analyze the data from tank tests, resulting in an analytical technique, or for using the numerical modeling, such as in the case of CFD.

The history of the experimental approach goes back to the Renaissance age, when Leonardo da Vinci performed tests on three models of ships having three different geometries [2]. Later, other tests were performed by Benjamin Franklin, Frederick Chapman, Jean d'Alembert, the Marquis de Condorcet, the Abbé de Bossut and Mark Beaufoy [3, 4]. Unfortunately, their effort has never been recognized, since no one succeeded to find a physical correlation between the model results and the full-scale ship until 1868, when the first approach to predict ship resistance from a model experiment was proposed by the British naval architect William Froude [5, 6]. His hypothesis stated the foundation of ship resistance calculations that are still in use nowadays. The basic principle he proposed was based on dividing the total resistance into two components: the frictional resistance and the wave-making resistance. He assumed that the frictional component is equivalent to the drag of a flat (plank) plate with the same length and wetted surface area as the ship and having the same speed, while the wave-making component results by subtracting the frictional drag from the total model resistance. As a result to Froude's success, by the end of the 19th century, several model basins were built all over the world to host model ship experiments, including special purpose tanks for applications like propeller performance, seakeeping and maneuvering.

Different facilities around the world had a significant interest in systematic experiments, which indeed led to continuous discussions regarding consistency and standardization. In 1933,

23 tank representatives from 10 different countries including 9 tank superintendents gathered for the first time in the Conference of Ship Tank Superintendent with the scope of discussing their own methods and publishing their tank results. This conference was later called the ITTC, which became as one of the most important maritime organizations that has always been and still is spending tremendous efforts to standardize the tank testing procedures as to impose a unified methodology for reporting the experimental results [7].

The EFD has evolved continuously through the past decades, which resulted recently in an extreme progress in predicting the associated physical phenomena, such as the boundary layer formation, velocity and pressure distributions, free-surface profiling, cavitation occurrence and hull motion development, based on the remarkable improvements of optical techniques, e.g. Particle Image Velocimetry (PIV), Particle Tracking Velocimetry (PTV), Laser Doppler Velocimetry (LDV), Laser Induced Fluorescence (LIF) and on the continuously increasing computer power [8]. Despite the development of the model testing facilities, and the high level of credibility in the test results, the experiments became significantly complex, requiring highly qualified personnel, they are very expensive and time-consuming processes. Recently, the overall reliance on this is waved towards the final stage model development or to the numerical solutions validation.

The statistical- and empirical-based methods were based on two different concepts: the use of systematic hull and propeller series and on the use of statistical data. The systematic series were developed based on a witnessing hull form called “parent” ship. The hull parameters are varied systematically to provide a similar ship from the hydrodynamic performance point of view. An example for this technique is the Taylor Standard Series, which was derived based on the results of extensive model tests that were performed between 1907 and 1914, for systematic variations of a parent form of the “Leviathan” hull ship that was designed in 1900 [9]. Some modifications on Taylor’s series were proposed by Gertler in 1954, based on reanalyzing the original data by using the Schoenherr’s friction line, which includes some specific particulars that were ignored in the first series, such as the water temperature, tank blockage effect and flow turbulence [10]. Later on, perhaps one of the newest systematic series was proposed in the mid-1970s, based on an extensive series of tests held in Delft for up to 50 sailing yachts models. More details about this series are given in [11].

As far as the statistical methods are concerned, a conclusive example for the unsystematic analysis of data was the formula proposed by Doust & O’Brien [12], in which they succeeded to derive a formula for the ship resistance based on a series of resistance tests performed for 150 fishing vessels. The hydrodynamic resistance was expressed as a function of speed-length ratio and based on different six shapes parameters, resulting in a second order polynomial. Nevertheless, their polynomial representation was nothing more than a numerical fitting problem, without including any physics behind. That was addressed lately in the Holtrop & Mennen method [13], which represented at that time a theoretical formulation by considering the wave resistance as being produced by two different pressure disturbances from the bow and stern of the ship. The approach included different coefficients that were derived from regression of 334 ships. The Holtrop-Mennen method is still used successfully until now by some design codes as a quick and effective theoretical method to predict the ship resistance in the preliminary design stage. In spite of its apparent attractiveness, it is considered as obsolete [14] mainly because it does not allow much flexibility in taking decisions for a new concept design. Besides, it is only concerned with the forces and moments acting on the hull, while the flow configurations and free-surface are completely disregarded.

The numerical-based methods started to take place in the late 1950s and were basically restricted with the computational power. However, after the advent of computers, the CFD method was implemented in marine hydrodynamics in the mid-1970s following its remarkable success in the aerodynamics field at that time. The largest majority of CFD solvers were initially based on potential flow due either to the limited computation capacity that was available in that era or to the insufficient development of appropriate numerical methods. The largest majority of CFD solvers nowadays implement the Reynolds-Averaged Navier-Stokes Equations (RANSE hereafter) with a wide range of turbulence models that can help the accurate prediction of the flow characteristics around the hull as well as the free-surface topology and wake flow structure. Recent research are based on Large Eddy Simulation (LES hereafter) or a hybrid RANSE and LES as a solution to reduce the needed number of cells in the far field which is known as Detached Eddy Simulation (DES hereafter). Most recently, the Direct Numerical Simulation (DNS hereafter), which includes the direct solution of Navier-Stokes Equations (NSE hereafter) without further assumptions for turbulence, is being used for relatively limited applications in ship hydrodynamics because it proved to be prohibitory expensive; yet, it is expected to gain more popularity in the coming decades.

1.3 Literature Review

In the followings, the most spectacular CFD achievements in the field of ship hydrodynamics will be reviewed separately for the four main areas previously mentioned, i.e., resistance, propulsion, seakeeping, and maneuvering, respectively. To make the review more specific to the scope of the present research studies, a special focus on the viscous flow solution of the NSE will be provided, aimed at covering as much as possible the specificity of the ship hydrodynamic solvers since they represent the basic tool used in the work performed in the following chapters of the present book. The alternative techniques such as experimental, empirical, theoretical or potential based methods are also reviewed but without entering into too many details, just to highlight their strengths and drawbacks.

Taking a closer look in the former research in the numerical ship hydrodynamics field, one can observe three referential milestones that marked the scientific progress. All three represent global references for networking and sharing advancements in the domain of naval architecture and maritime technology. The first is the Symposium on Naval Hydrodynamics which was established by the U.S. Office of Naval Research in 1956 and repeated every two years since then. Being a subject-free forum, the symposium set the stage for scientific debates related to the wave-induced ship motions and loads, wake dynamics, frontier experimental techniques, viscous ship hydrodynamics, water entries, wave hydrodynamics/stratified flow, bluff bodies' hydrodynamics, shallow water hydrodynamics, cavitation and bubbly flows, propulsor hydrodynamics/hydro-acoustics, CFD validation and so on. The symposium proceedings have always provided archival documentation of state-of-the-art research and development in naval hydrodynamics. Nowadays the symposiums have already reached its 32th edition being the repository of more than 25000 pages of first-hand valuable research works referred by the community years since.

The second important one is represented by the Workshop on Ship Hydrodynamics, which already reached in 2015 its seventh edition under the multi-party heritage of the Iowa Institute of Hydraulic Research (IIHR) which is recently known as IIHR–Hydroscience & Engineering,

Chalmers University of Gothenburg, Ecole Centrale de Nantes and National Maritime Research Institute (NMRI) of Japan. The very selective event is viewed by the organizers as a fair blind-competition between the enrolled scientific communities on particular given subjects relevant for the field. Being an open competition sustained against the first-hand experimental data freely provided by the most famous authorities in the field, the workshop is regarded nowadays as a compulsory reference point in all the reported progresses in the ship hydrodynamics. From this point of view, the vast majority of results reported in this research study are validated against the available data from the workshops, not only to investigate the accuracy of the obtained results, but also to ensure an up-to-date comparison with the provided solutions from the most recognized research communities in the world.

The third source of comparisons used in these research studies is represented by the third edition of the SIMMAN workshop, jointly organized by Trondheim and Hiroshima Universities, IIHR, Maritime Research Institute of Netherlands (MARIN), FORCE Technology of Denmark, Istituto Nazionale per Studi Ed Esperienze di Architettura Navale (INSEAN) of Italy and Korea Research Institute of Ships and Ocean Engineering (KRISO), proposes to benchmark the capabilities of maneuvering prediction methods through comparisons with towing tank results for a series of hull models such as the KRISO Very Large Crude Carrier (KVLCC), the KRISO Container Ship (KCS), David Taylor Model Basin (DTMB) surface combatant, and the Office of Naval Research Tumblehome (ONRT) modern surface combatant hull form test cases. Similar to the previous workshops in 2008 and 2014, a variety of methods including CFD predictions are available comparing for predictions of ship acting forces and trajectories.

1.3.1 Resistance

The early stage of assessing the associated ship hydrodynamic problems was basically standing for ship resistance and powering due to the need of an accurate estimation of the required power to reach the target design speed. Since the establishment of Froude's principle, the tank testing took the lead in predicting the ship resistance for many decades after that. However, even though the method was shown as being sufficiently accurate for predicting the overall resistance, the wave making component was not clearly defined. A remarkable effort was paid parallel to the development of new towing tank testing techniques and equipment, in advancing complementary analytical approaches meant to derive alternate tools to determine the otherwise unknown components. Early studies delivered by the end of the 19th century and the beginning of the 20th century [15–19] may sustain the statement before. Most of these approaches were mainly based on the regressive data obtained at the towing tank tests.

The first method that can be considered as computational was presented by Michell in the end of the 19th century [20]. Like all other early researchers in the field, he included three different assumptions for his hypothesis: the flow is inviscid; the ship is slender with a vanishingly limited beam and moving in a steady uniform flow. By integrating the fore and aft components of the pressure he computed on the hull, he could derive an expression for the total wave resistance, which was lately known as Michell's integral. To make the problem compliant to the existing mathematical methods and to avoid non-linear terms in his formula, Michell had to linearize the boundary conditions. It first applied the condition for the hull on the centerplane rather than on the solid hull, then the free-surface condition was applied on the non-disturbed free-surface, while the free-surface perturbations resulting from the wave pattern were neglected. Later, an alternative method to linearize the free-surface was proposed by Havelock who introduced the idea of

sources and sinks that he distributed on the centerplane of the hull. Each source was assumed as being proportional to the local waterline angle, positive on the fore body and negative on the aft. Summing up the wave making effect of the sources, the far-field waves could be determined, and thereby the wave resistance [21].

With the computers advent, the analytical approaches loosed in popularity and begun to be used less and less. Due to the limitations of the computational power, the potential flow theory-based methods, in which the flow is considered incompressible, inviscid and irrotational, were seen as a workable alternative for a certain period of time. Most of the research were suited to solve the problem in 2D. The first approach that succeeded to solve the problem for arbitrary 3-D bodies was the method developed by Hess and Smith [22]. The method was simple and fast to solve; nonetheless, it could not be used to solve free-surface flows, and the principle of hull mirroring caused other contradictions that led in some cases to zero resistance.

To solve the free-surface in the potential flow method, a need to model the free-surface mathematically was essential; nevertheless, this was not an easy task without extra assumptions, which lately were referred to as the “free-surface linearization”. Linearization of the free-surface potential flows was introduced, and promising achievements were reported in the mid of the 1970s and later on continued until the beginning of the 1990s. The principle was to replace the unknown quantities by the sum of known estimated quantities and unknown perturbations. This resulted in small perturbation and small higher order quantities that can be neglected. Three different approaches were introduced for free-surface linearization. The first was based on using Kelvin or Havelock source and Neumann boundary condition on the hull. Though the method was later reviewed as versatile and straightforward [23], it comes with high computational effort when evaluating Kelvin source potential at a large number of points. The second method was the thin ship linearization based on the aforementioned Michell’s principle for a vanishingly small beam to length ratio. The method applies Michell’s integral to give a direct definition of the wave resistance. It proved to be useful for applications of ship optimization where the computation time is required to be as small as possible [24]. The third is based on the slow ship linearization, which considers that the flow around the ship with the free-surface has small perturbation in contrast to the ship without the free-surface. The most commonly used method was the Dawson’s method [25] that has proven accurate solutions, as discussed in [26]. Dowson’s method used a source panel method and simple Rankine source potential field. This offered the possibility to use fewer panels on both sides of the free-surface. The first step was to compute double body flow using a panel method, then by using a panel distribution around the hull in still water, velocity components could be obtained by algebraic method. Dawson’s method works well not only for slow ships, but also for faster slender ships and gives more accurate results compared to other methods discussed previously. It also gives better prediction for wave resistance and it may be used for optimization of the fore body. However, sometimes the solution was considered unrealistic because Dawson neglected the radiation condition. Later, he found a solution to this problem by using upstream differencing for longitudinal derivatives of velocity. One more drawback in Dawson’s method was that the numerical errors led to incorrect wavelength estimation, also the low density of panels caused oscillations in the velocity field [26].

Wrapping up, in spite of all those drawbacks discussed before, the linearization of the free-surface flow problem has proven in most of the cases a satisfactory accuracy not only for the ship resistance, but also for the free-surface prediction, at low CPU costs, which is essentially important for common industry needs. Yet, the wave separation and radiation were neglected. That led to

the appearance of nonlinear methods to solve wave resistance problems. A well-recognized effort in this scope was made in [25] and [26]. The nonlinear methods for wave resistance simulations have better advantages than the linearized simulation. For example, in the linearized simulation, the domain is bounded by an undisturbed free-surface; this leads to low accuracy for large bow flares or bulbous bow and flat stern. Moreover, the linearization does not account for sinkage and trim, which might be essential for nonlinear contributions. On the other hand, one of the problems associated with the nonlinear simulations is often associated to the convergence. As said before, until the beginnings of 1990's it was common to avoid divergent solutions of the nonlinear simulations by employing the linearization [27]. The effort that was paid in developing and refining the method reached almost a dead end for further improvements, therefore the viscosity had to be taken further into account [28]. As a final conclusion, one may admit that potential flow methods offer a convenient and relatively simple way of determining general flow patterns and forces around arbitrary bodies in spite of the shortages induced by the inherent disregard of the viscosity that may sometimes affect the overall accuracy of the simulation [29].

A step ahead taken by the naval architecture community was represented by the use of the boundary layer theory in predicting the intrinsic features of the flow around the ship hull. Although restrictive to a very limited domain around the solid surface, the approach allowed a deeper insight into the frictional resistance estimation. The most frequently used technique to predict the boundary layer flow in the late 1970s and early 1980s was the momentum integral method, as mentioned in [30]. The method was successful for the 2D flows, but it was very difficult to extend it for the 3-D flows due to the complexity of modeling the crossflow velocity profile [31]. An alternative approach was developed based on a 3-D boundary layer finite differencing, which could successfully predict the thin boundary layer, but failed to solve the thick layers and large flow separations [32]. It is worth mentioning that in the Ship Boundary Layer Workshop Gothenburg 1980, 17 participating groups submitted their solutions for the two ship models of the HSVA tankers, but only in one case the flow was solved based on RANS, whereas all the rest were mainly based on the boundary layer-based methods (difference and integral). All the submitted solutions could predict properly the boundary layer of the fore part of the hull within a reasonable level of accuracy, but they all failed for the stern and in the wake [33].

A tremendous effort had to be paid in the early days of the numerical hydrodynamics to reduce the computation costs required to solve a given problem. Fig. 1.1 shows the classification of methods used in viscous computational hydrodynamics. Unlike the potential flow method, which implies only the discretization of the hull and water surface, in the viscous flow approach the full domain has to be discretized, therefore this led to a series of restrictions due to the existing computational resources limitations at that time.

Literally speaking, the information in the field is scarce comparing to other science branches. The limited number of journals which refer to a niche domain encouraged the tradition of a continuing custom of reporting the most prominent achievements in periodic scientific happenings such as the symposia held from almost a half of a century, used at a tremendous extent by all those with scientific interests in the field.

The problem of modeling the viscous flow around the ship hull is a challenging task since it is strongly nonlinear, it deals with a moving boundary whose geometry is not known a-priory, it is intensively turbulent and eddies of variable scales must be solved, therefore the viscous numerical solution requires an excessive number of points to discretize the computational domain. The grid requirements for DNS of the NSE for turbulent flows increase with Reynolds number. The

Reynolds number varies from $Re \sim 10^6$ for a simulation at a model scale to $Re \sim 10^9$ at full scale, therefore the discretization would require 10^{13} and 10^{20} grid points, respectively. However, the current high performance computing capabilities only allow a maximum number of 10^9 grid points [35], a fact that restricts its use in common applications. Obviously, the limitations of the DNS use are due to the fact that the number of grid points needed for sufficient spatial resolution scales is proportional to $Re^{9/4}$, whereas the CPU-time is of an order of Re^3. This does not mean that DNS is completely useless. It represents an important tool for understanding transition to the turbulence as well as the turbulent structures development and evolution in time and space. DNS also plays a vital role in the development and calibration of new or improved turbulence models [32]. However, for the time being, in common engineering applications closure to the turbulence can only be achieved approximately, by employing statistical-based models of various degrees of complexity.

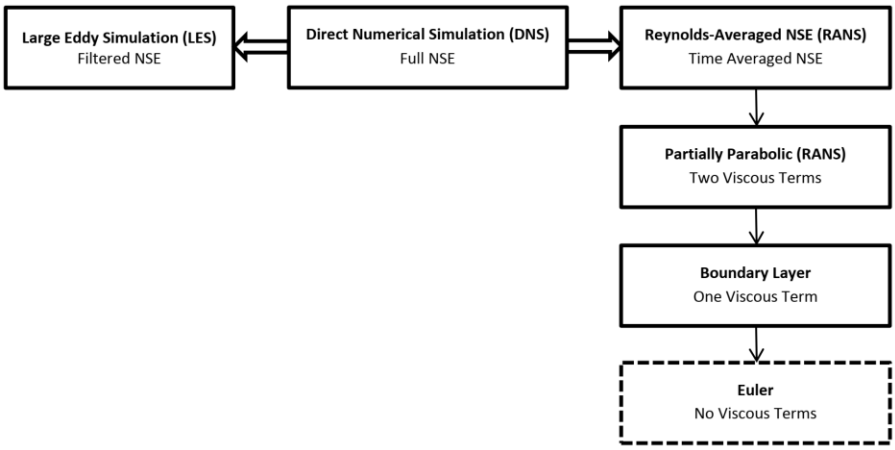

Figure 1.1 Classification of methods used in viscous computational hydrodynamics [27]

Historically, the first step taken in computing a RANS solution was based on the double-body approach, which simply neglected the free-surface existence and used the symmetry condition along the water surface. The method itself has been derived from the Hess and Smith work [22] which was devised for aerodynamics applications. Although the approach, in its initial formulation, could not predict the wave resistance, it proved to be enough suitable in determining not only the frictional resistance component, but also the flow structure in the wake.

To assess the state-of-the-art in ship viscous flow computation a workshop was organized in 1990 by SSPA Maritime Consulting AB, Chalmers University of Technology and the IIHR. Two test cases were specified by the organizers and sent out to all interested research groups, which were asked to submit results in a prescribed format. In September 1990 a meeting was held at Chalmers University of Technology. All results had then been collected and presented in a common format, and the theories based on responses to a questionnaire sent out earlier. During the meeting, each research group was first given the opportunity to briefly introduce their method and results. Thereafter, a considerable time was spent on general discussions on the performance of the different methods considering the differences in the underlying theories. Specific items that were addressed were grid generation, governing equations, boundary conditions, turbulence modeling, and numerical methods. Practical aspects of the computed solutions, for instance from the point of view of propeller design, were also discussed.

The focus on using RANS solvers was obvious in the 2nd Workshop on Ship Viscous Flow, Gothenburg 1990, where 19 research groups from 12 countries submitted their numerical solutions computed around the HSVA and "Mystery" tankers. 17 solutions were computed with RANS solvers while only one was based on boundary layer theory and one on the LES [37]. The advantage of the solutions reported in this workshop compared to the previous one was that most of them could predict the intrinsic features of the flow near the propeller plane; however, results inside the propeller disk were less satisfactory due to the inaccurate prediction of the bilge vortex and to the failure in capturing the characteristic "hook" shaped streamwise velocity distribution in the boundary layer, as revealed years later by Wilson in its monograph review [38].

To account for the free-surface, an interactive approach was developed by coupling the RANS solution with the linearized free-surface based on Dawson method for computing ship boundary layers and wakes for nonzero Froude number [39]. This was followed by the complete solution of the free-surface in the viscous flow based on two different techniques: interface fitting, where the computational mesh is deformed to make a boundary coincide with the water surface, and interface capturing, where the water surface is located in the interior of the mesh [40]; more details about these techniques will be discussed in details in the next chapter of the present book.

The third Workshop on Computational Ship Hydrodynamics that was held in Tokyo 1994 included viscous flow solution with the free-surface for a series 60 and HSVA tanker ships. Most of the RANS solutions predicted accurately the free-surface for the series 60 ship; however, a damping effect was observed away from the ship hull due to the insufficient grid resolution to predict the transverse and divergent wave systems [41].

One of the turning points in enhancing the performances of the viscous RANS solvers was marked by the continuous development of the turbulence modeling accuracy, which can be considered as the most important boost brought to the numerics behind any CFD simulation. Most of the models were formulated and refined based either on the classical eddy viscosity principle or on more sophisticated treatments such as in the Reynolds stresses models to provide a more accurate representation of the phenomenon. One of the most comprehensive cross analyses of the most popular models in use is provided by the remarkable review in [42].

In the Gothenburg 2000 Workshop on Computational Ship Hydrodynamics (G2K) the declared scope was to assess not only the state-of-the-art in the numerical ship hydrodynamics, but also to mark the latest progress in the field. Moreover, the organizers provided standards and guidelines for further developments. For that purpose, new modern designs were proposed for three different hulls: the KVLCC, the KCS and the US surface combatant DTMB [43, 44]. A special attention was given for predicting the stern flow of the KVLCC ship to capture the hook shape vortices, while a different interest in predicting the stern flow was for the DTMB hull due to the presence of the transom stern. For the first time in the workshop history, a self-propulsion case was considered and validation data from extensive tank tests were provided, so an assessment of the numerical simulation solutions was requested by the organizers to provide detailed validation studies. 20 groups participated with both commercial and in-house solvers with a dominant use of two equation turbulence models, while only two used Reynolds stress models. Six free-surface results were presented, out of which three were using surface capturing and three using surface tracking methods. The accuracy of the solutions was satisfactory, especially for the computed total resistance coefficient, the stern flow prediction of the KVLCC ship and the free-surface profile of the KCS even though the wave magnitudes were under predicted in most of the cases. The stern flow prediction of the DTMB showed that the vortex generated at the sonar dome

is convected back to the propeller plane causing a thinning of the boundary layer at the ship center plane and a “bulge” away from the center plane [37] and [43]. The solutions presented for the free-surface and boundary layer of the DTMB showed that the resolution of the computational grid is very important for the successful prediction of these features. The maximum grid resolution was within 2.6M points, while the average grid size was reported to be 1.3M.

Five years later, the workshop was held in Tokyo in 2005. The participants were subjected to submit their solutions computed for the same three hulls as in the previous edition of the workshop, but new tasks such as the self-propulsion at propulsion point for the KCS ship, the static drift for the KVLCC and the unsteady flow for forward speed diffraction seakeeping for the DTMB were imposed by the organizers. A total of 20 groups of researchers participated with solutions computed by using both in-house and commercial codes based mainly on RANS, as described in [45]. A comparative analysis of the submitted solutions revealed slight differences compared to the previous workshop. For the KVLCC model, the reported solutions for ship resistance computations unveiled a higher scatter for the computed force compared to the results obtained in the G2K Workshop, while the flow prediction in the stern revealed a better agreement in predicting the hook-shaped wake profile, especially for the Reynolds stress turbulent models. For the KCS model, the solution of the computed ship resistance was in a better agreement with the EFD data compared to the G2K Workshop, while for the local flow, a similar accuracy with a minor improvement for the boundary layer thinning nearby the center plane was reported. For the free-surface, a well predicted Kelvin wave pattern was observed with less dissipation in the far field in contrast with the previous workshop. The DTMB simulations were reported by 11 research groups and an encouraging overall accuracy in predicting the resistance was concluded. Aside of that, a better prediction of the free-surface topology seemingly due to the increment of grid resolution was reported in comparison with G2K. The streamwise wake flow structure inside the stern region was computed by 10 groups out of the 11 participants with a variable level of accuracy, showing a good prediction for the boundary layer thinning.

In 2008, an innovative method was applied on the Athena ship using a single run approach to compute the resistance and self-propulsion performances [46]. The method used an earth-fixed reference frame to solve the flow equation by increasing the ship speed gradually in a manner that made the time derivative mostly negligible and turned the local solution into a quasi-steady state one. The results were within an acceptable agreement limit in respect to the EFD data for both forces and vertical motions.

In 2010, the workshop was held in Gothenburg, Sweden. The same ship models of the KVLCC, KCS and DTMB hulls were proposed, but imposing new particular simulation conditions, i.e., resistance, propulsion and seakeeping. A total number of 89 competitors were registered in the prediction of the computed resistance for different speeds, fixed and free sinkage and trim conditions, for a hull with and without a rudder. Most solutions were based on finite volume with fewer finite difference methods. Two-equation turbulence models were the most used with few Spalart-Almaras and Menter one-equation models, besides LES/DES simulations and only one case DNS was reported. Classic or modified VOF method versions were the most employed approaches used to solve the free-surface equation. Several participants employed the novel level set method, whereas a few of others proposed the surface tracking technique to solve the problem. The numerical solutions witnessed a significant improvement compared to the T2005 Workshop, with a mean average error between measured values (D) and computed values (S) within 0.1%D and standard deviation 2.1%D; the latter for T2005 was within 4.7%D. The mean error for the

KVLCC was over predicted with 2.0%, for the KCS is also over predicted with 0.3%, while the maximum standard deviation was for the DTMB with 3.2%. For all the proposed computational cases, the sinkage and trim results stranded for a better agreement with the EFD data for lower Froude numbers. The global average number of cells was within 4M cells. One of the participations proposed a DNS-based simulation performed on about 300M cells; however, not much improvement was recorded for this approach, since the error range was slightly less than 3%. Here a doubt may be cast whether a DNS simulation may be credible or not when only a 300 million cells are used to solve the task.

For the free-surface water position prediction, the wave contours on the hull or nearby of it were well predicted. Nevertheless, the further waves from the hull suffered some rapid decay in magnitudes for most of the participants. On the local flow side, there was an obvious improvement in predicting the local features compared to the G2K and T2005 workshops especially for the KVLCC case. The Hybrid LES model proposed for the first time proved only a globally satisfying performance since the spatial discretization suffered from consistency because of the restrictions imposed by the limited computational resources. The Explicit Algebraic Stress Model (EASM) solution hosted a well predicted turbulence structure and a reasonable balance between the RSM and DES corresponding solutions from the CPU cost point of view. Complete details about the workshop findings and all the comments related to the obtained results can be found in [47].

The following workshop in Tokyo 2015 and the last one so far maintained the same principle of the previous workshops to assess the state-of-the-art in numerical ship hydrodynamics and to provide guidelines for further developments in the field. Two new hulls were introduced, i.e., the capesize Japan Bulk Carrier (JBC hereafter), which has been designed with an energy saving device at the aft region and the modern surface combatant ONRT, which has a wave piercing hull design with 10° inclined tumblehome sides and a transom stern. The model is appended with two bilge keel stabilizers, a pair of rudders, shafts, and propellers and four propeller shaft brackets [48]. The KCS hull was introduced again in the workshop with two proposed geometrical modifications in the forward part which include an extension of the bulwark on the forecastle to prevent the green water embarking during the seakeeping simulation. 88 research groups reported their solutions for the ship resistance computed for the JBC hull with and without the energy saving device. The systematic error for resistance was within the experimental error range, which was fairly better than the solutions reported at the G2010 Workshop, while the scatter was slightly higher. The error range of $\pm$4% was recorded for grids with number of cells within 10M cells compared to 3M for all the computational cases reported in G2010. The same conclusion regarding the turbulence models still holds as it was withdrawn in the previous editions of the workshops [49]. From the verification and validation point of view, about 68% of the participants reported their solutions computed on at least three different meshes as a compulsory grid convergence test requested by the organizers. In terms of sinkage and trim, the solutions were significantly improved in accuracy compared to the previous workshops. From the free-surface point of view, results predicted the wave pattern well, with a little difference between the methods used; besides, the grid density for the free-surface was enhanced compared to the G2010 Workshop. Obviously, for the KCS ship, the ship resistance solutions were of a better accuracy compared to G2010, while for the sinkage and trim computations, the results were almost similar to those of G2010 with relatively large departures for smaller Froude numbers and higher accuracy for large Froude numbers, as expected [50].

In general, surveying the results from the previous workshops shows that predicting the ship resistance for model-scale becomes extremely feasible and it promises to reach soon the level of accuracy within the towing tank test results as it was concluded in the T2015 workshop. Of course, this depends on the ship type and simulation conditions. Yet, one can say that for the type of ships that were presented in those workshops and for general resistance simulations, whether for fixed or free vertical motions conditions, the level of accuracy of the CFD solutions has surpassed the level of accuracy required in the initial design stage, a fact which might be considered more than satisfactory for the time being. A suggestive summary of the CFD resistance prediction methods development described in terms of its associated accuracy is drawn in Fig. 1.2, as it was provided in [51], with a slight modification that includes the T2015 workshop milestone.

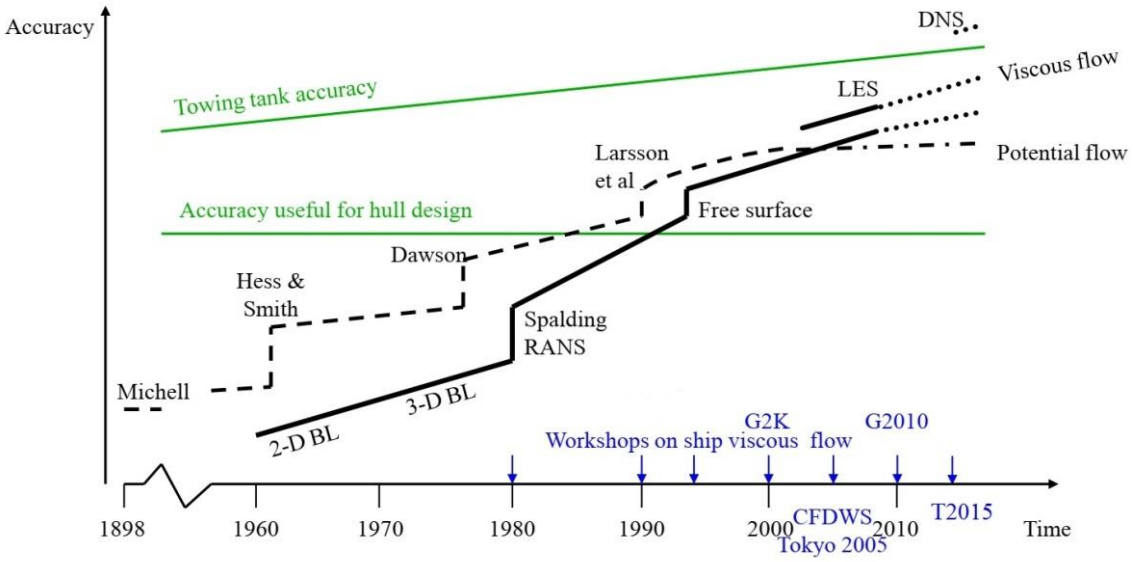

Figure 1.2 The development of CFD in ship hydrodynamics [51]

1.3.2 Propulsion

To accurately estimate the ship powering, predicting the propeller performance in open water is an important prerequisite since it helps obtaining the propeller performance diagrams. Based on that, the output of the propeller working behind the ship is then possible to estimate. Many methods were developed to predict the ship propulsion since the mid of the 19th century, which are revised thoroughly by Carlton in [52]. The first attempt was marked by the development of the axial momentum theory, which considered the propeller action as an actuator disk, i.e., a propeller with an infinite number of blades, having the same diameter as the propeller and infinitesimal thickness, working in an ideal fluid and producing thrust without causing any rotation in the slip stream [53]. This approach was later modified just by including the rotation in the downstream, as described in [54]. This method was simple and feasible except that it could not provide any details regarding the blade design nor the needed information regarding the effective wake. The blade element theory which uses the blade section to develop the forces applied to the fluid was later introduced in [55]. Due to discrepancies between the results obtained by the two methods, an intensive effort was made to combine them even though none of the attempts were

satisfactory until the experimental work of Prandtl in 1919, which later set the pace for the vortex analysis theory [56] and [57].

Later, a new method was proposed in [58] based on combining the momentum and blade element methods and considering some benefiting developments of the vortex analysis method. The method worked very well for moderately loaded propeller, but it failed for heavily loaded propellers. Lifting line method of analysis for moderately loaded propeller working in an inviscid flow and having a varying circulation in respect to the radius was proposed in [59], based on the concept of circulation and the Kutta–Joukowski theorem. Though the method developed slowly, it provided a noticeable improvement, and it is still being used in some codes for initial propeller design, as described later by Molland et al. in their monograph [60]. Attempts to replace the lifting-line approach by lifting-surface theories dates back to the 1950s, but the accomplishment of this goal was initially impossible for real ship propeller geometries due to the insufficient computing power. In spite of this drawback, the lifting line theory-based method was later developed to the lifting surface method where the blade is replaced with an infinitely thin surface fitted to the camber line; the vorticity was distributed in this approach in the spanwise and chordal directions. The earliest lifting-surface attempts were mainly based on the use of mode functions which prescribed continuous distributions of surface singularities. For lifting surfaces that had to fit the geometry of the blades, the mode functions needed a careful treatment and required a very tedious mathematical treatment. The ability of the method to describe arbitrary blade geometries was rather poor; therefore, its attractiveness was below the initial expectations. Nonetheless, with the development of the computers, the implementation of the numerical approach for lifting surface marked a boost, which allowed then more detailed studies such as the influence of skew and radial rotation distribution; see, for example [61, 62].

One of the developed approaches of the lifting surface method that was used until recent time is the vortex lattice method (VLM) which is regarded as a second-generation lifting surface-based method. The method was originally proposed by Kerwin, who continued developing the approach as described in [63–65]. VLM method was useful to solve complex flow field problems such as cavitation, propeller-induced trailing vorticity and propeller-induced pressure fluctuation [66]. Nonetheless, the unsteady phenomena such as the cavitation, requires additional singularities of both source and vortex type, therefore the method still remains a rather coarse approximation of the real phenomenon.

A step ahead in computing the unsteady propeller performances have been represented by the potential based Boundary Element Method (BEM hereafter) suitable to solve the Laplace equation that replaces the continuity under the hypotheses of incompressible, irrotational and inviscid flow by a superposition of sources and dipoles distributed over the boundaries of the solid computational domain. The kinematic and the Kutta conditions allow to solve the algebraic linear system of equations (one for each point on which the boundary condition itself is imposed) that originates from the discretization of the blades, hub and trailing wakes via quadrilateral panels, whose unknowns represent the values of the perturbation potential that, in turns, allow to calculate pressure through the Bernoulli theorem. The BEM method, in which the full propeller geometry could be modeled, was derived as described in [67]. Because its simplicity, the method gained a lot in popularity and is still being in rather wide use nowadays.

In the past three decades, the viscous RANS method begun to gain in popularity as well. The early attempts were applied on simplified propeller geometries such as the one considered in [68], where the propeller-shaft geometry was idealized based on infinite-pitch rectangular blades.

The obtained results were compared to another solution based on lifting-surface method showing that the proposed approach could predict accurately the blade loadings including the viscous effect and revealed the ability to solve the viscous region in distinction from the inviscid-slow approach. As the time went by, the numerics behind registered consistent progress and more realistic propeller geometries working in an incompressible viscous flow were considered in [69], where the viscous flow around the DTRC4119 and a SEIUNMARU propeller was simulated showing a promising accuracy in predicting the propeller thrust and torque. Besides, the viscous aspects of the propeller blade were well predicted, such as the tip-vortex generation, the blade roll-up wake and the global vortical structure. An early attempt to solve the propeller behind the ship was done based on combining the benefits of both BEM and RANS methods, hybrid RANS/BEM methods were consequently developed, in which the propulsor inflow is solved by using a viscous flow solver, while the propeller effect is represented by a body force model [70]. The obtained results were within a satisfying level of accuracy compared to the EFD data with a good prediction of flow details. Recently, the DES and LES methods are aggressively spreading due not only to the augmentation of the available computation power but also to their versatility in reproducing accurately the intrinsic flow features. Comprehensive research on the effect of turbulence closure on the wake prediction of the propeller working in open water using *SST k-ω* eddy viscosity model, EASM and hybrid URANSE/LES model was carried out in [71] showing a good agreement with the EFD data and well predicted propeller wake and vortices, especially based on the DES model. Another consistent survey on the correlation between the evolution of propeller trailing vortex wake and skew of propellers for 4 different designs for the model propeller of the DTMB ship having the same diameter and different skew is presented in [72].

In terms of the propeller working behind a ship hull, the largest majority of the self-propulsion modeling is based on fully RANS solvers, in which two different approaches are usually implemented: the body force method and the fully discretized propeller model. The body force method does not require modeling the propeller; however, the body forces are applied on the propeller location arbitrary grid points, then the body forces are defined so that they integrate numerically to the thrust and torque of the propeller [70]. A hybrid approach based on the body force method is to use a global propeller-performance code in an interactive fashion with the RANS solver to capture the propeller-hull interaction and to distribute the body force according to the actual blade loading, as described in [73].

CFD applications to real propellers operating in the ship wake are increasing rapidly in popularity as the numerics required to perform the computations have continuously been developed and the available computational resources increased spectacularly [74]. Unlike the previously discussed methods, in the viscous approach the propeller geometry is considered in every detail and the equations that describe de flow must be preceded by a rigorous discretization in space of the computational domain. The discretized propeller method is based on defining the real 3D propeller geometry in the computational domain, which involves the use of either sliding or overset grid approaches. From this point of view the computation is less efficient in terms of the required CPU time, but the accuracy of the solution is by far better. Aside of that, a fully viscous approach may set the scene for ultimately cope with tedious subjects such as the cavitation, noise propagation, vibrations and so on.

The past decade marked an increased interest among the ship hydrodynamics community members in solving accurately the self-propulsion solution problem. The consistent amount of the reported achievements in the literature may be considered as insufficient if the outputs of the two

workshops in the CFD ship hydrodynamics are not taken into account since they uniquely represent a competition between various methodologies, numerical techniques, solvers and solution accuracies. Keeping in line with these events, it is worth mentioning that in G2010, 17 contributions were reported for the KCS self-propulsion benchmark case, out of which nine used fully discretized propeller and eight employed the body force method [47], while in T2015, 26 results were submitted for the JBC case, and 7 submissions referred to the KCS benchmark case [50]. The outcomes of the two competitions were underlining that the achievements, although impressive are still subjected for further improvements which are expected to come from the turbulence closure techniques, from the accuracy of the discretization schemes as well as from the amount of the assumptions used to simplify the modeling inputs.

As a result, novel approaches were considered, and their overall accuracy was consequently emphasized. A CFD study of the rotating propeller based on body force method and 3D propeller model using sliding grid was reported for the propeller working behind a tanker and a good agreement with the EFD results, with a better prediction for the propulsion coefficient based on the 3D propeller model [75] was mentioned. A viscous flow study aimed at predicting the free-surface flow performances of a self-propelled tanker ship by using a sliding grid technique was described in [76] and the overall accuracy of the proposed approach was proven against the experimental data. The self-propulsion performances prediction at the ship point working condition for the JBC propeller-hull ensemble by using dynamic overset grid and a novel speed controller was proposed in [77] and the promising solution accuracy was invoked for advancing the techniques used as possible minimum standards for further research in the field.

In the past decade more sophisticated in their formulation and time-consuming techniques such as the LES, DES and Delayed Detached Eddy Simulation (DDES) were used and reported in the literature for studies related to the propellers working in open water and behind the ship hulls. For self-propulsion cases, a dynamic overset grid was used in [78] to solve the self-propulsion of the KCS full scale ship using DES method. A simulation of the DARPA Suboff submarine including open water and self-propulsion with the E1619 propeller based on RANS, DES and DDES models is given in [79]. A self-propulsion simulation for the JBC hull-propeller ensemble working at ship point using a dynamic overset technique based on URANSE, DES and DDES can be found in [80]. Although DDES results proved a good agreement with experimentally measured hull resistance, both RANS and DDES method-based approaches could predict the attached flow at the stern, while DES predicted the separation, which resulted in higher resistance prediction. More examples for propeller open water simulations and propeller operating behind the ship can be found in the proceedings of the 5 editions of the International Symposium on Marine Propulsors, covering all the associated topics including grid generation, turbulence modeling and cavitation performance and modeling [81].

Simulating the multiphase/multifluid flows has always been a challenge for the conventional CFD models because of the moving and deformable boundaries or interfaces between different fluids. Basically, the interfaces between different phases, e.g., liquid and air, originate from the specific interactions among fluid molecules. Under such circumstances, another step forward taken by the community is represented by the lattice Boltzmann method (LBM hereafter), which is a powerful method seen as a potential contender of the traditional models used for the time being in CFD. Unlike the traditional CFD methods, which solve numerically the conservation equations of macroscopic properties (i.e., mass, momentum, and turbulence), LBM models the fluid consisting of fictive particles, and such particles perform consecutive propagation and collision

processes over a discrete lattice mesh. Due to its particulate nature and local dynamics, LBM has several advantages over other conventional CFD methods, especially in dealing with complex boundaries and massive parallelization of the algorithm.

Summing up, the review of the state-of-the-art in ship propulsion whether in open water or working behind the ship shows that the viscous flow CFD-based method is gaining more popularity and rather becoming a common practice tool for engineers. The achieved level of accuracy of the numerical solutions obtained is more than sufficient for design purposes or for propeller design optimization.

1.3.3 Seakeeping

Studying the ship behavior in waves is an important issue for the initial design stage. The added resistance in waves is crucially important to be taken into consideration for an accurate ship powering estimation, as well as to satisfy the new powering requirements imposed by the Energy Efficiency Design Index (EEDI) and Energy Efficiency Operational Indicator (EEOI), which are regulated by the IMO and Marine Environment Protection Committee (MEPC). From the safety point of view, severe ship motions in waves may have a considerable influence on the ship stability and operability. Many researchers have developed approaches to predict ship performance in waves using EFD, potential flow solvers and viscous-based methods.

The experimental approach was the fundament of predicting the seakeeping performances along with the analytical methods till the early 1970s. Experiments are usually performed for the ship models moving either in regular or in irregular waves artificially generated by hydraulically powered wave makers. Seakeeping tests are extremely expensive especially due to the prohibitive costs of the onset equipment. Aside of that, because the number of the personnel involved in such an experiment is larger than usual, the human resources costs are also high. Last, but not the least, the experimental investigation is expensive because of the long waiting periods required between tests until the water has to completely calm down and come back to the initial rest condition again. The waiting periods are especially long in standard towing tanks. Aside of that, depending on the number of the degrees of freedom of the model and the sea state, the scope of the experiments is usually complicated considering the fact that many parameters need to be varied, e.g. wave length, wave height, angle of encounter, ship speed, draught and trim, metacentric height etc. [14].

The potential flow-based methods either linear or nonlinear were the most frequently used method in the theoretical seakeeping investigation for the past five decades because of its simplicity and efficiency in terms of the CPU time needed to be performed at a satisfactory level of accuracy. The linear potential flow seakeeping solvers based on the strip theory, source distribution method, panel method and more recently enhanced unified theory, were widely used by ship researchers [82]; but because of limitations of the models, the solutions had some drawbacks determined mainly by the neglected viscous effect, otherwise very important for the phenomenon in itself.

Recently, as computational facilities have become more powerful and more accessible, CFD tools are commonly used to predict not only the added resistance, but also the ship motions in waves of different characteristics. They have proven obvious advantages over the potential codes as they can deal directly with large amplitude ship motions and nonlinear flow phenomena such as breaking waves and green water embarking, without explicit approximations and empirical value corrections [83]. The vast majority of the seakeeping computations conducted nowadays

are performed based on the URANSE solvers, whereas only a few simulations are based on the LES and DES approaches. The capturing of the free-surface is made based either on the VOF method or on the level set method. Incoming waves are mainly assumed as being linear and enforced on the domain boundaries. Structured or unstructured multi-block or overset grids are used for the numerical study of the ship motions. Numerical methods mainly use second order discretization schemes for spatial and temporal terms. High performance computers are more and more frequently used in the simulations, a fact which allows the use of small grid sizes at the free-surface and inside the boundary layer as well as smaller time-steps aimed to capture the motions in waves more accurately [35].

Historically speaking, much research were reported aimed at solving the seakeeping problems, including incident waves and prescribed or free pitch, heave and roll motions. One of the first attempts to solve the ship motion in waves based on URANSE simulation was presented in [84], which encountered some problems regarding the accuracy of the free-surface profile due to the limited grid quality. A different CFD simulation was conducted four years later for the DTMB surface combatant moving in regular head waves for a given forward speed diffraction as reported in [85], and a good agreement with experimental results was reported for the first harmonics and phases of the resistance, forces and moments. The wave pattern and the nominal wake were also investigated and a good agreement with the experiments was emphasized. A thorough study for the DTMB ship model was presented in [86], which included several numerical simulations using single phase level set method to capture the free-surface and dynamic overset grid for predicting the ship resistance and vertical motions in regular head waves with both small and large amplitudes. Numerical solutions for motion were also computed and the comparison with the experimental data found in [87] proved a satisfying agreement. Aside of that, a verification and validation study was performed for the added ship resistance in waves on three different grids and showed a monotonic convergence; however, no EFD data were available for forces validation. An extension for the ship behavior when interacting with another ship was also included. Two years later, an URANSE approach based on the finite volume technique and the VOF method for capturing the free-surface was used to solve the KVLCC2 ship model in regular head waves being conducted for three different wave lengths with a single wave height [88]. The scope of the study was focused on investigating the numerical uncertainties in the code by performing grid convergence verification study on three different grids for each case considered. The authors concluded that a good combination between a fine grid and a suitable time step is always necessary for keeping the stability of the solver and for reducing the numerical errors, especially when motions such as pitch and roll are included in the simulation. Another study based on the same computational code was also carried out in [89] to solve the speed diffraction problem for the DTMB hull as well as vertical motion for a medium speed. A special attention was given for the short and steepy waves and a strong non-linear ship-wave interaction causing breaking waves generated by the dry transom was reported.

A CFD study aimed at predicting the seakeeping performance of the KCS ship with and without a rotating propeller in head waves based on the dynamic overset grid was performed in [90], where a verification and validation study was also presented for the 6DOF motion. The validated solutions proved not only a good agreement with the experimental data but also the versatility in predicting forces and motion in head waves based on the proposed approach; nevertheless, the authors suggested that including more wave conditions with further V&V for the heave and pitch responses might be a better choice. Another valuable verification and validation

study devoted to predicting the added resistance and motions of KVLCC2 with fixed and free surge in short and long head waves can be found in [82], their study included a consistent verification and validation studies for added resistance and motions in waves for fixed and free surge conditions. The numerical solutions showed a good agreement with the EFD data especially for the wake flow results which were compared to the PIV towing tank measurements. A rigorous study on added resistance and motions of the KVLCC2 in head seas for various ship speeds is given in [83], where the seakeeping performance was investigated based on a 3D BEM and CFD methods showing that the obtained solutions based on CFD method had a better agreement with the available EFD data.

The major problem associated to the CFD seakeeping simulations is the significant simulation time required to accomplish the task. This problem can be partially alleviated by using the procedure proposed in [91] that computes the Response Amplitude Operator (RAO hereafter) for one Froude number in a single run, thus significantly reducing the computational time. The methodology was tested on the DTMB model and has been proven to be as accurate as the standard single wave run, at least within the limits of the hypothesis of linear response [92].

Generally, the roll motion is dominated by viscous effects; therefore, the potential flow-based method is largely ineffective to address this problem. From this point of view, the CFD computations have proven to effectively lead to very good level of accuracy for the ship roll decay simulation. A roll decay prediction for the DTMB ship appended with bilge keels is proposed in [93], where a special attention is given to the free-surface and viscous flow around the hull during the roll period. A comparative experimental and theoretical investigation on a ship model with bilge keels of six different sizes being immersed at three drafts can be found in [94]. Their study included extensive comparisons of experiments with CFD establishes the practical usefulness of CFD in estimating roll damping and hence prediction of roll motion. A numerical study of the roll decay of ship in intact and damaged conditions is presented in [95], showing a good agreement for the time history of the roll angle and the local flow prediction; moreover, the influence of damaged ship was successfully analyzed including the coupling between roll and sway in damaged condition, showing the influence of sway on the roll damping.

Without restricting the area of the bibliographic introspection, in the followings most of the references will target to the CFD workshops, which represent real milestones in the field of ship hydrodynamics. Although in the T2005 Workshop, only one computation was reported for a speed diffraction problem including no motion [45], in G2010 Workshop, several different studies were advanced with speed diffraction and surge in head waves including heave and pitch motion [47]. In the T2015 Workshop, most of the computations were performed for the KCS hull moving in head waves. Nevertheless, two sets of numerical solutions referred to the more complex case of the six degrees of freedom motion of the ONRT benchmark hull [48]. Aside of that, the roll decay benchmark case in G2010 Workshop had 4 participations with solutions based on the URANSE approach with a promising level of accuracy, especially in predicting the viscous flow around the bilge keels and the free-surface [47].

Summing up, the CFD methods are now applied to a wide variety of seakeeping problems, including added resistance and motions in waves, roll decay, parametric rolling, and to violent and complex flows such as green water, sloshing, slamming, water embarking and water entry. The ability of CFD to simulate the free running vessels in waves has been improved significantly through the past decade, opening up the possibility of applying CFD to the complex problem of a ship maneuvering in waves [96].

1.3.4 Maneuvering

Maneuverability of a ship has a very significant influence on the efficiency and safety of maritime transportation in general. The maneuvering quality of a ship has to be assessed in the various design stages and after the ship is built to ensure that the quality of the designed ship is compatible with the requirements of the IMO Maritime Safety Committee. This assessment can be done based on experimental tests, mathematical models, or a combination of both. Experimental methods for ship maneuvering are done for model scales in radio-controlled model basins or using radio-controlled models in lakes and large reservoir [97]. Though model testing is always considered as accurate as physical tests, unlike resistance and propulsion tests, the scale effect in maneuvering is quite significant and requires special treatment due to the fact that the forces and moments on the hull are highly dominated by the viscous effect and flow separation. Obviously, the most accurate results will be those predicted in the full-scale ships in the sea trials; nevertheless, imposing modifications after the ship is delivered is extremely difficult. The mathematical models can be divided in two categories; the first is using Taylor series expansion for hydrodynamic forces and moments about a suitable initial condition [98]. This approach is suitable for computer simulations since it contains the hydrodynamic added mass and damping coefficients that are necessary in predicting the maneuvering characteristics of a marine vehicle. The second is the response or modular model; in which, the hydrodynamic forces and moments are divided in three components for the bare hull, rudder and propeller. This approach investigates the responses of the ship motion due to the rudder action to solve the course keeping problems [98]. In practice, there also existed some series to predict maneuvering performance of a ship, such as the one presented in [99]. An early commonly used method for predicting the turning and steering of a ship is to use equations of motion with experimentally determined coefficients. Once these coefficients are determined for a specific ship design, equations of motion are used to simulate the dynamic behavior and controllability of that ship in various operating conditions [97]. This Coefficient based predictions have been used in the selection of rudder size and steering control systems, and in estimating the turning characteristics of ships [100].

Numerically, the simplest approach to body force computations is the use of regression formulae based on slender-body theory, but with empirical coefficients found from analyzing various model experiments, e.g. [101]. The next more sophisticated approach would be to apply slender-body methods directly, deriving the added mass terms for each strip from analytical or BEM computations [14].

Most of the maneuvering simulations conducted nowadays are based on URANSE. Free-surface is mostly modeled by a surface capturing method, while a few simulations use surface tracking approaches. For numerical methods, spatial discretization is done by finite difference and finite volume methods with structured/unstructured grids. The order of accuracy in time integration is mostly second order or higher. The divergence-free condition is satisfied either by velocity-pressure correction or an artificial compressibility approach. Analytical weighted regridding, mesh morphing, and dynamic overset approaches are used to handle dynamic ship motions. HPC and Multi grid technique is also used in some simulations for speeding up computations [35].

CFD computations of static maneuvers were presented in the literature, e.g. G2K and T2005 Workshops; where one case of static drift was presented [43–45]. In the Workshop on Verification and Validation of Ship Maneuvering Simulation Methods (SIMMAN 2008) various cases of static drifts and Planar Motion Mechanism (PMM hereafter) were presented for three ships: the KVLCC,

KCS and DTMB. A total of 64 submissions were received for the free maneuver simulations, which included a wide range of the state-of-the-art methods in use, such as PMM and Circular Motion Test (CMT) based methods, CFD based methods, system identification, neural network tools and various empirical methods. For the forced motion simulations, a total of 16 submissions were received, comprising different CFD-based methods such as RANS, URANS, and DES. More details about the presented results can be found in [102]. CFD study for the static drift and steady turning of the KVLCC including verification and validation study for the effect of water depth on the computed results was presented in [103]. The results obtained were in a good agreement; however, it was observed that the error increases as the drift angle increases. A study for the DTMB ship in 20º static drift conditions based on DES approach with grid up to 276M cells was presented in [104]. The results showed an enhancement in the obtained results for the proposed study compared to their previous study based on RANSE with more detailed resolution of the free-surface, breaking pattern, vortical and turbulent structures.

For captive maneuver in 6DOF including the free-surface, a turning and zigzag maneuver of the KVLCC1 ship was performed and presented in [104] based on DES technique with the free-surface captured using level-set method. The rudder of the KVLCC1 was simplified by replacing the horn rudder with a spade one, which result in over predicted steering.

CFD simulation for the full-scale Athena twin screw ship in steady turning based on both RANSE and DES models was presented in [105]. A full comparison between EFD and CFD results was performed for local flow quantities and global parameters. The results obtained by DES showed a better agreement with the EFD. An experimental and numerical study was presented in [106] for a course keeping and turning maneuver in waves. Computations were performed for different wave headings and results were in good agreement with experimental data. CFD simulation for the PMM captive model tests for the KVLCC2 based on a RANSE solver including the effect of vertical banks was presented in [107]. Good agreement was concluded for the comparison between the CFD results and the PMM tests conducted in a circulating water channel.

One of the main advantages of CFD is its ability to provide information about hydrodynamic loads and motions of the vessel together with detailed flow field information, which can help to understand the flow physics related to maneuvering. Another advantage is that this type of simulation does not rely on model testing with physical scale models, which means that for instance the hull form or the rudder can be changed relatively easy. This is useful in the early design phase where CFD can help to investigate maneuvering related issues and help to improve the design. Therefore, CFD is used ranging from detailed flow studies (to learn about the features of the flow field) for prediction of hydrodynamic forces and moments to direct simulation of maneuvers. This applies to both surface ships and submarines. It seems that in addition to the traditional RANS approach, also DES and DDES have started to show up in practical applications [108].

1.4 Scope and Objectives

The general scope of this research study is to study numerically the ship hull hydrodynamic performances in different operating conditions. Nonetheless, an experimental validation of the numerical computed solutions is provided within the limits of the existing experimental facilities in the laboratory the studies were carried out. The rest of validations were done based on experimental data provided for several benchmarking casas by the most appreciated

hydrodynamic labs in the world, whose data are freely provided in the public domain. The red wire of the present work was to develop several robust and reliable methods to simulate various ship hydrodynamic problems using the CFD tools as a complementary or even as an alternative method to the experimental and empirical approaches. Viscous flow solver is utilized for this purpose, based on the RANSE, either in steady or unsteady regimes, depending on the problem of concern. A thorough investigation for the physical hydrodynamic phenomena in each case study is included, such as: velocities, pressure, free-surface, turbulence, boundary layer, vorticity, motions and general flow visualization, to provide a proper understanding for each case, and discuss upon the credibility and/or finding practical solutions for the given problems of interest. The ultimate goal was to investigate the capabilities and limitations of the CFD methods to simulate accurately the ship performances related to the: hydrodynamic resistance, powering, seakeeping. The numerical solutions are rigorously evaluated through systematic verification and validation procedures to assess the numerical uncertainties and to account for the errors associated in the numerical approach, to demonstrate, not just the accuracy of the numerical model, but also its robustness.

To achieve this purpose, extensive numerical studies are performed for the selected types of ships, which can be categorized based on type as commercial and special purpose ships, and based on mode of operation as slow and fast ships. The present study is aimed at complying with the previous research in the field, as previously described in the literature review, and providing, when necessary, alternative, and more simplified solutions for some problems.

Since the scope of this research work is sufficiently broad and rather challenging to cover entirely all the associated topics, the following main objectives will be considered during the preparation of the present studies, to make the problem understandable for the reader. The research studies objectives can therefore be simply outlined as follows:

1. Ship resistance. Studies on:
    i. the bare hull ship resistance for fixed and free sinkage and trim conditions;
    ii. the effect of special appendages on the ship resistance and the wake flow in the stern, such as rudders and energy saving devices (ESD);
    iii. the fully appended ship to investigate the capability of the numerical model to predict the influence of the appendages on the flow around the hull;
    iv. the integration between experimental and numerical approaches to account for the banking effect for the fast ships in towing tank
2. Ship propulsion. Studies on:
    i. propeller performance in open water;
    ii. propeller performance behind the ship using two different approaches, including the body force method and fully discretized propeller;
    iii. the influence of the ESD on the propulsion efficiency;
    iv. the interaction between ship, propeller and rudder;
3. Ship seakeeping. Studies on:
    i. seakeeping performance in speed diffraction problem;
    ii. seakeeping performance of ship hull in different sailing conditions, including vertical motions and added resistance in waves;
    iii. local flow assessment during ship sailing in waves and its influence of the flow characteristics;

iv. the viscous effect on the roll decay of the ship at different roll angles, including the effect of bilge keels.

1.5 Structure of the Book

This book is structured in seven chapters; the review, which includes an introduction and a background survey of the most relevant issues that shape the essence problem, accompanied by a historical review of the most significant previous research in the field, are given in the first chapter.

The second chapter is devoted to the mathematical model that describes the physics behaving the phenomena studied in the book. The chapter includes the numerical representation of the governing equations and solution algorithms and finally, the basic procedures for the solution process of a general CFD approach in ship hydrodynamic.

Since the CFD is a numerical method that is subjected to the presence of errors and uncertainties, the error classification and the systematic verification and validation process are presented in Chapter III, with a special focus on the possible techniques and the main aspects to reduce or mitigate the numerical errors. A special concern regarding the grid generation for an unstructured grid solver is covered to ensure the grid similarity during the simulations.

The numerical solutions are presented and discussed starting from chapter four, which includes the results for ship resistance computations. The first study includes a detailed investigation of the JBC, which includes an ESD between the hull and propeller to enhance uniformity of the wake inflow into the propeller. The study includes analyses for the resistance, ship motions, free-surface configuration, and wake flow inner particularities for the ship with and without the ESD; besides, a detailed investigation of the effect of the ESD on the total resistance is carried out.

The second part of the chapter includes a numerical simulation for the KVLCC2 hull model to compute the bare hull ship resistance and the free-surface topology for a fixed and free sinkage and trim conditions. The results are presented for the computed forces, velocity and pressure contours on the hull and the wake, and finally, the free-surface flow in the near and far-field region with respect to the hull is detailed. The influence of the rudder existence at the aft of the ship is also investigated for different ship speeds.

Since both ships can be included in the high block-coefficient and slow speed ship category, a third study is applied on the surface combatant DTMB ship model, which can be considered as a medium-to-high speed ship. The scope of the investigation is to assess the accuracy of the numerical model for the high-speed ships and to set the base for the appended ship resistance simulations which are applied specifically on the DTMB ship in the end of this chapter. Both studies are concerned with the forces, motions, free-surface and local flow around the hull and particularly the appendages.

The final part of the fourth chapter describes the validation of the numerical results based on the experimental work performed by the author in the towing tank. The experiment is carried out for the DTMB ship hull to assess and validate the numerical solutions from the global hydrodynamic forces and free-surface topology point of view. The tank banking effect is also investigated and its influence on the ship resistance and free-surface reflections is covered experimentally and numerically.

The fifth chapter contains the propulsion simulations divided into two sections. The first section of this chapter covers the Propeller Open Water (POW) simulations for the model propellers of the JBC ship. The study stands as a basic step to predict the open water performance of the propeller to use further in the self-propulsion simulations. In this study, a special focus is devoted to the accurate estimation of the forces and moments acting on the propeller, as well as to the distributions of pressure, velocity, turbulent kinetic energy on the propeller blades. Consideration is also given to the vortices formation process. The second section includes the self-propulsion performance estimation of the JBC propeller for two cases when the ship is equipped or not with the ESD. Two different approaches are used to solve this problem based on the body force method and fully discretized propeller.

The second part includes similar analysis for the open water performance of the KVLCC2 propeller model using different turbulence models based on RANS and Hybrid RANS/LES models to have a proper representation of the wake flow of the propeller and better understanding of the vortices formation. Later, the interaction between the hull, propeller and rudder is numerically studied and discussed for the KVLCC2 ship based on the body force method and fully discretized propeller.

The sixth chapter is covering the seakeeping simulation for the DTMB ship in regular head waves. Two different scenarios are analyzed for this particular hull, including speed diffraction problem, when all the motions of the ship are restrained, while the second is presented for radiation problem including 3-DOF, surge, heave and pitch. A special consideration for the roll motion is also analyzed for the same ship in the roll decay condition in calm water. The roll decay is computed for different initial roll angles and compared with the existent experimental data. The effect of numerical parameters on the accuracy of the roll decay simulation is investigated, along with the speed effect on the roll damping process and free-surface prediction during roll damping process. Finally, a consistent study is focused on the viscous flow interaction between the hull and bilge keels in order to understand the viscous mechanism of damping.

The final conclusions, the personal contribution as well as the steps to be taken in a future work are summarized in chapter seven.

Appendix A gives a general overview about the solution method in ship hydrodynamic viscous flow applications based on the RANSE approach, with a general description of the mostly employed techniques in terms of the: spatial and temporal discretization methods, grid generation, free-surface definition (interface capturing/tracking), turbulence modeling, motion adaptation, and boundary conditions formulation.

This page is intentionally left blank.

Chapter II
Mathematical Model

Since the CFD method is basically a numerical representation of a physical problem, it is important to turn the focus now on the mathematical model representation for the flow solver used in all the various numerical solutions obtained in this book.

The numerical solver used exclusively in all the numerical simulations whose results will be presented in the following chapters of this research work is the ISIS-CFD viscous flow solver of the commercial software FINE^{TM}/Marine available under the NUMECA suite. The solver is created by EMN "Equipe Modélisation Numérique", i.e., the Department of the Fluid mechanics Laboratory and developed by Ecole Centrale de Nantes and Centre National de la Recherche Scientifique CNRS [88, 109]. It is based on the finite volume method to build the spatial discretization of the transport equation in order to solve the incompressible, unsteady Navier-Stokes equation. The spatial discretization is face-based which constructs the fluxes face by face, giving the solver a flexibility to use unstructured meshes with non-overlapping control volumes bounded by an arbitrary number of arbitrarily shaped faces. The temporal discretization is enforced through a cell centered implicit second order three-level scheme. The velocity and pressure coupling is achieved through a Rhie and Chow SIMPLE algorithm, in which the velocity field is obtained from the momentum conservation equations and the pressure field is extracted from the mass conservation constraint, or continuity equation, transformed into a pressure-equation [40]. Turbulent flows are treated by introducing additional transport equations for modeled variables in the same principle as the momentum equation and they are discretized and solved accordingly. A variety of turbulent closure models are available such as the eddy viscosity models including the one-equation Spalart-Allmaras model, two-equation standard k-ε and the standard k-ω Wilcox model, Menter's k-ω baseline and SST models. One Algebraic Reynolds Stress models is also available represented in the EASM model. Finally, hybrid models are also available such as DES models and most recently the DDES and IDDES were introduced starting from version FINE^{TM}/Marine 8.1. Gradients are computed based on a Gauss's theorem approach. Formal first-order and second-order accuracy are achieved, respectively, through non-orthogonal corrections and piecewise linear upwind stabilizing approach for inviscid fluxes. Central difference scheme is used for viscous fluxes to ensure a first-order formal accuracy. The free-surface is modeled using a multi-phase flow approach applying the volume of fluid VOF free-surface capturing technique. Incompressible and non-miscible flow phases are modeled through the use of conservation equations for each volume fraction of phase/fluid [88]. Propeller modeling is allowed based on both, the body force method solved based on the infinite-blade actuator disk; besides, a fully discretized propeller can also be handled with the aid of sliding or overset grid.

Governing equations and all the related mathematical modeling of the solver, turbulence closure equations for k-ω and EASM models, general boundary conditions are given in the following sections. All the numerical details including their applications and mathematical representation in the solver can be found with complete details provided by Queutey and Visonneau in [109].

2.1 Governing Equations

For a multi-phase, continuum, under the assumption of incompressible, isothermal viscous flow condition, the mass and momentum conservation equations can be written as follows [109]

$$\frac{\partial}{\partial t}\int_V \rho dV + \int_S \rho\left(\vec{U} - \vec{U}_d\right).\vec{n}dS = 0 \tag{2.1}$$

$$\frac{\partial}{\partial t}\int_V \rho U_i dV + \int_S \rho U_i\left(\vec{U} - \vec{U}_d\right).\vec{n}dS = \int_S \left(\tau_{ij}I_j - pI_i\right).\vec{n}dS + \int_V \rho g_i dV \tag{2.2}$$

where V is the control volume (bounding domain), enclosed by the closed surface S moving at a velocity $\vec{U}_d$ with a unit normal vector $\vec{n}$ directed outward. $\vec{U}$ and p represent the velocity and pressure fields, respectively. τ_{ij} and g_i represent the components of the viscous stress tensor and the gravity vector, whereas I_j is the unity vector whose components vanish, except for the component j.

Since the flow is resolved in an air-water interface based on the volume of fluid (VOF) method, an extra equation is added to the governing equations for the volume fraction conservation equation, which can be written as [109]

$$\frac{\partial}{\partial t}\int_V c_i dV + \int_S c_i\left(\vec{U} - \vec{U}_d\right).\vec{n}dS = 0 \tag{2.3}$$

where c_i is the i^{th} volume fraction for fluid i and is used to distinguish the existence ($c_i = 1$) or the absence ($c_i = 0$) of fluid i. Since volume fraction between 0 and 1 indicates the presence of a mixture, the value of 0.5 is chosen to define the interface.

The actual physical properties of the flow including viscosity and density can be predicted from each phase physical properties μ_i and ρ_i with the following equations [109]

$$\rho = \sum_i c_i\rho_i \qquad \mu = \sum_i c_i\mu_i \qquad \sum_i c_i = 1 \tag{2.4}$$

If the grid is moving, a space conservation law must also be satisfied

$$\frac{\partial}{\partial t}\int_V dV + \int_S \vec{U}_d.\vec{n}dS = 0 \tag{2.5}$$

The general mass conservation equation in (2.1) can be simplified by considering incompressible phases with constant densities ρ_i. Substituting from the equations in (2.4) it is possible to isolate one arbitrary phase j and such that $\rho_j \neq 0$

$$c_j = 1 - \sum_{i\neq j} c_i\rho_i \tag{2.6}$$

$$\rho = c_j\rho_j + \sum_{i\neq j} c_i\rho_i = \rho_j + \sum_{i\neq j} c_i\left(\rho_i - \rho_j\right) \tag{2.7}$$

Now, using the obtained equations in (2.6) and (2.7) to substitute in the global mass conservation equation in (2.1) yields

$$0 = \frac{\partial}{\partial t}\int_V \left(\rho_j + \sum_{i\neq j} c_i(\rho_i - \rho_j)\right) dV + \int_S \left(\rho_j + \sum_{i\neq j} c_i(\rho_i - \rho_j)\right)(\vec{U} - \vec{U}_d).\vec{n}dS$$

$$= \rho_j\left[\frac{\partial}{\partial t}\int_V dV - \int_S (\vec{U} - \vec{U}_d).\vec{n}dS\right] + \left(\sum_{i\neq j}(\rho_i - \rho_j)\right)\left[\frac{\partial}{\partial t}\int_V c_i dV + \int_S c_i(\vec{U} - \vec{U}_d).\vec{n}dS\right] \quad (2.8)$$

$$= \rho_j\left[\int_S \vec{U}.\vec{n}dS\right]$$

hence, the mass conservation can be simplified as

$$\int_S \vec{U}.\vec{n}dS = 0 \quad (2.9)$$

or, simply it can be composed in a non-integral form using Divergence operator $\mathcal{D}(\,)$,

$$\mathcal{D}(\vec{U}) = 0 \quad (2.10)$$

Finally, the continuity equation can be written as

$$\frac{\partial U_i}{\partial x_i} = 0 \quad (2.11)$$

2.2 Turbulent Closure Equations [110]

The closure to the Reynolds-averaged equations requires the definition of the turbulent Reynolds stresses, as it is presented in the following equations

$$\tau_{ij} = \tau_{t_{ij}} + \tau_{l_{ij}} \quad (2.12a)$$

$$\tau_{l_{ij}} = 2\mu\left(S_{ij} - S_{nn}\frac{\delta_{ij}}{3}\right) \quad (2.12b)$$

$$\tau_{t_{ij}} = -\rho\overline{u'_\iota u'_\jmath} \quad (2.12c)$$

$$S_{ij} = \frac{1}{2}\left(\frac{\partial u_i}{\partial x_i} + \frac{\partial u_j}{\partial x_j}\right) \quad (2.12d)$$

If the eddy viscosity is taken into consideration, the Reynolds stress tensor is proportional to the average strain rate tensor. In this case, the assumption will be based on the Boussinesq hypothesis in terms of the eddy viscosity, such that

$$\tau_{t_{ij}} = 2\mu\left(S_{ij} - S_{nn}\frac{\delta_{ij}}{3}\right) - \frac{2\rho K\delta_{ij}}{3} \quad (2.13)$$

Taking into consideration an incompressible flow, and bearing in mind that the isotropic part of the Reynolds stress tensor ($2K/3$) is not explicitly needed, the Reynolds stress tensors can be written as follows

$$\tau_{ij} = \tau_{t_{ij}} + \tau_{l_{ij}} \quad (2.14a)$$

$$\tau_{l_{ij}} = 2\mu S_{ij} \tag{2.14b}$$

$$\tau_{t_{ij}} = 2\mu S_{ij} - \frac{2\rho K \delta_{ij}}{3} \tag{2.14c}$$

Taking the time average of the continuity equation gives

$$\overline{\frac{\partial U_\iota}{\partial x_i}} = \frac{\partial u_i}{\partial x_i} = 0 \tag{2.15}$$

Subtracting (2.15) from (2.11) shows that also the time fluctuating velocity fulfills the incompressible continuity equation

$$\frac{\partial u''_i}{\partial x_i} = 0 \tag{2.16}$$

Then taking the time average of the NSE after rearranging the terms

$$\begin{aligned} &\overline{\rho \frac{\partial U_\iota}{\partial t} + \rho \frac{\partial (U_J U_\iota)}{\partial x_J} - \rho R_\iota + \frac{\partial P}{\partial x_\iota} - \frac{\partial}{\partial x_J}\left(\mu\left(\frac{\partial U_\iota}{\partial x_J} + \frac{\partial U_J}{\partial x_\iota}\right)\right)} \\ &= \rho \frac{\partial \bar{U}_\iota}{\partial t} + \rho \frac{\partial (\overline{U_J U_\iota})}{\partial x_j} - \rho \bar{R}_\iota + \frac{\partial \bar{P}}{\partial x_i} - \frac{\partial}{\partial x_j}\left(\mu\left(\frac{\partial \bar{U}_\iota}{\partial x_j} + \frac{\partial \bar{U}_J}{\partial x_i}\right)\right) \\ &= \rho \frac{\partial u_i}{\partial t} + \rho \frac{\partial (u_j u_i + \overline{u''_j u''_\iota})}{\partial x_j} - \rho \bar{R}_\iota + \frac{\partial \bar{p}}{\partial x_i} - \frac{\partial}{\partial x_j}\left(\mu\left(\frac{\partial u_i}{\partial x_j} + \frac{\partial u_j}{\partial x_i}\right)\right) \end{aligned} \tag{2.17}$$

Now, the RANS equations for incompressible flows including external forces, the averaged continuity and momentum equations can be written in tensor form, in the Cartesian coordinate system as

$$\frac{\partial (\rho \bar{u}_i)}{\partial x_i} = 0 \tag{2.18}$$

$$\frac{\partial (\rho \bar{u}_i)}{\partial t} + \frac{\partial}{\partial x_j}\left(\rho \bar{u}_i \bar{u}_j + \rho \overline{u'_\iota u'_J}\right) = -\frac{\partial \bar{p}}{\partial x_i} + \frac{\partial \bar{\tau}_{ij}}{\partial x_j} \tag{2.19}$$

where $\bar{u}_i$ is the relative averaged velocity vector of flow between the fluid and the control volume, $\overline{u'_i u'_j}$ is the Reynolds stresses, $\bar{p}$ is the mean pressure and τ_{ij} is the mean viscous stress tensor components for Newtonian fluid under the incompressible flow assumption, and it can be expressed as

$$\bar{\tau}_{ij} = \mu\left(\frac{\partial \bar{u}_i}{\partial x_j} + \frac{\partial \bar{u}_j}{\partial x_i}\right) \tag{2.20}$$

2.2.1 Menter Two-Equation Model $k - \omega$ SST [110]

The eddy viscosity is defined as the following function of the turbulent kinetic energy K, and specific dissipation rate of turbulent frequency ω:

$$\mu_t = \frac{\rho K/\omega}{max\left\{1, \frac{\Omega F_2}{a_1 \omega}\right\}} \qquad (2.21)$$

$$a_1 = 0.31$$

In turbulent boundary layers, the maximum value of the eddy viscosity is controlled by forcing the turbulent shear stress to be confined by the turbulent kinetic energy times a_1. This effect is achieved with an auxiliary function F_2 and the absolute value of the vorticity. The auxiliary function F_2 is defined as a function of wall distance d as

$$F_2 = \tanh\left(\left[max\left\{2\frac{\sqrt{K}}{0.09d\omega}, \frac{500\mu}{\rho d^2 \omega}\right\}\right]^2\right) \qquad (2.22)$$

The two transport equations of the model are given in (2.23) with a blending function F_1 for the model coefficients of the original ω and ε model equations.

$$\frac{\partial \rho K}{\partial t} + \frac{\partial}{\partial x_j}\left(\left(\rho U_j K - (\mu + \sigma_k \mu_t)\frac{\partial K}{\partial x_j}\right)\right) = \tau_{t_{ij}} S_{ij} - \beta^* \rho \omega K \qquad (2.23a)$$

$$\frac{\partial \rho \omega}{\partial t} + \frac{\partial}{\partial x_j}\left(\left(\rho U_j \omega - (\mu + \sigma_\omega \mu_t)\frac{\partial \omega}{\partial x_j}\right)\right) = P_\omega - \beta \rho \omega^2 + 2(1 - F_1)\frac{\rho \sigma_{\omega 2}}{\omega}\frac{\partial K}{\partial x_j}\frac{\partial \omega}{\partial x_j} \qquad (2.23b)$$

where the last source term of equation (2.23b) represents the cross-diffusion term that appears in the transformed ω equation from the original ε equation. The production term of ω is sometimes approximated as proportional to the absolute value of vorticity:

$$P_\omega = 2\gamma\rho\left(S_{ij} - \omega S_{nn}\frac{\delta_{ij}}{3}\right)S_{ij} \approxeq \gamma \rho \Omega^2 \qquad (2.24)$$

The auxiliary blending function F_1 designed to blend the model coefficients of the original $K - \omega$ model in boundary layer zones with the transformed $K - \varepsilon$ model in free-shear layer and free-stream zones, is defined as:

$$F_1 = \tanh\left(\left[min\left\{max\left\{\frac{\sqrt{K}}{0.09d\omega}, \frac{500\mu}{\rho d^2 \omega}\right\}, \frac{4\rho\sigma_{\omega 2} k}{CD_{k\omega} d^2}\right\}\right]^4\right) \qquad (2.25)$$

where $\mathrm{CD}_{\mathrm{k}\omega}$ stands for cross-diffusion in the $K - \omega$ model.

$$CD_{k\omega} = max\left\{\frac{2\rho\sigma_{\omega 2}}{\omega}\frac{\partial K}{\partial x_j}\frac{\partial \omega}{\partial x_j}, 10^{-20}\right\} \qquad (2.26)$$

2.2.2 Explicit Algebraic Stress Model (EASM) [110]

A quadratic Explicit Algebraic Stress Model (EASM $k - \omega$) that takes into account the variation of production-to-dissipation rate ratio is presented. A new implementation of algebraic stress model where the turbulent eddy viscosity provided by the explicit solution is implied which is providing a robust solution model.

The Reynolds stress transport equations can be written as

$$\frac{D\tau_{ij}}{Dt} = P_{ij} + \emptyset_{ij} - \varepsilon_{ij} + D_{ij} \tag{2.27}$$

where P_{ij} is the production terms given by

$$P_{ij} = -\left(\tau_{jk}\frac{\partial U_i}{\partial x_k} + \tau_{ik}\frac{\partial U_j}{\partial x_k}\right) = -2k\left(b_{ik}S_{kj} + S_{ik}b_{kj}\right) + 2k\left(b_{ik}W_{kj} + W_{ik}b_{kj}\right) - \frac{4}{3}kS_{ij} \tag{2.28}$$

An isotropic model is used for the dissipation rate tensor $\varepsilon_{ij} = \frac{2}{3}S_{ij}\varepsilon$. The term D_{ij} combining the influence of turbulent transport and viscous diffusion is modelized with the Daly and Harlow model:

$$D_{ij} = \frac{\partial}{\partial x_k}\left(0.22\frac{k}{\varepsilon}\tau_{kl}\frac{\partial \tau_{ij}}{\partial x_l} + \nu\frac{\partial \tau_{ij}}{\partial x_k}\right) \tag{2.29}$$

Adopting the quasi-linear SSG model for the pressure-strain rate correlation $\emptyset_{ij}$

$$\begin{aligned}\phi_{ij} = {} & \left(3.4 + 1.8\frac{P}{\varepsilon}\right)\epsilon b_{ij} + 0.36kS_{ij} + 1.25k\left(b_{ik}S_{jk} + b_{jk}S_{ik} - \frac{2}{3}b_{mn}S_{mn}\delta_{ij}\right) \\ & - 0.4k\left(b_{ik}W_{kj} + W_{ik}b_{kj}\right)\end{aligned} \tag{2.30}$$

where W_{ij} is the rotation rate tensors defined as

$$W_{ij} = \frac{1}{2}\left(\frac{\partial U_i}{\partial x_i} - \frac{\partial U_j}{\partial x_j}\right) \tag{2.31}$$

and b_{ij} is the Reynolds stress anisotropy tensor defined as

$$b_{ij} = \frac{\tau_{ij}}{2k} - \frac{1}{3}\delta_{ij} \tag{2.32}$$

To obtain the transport equation for the Reynolds stress anisotropy tensor b_{ij}, the turbulent kinetic energy equation $K = 0.5\tau_{ii}$ is required. It can be easily obtained from the contraction of the Reynolds stress transport equation (2.27) using the fact that the pressure-strain rate tensor is traceless $\phi_{ij} = 0$. The result reads,

$$\frac{Dk}{Dt} = P - \varepsilon + D \tag{2.33}$$

where P is the turbulent production $P = \tau_{ik}\frac{\partial u_i}{\partial x_k}$, and $D = 0.5D_{ii}$. From equation (2.27) and (2.33), the following transport equation for the Reynolds stress anisotropy tensor can be deduced

$$\begin{aligned}&\frac{Db_{ij}}{Dt} - \frac{1}{2k}\left(D_{ij} - \frac{\tau_{ij}}{k}D\right) \\ &= -\frac{\varepsilon}{k}\left(\left[1.9\frac{P}{\epsilon} + 0.7\right]b_{ij} - 0.4867S_{ij} - 0.375\left(b_{ik}S_{jk} + b_{jk}S_{ik} - \frac{2}{3}b_{mn}S_{mn}\delta_{ij}\right)\right. \\ &\qquad \left. + 0.8\left(b_{ik}W_{kj} + W_{ik}b_{kj}\right)\right)\end{aligned} \tag{2.34}$$

To achieve an algebraic equation for b_{ij}, approximation must be made on the left-hand side of equation (2.34). For this reason, the first term Db_{ij}/Dt is assumed to be zero using the so-called

weak equilibrium assumption. Other approximations were provided in different research. The following approximation is applied to the second term,

$$\frac{1}{2k}\left(D_{ij}-\frac{\tau_{ij}}{k}D\right)=\frac{1}{2k}\left[D_{ij}-\left(2b_{ij}+\frac{2}{3}\delta_{ij}\right)D\right]=\frac{1}{2k}\left(D_{ij}-\frac{2}{3}\delta_{ij}D\right)-\frac{D}{\epsilon}\frac{\epsilon}{k}b_{ij} \tag{2.35}$$

In the EASM approach, an explicit analytic solution of equation (2.36) is derived. Final result of the explicit solution of Eq. (2.35) for two-dimensional flow is briefly repeated here for completeness. The Reynolds stress tensor can be written as

$$\tau_{ij}=\frac{2}{3}k\delta_{ij}-2\nu_t\left[S_{ij}+0.8a\left(S_{ik}W_{kj}+W_{ik}S_{kj}\right)\right]-0.75a\left(S_{ik}S_{kj}-\frac{1}{3}S_{mn}S_{mn}\delta_{ij}\right) \tag{2.36}$$

The turbulent eddy viscosity is determined from

$$\nu_t=max\left(-k\alpha_1,0.0005\frac{k^2}{\epsilon}\right);\ a=\left[2.17-1.8\left(\frac{\alpha_1}{\tau}\right)2\eta^2\tau^2\right]^{-1}\tau \tag{2.37}$$

where α_1 is obtained from the solution to the following cubic equation

$$\left(\frac{\alpha_1}{\tau}\right)^3+p\left(\frac{\alpha_1}{\tau}\right)^2+q\left(\frac{\alpha_1}{\tau}\right)+r=0 \tag{2.38}$$

where $\tau=k/\epsilon$ is the turbulence time scale, and

$$p=\frac{2.68}{\eta^2\tau^2}$$

$$q=\frac{1}{(2\eta^2\tau^2\gamma_0)^2}(4.71-0.88\eta^2\tau^2-0.094\eta^2\tau^2+1.28R^2\eta^2\tau^2), \tag{2.39}$$

$$r=\frac{1.056}{(1.8\eta^2\tau^2)^2}$$

where

$$\eta^2=S_{ii}S_{ii},\ W^2=-W_{ii}W_{ii}\ \&\ R^2=\frac{-W^2}{\eta^2} \tag{2.40}$$

The root of equation (2.38) may be real or complex. The correct root is the root with the lowest real part [110].

2.3 Boundary Conditions

The NSE is as second-order partial differential equations. In order to solve this system of equations, it is necessary to define the initial conditions on all the boundaries of the computational domain. The unknown variables in the domain must be clearly defined, such as the three components of velocity, u,v,w, the pressure p and the turbulent model unknown variables, such as in case of the two-equation eddy viscosity models it stands for turbulent kinetic energy K and turbulent dissipation ε or dissipation rate ω.

It is worth mentioning that boundary conditions in ship hydrodynamic are dependent of the type of simulation performed; however, there are generic boundary conditions that can be applied on the main boundaries that must be included in the computational domain, such as the solid body (hull), free-surface and far-field. There are also other boundary conditions that are specific to the

simulations such as the wave generators in the inlet for seakeeping simulations or the specific boundary conditions for sliding or overset grids.

In the following context, an outline of the generic boundary conditions is given for each boundary individually, while the specific boundary conditions are going to be noted in particular regarding the type of simulation performed, as for seakeeping, sliding grids or other simulations that will be presented in the following chapters.

Solid Body (Ship Hull)

Because of the viscous interaction between the submerged part of the hull and fluid, the moving hull is causing a disturbance on the molecular level. Molecules from one phase interact with another phase due to ship motion, colliding with the molecules of the other phase. The phases are thus combined in a very thin layer, and the tangential velocity of the molecules is transferred from one side to another. The velocity difference between the two phases is smoothed out, and basically it is assumed that the difference is equal to zero, which means that the fluid is attached to the solid surface. This is known in the CFD field as the "no-slip" condition which can mathematically be expressed as

$$u = v = w = 0 \tag{2.41}$$

In general, the ship hull is not the only solid wall included in the domain, there are other surfaces that are treated as a solid wall, such as the seabed and banks, which are very common to be found in restricted water channels and depth simulations, the corresponding boundary condition could be written as

$$u = -U \;\&\; v = w = 0 \tag{2.42}$$

where these surfaces are assumed to be moving backward with respect to the ship speed U.

Free-Surface

The aforementioned no-slip condition is applicable for both air and water parts, though the density of air is very much less than that in water. As a result for the molecular interchange at the interface between air and water, both will gain the same speed at the free-surface. Besides, the equilibrium of the tangential forces at the interface must be maintained

$$\begin{aligned} \sigma_{(ns)_w} &= \sigma_{(ns)_a} \\ \sigma_{(nt)_w} &= \sigma_{(nt)_a} \end{aligned} \tag{2.43}$$

where w and a refer to water and air, respectively, and s,t,n represent a local Cartesian coordinate system with n normal to the surface [27]. The effect of surface tension Δp_γ should be also taken into consideration; hence, the normal force equilibrium that represents the dynamic boundary condition on the free-surface is given by

$$(\sigma_{nn} - p)_w = (\sigma_{nn} - p)_a + \Delta p_\gamma \tag{2.44}$$

However, the viscous stresses are usually very small and can be neglected. Thus, the inviscid dynamic boundary is basically transformed into a water surface pressure as

$$p = p_a - \Delta p_\gamma \tag{2.45}$$

where Δp_γ expresses the pressure jump due to surface tension and can be defined as

$$\Delta p_\gamma = \gamma \left(\frac{1}{r_1} + \frac{1}{r_2} \right) \tag{2.46}$$

where γ is the surface tension and r_1 and r_2 are the principal radii of curvature of the free-surface [27].

The kinematic condition on the surface also must be fulfilled, where it indicates that there is no flow through the surface. This is satisfied if the vertical velocity of a water particle moving along the surface are to be equal to the total time derivative of the wave as [27]

$$w = \frac{d\zeta}{dt} \tag{2.47}$$

where $\zeta = \zeta(x, y)$ is the equation for the free surface.

As previously mentioned in the interface modeling section that the new techniques in the air-water interface modeling that are used recently, such as level set or VOF methods, do not explicitly enforce these boundary conditions; however, the conditions are satisfied automatically from the implementation of the indicator function.

Infinity

Despite the fact that the computational domain is usually bounded, it is common practice to consider the flow domain to be infinite at one or more boundaries. Hence, the boundary condition can be applied based on the assumption that the flow at the infinity is not disturbed such that

$$u = U,\ v = w = 0,\ p = p_\infty \tag{2.48}$$

where p_∞ represents the undisturbed pressure.

It is worth mentioning that these are the mathematical boundary conditions. Since the computational domain is always limited in numerical methods, artificial numerical boundaries must be introduced, where the pressure and velocities, or their derivatives in one direction, will have to be essentially identified.

The Turbulence Model

The vast majority of the numerical simulations performed in these research studies used mainly the $k-\omega$ SST model or EASM after proving their capabilities of giving a reasonable balance between the accuracy and computational cost. Though some other turbulence closure models were investigated, as it will be introduced in Chapter IV, these models were the ones selected for the rest of the numerical simulations to be followed. For this reason, the boundary conditions for the default free-stream values of the turbulent kinetic energy, turbulent viscosity, and the dissipation rate, which are applicable for both models $k-\omega$ SST and EASM, can be expressed mathematically as

$$K_\infty = \lambda \frac{\mu_{t_\infty} \omega_\infty}{\rho}\ ;\ \omega_\infty = \lambda \frac{U_\infty}{L}\ \&\ \mu_{t_\infty} = 10^{-3} \mu_t \tag{2.49}$$

where L and U_∞ are the characteristic length and a characteristic velocity of the simulation, respectively. The factor of proportionality λ can be chosen between 1 and 10. Default value is chosen as $\lambda = 1$ [110].

Wall boundary conditions are given by the following equations

$$K = 0\ \&\ \omega = 10 \frac{6\mu}{\beta \rho (\Delta_y)^2} \tag{2.50}$$

where Δ_y is the distance of the first point away from the wall, such that $y^+ < 1$.

In addition to all the aforementioned conditions, there are other conditions that might be considered general for numerical simulations in viscous ship hydrodynamic solvers such as the outflow and the symmetry boundary conditions.

In the outflow boundary condition, it is common practice to set the derivatives in the longitudinal direction for all unknowns to zero. This condition ensures that the flow leaving the domain must preserve the continuity of the flow inside the entire domain. The longitudinal derivatives are in fact not essentially zero, but this boundary condition is proposed to prevent upstream propagation of any reflections or disturbances that can be created by the numerical method. Numerical experiments show that these boundary conditions affect results only in a small local region near the outlet [14].

At the symmetry planes, due to the fact that the normal derivatives of the tangential velocities and the shear stresses vanish, the normal velocity and all the derivatives in the normal direction are basically set to zero.

2.4 CFD Process

The generic procedures for performing a numerical simulation for a general ship hydrodynamic performance are illustrated in Fig. 2.1. The outlined hierarchy shows that the CFD process is decomposed mainly of three major steps: the first is the computational set up process, which can be categorized in this context with respect to the numerical methods represented in Appendix A under the modeling process; while the second stands for the execution of the numerical solution of the presented model; and finally, the third is for the assessment and evaluation of the numerical solution. Worth mentioning that the sub steps included within the presented hierarchy might add or exclude one or two more steps or might slightly differ based on the problem of concern; nevertheless, this structure was chosen to be as general and possible to be suitable for the four fields of ship hydrodynamics that will be covered in this book, i.e., resistance, propulsion, seakeeping and maneuvering.

Prior to performing any of these stages, a proper definition for the problem is essential, since each and every problem in ship hydrodynamic require special considerations, which may influence the entire step coming afterwards. After establishing a proper definition for the problem, the three main stages can be broken down as follows:

1. Solution set up, which involves:
   i. *Preparing the CAD model*. In this step, all the model components, such as ship hull, propeller, rudder and/or appendages must be geometrically refined, without imposing any distortion or changes in the geometry, to eliminate any defects, such as tangled, skewed or detached surfaces;
   ii. *Selecting the solution approach*, which involves the proper choice of how the discretization in space is conducted; for example, in case of a propulsion model, one can chose between body force method and a 3D propeller model. In the latter, a decision should be made on the propeller modeling, whether it will be held based on a sliding grid or an overset grid technique. Besides, if the discretized propeller is going to be used, one may also decide using the total number of propeller blades or to use a single blade with a periodical boundary conditions, and so on;

iii. *Selecting the domain size*. This step is very important and usually depends on the category of simulation. It is crucially important for the domain size to fit the nature of the simulation to avoid any undesired drawbacks, such as wave reflections on the boundaries in seakeeping problems. Another example was noticed by the author for the roll damping and maneuvering simulations that the lateral domain size can significantly influence the accuracy of the solution, as it will be described in the corresponding section within the following chapters;

iv. *Grid generation*, this is the milestone step for a successful numerical simulation. It must be performed with a superior level of prudence, especially for zones with high gradients and wherever appendages and similar hull components exist.

v. *Grid quality check,* It is absolutely crucial before starting any simulation to verify thoroughly the grid quality to avoid any undesired grid quality issues, such as the existence of negative, concave or twisted cells; besides, skew and aspect ratio, since their influence on the solution accuracy might be highly notable, as explained in Appendix A;

2. Preparing and performing the numerical solution, which includes:

vi. *Boundary condition*, all the boundary conditions must be defined for the domain boundaries and solid body as previously described in the previous section;

vii. *Choosing a proper turbulence model*, especially when the wake flow is to be considered in the study, the choice of the turbulence model can really affect the quality of the solution, as previously described in Chapter I and Appendix A;

viii. *Choosing a proper time step*, in the explicit solvers, the time step is usually governed by the Courant–friedrichs–Lewy (CFL) condition which indicates that the information travels during the time step length must be smaller than the distance between the grid cells; i.e., the information travels from one cell to its direct neighbor cell; simply, in a mathematical presentation, the $CFL = \frac{u\,\Delta t}{\Delta x} \leq 1$. For the implicit solvers, the time step is governed by the flow features;

ix. *Selecting the convergence criteria*, this step is very important especially for the problems where the convergence criteria might have a significant influence on the accuracy of the solution, such as in case of seakeeping simulations, as it was explained in Appendix A;

x. *Performing the computation.*

3. Solution assessment or checking the numerical results, which include:

xi. *Checking global parameters*, such as forces, motions, velocities and pressure;

xii. *Checking surface and field parameters*, such as free-surface visualization and wake flow prediction;

xiii. *Flow visualization*, the interaction between fluid and hull can be predicted in this stage to investigate any existence of flow separation, viscous diffusion, vortex shedding, etc.

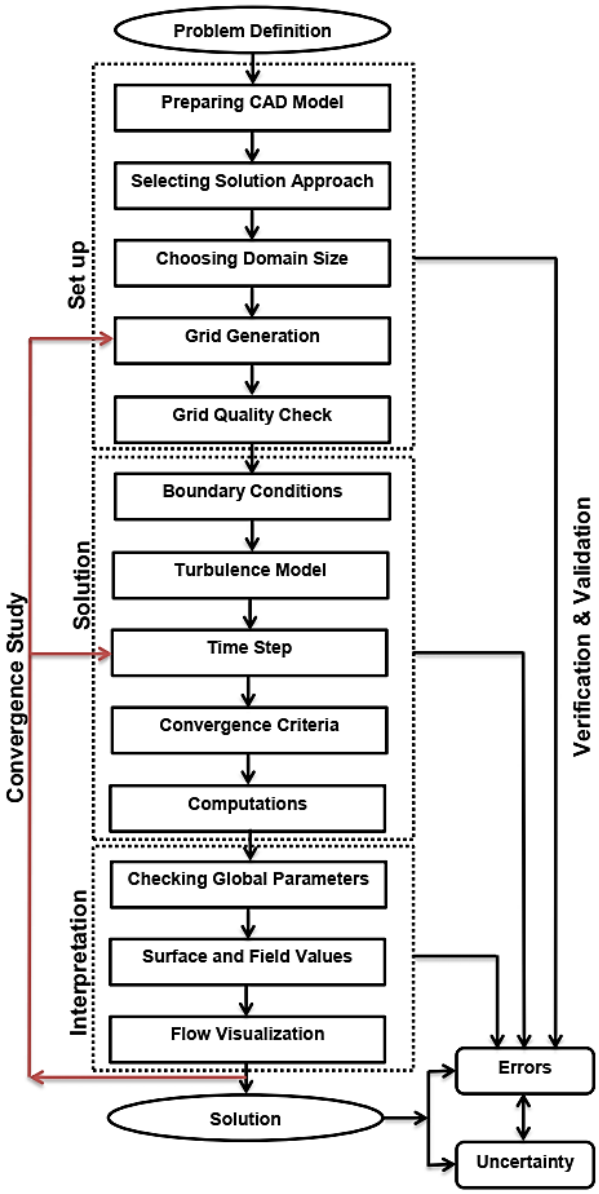

Figure 2.1 General CFD process [60]

The next step after this final stage is to assess the numerical uncertainties, which requires the execution of the quantitative verification and validation study. Since this step is crucially important and rather becoming essential in all the recent numerical simulations, Chapter III is describing the basic procedures for performing this study, describing in brief the available standard procedures from the literature, and how it is applied particularly in this research work.

Chapter III
Verification and Validation

Investigation of CFD errors is crucially important for the consistency and accuracy of any numerical solution. Despite the fact that the recent maturity in the numerical methods have led to high quality solutions which can provide a very good interpretation for the physical phenomenon, there are always approximations and assumptions that might include errors and uncertainties. Theoretically, solving the full NSE can provide superior results for almost all flow phenomena; unfortunately, it is not feasible to perform this operation for most of marine applications, as described clearly in Appendix A. The applicable solution for this problem is to use the filtered NSE either in space or time. Thus, the CFD user must be aware of the main steps followed to perform a numerical simulation in order to understand the different levels of errors included in the numerical method and to be able to judge reasonably the validity of the used method. The principal procedures to model the physical problem in general can be visualized in Fig. 4.1, where the sequence of the numerical solution starting from the physical problem ending with the obtained results is illustrated. Consequently, each step may result in one or more level of errors as a result for the different approximations and assumptions involved. For example, the first stage is to establish the conceptual model, which includes a proper definition for the physical problem ignoring less important effects, such as assuming the flow around the freeboard to be less important compared to the underwater part in some resistance problems, as in case of ship resistance simulations.

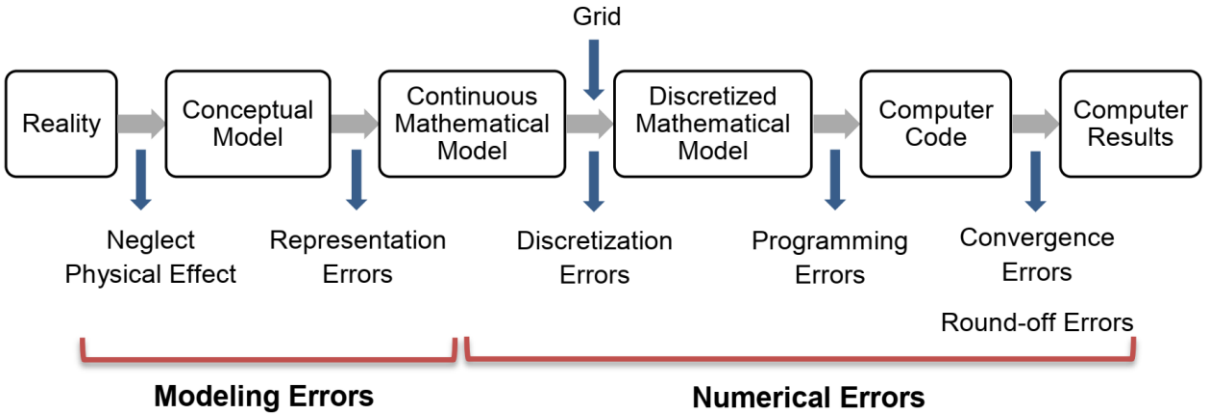

Figure 3.1 Sources of errors in CFD results [27]

The second step is to interpret the conceptual model into a continuous mathematical model, converting the problem into a set of differential or integral equations. This may include some approximations such as linearization or selection of turbulence model, which result in the so-called representation errors. The mathematical model is usually discretized in space based on either finite difference or finite volume approaches, as previously explained, which consequently results in discretization error because of the numerical representation of the actual derivatives and ignoring higher order terms, for example. Different sources of errors might be developed in the next stage due to the choice of domain size or boundary conditions and the selection of the proper solution algorithm. The numerical solution is usually performed in an iterative approach to avoid

complications of the direct solution such as nonlinearities and computation costs. This iterative approach results in convergence error, since the solution is said to be converged when the two sides of the governing equation produce the lowest difference (≤1% between maximum and minimum iterative values is considered acceptable). It is also worth mentioning that there are other types of errors called the round-off errors, which are caused by the representation of numbers in the computer code. Though it might seem to be insignificant, when they accumulate, a serious effect might occur. Faster computer codes use single precision for numbers representation in the computer code; however, double precision is usually recommended.

As it was formerly introduced in the previous chapters that it is very important to assess the numerical solution with a physically measured data from towing tank or sea trials, for many years this process was conducted through direct comparison between CFD and EFD data. Though this method is a straightforward and logic from one perspective; it remains deceiving since the numerical errors as we previously mentioned may tend to interact mathematically and eliminate one another. This may pose a lack of confidence in the numerical solution even when it shows a good agreement with the experimental data. One may ask, is it really a result for a high-quality solution, or just the different types of errors were eliminated? From this point systematic procedures were required to judge the numerical solution to investigate this problem. A consistent effort was paid in the past two decades to develop standard procedures for verification and validation of the numerical solutions. In 1998, the American Institute of Aeronautics and Astronautics (AIAA) introduced one of the milestone standards for verification and validation for CFD simulations [111]; besides, Patrick Roache in 1998 also presented his fundamental reference book Verification and Validation in Computational Science and Engineering [112]. Other efforts may be recognized in the early stage in the last decade of the 20th century; however, these remarkable references build the basic foundation for the verification and validation standard procedures that are still being improved until nowadays.

In Appendix A, the basic division of the numerical method was basically introduced in two main steps which are physical and numerical modeling. The verification and validation process are aimed at assessing the errors associated with these two steps such that, the verification process is concerned with the assessment of the numerical errors verification is said to be the process stands for solving the equations correctly. On the other hand, validation is concerned with the assessment of the modeling errors, i.e., it stands for solving the correct equation [112]. In the following section, the generalized basic concept of the verification and validation process is described, while the various procedures for implementing them in the numerical solution assessment is also introduced with a special focus on the method that is chosen in this research work.

3.1 Verification and Validation Concept

In the spirit of the original comparison concept, the simulation data which can be indicated by the symbol S is compared to the experimental data D; both are representation of the true value T. Fundamentally, the error δ in this case can simply be defined as the difference between simulation or experimental data and the true value. Regardless of its simple concept in definition, it is difficult to define this error as it is basically unknown, so it is usually estimated. This estimate produces another question regarding how accurate this estimate is. For this reason, the uncertainty U was introduced, which indicates that the estimate of an error δ is bounded by the

uncertainty interval $\pm U$ that contains the true value 95 times out of 100. The uncertainty interval can only indicate the magnitude of the error δ not its sign. Yet, this is not happening always, because in some cases when there is enough information available regarding the performed simulation, both magnitude and sign can be estimated and used as correction values for the obtained results.

This basic definition leads us to define two different types of errors or uncertainties, the data and the simulation errors/uncertainty. The former represents the data errors δ_D and uncertainties U_D which are resulting from the difference between the true value and experiment. This is estimated based on the experimental uncertainty analysis procedures, which are not covered here in this context as it is beyond the numerical concept. The reader is referred to the standard procedures by the ITTC [113] for more details. The latter represents the simulation errors δ_S and uncertainties U_S which are the main concern in the verification and validation process. Returning back to the main decomposition of the numerical methods, which include modeling and numerical representation, the simulation error is accordingly decomposed of two types of errors; modeling errors δ_{SM} and numerical errors δ_{SN} [114,115] such that

$$\delta_S = S - T = \delta_{SM} + \delta_{SN} \tag{3.1}$$

and accordingly, the corresponding simulation uncertainty can be presented from the summation of the modeling and numerical uncertainty as

$$U_S^2 = U_{SM}^2 + U_{SN}^2 \tag{3.2}$$

Now, according to the ITTC recommended procedures and guidelines for uncertainty analysis in CFD verification and validation methodology and procedures [114], the verification process can now be defined as the process performed to assess the simulation numerical uncertainty U_{SN} and, when possible, to estimate the sign and magnitude of the simulation numerical error δ_{SN} and to predict the uncertainty in that estimate. In this case, the numerical error which is decomposed from both sign and magnitude, can be written as

$$\delta_{SN} = \delta_{SN}^* + \varepsilon_{SN} \tag{3.3}$$

where δ_{SN}^* represents the estimated value with sign and magnitude of the numerical error δ_{SN}, and ε_{SN} stands for the possible error in that estimate. Hence, the simulation value S should be corrected based on Eq. (3.3) to provide a numerical benchmark S_C, which can be presented as

$$S_C = S - \delta_{SN}^* \tag{3.4}$$

The verification procedures of a numerical solution can be used to provide estimation for errors and uncertainties for all possible numerical error sources such as: iterative; grid size and time step errors. Other error sources might also include artificial compressibility, domain size or round-off errors. For some error sources, such as in case of domain size and turbulence model parameters, estimates can be based on sensitivity studies [115].

The numerical error can be subdivided into different levels, such as: iteration error δ_I; grid error δ_G; time step error δ_T; and errors produced by other parameters δ_P, which can be mathematically formatted as

$$U_{SN}^2 = U_I^2 + U_G^2 + U_T^2 + U_P^2 \tag{3.5}$$

For the corrected simulation approach, the solution is corrected to obtain the numerical benchmark S_C; in this case, the estimated error in the numerical simulation δ_{SN}^* and the corrected uncertainty U_{S_CN} can be written as

$$\delta_{SN}^* = \delta_I^* + \delta_G^* + \delta_T^* + \delta_P^* \quad \& \quad U_{S_CN}^2 = U_{I_C}^2 + U_{G_C}^2 + U_{T_C}^2 + U_{P_C}^2 \tag{3.6}$$

On the other hand, validation is defined as a process performed to assess the modeling uncertainty in numerical simulation U_{SM} by direct comparison with benchmark experimental data and, when possible, to estimate the sign and magnitude of the modeling error δ_{SM}.

This leads us to the definition of the comparison error which is given as the mathematical difference between the data D and simulation S values

$$E = D - S = \delta_D - (\delta_{SM} + \delta_{SN}) \tag{3.7}$$

Modeling errors δ_{SM} can result from modeling assumptions and use of previous data. Modeling errors and uncertainties are not estimated from the numerical solution as the numerical errors and uncertainties are done. Instead, they are obtained through comparison with experimental data in which the uncertainty and errors were taken into considerations.

To distinguish if validation level has been achieved, E must be compared to the validation uncertainty U_V, which can be written as

$$U_V^2 = U_D^2 + U_{SN}^2 \tag{3.8}$$

If $|E| < U_V$, the summation of all the associated errors in D and S are smaller than U_V which this means that the validation is achieved at the U_V level. In case if $U_V \ll |E|$, the sign and magnitude of $E \approx \delta_{SM}$ can be used to make some modeling improvements [114, 115].

For corrected simulation, Eq. (3.7) and (3.8) are modified to

$$E = D - S_C = \delta_D - (\delta_{SM} + \varepsilon_{SN}) \tag{3.9}$$

$$U_{V_C}^2 = U_{E_C}^2 - U_{SM}^2 = U_D^2 + U_{S_CN}^2 \tag{3.10}$$

Having all the possible errors and uncertainties computed, and taking into consideration their magnitude and signs, a clear vision for the accuracy of the numerical solution can be achieved and reasonable conclusions can be withdrawn.

The basic procedures to perform the verification and validation process are introduced in the following section based on different well recognized methods that were proposed in the literature. A special focus is given for the method provided by the ITTC in [114], as it is the conceptual technique applied in this research work for its simplicity and for being general to different applications for CFD in ship hydrodynamics.

3.2 Verification Methodology

According to the aforementioned concept for verification and validation process, the numerical uncertainties and errors can occur due to different sources in the numerical solution such as the discretization grid, time step, iterative method applied by the CFD code and any other parameter that might be related to the numerical solution including round of errors or statistical data sampling, etc. In general, there are two levels for the verification process a CFD user must perform to make sure his numerical solution can be reliable, code verification and solution verification. The former is concerned with verifying the CFD solver itself to ensure that it solves

the equation correctly regardless of the user's interference, whereas the latter is concerned with the application of the solver in the numerical simulation, which might be affected by the user's input parameters such as the choice of the grid size or time step, etc. It is worth mentioning that the solution verification is the only one covered in all the studies performed in this research work, since the ISIS_CFD code was thoroughly verified in multiple occasions such as the in the different versions of the International Workshops on CFD in Naval Hydrodynamics, SIMMAN Workshops for Ship Maneuvering Simulation Methods and other well recognized workshops and research, as previously discussed in details in Chapter I. Prior to presenting the methods used for performing the verification studies, it is important to establish some important concepts in the verification procedures, based on which, the whole process is conducted, such as the estimation of iterative uncertainties and convergence criteria.

Iterative uncertainty and errors: Basically, for RANS simulations, an iterative technique for the numerical solution is used, i.e., the solution starts with an initial guess or an assumption and the time marching (iteration) is then applied until the steady state is achieved. In some cases, the solution may diverge due to numerical instabilities resulting from the grid, time step, etc. In most of the cases, if all the numerical parameters are well considered, the solution should converge to a steady state value and iterative convergence is then said to be achieved. Theoretically, the residuals resulting from the balance of both sides of the equation in the optimum condition should reach a machine zero; however, for practical applications, this is not always possible. For this reason, it is common practice to consider a drop of the residuals to a level of 10^{-3} or 10^{-4} as acceptable. This leads us to three categories for the iterative convergence depending on the convergence history of the numerical solution: oscillatory; convergent or mixed oscillatory/convergent [115].

When the first case occurs, the oscillatory iterative uncertainty is recognized based on the maximum and minimum value of oscillation around the average value. This means that the iterative error and uncertainties can be estimated as

$$\delta_I = S - \frac{1}{2}(S_U - S_L) \;\&\; U_I = \left|\frac{1}{2}(S_U - S_L)\right| \tag{3.11}$$

where S_U stands for the maximum oscillation values and S_L represents the minimums. For the convergent iterative uncertainties, the solution will exponentially converge to a known value as the iteration number increases. In this case, the iteration errors and uncertainties are achieved based on an exponential function or a curve-fit for large number of iterations such that

$$\delta_I = S - CF_\infty \;\&\; U_I = |S - CF_\infty| \tag{3.12}$$

where the CF_∞ is the value for the fitted function as the number of iterations tend to infinity. Finally, in the mixed oscillatory/convergence iterative uncertainties are recognized by a general behavior that tends to be oscillated yet decaying as the iterative number increases. In this case the iterative errors uncertainties and corrected uncertainties can be computed based on maximum and minimum oscillation that envelop the solution values in the ending iteration

$$\delta_I = S - \frac{1}{2}(S_U - S_L) \;\&\; U_I = \left|\frac{1}{2}(S_U - S_L)\right| \;\&\; U_{I_c} = 0 \tag{3.13}$$

More details about iterative uncertainties and the different methods to estimate them can be found in [116].

Convergence uncertainty and errors: the convergence studies are usually conducted based on multiple solutions (at least three are required). This is applicable for numerical parameter such as space and temporal discretization represented in the grid spacing and the time step, respectively, which can be referred to as Δx_i. For a successful study, this parameter must be changed systematically based on the refinement ratio r_i which describes the ratio between the initial parameter and the systematically varied (refined) parameter. It is recommended for this ratio to be uniform such that $r_i = \Delta x_{i,2}/\Delta x_{i,1} = \Delta x_{i,3}/\Delta x_{i,2} = \Delta x_{i,m}/\Delta x_{i,m-1}$ but it is not obligatory, especially that it is difficult to maintain this condition in some cases, such as for unstructured grids. Despite how simple it is to express the refinement ratio, it is rather difficult to select a proper value for it. Small values, i.e., the refinement ratio is close to unity, are practically not favorable due to the fact that the change in solutions might be very small and difficult to be triggered. On the other hand, large values tend to generate a very small step size for the finest level. This might produce an inverse effect, as the very small step size may produce some difficulties in predicting discretization errors. Besides, with the smaller time-steps and very fine grids other issues may occur related to computation cost and the significantly longer simulation time. For industrial CFD applications, $r_i = 2$ is favorable when the condition permits; otherwise, a good alternative may be $r_i = \sqrt{2}$ or similar values according to the user judgment with respect to the available resources [114].

Convergence studies are usually achieved through a minimum of three solutions $m = 3$ to evaluate the convergence based on the input parameters, while $m > 3$ is usually required. The three levels are usually defined as coarse medium and fine. Principally, the finest solution is considered the most accurate. The difference between the solutions in the refinement levels can give us an indication about the solution behavior. For example, assuming there are three solutions, the simulation results obtained can be identified as $\hat{S}_{i,1}, \hat{S}_{i,2}, \hat{S}_{i,3}$ representing respectively, the simulation results for fine, medium and coarse mesh. Conceptually, the finer solution is more accurate than the coarser; thus, the changes between the solutions is usually referred to the finer one computed as follows

$$\varepsilon_{i,21} = \hat{S}_{i,2} - \hat{S}_{i,1} \;\&\; \varepsilon_{i,32} = \hat{S}_{i,3} - \hat{S}_{i,2} \tag{3.14}$$

and they can be used to define the convergence ratio

$$R_i = \frac{\varepsilon_{i,21}}{\varepsilon_{i,32}} \tag{3.15}$$

If the solution is converging, the difference between the fine and medium grids should be less than that between medium and coarse. Eq. (3.15) can lead to three possible convergence conditions

i. Monotonic convergence: $0 < R_i < 1$
ii. Oscillatory convergence: $R_i < 0$
iii. Divergence: $R_i > 1$

For the first condition, the uncertainties and errors can be estimated based on one of the generic methods, such as generalized Richardson Extrapolation method. For condition (ii), uncertainties are estimated simply by implementing the oscillatory concept from the iterative uncertainty based on oscillation maximums S_U and minimums S_L; which mean that a general uncertainty U_K for any convergence parameter such as grid, time step or any other input value can

be expressed as $U_K = \frac{1}{2}(S_U - S_L)$. It is worth mentioning that in this condition it may be deceiving only three levels to judge the convergence or the divergence of the solution, and it is advised in this case to use $m > 3$. Finally, for condition (iii), errors and uncertainties cannot be estimated [114, 115].

3.2.1 Generalized Richardson Extrapolation (RE)

The RE method is essentially accomplished as a quantitative representation for a grid convergence test. The grid convergence test is performed for the numerical solution using iterative and input parameters, such as grid or time step size, for multiple solutions, basically three or more. The results obtained are containing, by default the three main numerical sources of errors: iterative, grid and time step errors.

Generalized RE is performed to estimate the error δ_i^* resulting from the selection of the *i-th* input parameter with respect to an order of accuracy p_i. A power series expansion with integer powers of Δx_i is used to expand the error as a finite sum. The accuracy of the estimates is highly affected by three important elements: the number of terms retained in the expansion, the magnitude (importance) of the higher-order terms, and the validity of the assumptions made in RE theory [114].

For three solutions, when the monotonic convergence is achieved with respect to condition (i) of Eq. (3.15), errors can be estimated based on the leading term $\delta^*_{RE_{i,1}}$ according to Eq. (3.16) based on the solution order of accuracy p_i and grid refinement ratio r_i as it is expressed in Eq. (3.17) as follows

$$\delta^*_{RE_{i,1}} = \frac{\varepsilon_{i,21}}{r^{p_i} - 1} \tag{3.16}$$

$$p_i = \frac{ln\left(\varepsilon_{i,32}/\varepsilon_{i,21}\right)}{ln(r_i)} \tag{3.17}$$

Most favorably is to use more than three solutions as previously described in the grid convergence section. For this reason, another equation can be introduced for five solutions based on two terms estimates for errors and order of accuracy p_i & q_i such that

$$\delta^*_{RE_{i,1}} = \frac{r^{q_i}\varepsilon_{i,21} - \varepsilon_{i,32}}{(r^{q_i} - r^{p_i})(r^{p_i} - 1)} - \frac{r^{p_i}\varepsilon_{i,21} - \varepsilon_{i,32}}{(r^{q_i} - r^{p_i})(r^{q_i} - 1)} \tag{3.18}$$

$$p_i = \frac{\ln\left|\left(a_i + \sqrt{b_i}\right)/\left[2\left(\varepsilon_{i,21}\varepsilon_{i,43} - \varepsilon_{i,32}^2\right)\right]\right|}{ln(r_i)} \;\&\; q_i = \frac{\ln\left|\left(a_i - \sqrt{b_i}\right)/\left[2\left(\varepsilon_{i,21}\varepsilon_{i,43} - \varepsilon_{i,32}^2\right)\right]\right|}{ln(r_i)} \tag{3.19}$$

where $a_i = \varepsilon_{i,21}\varepsilon_{i,54} - \varepsilon_{i,32}\varepsilon_{i,43}$
and $b_i = -3\varepsilon_{i,32}^2\varepsilon_{i,43}^2 + 4\left(\varepsilon_{i,21}\varepsilon_{i,43}^3 + \varepsilon_{i,32}^3\varepsilon_{i,54}\right) - 6\varepsilon_{i,21}\varepsilon_{i,32}\varepsilon_{i,43}\varepsilon_{i,54} + \varepsilon_{i,21}^2\varepsilon_{i,54}^2$

In general, the RE method is very simple and straightforward to apply; yet, it is important to ensure four important factors for the RE to be successfully applied:

1. the grid spacing must be as uniform as possible, which is difficult to achieve in the unstructured grid solvers. Nevertheless, the unstructured grid spacing is usually controlled by an important factor related to the initial cell size, which is usually computed based on the volume of the computational domain and the number of cells. This will be explained clearly in the final section of this chapter;

2. to ensure a systematic grid refinement;
3. the asymptotic range is achieved for the order of accuracy p_i, i.e., the order of accuracy should be similar or within the same range as the theoretical order of accuracy p_{th}, which equals 2 by default for finite volume method framework;
4. and the solution is continuous, i.e., the solution should not include any discontinuities, since the RE method is basically derived form the mathematical derivative of an exact solution of the mathematical model.

Another aspect that should be taken into consideration for RE method when applied on five solutions as it is proposed in Eq. (3.18) is to ensure a monotonic convergence for all the five solutions; besides, the two orders of accuracy must be within the symptotic range. This may pose some extra diffculties in applying the RE method with five solutions.

3.2.2 Estimating Errors and Uncertainties with Correction Factor

The correction factor concept was introduced based on different verification studies and analytical benchmarks applied for 1D wave equation, 2D Laplace equation and Blasius boundary layer [114]. The concept can be used to define the distance of the solution from the asymptotic range and to account for the higher order terms in the error estimates, which might be disregarded in RE method. The principle is to multiply the error obtained from the RE method, which is computed based on one-term order of accuracy and far from the asymptotic range, in order to improve the error estimate. Hence, the error according to the correction factor C_i with respect to Eq. (3.16) is defined as

$$\delta_{i,1}^{*} = C_i \delta_{RE_{i,1}}^{*} = C_i \left(\frac{\varepsilon_{i,21}}{r^{p_i} - 1} \right) \tag{3.20}$$

where C_i is the correction factor and it can be estimated from Eq. (3.17) by simply replacing the estimated order of accuracy p_i with the improved estimate $p_{i_{est}}$

$$C_i = \frac{r^{p_i} - 1}{r^{p_{i_{est}}} - 1} \tag{3.21}$$

For three solutions where the correction factor and RE methods are applicable, C_i is sufficiently less than or greater than 1. The uncertainty U_i estimate based on the correction factor is achieved by bounding the error $\delta_{i,1}^{*}$ by the sum of the absolute value of the corrected RE estimate and the amount of correction [114]. In its simple form, the uncorrected uncertainty U_i for $C_i \geq 1$ and $C_i < 1$, respectively; besides the corrected uncertainty U_{i_c} can be estimated as

$$U_i = (|C_i| + |1 - C_i|) \left| \delta_{RE_{i,1}}^{*} \right| \;\&\; U_i = (2|1 - C_i| + 1) \left| \delta_{RE_{i,1}}^{*} \right| \tag{3.22}$$

$$U_{i_c} = |1 - C_i| \left| \delta_{RE_{i,1}}^{*} \right| \tag{3.23}$$

An extensive discussion for this concept was introduced in the literature and finally was concluded by Wilson et al. in [118] to compute the uncorrected and corrected uncertainty estimate according to

$$U_i = \begin{cases} [9.6(1-C_i)^2 + 1.1]\left|\delta^*_{RE_{i,1}}\right|, & |1-C_i| < 0.125 \\ [2|1-C_i| + 1]\left|\delta^*_{RE_{i,1}}\right|, & |1-C_i| \geq 0.125 \end{cases} \quad (3.24)$$

$$U_{i_c} = \begin{cases} [2.4(1-C_i)^2 + 0.1]\left|\delta^*_{RE_{i,1}}\right|, & |1-C_i| < 0.125 \\ |1-C_i|\left|\delta^*_{RE_{i,1}}\right|, & |1-C_i| \geq 0.125 \end{cases} \quad (3.25)$$

The uncertainty estimate based on Eqs. (4.24) and (4.25) provides 10% factor of safety in the limit of the correction factor $C_i = 1$ [114].

3.2.3 Estimating Uncertainties with Factor of Safety

An alternative approach of the correction factor is to use the factor of safety F_s that was proposed by Roache [112, 117]. It can similarly be used to define the uncertainty U_i based on the error estimate from RE as

$$U_i = F_s\left|\delta^*_{RE_{i,1}}\right| \quad (3.26)$$

Also, the factor of safety approach can be used for situations where the solution is corrected with an error estimate based on the RE method as

$$U_i = (F_s - 1)\left|\delta^*_{RE_{i,1}}\right| \quad (3.27)$$

The choice of the value for the factor of safety is ambiguous; however, it is recommended to use the exact value for factor of safety as $F_s = 1.25$ for systematically performed convergence studies and $F_s = 3$ for cases when only two grids are used and the accuracy is set to the theoretical order of accuracy p_{th} [114, 119].

3.3 Validation Methodology

After the verification process is conducted and all the associated numerical uncertainties and errors are estimated, the validation process takes place, which is aimed at assessing the modeling uncertainties and errors through comparison with benchmark data, basically obtained from experiment or sea trials. The basic concept is to correlate the error E, which was previously introduced in Eq. (3.9) with the validation uncertainty U_V from one side, and the required level of validation U_{reqd} on ther side. Here, U_{reqd} is selected for practical application based on the level of accuracy required for a certain type of simulation, which can be established based on the common level of accuracy for this type of simulation from previously collected data, for example as in the ship hydrodynmic workshops. The combination between the three variables, just assuming that they are not matching, can lead us to six different scenarios as it was presented in [114, 115] as follows

$$\begin{aligned} &1)\quad |E| < U_V < U_{reqd} \\ &2)\quad |E| < U_{reqd} < U_V \\ &3)\quad U_{reqd} < |E| < U_V \\ &4)\quad U_V < |E| < U_{reqd} \end{aligned} \quad (3.28)$$

5) $U_V < U_{reqd} < |E|$

6) $U_{reqd} < U_V < |E|$

In case 1, 2 and 3, $|E| < U_V$ hence, the validation process is achieved at the U_V level which indicates that the comparison error is below the noise level. For this reason, it is not reasonable to improve the model assumptions in the CFD process in order to decrease the model uncertainty δ_{SM}. Case 1 shows that the validation process is achieved at a level below U_{reqd} which means that from a programmatic point of view, the validation is successful.

In case 4, 5 and 6 $U_V < |E|$, it means that comparison error is above the noise level. In this case it is feasible from the uncertainty point of view to use the sign and magnitude of E to estimate the modeling error δ_{SM}. In this case it is more likely that E corresponds to modeling error, so in case if $U_V \ll |E|$, errors can be unambiguously determined. In case 4, validation is successful at the E level from a programmatic point of view as in case 1. The same conditions are applicable for corrected error E_c which will be compared to U_{V_c}, except for the fact that E_c may be smaller or greater than$E$, while U_{V_c} is always less than U_V.

Concluding the previously introduced sections, it is usually misleading to judge a numerical solution only based on the direct comparison with experimental data for the obvious reasons that were introduced. However, since the numerical simulations are actually performed to reproduce real case scenarios or phenomena that take place in real life, experimental data have been and will still be the basic reference benchmarks for numerical solutions assessment. For this reason, a standard, structured and quantitative verification and validation procedures are crucially important to increase the confidence level in the obtained results from CFD simulations and to provide a proper understanding for different sources of error in order to help developing the CFD codes and reducing the errors in numerical solutions. Besides, it also can be subjective for judging other cases where the EFD data are not available, by correlating the errors and uncertainties to similar cases, such as accidental cases including, sinkage, flooding, etc., which are not feasible to be analyzed in real cases.

3.4 Unstructured Grid Generation for Verification and Validation Studies

Grid similarity and systematically refined grids are essential for a successful RE method adaptation in the verification and validation process. Structured grids can be easily controlled by the imposed initial and target cell size; besides, the refinement ratio in each direction can also be established in the grid generation process. Unfortunately, the grid generation process is completely different when speaking about the unstructured grids. Despite the fact that the initial cell size can be controlled by the number of segments used to divide the initial computational domain, the target cell size cannot be controlled easily. One of the advantages of the unstructured grids is that it can handle complicated geometries easily due to its flexibility for adapting the cell configuration to fit for curved surfaces and sharp bends. This is problematic on the other hand, because this makes it difficult to control the number of refinements in the Cartesian directions. The grids included in all the numerical studies performed in this research work are generated using the HEXPRESS™ unstructured grid generator incorporated within the FINE™/Marine package. This module is applying a constructed technique to generate what is called *trimmed*

meshes. The principle in this type is to configure the grid starting from the initial background domain that includes the input geometry. The following step is to divide the initially constructed grid into smaller segments to adapt to the geometry details. Final step is to insert the sub-layers that will be attached to the geometry in order to provide a sufficient resolution near the walls to capture the boundary layer. Basic user inputs in this case is the initial cell size which is determined by the number of divisions chosen for the simulation domain in (*x*-, *y*-, *z-)* directions, the number of refinement levels for the geometrical elements that should be captured (curves or surfaces), the density of the transition zone between two refinement levels, which is called the refinement diffusion and finally, the number of refinement levels (layers) that should be inserted in the viscous sub-layer.

In order to ensure the geometrical grid similarity, the refinement process should be conducted following systematic steps. The basic variables that are controlled in this case are the initial cell size and the refinement diffusion depth. This method was applied successfully for unstructured grids generated by HEXPRESS™, as it was presented in [120, 121] and even for another similar grid generator as described in [122]. The basic steps can be demonstrated for a simplified configuration of a solid cube; an initial high-quality grid is generated and then successively refined to obtain as geometrically similar grids as possible, executing the following steps:

a. the initial cell size is reduced by imposing more divisions for the initial grid in (*x*-, *y*-, *z-)* directions;
b. all the refinement levels for the geometry elements (curves and surfaces) are maintained unchanged;
c. the refinement diffusion is increased to adapt to the required final grid size;
d. finally, the number of levels for the viscous sub-layer are adapted to match the grid refinement.

The grids obtained, especially after the third step, are guaranteed to be geometrically similar. The resulted grids after the third step for a simple cube configuration are presented in Fig. 4.2, while the corresponding grid generation details are listed in Table 3.1.

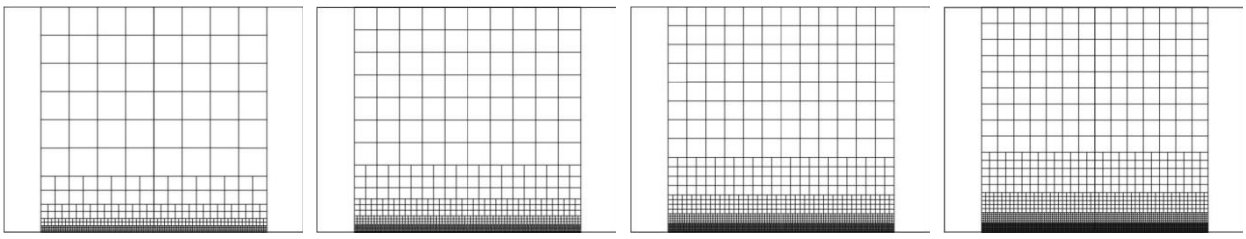

Figure 3.2 Geometrically similar grid for a simple cube configuration

Table 3.1 Geometrically similar grids parameters for a cube

Grid	Directional Subdivisions			Refinement Diffusion
	x	y	z	
Coarse	8	8	8	1
Coarse – Medium	10	10	10	2
Medium – Fine	12	12	12	3
Fine	14	14	14	4

It is worth mentioning that this sequence is followed for an ascending refinement approach, i.e., the coarsest grid is generated first then refined; while, a descending approach is also possible to be applied starting with the finest grid then coarsened gradually. The first approach is the one applied in this research work, while the later was proposed and followed by some other researchers.

Extra details regarding the fourth step is related to the condition of the wall; for example, in wall modeled approach, the number of viscous layers is usually chosen as a float of a minimum and maximum number of layers, while the wall function is set to a suitable value that is usually maintained unchanged in wall modeled simulations $y^+ = 30\sim50$ based on the geometry (bearing in mind that all the simulations performed in this research work are for model scale geometries, otherwise the y^+ value could be larger as for full scale simulations or it can be chosen such that $30 < y^+ < 300$, according to ITTC [123]). On the other hand, for wall resolved simulations, $y^+ \leq 1$ is set initially and its value is reduced gradually to ensure a denser viscous layer, while the number of viscous sub-layers is still kept floating of minimum and maximum values, yet the range is almost doubled compared to the wall modeled simulations. An example for geometrically similar grids generated based on the same principle for the Japan Bulk Carrier JBC is depicted in Fig. 4.3 showing the forepeak of the ship highlighting the refinement criteria based on the previously described details in the cube example; nevertheless, the initial grid size in this case is refined by increasing the directional divisions with a value of 4 in each time instead of 2, while the refinement diffusion here starts with a value of 2 for the coarsest grid. Similarly, the criteria can be applied for any geometry or in case if the ship is equipped with appendages.

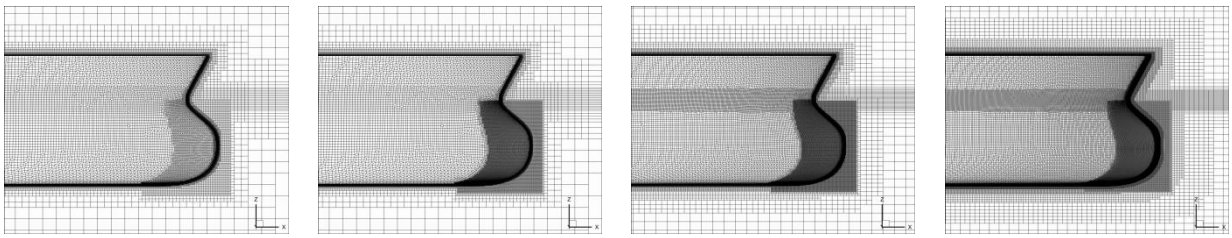

Coarse Coarse – Medium Medium – Fine Fine

Figure 3.3 Geometrically similar grids for the JBC ship model

After the grid similarity is ensured, the other parameters of the numerical uncertainties such as the time step is handled in the solver by imposing proper refinement criteria to reduce the time step accordingly in order to examine its influence on the solution errors and uncertainties. Later after the results are obtained, analyzing the residuals and the iterative behavior of the solutions, the iterative and other sources of uncertainties can be easily applied. More details about the verification and validation studies will be given correspondingly for the simulations performed whose results are to be presented in the following chapters.

Chapter IV
Ship Resistance Performance

Ship resistance represents the principal parameter that must be predicted in the early design stage of the ship by means of numerical, statistical or experimental methods, as it was previously introduced in Chapter I. The main parameter for the new design and sometimes the only given information for a designer beside the ship type, is the service speed or basically called the contract speed. This speed is usually assigned by the owner based on the highest possible profit from the ship voyage for commercial ships or based on achieving the most optimum performance for other ship types. This will be the first parameter taken into consideration during the sea trials after the ship is constructed, and in case if the difference between the actual and contract speed is significant, the owner has the right to even refuse the ship. The required power to drive the ship depends mainly on resistance and propulsive efficiency. The latter is influenced by the propeller performance and its interaction with the hull. Other considerations should be also made for sailing in waves, mechanical and power train losses. Yet, ship resistance remains the main parameters used to decide the required power. Since the resistance and the other forces acting on the hull result from the interaction between the hull surfaces and the surrounding flow in forms of shear and normal stresses, it is crucially important to study this interaction between the hull and the flow in order to understand the different components of forces and consequently use this information to achieve an optimum design from the resistance point of view. Besides, the flow in the stern region is highly important to be considered as it determines the working condition for the propeller.

Heading from this perspective, it is very important to predict the total ship resistance with the highest possible accuracy. Also, the other characteristics such as the flow wake, free-surface and hull-fluid interaction have to be well evaluated in order to achieve the most optimum design and increase the propulsion efficiency from both economic and environmental point of view.

Resistance is recently becoming a common practice for CFD applications where it showed to have the highest level of accuracy within the other hydrodynamic aspects. Thanks to the continuous development in the numerical solvers along with the massive evolution of the computer powers and availability of hardware resources, the maturity in predicting the ship resistance is becoming highly competitive to those measured in the towing tanks, as it was proved in the latest Workshops for Ship Hydrodynamics and the recent research. Nevertheless, the integrity of the numerically solved ship resistance problem should be achieved through systematic verification and validation against the tank test results in order to ensure the quality of the computed results and the compatibility between the practically and numerically obtained resistances. From this perspective, the integration between numerical and experimental based approaches is crucial for continuous improvement and better prediction of ship performance from all the hydrodynamic aspects. In this scope, the following sections shows a rigorous investigation of the CFD capabilities in predicting the total ship resistance for three ships; two commercial ship and a medium-high speed surface combatant, all aimed at validating the commercial software in for various ship types, different sailing speeds and hull forms. A special focus is also made for the prediction of the free-surface flow and the local flow in the vicinity of the ship, especially in the wake zone where the propeller is performing.

4.1 Japan Bulk Carrier (JBC)

The Japan Bulk Carrier (JBC) is a Capesize bulk carrier equipped with wake equalizing duct located upstream the propeller to work as an energy saving device (ESD). The ship model was introduced as a new design in the Tokyo 2015 Workshop on CFD in ship hydrodynamics (T2015) in order to o assess the capability and accuracy of CFD methods to predict new concept designs, as previously described in Chapter I. The design of Hull, propeller, duct and rudder was conducted by The National Maritime Research Institute (NMRI), Yokohama National University and Ship Building Research Centre of Japan (SRC) under the supervision and the support of ClassNK. A model with a scale ratio 1:40 (i.e., L_{PP}=7.0m) was constructed and tested in NMRI towing tank for resistance and propulsion conditions with and without the duct. The results available in the public domain were uploaded on the Workshop's website [48] for validation purposes including resistance in calm water, self-propulsion tests and SPIV (Stereo Particle Image Velocimetry) measurements of stern flow fields. The available data from the tank test does not include the rudder since it would have interfered with the laser sheets from the SPIV controller. The geometry of hull, duct, propeller and rudder are depicted in Figure 4.1, while the main particulars of the ship model and duct only are tabulated in Table 4.1, considering the fact that for resistance tests, only the hull and duct were included. The propeller will be covered in the Chapter V, where the open water and self-propulsion simulations are presented.

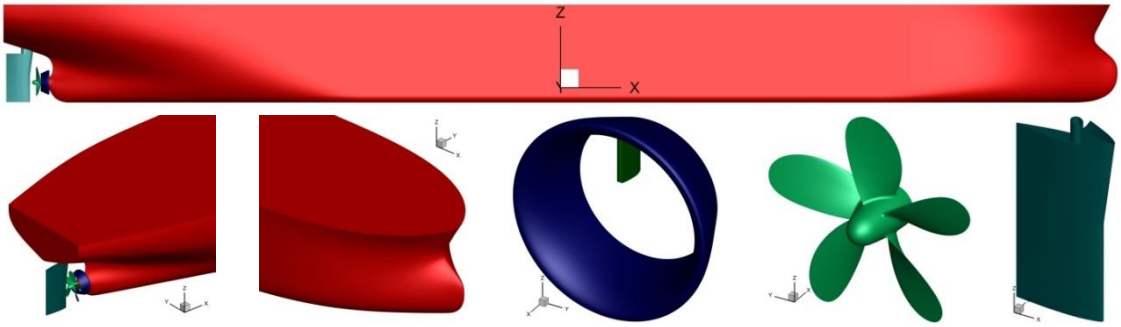

Figure 4.1 JBC model geometry highlighting stern, fore, duct, propeller and rudder

Table 4.1 Principal particulars of ship and duct

	Particulars	Unit	Value
Ship	Length between Perpendiculars (L_{PP})	[m]	7.0
	Beam (B)	[m]	1.125
	Depth (D)	[m]	0.625
	Draft (T)	[m]	0.4125
	Volumetric Displacement (∇)	[m^3]	2.787
	Wetted Surface Area (S_0) (without ESD)	[m^2]	12.225
	Wetted Surface Area (S_0) (with ESD)	[m^2]	12.272
	Block Coefficient (C_B)	[-]	0.858
	LCB (%L_{PP}), fwd+	[-]	-2.548
Duct	Duct Outlet Diameter (0.55D_p)	[m]	0.11165
	Duct Cord Length (0.3D_p)	[m]	0.0609
	Duct Angle of Attack	[Degree]	20
	Duct Foil Section	NACA4420	

4.1.1 Analysis Conditions

The numerical simulation performed for the JBC repeats the resistance towing tank conditions for the model towed in calm water at the design speed U=1.179 m/s with a Froude number $Fr=U/(gL_{PP})^{0.5}$=0.142 and Reynolds number $Re=(UL_{PP})/\upsilon = 7.46\text{E}{+6}$, where U represents the ship speed in m/s and υ represents the water kinematic viscosity in m^2/s. Only two degrees of freedom for the vertical ship motions are included in both experimental and numerical studies, i.e., the axial translation in z-directions (heave, or in calm water resistance is called sinkage) and rotation around y-axis (pitch or trim), while all the other motions are locked. Two analysis conditions included based on the existence of the ESD where case 1 is assigned for the hull without the ESD, while case 2 is assigned for the model equipped with the ESD.

4.1.2 Domain & Boundary Conditions

The computational domain for all the resistance computations performed in the present research is configured of a rectangular prism whose length, breadth and height dimensions in (x–, y–, z–) directions are set, respectively as (5.0L_{PP}, 2.0L_{PP}, 2.0L_{PP}), which are decided with respect to the ITTC recommended procedures for ship CFD applications [123]. The forward inflow boundary is located at 1.0L_{PP} upstream, while the outflow boundary is at 3.0L_{PP} downstream, side boundary is set at 2.0L_{PP}, top and bottom boundaries are placed at 1.5L_{PP} and 0.5L_{PP}, respectively from the initial undisturbed free-surface level that corresponds to the design draft at z=0.4125 m, as depicted in fig. 4.2. Taking advantage of the hull symmetry and the fact that ship is towed ahead with only sinkage and trim motions considered; only half the body is presented in the simulation applying a symmetry boundary condition on the centre-line plane of the ship (i.e., at y=0) in order to reduce the computational effort, time and cost. For this analysis, a global earth-fixed reference frame is set at the point (0, 0, 0) which coincides with the reference point of the ship that results from the intersection of the aft perpendicular (A.P.) and base line. This is basically the general reference for the majority of simulations performed in this research; otherwise it will be mentioned for the corresponding simulation.

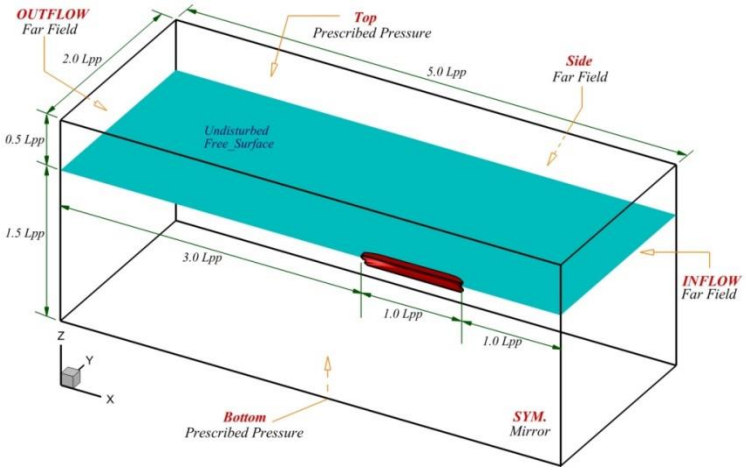

Figure 4.2 Computational domain, dimensions and boundary conditions

The corresponding boundary conditions either Dirichlet or Neumann are applied on the open boundaries and the solid wall according to the ITTC recommended procedures for ship CFD applications [123]. The velocity inlet is applied upstream, pressure outlet is applied downstream,

No-slip condition is chosen for the ship hull, except for the deck, where a slip condition was set, bearing in mind the fact that it remains in the air during the simulation, where the viscosity in the air can be disregarded compared to that in water. Finally, the symmetry condition is applied on the centre-line of the ship as described earlier. The full details for the boundary conditions and the corresponding initial condition for the simulation variables are summarized in Table 4.2.

Table 4.2 Boundary conditions for open boundaries and solid walls

Boundary	U	V	W	p	K	ω	c
Inflow	$U = U_\infty$	$V = W = 0$		$\frac{\partial p}{\partial n} = 0$	$K = \lambda \frac{\mu_{t_\infty} \omega_\infty}{\rho}$	$\omega = \lambda \frac{U_\infty}{L}$	$c = \begin{bmatrix} 0 \; if \; z > 0.4125 \\ 1 \; if \; z < 0.4125 \end{bmatrix}$
Outflow	$\frac{\partial^2 U}{\partial n^2} = \frac{\partial^2 V}{\partial n^2} = \frac{\partial^2 W}{\partial n^2} = 0$			$\frac{\partial p}{\partial n} = 0$	$\frac{\partial K}{\partial n} = 0$	$\frac{\partial \omega}{\partial n} = 0$	$\frac{\partial c}{\partial n} = 0$
Top	$\frac{\partial U}{\partial n} = \frac{\partial V}{\partial n} = \frac{\partial W}{\partial n} = 0$			$p = 0$	$\frac{\partial K}{\partial n} = 0$	$\frac{\partial \omega}{\partial n} = 0$	$c = 0$
Bottom	$\frac{\partial U}{\partial n} = \frac{\partial V}{\partial n} = \frac{\partial W}{\partial n} = 0$			$p = 0$	$\frac{\partial K}{\partial n} = 0$	$\frac{\partial \omega}{\partial n} = 0$	$c = 1$
Side	$U = U_\infty$	$V = W = 0$		$\frac{\partial p}{\partial n} = 0$	$\frac{\partial K}{\partial n} = 0$	$\frac{\partial \omega}{\partial n} = 0$	$\frac{\partial c}{\partial n} = 0$
Symmetry	$\frac{\partial U}{\partial n} = 0$	$V = 0$	$\frac{\partial W}{\partial n} = 0$	$\frac{\partial p}{\partial n} = 0$	$\frac{\partial K}{\partial n} = 0$	$\frac{\partial \omega}{\partial n} = 0$	$\frac{\partial c}{\partial n} = 0$
Hull	$U = V = W = 0$			$\frac{\partial p}{\partial n} = 0$	$K = 0$	$\omega = 10. \frac{6\mu}{\beta \rho (\Delta y)^2}$	$\frac{\partial c}{\partial n} = 0$
Deck	$U = U_\infty$	$V = W = 0$		$\frac{\partial p}{\partial n} = 0$	$\frac{\partial K}{\partial n} = 0$	$\frac{\partial \omega}{\partial n} = 0$	$c = 0$

where c refers to the volume fraction parameter in the VOF formula, as described in Chapter II, Eq. 3.3; while the factor of proportionality λ can be chosen between 1 and 10. Default value is chosen as $\lambda = 1$ and $\mu_{t_\infty} = 10^{-3} \mu_t$, as described in Chapter II, Eq. 3.49.

4.1.3 Computational Grids

Computational grids are generated by making use of the unstructured hexahedral grid generator HEXPRESS™ included in the Fine™/Marine package. Individual sets of grids are generated for both conditions with and without ESD starting with a coarse mesh and then refined to provide geometrically similar grids for the verification and validation studies, as described in Chapter III. For the consistency of the numerical results, the basic discretization parameters such as: initial cell size; refinement levels for curves, surfaces, free-surface and wake zone; refinement diffusion and finally, the viscous layer insertion parameters for the ship with and without ESD are kept identical. Two levels local refinements are applied on the free-surface by imposing a global surface refinement at the undisturbed water level for the entire domain with relatively coarse intensity, while an extra conical sector refinement is applied to coincide with the Kelvin pattern nearby the hull and extended for $1.0 L_{\mathrm{PP}}$ downstream with an opening angle of 20º, in order to capture more details of the wave, as shown in Fig. 4.3.c. The refinement criteria for the Kelvin pattern is decided to provide at least 60 grid cells per wave length in *x*- and *y*-directions, such

that $\Delta x = \Delta y = 2\pi Fr^2 L_{\mathrm{PP}}/60$; while in *z*-direction, the thickness of the refinement zone is chosen to cover the stagnation wave amplitude defined by ζ_{max}=$0.5U^2/\mathrm{g}$. The cell size in *z*-direction for the free-surface refinement sector is set as $\Delta z = L_{\mathrm{PP}}/1000$. Two refinement boxes are located fore and aft to provide sufficient grid resolution for the zones with higher gradients fore and particularly aft to capture more details in the wake, as it can be observed in Fig. 4.3 a & d. The solid wall is treated based on a wall function setting y^+=31.0. Table 4.3 summarizes the computational grids, where M1 refers to the finest grid, while M5 refers to the coarsest grid, where the comparison between both meshes is brought to attention in Fig. 4.3 e.

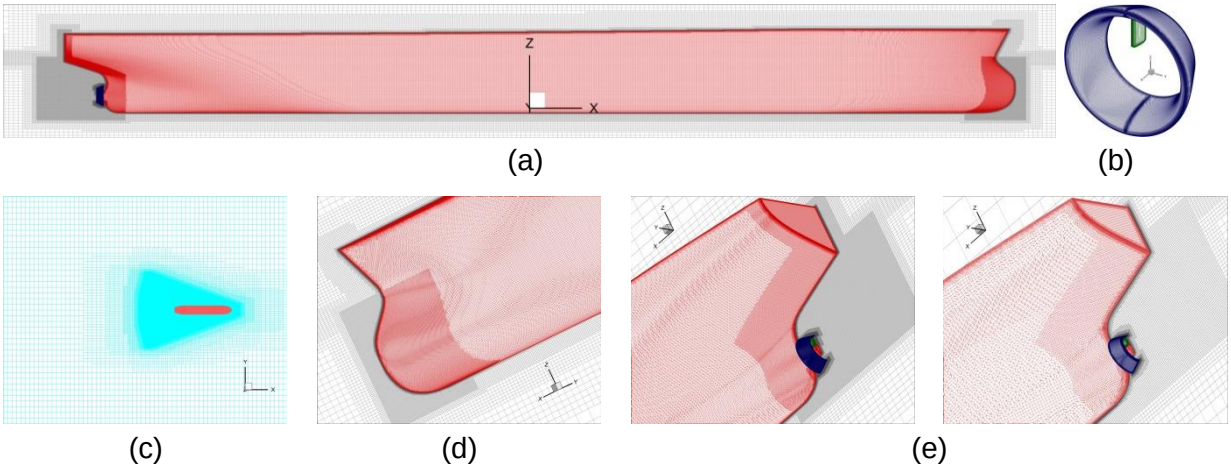

Figure 4.3 Computational grid, showing: (a) JBC with ESD, (b) duct and strut, (c) free-surface refinement, (d) fore and (e) stern comparison between fine and coarse grids

Table 4.3 Computational grids

	Grid Size (Million Cells)			
Ship Model	M1	M2	M3	M4
JBC w/o. ESD	7.462	4.587	2.602	1.506
JBC w. ESD	9.670	5.881	3.583	2.107

4.1.4 Simulation Strategy

The simulation is performed for 30 seconds to achieve a sufficient convergence for the forces and vertical motions, which was decided after a serious of initial pilot computation performed in order to ensure the solution stability and to estimate the entire convergence time. The flow is accelerated in half-sinusoidal wave pattern based on a steady quasi-static approach for a selected period based on the ship speed to satisfy the condition $T_{acc} = 2L_{PP}/U$ in order to avoid any numerical instability issues in the beginning of the simulation. Second order convergence criteria is applied with 10 nonlinear iterations, while the time step Δt is decided based on the formula $\Delta t = 0.005L_{PP}/U$ suggested by the ITTC for the two equations turbulence models or $\Delta t = 0.001L_{PP}/U$ for Reynolds stress models. The time step law is imposed adapted to CFL number to maintain its value less than unity. The numerical discretization scheme for momentum and turbulence model is set to the AVLSMART while the multi-fluid discretization scheme is set to BRICS; both schemes are described in detail in [109].

4.1.5 Resistance and Motion Results

The convergence is achieved after about 22 seconds of physical simulation time for total ship resistance and approximately 25 seconds for sinkage and trim motions. For the sake of achieving the most accurate results, different turbulence models are tested; the most accurate results were recorded for the *SST* k-ω and the EASM models. The results obtained for total ship resistance coefficient $C_T = R_T/0.5\rho S_0 U^2$ are tabulated in Table 4.4, where $S1$ refers to the simulation results from the finest grid M1, while $S4$ refers to the results from M4 and finally, the error $\varepsilon\%$ refers to the percentage difference between EFD and CFD results, such that $\varepsilon\% = 100 \times (EFD - CFD)/EFD$.

Table 4.4 C_T results computed at *T*=30s compared to EFD data [124]

		JBC w/o. ESD		JBC w. ESD	
EFD		C_T= 4.289 × 10^3		C_T= 4.263 × 10^3	
CFD	Turbulence model	EASM	*SST k-ω*	EASM	*SST k-ω*
	$S1$	4.231	4.169	4.282	4.131
	$\varepsilon\%$	1.36	2.80	-0.45	3.09
	$S2$	4.227	4.112	4.227	4.097
	$\varepsilon\%$	1.45	4.13	0.84	3.89
	$S3$	4.224	4.087	4.206	4.055
	$\varepsilon\%$	1.52	4.71	1.33	4.88
	$S4$	4.179	4.014	4.088	3.970
	$\varepsilon\%$	2.57	6.42	4.11	6.87

The obtained results reveal that the EASM model provides the lowest error for the total ship resistance coefficient C_T in both cases with and without ESD. The error range is limited between 1.36% and 2.57% for the coarsest and finest grids, respectively in case when the ship is not equipped with the ESD, while the error for ship with the ESD is between -0.45% and 4.11% for finest and coarsest grid, respectively. On the other hand, the results obtained with the *SST* k-ω model are within an error range between 2.80% and 6.42% for JBC without ESD and between 3.1% and 6.87% for JBC with duct. The overall agreement between CFD and EFD can be considered satisfying.

Similarly, the computed sinkage and trim had a reasonable agreement with the experimental data, regardless of the turbulence model used. Table 4.5 brings to attention the comparison between the CFD results computed using the EASM model and the EFD data for the hull with and without ESD. Obviously the coarser grids give the highest discrepancy between computed and measured data. The reason for this inconsistency resides apparently in the insufficient grid resolution measured in the free-surface vicinity at the ship extremities.

Table 4.5 Sinkage and trim results computed at *T*=30s compared to EFD data [124]

		Sinkage σ (Upward +)		Trim τ (Bow Up +)	
		JBC w/o. ESD	JBC w. ESD	JBC w/o. ESD	JBC w. ESD
EFD		σ=-0.086 %L_{PP}	σ=-0.085 %L_{PP}	τ=-0.180 %L_{PP}	τ=-0.182 %L_{PP}
CFD	$S1$	-0.0872	-0.0877	-0.178	-0.180
	$\varepsilon\%$	1.39	3.18	1.11	1.10
	$S2$	-0.0878	-0.0902	-0.176	-0.176
	$\varepsilon\%$	2.09	6.12	2.23	3.13

	$S3$	-0.0919	-0.0902	-0.172	-0.175
	$\varepsilon\%$	6.86	6.12	4.45	3.96
	$S4$	-0.0922	-0.0903	-0.169	-0.173
	$\varepsilon\%$	7.21	6.23	6.11	4.95

The analysis of the free-surface results in the following section can reveal some details regarding this outcome. Overall, the resemblance between the CFD results and the EDF data is reasonable, especially at the level of medium and fine grids.

Verification and validation of the numerical results are initiated by reviewing the data obtained in the grid convergence study for the C_T summarized in Table 4.4. A descendent behavior can be observed for the total ship resistance coefficient, where the highest value is achieved by the coarsest grid, while the lowest is obtained by the coarsest one. The quantitative Richardson Extrapolation (RE) of the numerical data shows a monotonic convergence except for the analysis between grid 1-3, where a monotonic divergence occurred for the EASM turbulence model, where R_{G1-3}>1. The grid convergence parameters are tabulated in Table 4.6, where the numerical errors and uncertainties are related to the finest grid solution S1, assuming by default that it should produce the most accurate results.

Table 4.6 Grid convergence parameters for total ship resistance coefficient C_T

Convergence parameters		r_{G2-4}	$R_{G_{2-4}}$	$p_{G_{2-4}}$	$\delta_{G_{2-4}}\%S_1$	$U_{i_{2-4}}\%S_1$	$U_{G_{2-4}}\%S_1$	$U_{SN_{2-4}}\%S_1$
JBC w/o. ESD	EASM	1.7	0.07	5.1	0.02	0.1	1.36	1.36
	SST k-ω	1.7	0.34	2.02	1.3	1.37	3.13	3.41
JBC w. ESD	EASM	1.7	0.18	3.25	0.45	1.28	1.0	1.62
	SST k-ω	1.7	0.49	1.33	4.1	0.82	3.4	3.5

On the other hand, the validation parameters for total ship resistance Coefficient C_T are tabulated in Table 4.7 after correlating the estimated uncertainties to the EFD data, where the numerical uncertainties are included in the validation process to reproduce the validation uncertainty U_V based on imposing the data uncertainty $U_D = 1$ from the experiment, such that $U_V^2 = U_D^2 + U_{SN}^2$, as described in Chapter III.

Table 4.7 Validation data for total ship resistance coefficient C_T

Validation		$U_{i_{2-4}}\%S_1$	$U_{G_{2-4}}\%S_1$	$U_{SN_{2-4}}\%S_1$	$U_{SN}\%D$	U_D	U_V
JBC w/o. ESD	EASM	0.1	1.36	1.36	1.34	1.0	1.67
	SST k-ω	1.37	3.13	3.41	3.32	1.0	3.47
JBC w. ESD	EASM	1.28	1.0	1.62	1.61	1.0	1.89
	SST k-ω	0.82	3.4	3.5	3.39	1.0	3.53

Following the obtained results from the verification and validation study, it is clear that for the results obtained by the EASM model, especially for fine grids, validation is achieved at the validation uncertainty level U_V, which means that modeling error resides within the noise level of the numerical and experimental uncertainties. For the coarsest grid, the validation level was not achieved; nevertheless, the average error level for the G2015 for grids less that 10M cells was recorded within 4%, which means that the error range obtained in the current study lies within this criteria, except for the coarsest grids where the RE error compared to EFD data is more than 4% as it can be observed in Figure 4.4.

4.1.6 Free-Surface Results

The free-surface represents one of the most important aspects in ship hydrodynamics since it affects directly the wetted surface area of the hull, which is used to estimate the total ship resistance. Significant discrepancies in predicting the wave height consequently can result in wrong judgement concerning other important variables, such as wave breaking, sinkage and trim, freeboard height selection, etc. For this reason, the theory emphasizes the importance of the well prediction of the free-surface position, despite the methodology applied.

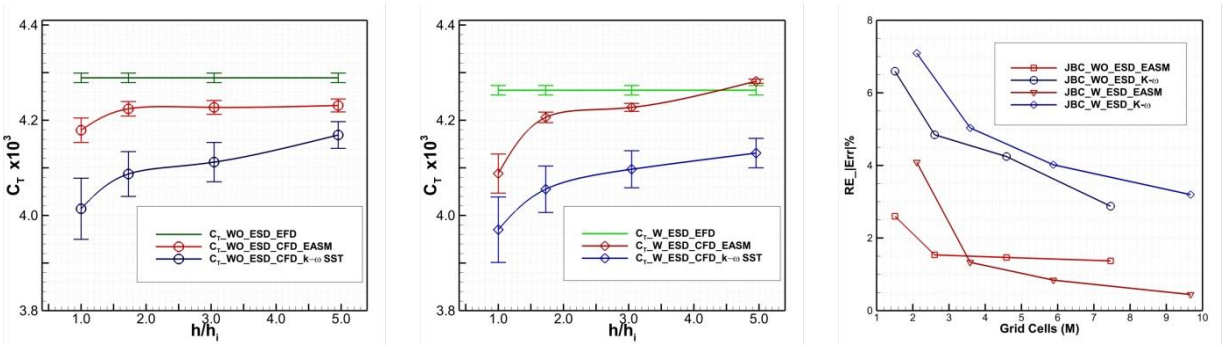

(a) (b) (c)

Figure 4.4 Computed total resistance coefficient C_T with: (a) JBC w/o. ESD, (b) JBC w. ESD and (c) Richardson Extrapolation error

For validation purposes, in order to highlight the accuracy of predicting the free-surface in the current study, a focused comparison between the computed free-surface topology, as well as the wave profile at different sections in *y*-direction and the measured data in the towing tank summarized by Hirata in [125], is brought to attention in Fig. 4.5. The geometry of the produced wave and mass fraction is depicted in Fig. 4.5 b & f, respectively; while the comparison between CFD and EFD regarding the wave topology is highlighted in Fig. 4.5 a, the wave profile at the ship hull is depicted in Fig. 4.5 c and finally, two consecutive sections at y/L_{PP}=0.1043 and y/L_{PP} =0.19 in Fig 4.5 c & d, respectively.

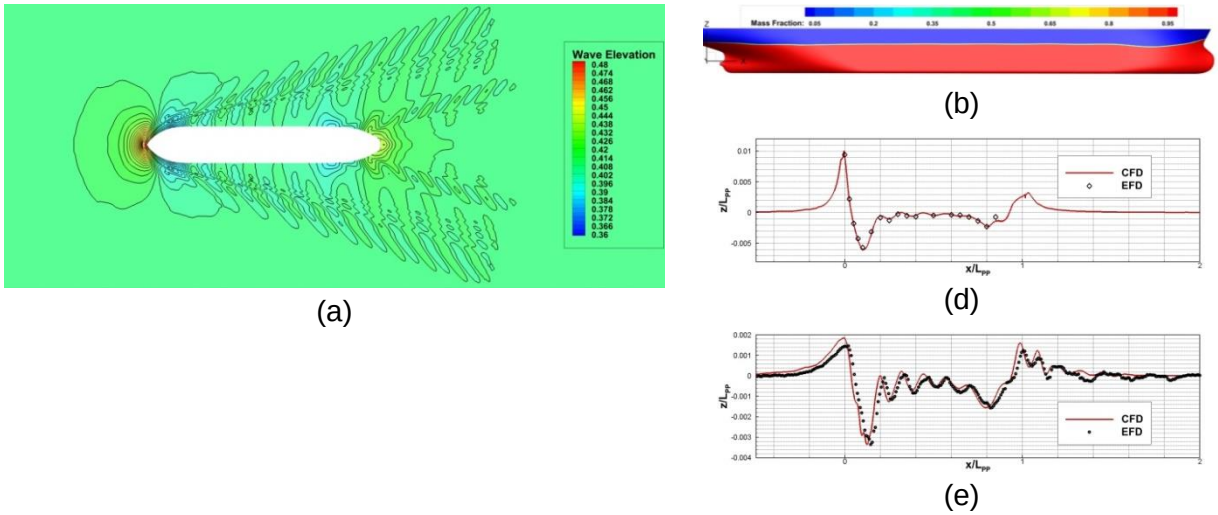

(a) (b) (d) (e)

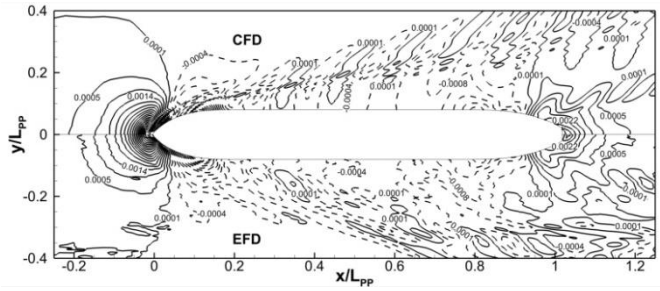

(c)

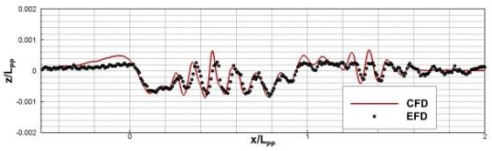

(f)

Figure 4.5 Computed free-surface at T=30 s, showing: (a) free-surface configuration, (b) mass fraction, (c) CFD vs. EFD for the free-surface topology, (d, e and f) CFD vs. EFD for wave profile at the hull, at distances y/L_{PP}=0.1043 and y/L_{PP} =0.19*,* respectively

The computed wave profile as well as the wave elevation shows a good agreement with the EFD data especially in the near field region close to the hull. The height of the obtained wave crest at the bow is over predicted with an approximate error 2.52% compared to the EFD. Heading in the far field, it can be observed that the over predicted wave height still persists beside a minor phase shift. Two possible reasons may result in this over prediction for the wave height; the first may be due to the radiation induced by the numerical scheme towards the upstream, while the second is apparently due to a lack of the sub-breaking regime treatment ability, which usually occurs in the area where the bow intersects the water surface. It was theoretically proven that not only the necklace vortices generation, but also their maintenance requires energy consumption; as a result, the wave crest might be predicted smaller than expected. Therefore, when the numerical scheme fails to well predict those heavy turbulence structures, the height of the bow crest will be over predicted, which supposedly is the case here. In the downstream, the computed wave encounters an observed damping which is obviously due to the coarse grid in that area where the large grid size at the free-surface acts as a numerical damper. This appears directly after the refinement section of the free-surface vanishes, since the Kelvin section refinement is extended only one time the ship length downstream, as previously mentioned in section 4.1.3 regarding the computational grid. In order to enhance the results on the free-surface, a special refinement might be imposed in that zone to capture more details. A side of that, bearing in mind that the ship is working on a considerably small Froude number, increasing the number of grid cells per wavelength more than 60 can improve the results. Yet, it is worth mentioning that both suggestions come with a considerable extra computational cost.

4.1.7 Local Flow Results

Quoting from the objectives in designing the JBC hull to make it more challenging for CFD validations, it was intended to increase the C_B and to keep the stern shape as full as possible in order to produce strong axial vortices [125, 126]. This resulted in a complex wake flow in the stern which is basically characterized by a gradual development of the bilge vortex leading to an observed distortion of the velocity iso-contours at the vicinity of the propeller plan. This distortion is a result of the low momentum fluid transport form the hull vicinity to the center plane enforced by strong longitudinal axial vortices. Close to the vertical plane of symmetry, one can observe a second counter-rotating vortex. The interaction between both vortices results in a famous effect called the “hook-shape” that can be observed in the PIV measurements in the towing tank and wind tunnel. Numerically, the latest development in the CFD turbulence modeling accompanied

with the increased computational power made it possible to properly predict the stern flow accurately due to the reduction in modeling and discretization errors.

For validation reasons, the PIV measurements were applied at seven different sections, three of which were provided in the public domain for local flow comparisons denoted by S2, S4 and S7, as can be observed in Fig. 4.6, where S2 is positioned before the ESD, S4 is located between ESD and propeller, and finally, S7 is at *x*=0, i.e., at the A.P.

In order to highlight the influence of the turbulence model in predicting the wake flow, an individual analysis for the application of turbulence model is performed on a separate grid with about 12.36 M cells for the hull without ESD with a wall resolved model having $y^+ \cong 0.84$, bearing in mind that some turbulence models do not support the wall modeled approach, such as Spallart–Allmaras. Seven different turbulence models are used, which are: EASM, the classic Menter *SST* k-ω, the modified k-ω *SST*-2003 [127], base line *BL* k-ω, the original k-ω, the one equation Spallart–Allmaras and finally the k-ε model.

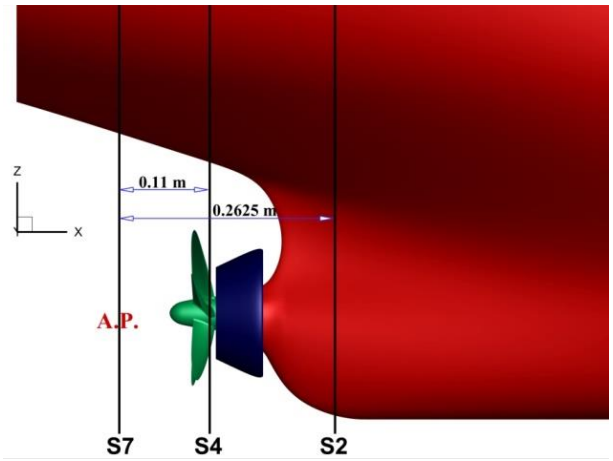

Figure 4.6 PIV measuring sections

The obtained results were checked from the forces point of view as well as from the wake flow quality. As previously mentioned, the EASM and *SST* k-ω models, either the classic or modified, produced the best results. Fig. 4.7, Fig. 4.8, and Fig. 4.9 previews the comparison between measured and computed the axial flow iso-contours in *x*-direction at section S2, S4 and S7, respectively sorted based on the accuracy of the turbulence model.

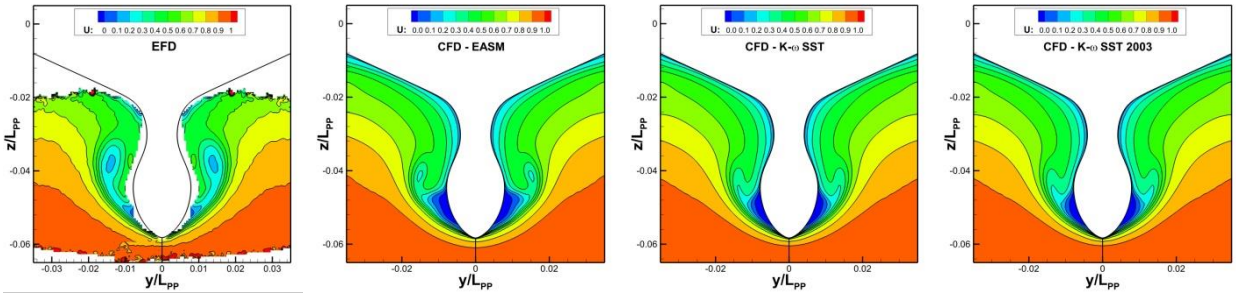

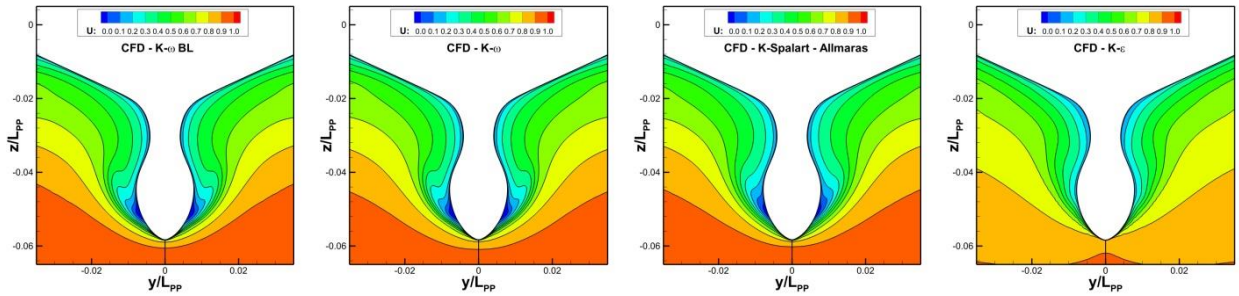

Figure 4.7 EFD and CFD results for the axial velocity contours computed at T=30s for ship without ESD at section S2 using different turbulence models

The overall observation is that the iso-contours are considerably under predicted, while the development of the "hook-shape" vortex is well predicted by the EASM and *SST* k-ω models. The least accurate model in this context was the k-ε which resulted in a very significant over predicted forces and rather poorly developed wake. This may require further investigation; yet, for the scope of this analysis, it was sufficient to decide the turbulence model based on the accuracy of the obtained results.

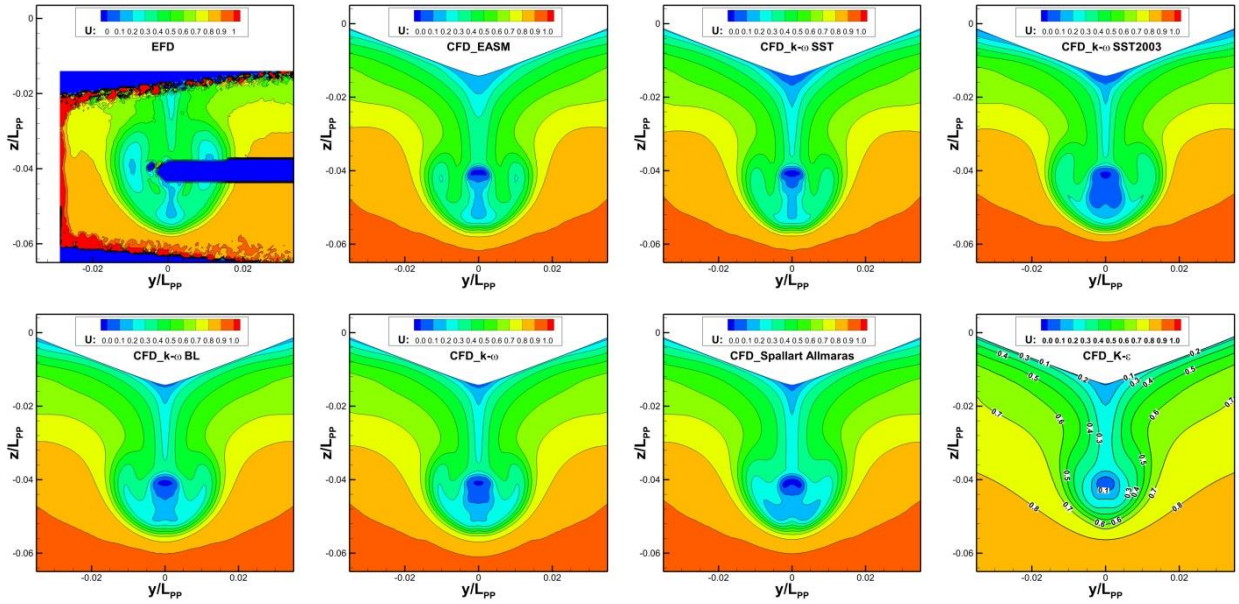

Figure 4.8 Section S4 EFD and CFD results for the axial velocity contours computed at T=30s for ship without ESD using different turbulence models

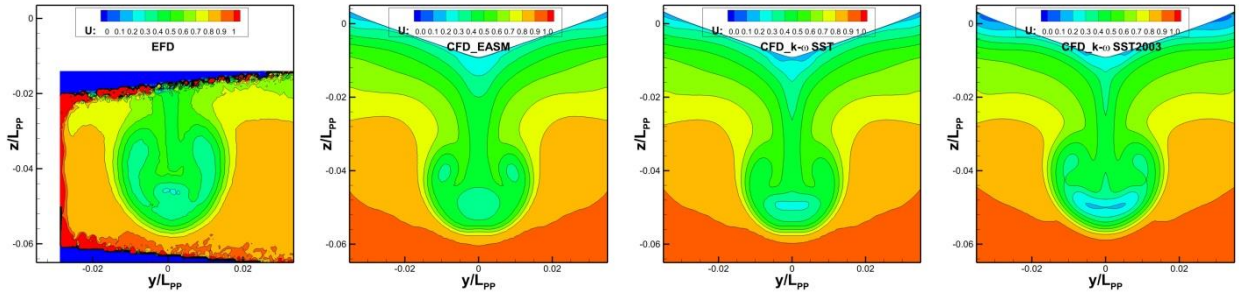

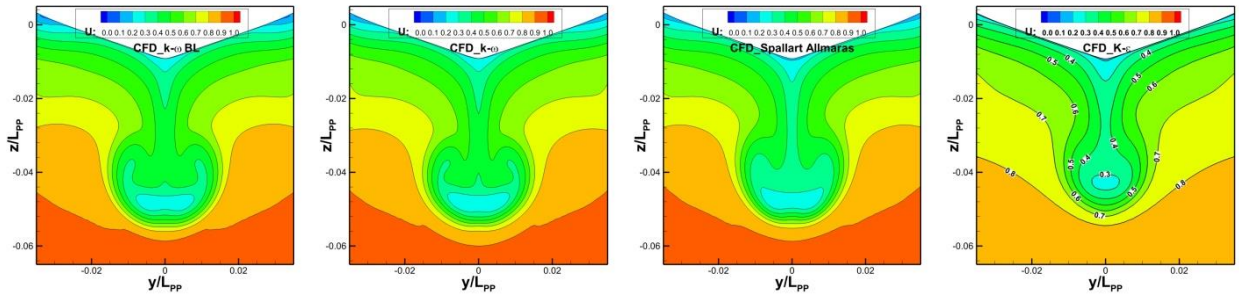

Figure 4.9 Section S7 EFD and CFD results for the axial velocity contours computed at T=30s for ship without ESD using different turbulence models

Having an insight in the flow wake computed using the EASM model on the finest grid M1 for the JBC with ESD to compare the obtained results with the EFD data, Fig. 4.10 shows a comparison between the axial flow velocity contours in *x*-direction for the three sections S2, S4 and S7. The resemblance between CFD results and EFD data may emphasize the solver capability to reproduce the complexity of the wake flow structure, a fact that is significantly important for a proper propeller design.

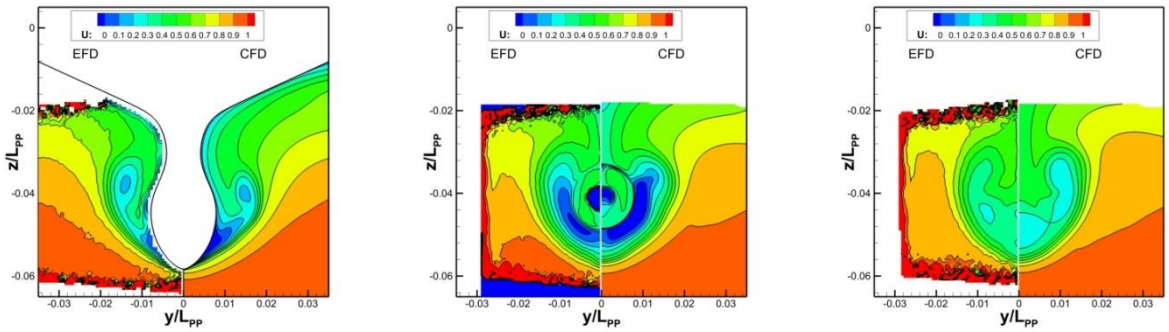

S2 S4 S7

Figure 4.10 Comparison between the streamwise velocity contours measured and computed at T=30 s using EASM turbulence model for ship with ESD for sections S2, S4 and S7

Unlike the common practice to represent the local flow through cross-section where the experimental data are available, an alternative approach is to represent the local flow based on the second invariant Q^* criterion which can be computed based on the equation

$$Q^* = Q\frac{L_{PP}^2}{U_{ref}^2} \quad \text{where} \quad Q = \frac{1}{2}\left(\Omega_{ij}\Omega_{ij} - S_{ij}S_{ij}\right) \tag{4.1}$$

where Ω_{ij} is the vorticity magnitude and S_{ij} represents the mean rate of the strain tensor.

In the scope of having a closer insight into the mechanism of the vortices produced in the stern of the JBC ship, the computed vortical structures for the ship without ESD compared to the data provided in the Workshop as it can be found in [126] is depicted in Fig 4.11 for the second invariant Q criterion at an iso-surface Q*=25 colored by the non-dimensional helicity defined by

$$\mathrm{He} = \frac{\vec{U}.\vec{\Omega}}{|\vec{U}|.|\vec{\Omega}|} \tag{4.2}$$

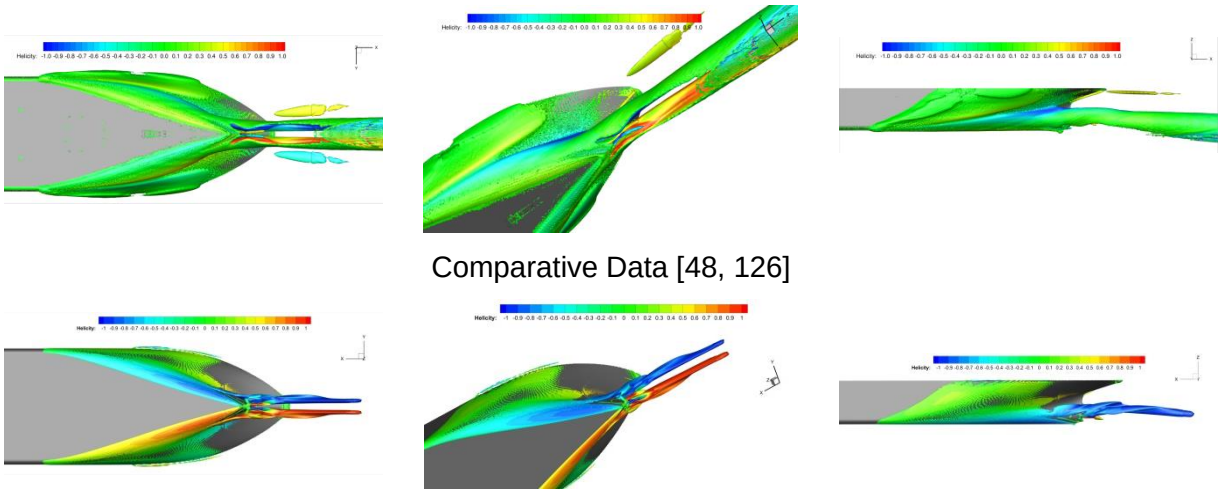

Figure 4.11 Workshop data for the second invariant iso-surface Q^*=25 colored by helicity and the corresponding CFD results computed at *T*=30 s using EASM model

Following the same description that was presented in the early part from this section, two vortices can be observed; the first is generated from the separated flow at the bilge and the second comes from the separated flow at the boss. Due to the interaction between the vortices, a slight distortion can be observed in both the provided data and the computed results. The similarity between the CFD and the provided data is promising; yet, some differences can be observed apparently due to either the grid consistency or the wall modeled approach. Also, the refinement zone in the stern should be extended.

Finally, all the results obtained for the JBC ship model concerning the resistance, vertical motions, free-surface and local flow have been published in [132, 133].

4.2 KRISO Very Large Crude Carrier (KVLCC2)

Though the JBC model represents a challenging hull especially with the existence of the ESD before the propeller, the absence of the rudder from the propeller wake creates a big gap in the simulation, since the vast majority of commercial or special purpose ships are equipped with rudders. It is necessary to compare the CFD results against the EFD data for a ship model that is equipped with rudder. For this reason, the KVLCC2 was selected for this purpose, bearing in mind the fact that it has similar geometry regarding the high block coefficient, which makes the wake flow as challenging as the one from JBC. Besides, the G2010 Workshop included EFD data for the total resistance for the ship with rudder sailing at different speeds.

The Maritime and Ocean Engineering Research Institute (MOERI) now called Korea Research Institute of Ships and Ocean Engineering (KRISO) Very Large Crude Carrier was conceived as a 300 K modern tanker with a bulbous bow and stern to provide benchmark data for explanation of the flow physics and for CFD validation. KVLCC2 ship is the modified stern shape of the previous design KVLCC1 hull. The original ship had a barge type stern with a fine bulb and V-shape frame lines; however, the KVLCC2 has rather U-shape sections. Full scale ship does not exist; yet, several models were built and tested by various internationally well recognized towing tank organizations such as (NMRI) and Osaka University (OU) in Japan, (INSEAN) in Italy, Norwegian University of Science and Technology (NTNU), Hyundai Maritime Research Institute (HMRI) in Korea and others. Various types of experiments were performed on different size ship models including ship resistance, free-surface, local flow configurations, seakeeping and maneuverability and abundant database is available in the public domain. The geometry of the KVLCC2 model showing the propeller and rudder is depicted in Fig. 4.12, while the principal dimensions of the 7.0 meters INSEAN model are tabulated in Table 4.8.

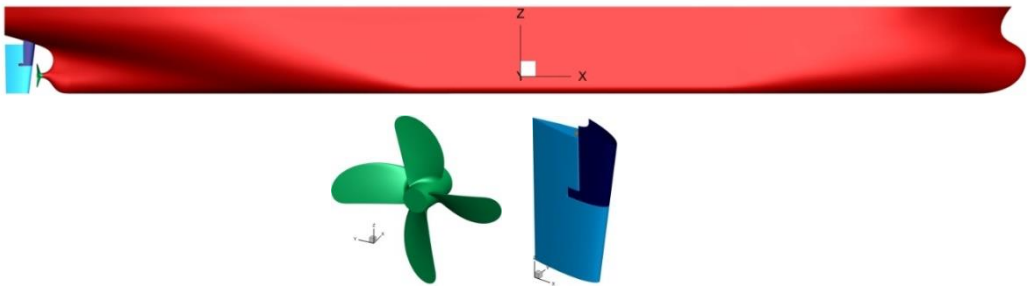

Figure 4.12 KVLCC2 model geometry highlighting propeller and rudder

Table 4.8 Principal particulars of ship and rudder

	Particulars	Unit	Value
Ship	Length between Perpendiculars (L_{PP})	[m]	7.0
	Beam (B)	[m]	1.1688
	Depth (D)	[m]	0.6563
	Draft (T)	[m]	0.4550
	Volumetric Displacement (∇)	[m^3]	3.2724
	Block Coefficient (C_B)	[-]	0.8098
	Mid-ship section coefficient (C_M)	[-]	0.9980
Rudder	Rudder type	-	Horn
	Rudder area (S_R)	[m^2]	0.1308

4.2.1 Analysis Conditions

The numerical simulations performed for the KVLCC2 ship model include two cases: the first is corresponding to Cases 1.1a and 1.1b from G2010 Workshop where the ship is not equipped with rudder and sailing in calm water with no degrees of freedom at the design speed, i.e., Fr=0.142 and Re=4.6x10^6; the second is corresponding to Case 1.2b from G2010 Workshop, where the ship is equipped with the rudder and sailing in calm water at six different speeds with 2 degrees of freedom including sinkage and trim. Table 4.9 summarizes the computational cases with the corresponding ship speed, Froude number and Reynolds number.

Table 4.9 Computational cases and corresponding ship speed parameters

Case Number	C1	C2	C3	C4	C5	C6
U [m/s]	0.8370	0.9894	1.1411	1.1792	1.2173	1.2554
Fr [-]	0.1010	0.1194	0.1377	0.1423	0.1469	0.1515
Re [-] x10^6	3.5	4.1	4.8	4.9	5.1	5.2

4.2.2 Domain & Boundary Conditions

The computational domain dimensions and boundary conditions are imposed exactly similar to those given in section 4.1.2 for the JBC hull, the only difference is that the initial undisturbed free-surface level is set at the design draft of the KVLCC2 model at z=0.455 m from the baseline.

4.2.3 Computational Grids

The discretization grids are also generated using the automatic unstructured hexahedral grid generator HEXPRESS^{TM} available in the NUMECA package. The same principals followed for the JBC grid generation process are repeated here, which implies the choice of the initial cell size, the refinement levels and the refinement zones at the free-surface and wake area. For the ship without rudder in cases 1.1a and 1.1b, a set of three grids are generated to perform a grid convergence study in order to assess the numerical uncertainties. While for the ship with rudder, two different approaches were used to model the rudder based on the rudder configuration; the actual rudder configuration, which consists of a stator, rotor and rudder stock; whereas, the simplified rudder configuration is introduced to avoid the gaps between the stator and rotor parts to simplify the grid generation process and to reduce the total number of grid cells, since a proper discretization of this gap between both rudder parts may requires few hundreds thousands to millions of cells, as it can be observed in Table 4.10. For consistency purposes, the forces and motion results for both approaches were compared at the design speed and showed to be in a very close agreement with less than 1% difference. Hence, the simplified rudder approach was kept for analyzing the rest of the computational cases for the model equipped with rudder. It is worth mentioning that this principal is considered acceptable and has been introduced in much research; however, from a practical standpoint, it may be applicable only when the ship is sailing in the forward direction and no interference from the rudder forces will be included. This simplification should be avoided for the following analyses which include self-propulsion and maneuvering, since for the self-propulsion the wake domain can be influenced with the rudder configuration, while for the maneuvering, the effective rudder area will differ which consequently will influence the rudder forces. The details of the computational grids are given in table 4.9, while the stern area of the discretized domain can be visualized in Fig. 4.13 for both rudder configurations.

Table 4.10 Computational grids for ship with and without rudder

	Bare Hull			With Rudder	
	M1	M2	M3	Simplified	Actual
Number of grid cells (M)	20.33	10.84	4.56	4.752	5.577

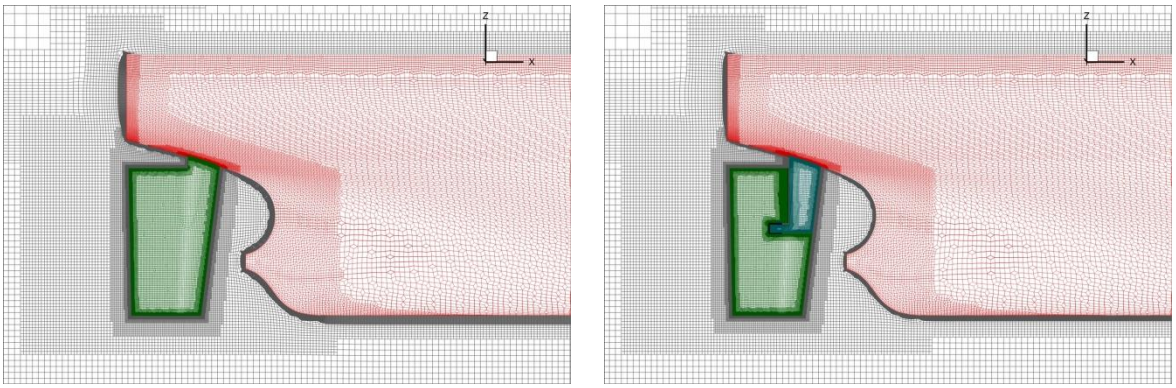

Figure 4.13 Discretization grid for ship with simplified rudder (left) and actual rudder (right)

4.2.4 Resistance and Motion Results

The resistance results are obtained for the first condition where the ship is fixed. The total simulation time is also 30 seconds as in case of JBC model; yet, the convergence is achieved faster (approximately within 18 seconds), since the ship is fixed. The forces are obtained and compared to the EFD data for the grid convergence study as it can be observed in Fig. 4.14.

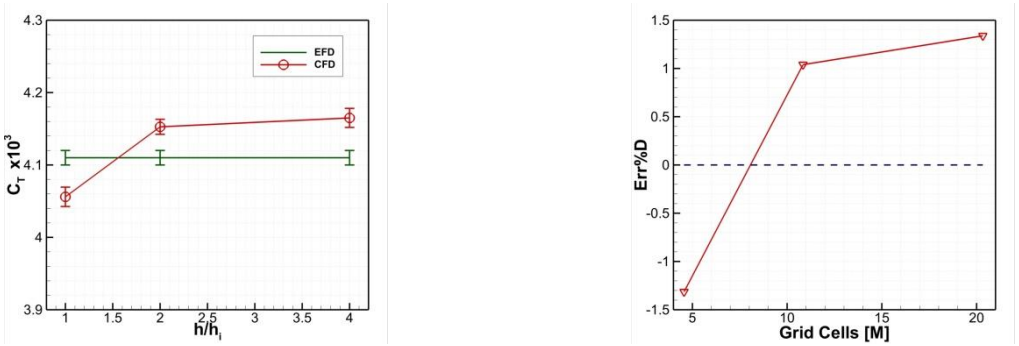

(a) (b)

Figure 4.14 Obtained results for ship without rudder: (a) Computed total resistance coefficient C_T compared to the EFD, (b) estimated error as a function of grid density

The resistance force is under predicted for the coarsest grid (M3) with about 1.33% error, while for medium and fine grids (M2 and M1, respectively), the force is over predicted within 1.04 and 1.31%, respectively. This may highlight the accuracy of the numerical interpretation of the current problem. Worth mentioning that it is easier to predict the forces for a fixed ship compared to a ship with various degrees of freedom. Though the error seems to be oscillating around the zero value, a monotonic convergence is achieved for the grid convergence study; besides, the validation level was reached for the computational uncertainties since the estimated error for the three grids remains beneath the validation uncertainty level. The verification and validation parameters are summarized in Table 4.11. Worth mentioning that the iterative uncertainty is neglected in this analysis, since the lack of ship oscillation from the fact that the ship does not

heave keeps the results steady in the final iterations, especially after the convergence is achieved. This was also checked with respect to the condition $U_i/\varepsilon_{1-2} \ll 1$.

Table 4.11 Grid convergence parameters for total ship resistance Coefficient C_T

Convergence Test	r	R_G	p_G	$\varepsilon\%S_1$	$U_G\%S_1$	$U_{SN}\%D$	E_{AV}	U_D	U_V
C_T	2.0	0.127	1.38	0.295	4.44	4.50	1.23	1.0	4.61

For the ship with rudder, the resistance results are computed including two degrees of freedom motion for sinkage and trim. Since the previous study showed that the results are within a close absolute error range, for a simplification reason, the coarsest grid parameters were maintained for the ship with the simplified rudder configurations. The obtained results from the numerical simulation for different Froude numbers are depicted in Fig. 4.11 compared to the experimental data. Bot *SST* k-ω and EASM models were applied as in the case of JBC for further investigation of the effect of turbulence model on the results accuracy. The EASM as usually provided more accurate results compared to the *SST* k-ω model in both cases for forces and motions. Though the same conclusion in the JBC still persists that the difference in sinkage and trim values between the two models are insignificant; for this reason, the sinkage and trim results in Fig. 4.15 are provided for EASM results only. It can be observed that the error for the forces obtained using the EASM is almost as half as the ones obtained using *SST* k-ω model. It can also be observed from the sinkage and trim results that the error is significant for the low Froude numbers compared to those obtained for the high Froude numbers. This is related to the fact that the grid generation parameters are applied based on the design Froude number 0.142, which, for example, if the number of cells chosen for the free-surface is based on the criteria 60cells/wave length, it will be sufficient for the higher Froude number; unfortunately, for the lower Froude number is much less than this criteria, especially that the number of grid cells is relative to the Froude number square. This leads to an artificially coarser grid on the free-surface that will act as a numerical wave damper, consequently resulting in these discrepancies in sinkage and trim values. Besides, the wetted surface area might be incorrectly predicted, which may influence the total resistance force. It is advisable in such case to choose the cell size criteria based on the lowest Froude number and the wave refinement depth in z-direction based on the highest Froude number; nevertheless, this may result in an extreme number of cells that might not be applicable to handle, especially for this type of ship with very low Froude numbers.

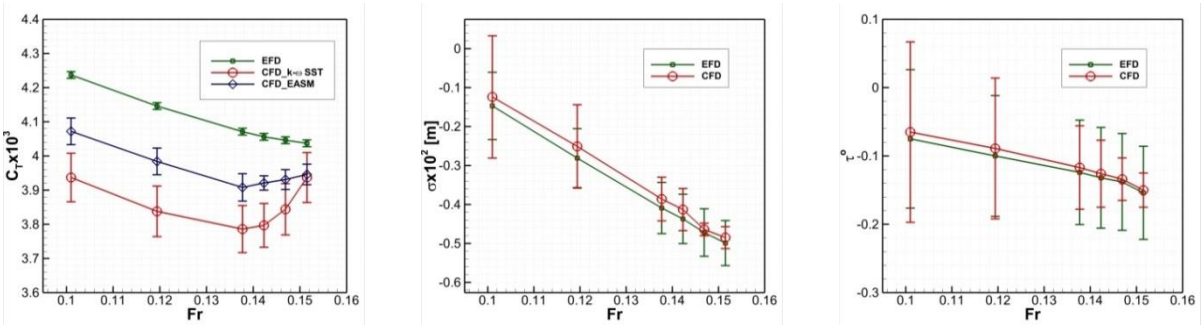

(a) (b) (c)

Figure 4.15 CFD results compared to EFD showing: (a) total resistance coefficient C_T (b) sinkage σ and (c) trim τ

4.2.5 Free-Surface Results

Following the same concept like in the JBC ship model, the free-surface results for the KVLCC2 models, sailing in calm water without rudder, are depicted in Fig. 4.16 for the free-surface pattern and two lateral sections distanced at y/L_{pp}=-0.0964 and -0.1581, respectively, from the ship centerline. A very good resemblance can be observed from the comparison between the CFD results and the provided EFD data from the G2010 Workshop [47] and Kim et al. [138]. The free-surface results accuracy obtained in this study matches the level of accuracy of the CFD results presented in the G2010 by the ISIS-CFD code developer (École Centrale de Nantes) that were remarked as the best free-surface results delivered to the Workshop [47]. This may indicate along with the V&V studies performed in the previous sections that the application of the solver in this study is performed correctly.

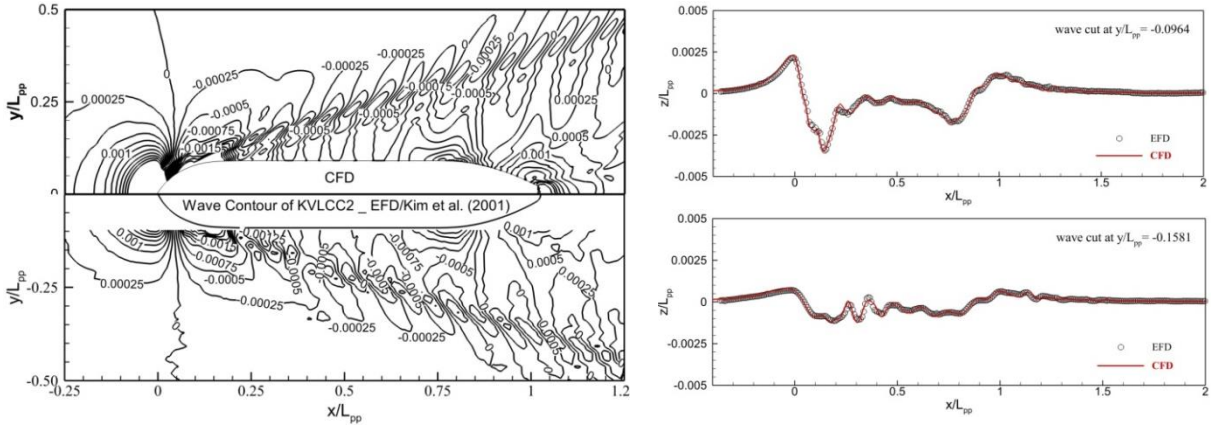

Figure 4.16 Free-surface topology (left), and wave cuts at y/L_{pp}=-0.0964 and -0.1581(right)

4.2.6 Local Flow Results

For the sake of validating the obtained wake flow results against the available EFD data, the computed streamwise velocity contours using the EASM turbulence model at two different sections distanced from the Forward Perpendicular (F.P.) at x/L_{pp}=0.85 (before the propeller) and x/L_{pp}=0.9825 (propeller plan), respectively, are plotted in Fig. 4.17 compared to the experimental data. The development of the bilge vortex can be observed comparing the iso-contours from section x/L_{pp}=0.85 and the propeller plan section. The resemblance between the CFD results based on the EASM turbulence model and the EFD data is reasonable except a slight discrepancy in the center zone, which might be related to the fact that the hub cap is not included in this simulation compared to the experiment where it was included. Otherwise, the CFD iso-contours are qualitatively and quantitatively within a good congruence with the EFD and the hook-shape vortices seem to be well captured.

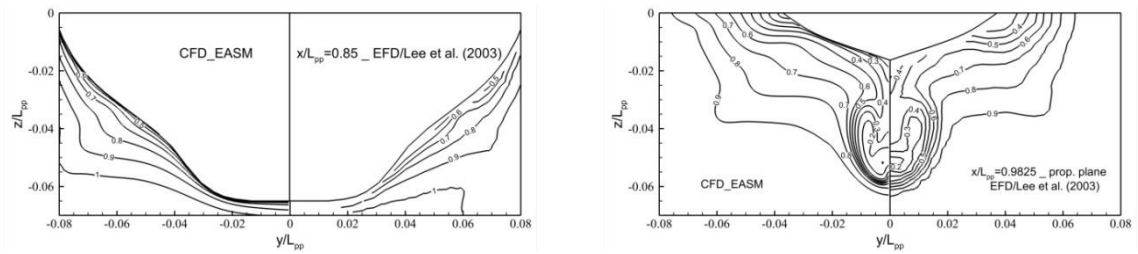

Figure 4.17 CFD vs. EFD streamwise velocity contours at sections: x/L_{pp}=0.85 and 0.9825

In order to have a better insight in the wake region, more details of the wake development is presented in Fig. 4.18 through the streamwise iso-contours for the longitudinal axial velocity and for the turbulent kinetic energy for seven selected sections at 0.1m before and after the propeller plan. The development of the vortices can be observed clearly, and the hook-shape is properly predicted, where the distortion of the iso-contours in the wake can be observed due to the transfer of low momentum flow at the hull vicinity to the center of the flow. On the other hand, near the centerline plan, the counter-rotating vortices are visible for both turbulence models and their development through the different sections can be noticed.

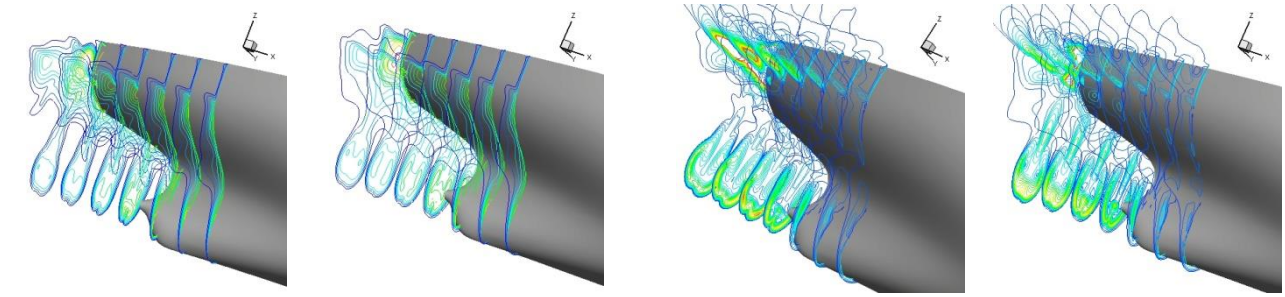

U contours_*SST k-ω* U contours_EASM TKE contours_*SST k-ω* TKE contours_EASM

Figure 4.18 Velocity and TKE contours in the wake

More details for the core of the vortices can be configured through the presentation of the second invariant Q criterion at an iso-surface Q^*=25 colored by the non-dimensional helicity which is depicted in Fig. 4.19. It can be observed that the pattern is like the one presented for the JBC hull in section 4.1.6.

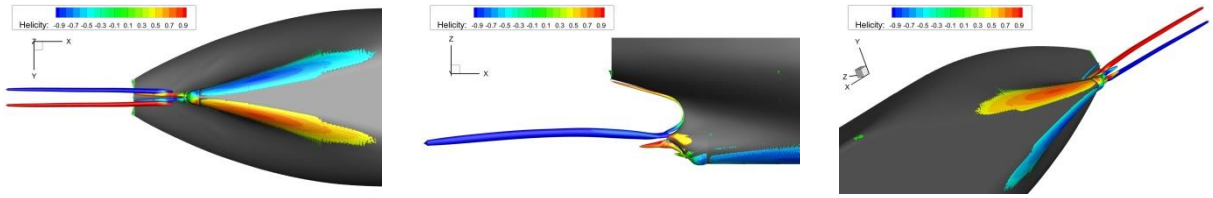

Figure 4.19 Second invariant iso-surface Q^*=25 colored by non-dimensional helicity

Finally, all the results presented for the KVLCC2 ship model have been fully or partially published in [134].

4.3 David Taylor Model Basin (DTMB) Surface Combatant

The third ship to be analyzed in the resistance study is the US Navy surface combatant ship model known as the David Taylor Model Basin (DTMB) – recently known as Naval Surface Warfare Center, Carderock Division (NSWC) – whose preliminary design was introduced in 1980 as a benchmark hull for both explication of flow physics and CFD validation for a non-conventional ship with a sonar dome, bilge keels, two suspended propellers supported with two brackets, two rudders and a transom stern. The full-scale ship does not exist; however, several models were built and tested by various internationally well recognized towing tank organizations such as the NMRI in Japan, INSEAN in Italy, Maritime Research Institute Netherlands (MARIN) in Netherlands, FORCE Technology in Denmark, IIHR and the NSWC in the USA. The ship was officially introduced as a benchmark for ship hydrodynamic applications in the Gothenburg 2000 Workshop on Computational Ship Hydrodynamics along with two other geometries (KVLCC and KCS). Series of experiments were performed on different geometrically similar ship models built and tested, such as the 5.72 m length model which was built and tested in (INSEAN) and the model of 3.048 m length which was built and tested in IIHR. A massive database for the ship model tests can be found in the public domain contains experimental data for several experiments performed for various ship hydrodynamic aspects including ship resistance, vertical motion, free-surface, local flow configurations, seakeeping, roll decay, static drift and captive maneuvering. The appended model geometry is presented in Fig. 4.20, while the principal dimensions of the INSEAN and IIHR models used for ship resistance simulations are tabulated in Table 4.12 compared to the full-scale ship.

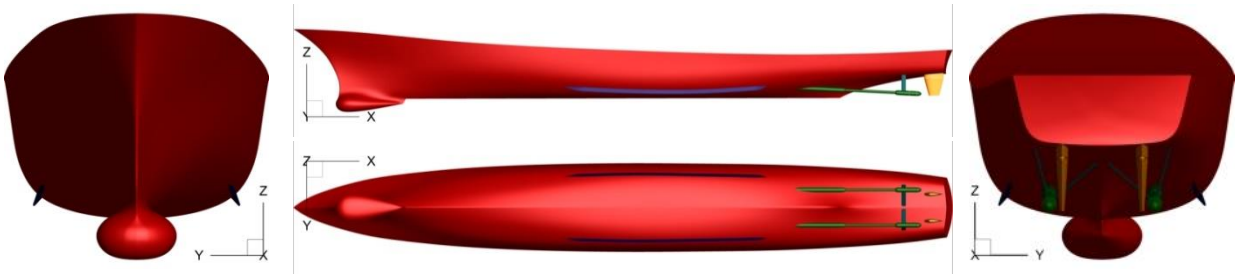

Figure 4.20 DTMB model geometry viewing: front, profile, bottom and rear

In this study, both models are analyzed for bare hull ship resistance, free-surface and local flow. The reason behind analyzing both models in this study is because the available EFD for resistance, free-surface and local flow analysis data are partially dispersed; a set of data for ship resistance are given based on the INSEAN model reported in [129] and some other data are given based on the IIHR model reported in [130]. For consistency purpose, both models are numerically analyzed, and the results are compared with both models with respect to the model size and the given data.

The ship resistance analysis is handled in three levels: the first is to analyze the bare hull model with only the sonar dome and the transom stern, while the second is dedicated for analyzing the appended hull including the bare hull plus the bilge keels, the propellers shafts, the propellers brackets and the rudders; finally, a towing tank test is performed for validating the CFD data at different towing speeds in the medium-high speed domain for a model built and tested in the “Dunarea de Jos” University of Galati (Model – UGAL) which will be introduced in the final part of this chapter.

Table 4.12 DTMB ship models and full-scale characteristics

Particulars	Unit	Full Scale	Model – INSEAN	Model – IIHR	Model – UGAL
Scale (λ)	-	1:1	1:24.830	1:46.558	1:44
Length of Waterline (L_{PP})	[m]	142.0	5.719	3.048	3.232
Beam (B)	[m]	19.06	0.768	0.409	0.434
Depth (D)	[m]	10.98	0.442	0.236	0.25
Draft (T)	[m]	6.15	0.248	0.132	0.14
Volumetric Displacement (∇)	[m^3]	8424.4	0.554	0.0826	0.099
Wetted Surface Area (S)	[m^2]	2972.6	4.828	1.371	1.54
Block Coefficient (C_B)	-	0.507	0.507	0.507	0.507
Long. Position of C.O.G (x_{CG}) from F.P.	[m]	71.676	2.887	1.539	1.629
Vertical Position of C.O.G (z_{CG})	[m]	7.54	0.304	0.162	0.1718
LCB (%L_{PP}), fwd+	-	-0.683	-0.683	-0.683	-0.683

4.3.1 Bare Hull Ship Model

The two models from INSEAN and IIHR are introduced and analyzed individually in the numerical simulation in order to predict the total ship resistance at three velocities that correspond to Fr=0.1, 0.28 and 0.41 in order to investigate the solution quality at different speeds (slow, medium and high-speed sailing conditions). The total ship resistance and vertical motions are recorded and compared for every case, while a special concern is given for the free-surface and local flow at the design speed Fr=0.28. This analysis will be the base for comparing the results with the following section that deals with the appended ship.

4.3.1.1 Analysis Conditions

The analysis conditions for the DTMB ship model for bare hull and fully appended ship can be subdivided in three simulation cases based on the ship speed as summarized in Table 4.13 showing the corresponding Froude and Reynolds numbers for both INSEAN and IIHR models.

Table 4.13 Computational cases and corresponding ship speed parameters

Ship Model	Case Number	C1	C2	C3
Model – INSEAN	U [m/s]	0.749	2.097	3.071
	Fr [-]	0.1	0.28	0.41
	Re [-] x10^6	2.154	6.030	8.830
Model – IIHR	U [m/s]	0.547	1.531	2.242
	Fr [-]	0.1	0.28	0.41
	Re [-] x10^6	1.572	4.403	6.447

4.3.1.2 Domain & Boundary Conditions

The computational domain dimensions and boundary conditions are imposed exactly like those given in section 4.1.2 for the JBC hull, the only difference is that the initial undisturbed free-surface level is set at the design draft of the DTMB model at z=0.248 and 0.132 m from the

baseline, for the INSEAN and IIHR models, respectively, corresponding to the design draft as represented in Table 4.12.

4.3.1.3 Computational Grids

The HEXPRESS^{TM} module from the FINE^{TM}/Marine NUMECA package is used to generate the discretization grids for this analysis. Four grids are generated for the grid convergence purpose, with two conditions regarding the wall treatment: the wall modeled condition with y^+=35 and the resolved wall with y^+<1. Both models are tabulated in Table 4.14 showing the number of grid cells in millions for every case. M1 and M4 refer to the finest and the coarsest mesh, respectively; while, the grid configuration is represented in Fig. 21, showing the comparison between fine and coarse grid, free-surface refinement and finally a longitudinal section.

Table 4.14 Computational grids for ship based on the wall treatment modeling

Wall Condition	Number of grid cells (M)			
	M1	M2	M3	M4
WM	9.85	6.74	4.31	2.91
WR	16.55	10.17	6.81	4.34

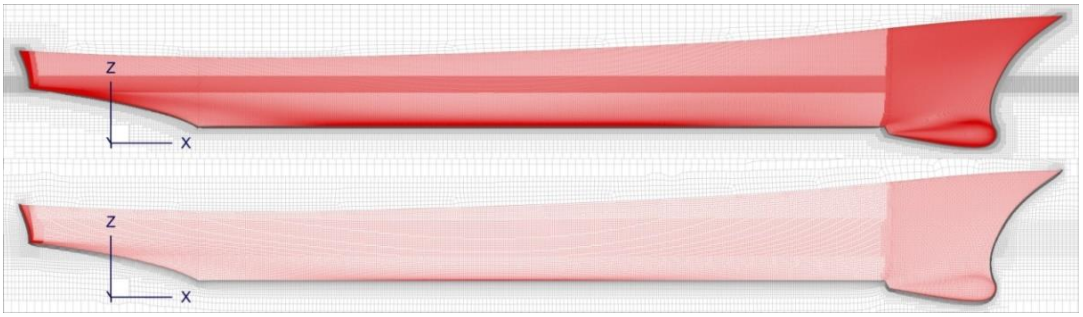

(a)

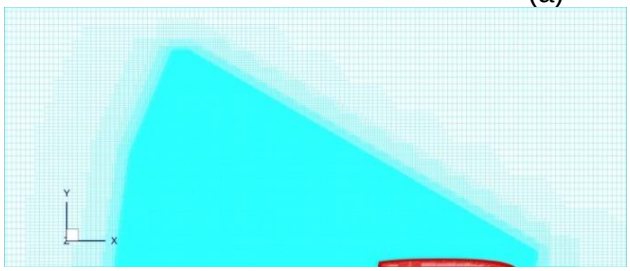

(b)

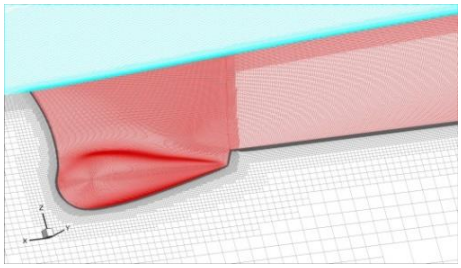

(c)

Figure 4.21 Computational grids showing: (a) Fine and coarse grids, (b) free-surface refinement and (c) a forward section

4.3.1.4 Resistance and Motion Results

The resistance results are obtained for ship in calm water free to sink and trim condition. The total simulation time is set to 40 seconds to ensure a proper convergence and to reduce the iterative errors, since the ship is sailing in the medium and high-speed mode, which may cause oscillation in the resistance convergence curve. Convergence is achieved faster for the slow speed case with *Fr*=0.1 after approximately 16 seconds; while 28 and 34 seconds were necessary for converging the medium speed case *Fr*=0.28 and the high-speed case with *Fr*=0.41, respectively.

The forces are obtained and compared to the EFD data for the grid convergence study as it can be observed in Fig. 4.22, which reveals a proper agreement with the EFD data with an error range between 2.23% up to 6.74% for the slow the high-speed case, respectively. This complies well with the theory as the grid parameters for this simulation cases are selected based on the high-speed condition to ensure a reasonable grid resolution; otherwise, if it will be set based on the slow speed case, the grid density will be significant and the simulation cost may increase exponentially. Considerably, the error range up to 6.74% is reasonable taking into consideration the fact that the slow speed case simulation is very difficult to perform and the numerical errors for the hull to speed response are expected to be obvious. Finally, the average error for all the simulation cases is within 3.83%, which is considered acceptable.

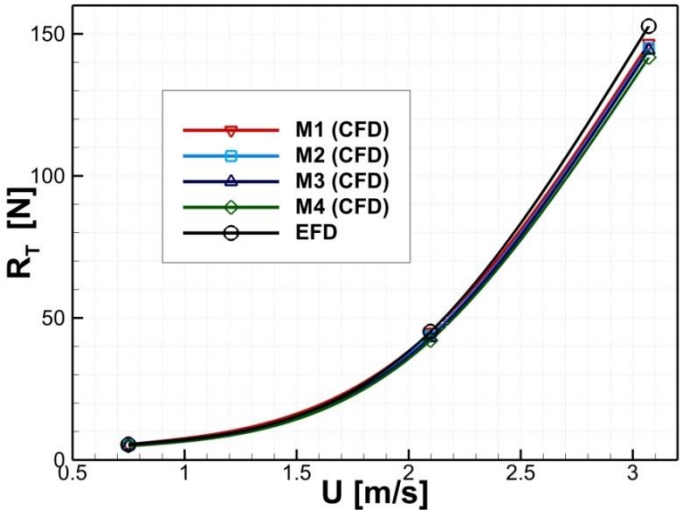

Figure 4.22 Total resistance results based on the grid density

The grid convergence parameters for the analysis based on the ship speed are tabulated in Table 4.15 showing that the convergence study resulted in a monotonic convergence for all the simulation cases. The iterative errors were less in the slow speed cases as expected and almost doubled in the high-speed simulations. All the numerical errors are validated to the U_V level, which indicates that the comparison error is below the noise level and the validation process was successful, as described in chapter III.

Table 4.15 Verification and validation parameters for total ship resistance in the wall modeled case

Convergence parameters	r_G	R_G	p_G	δ_G	$U_i\%S_1$	$U_G\%S_1$	$U_{SN}\%S_1$	$U_{SN}\%D$	$U_D\%D$	U_V
Fr=0.1	≈1.5	0.205	1.71	3.08	3.94	3.11	5.02	4.82	1.32	5.19
Fr=0.28		0.421	1.52	1.71	3.39	1.73	3.81	3.48	0.64	3.86
Fr=0.41		0.487	3.34	1.53	2.89	1.55	3.28	2.86	0.61	3.34

In order to highlight the effect of wall treatment on the simulation results, a comparison between the wall modeled and wall resolved approaches were carried out for the design speed condition where the *Fr*=0.28. The comparison is brought to attention in Fig.4.23 showing the error percentage change with respect to the number of grid cells, and based on the wall treatment approach. The error is increasing as the grid density decreases, it can also be observed that the wall resolved has a less error for the coarser grids compared to the wall modeled approach. On the other hand; as the grid is refined, the wall modeled approach gives less error compared to the

wall resolved approach. This can give a proper alternative for this type of ships to avoid adding a dense grid in boundary layer, which may impose some drawbacks regarding the mesh orthogonality and cells aspect ratio; besides, the associated significant simulation time.

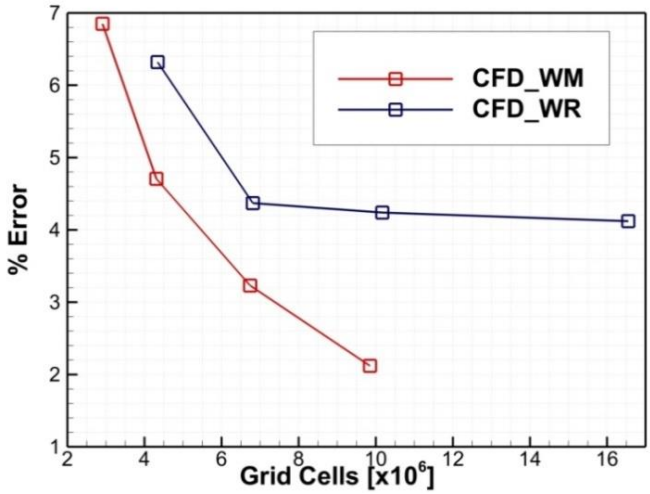

Figure 4.23 Total resistance error computed for *Fr*=0.28 based on the wall treatment approach

Ship motion results are tabulated in Table 4.16 showing that the motion outcomes are within a reasonable agreement with the EFD data except for the significant error recorded for the sinkage results obtained for the high-speed condition. This is contradictory to the theory, which requires a further investigation. Trim results are better estimated compared to the sinkage values. For the design speed, the results for wall modeled and wall resolved were almost within the same range, no effect resulted from the wall treatment approach. For this purpose, only the wall modeled results were introduced in the results. The CFD comparative data obtained for the design speed, which is the major concern in this study, are within a satisfying level of accuracy.

Table 4.16 Sinkage and trim results

Sinkage					
Fr	EFD	CFD			
		M1	M2	M3	M4
0.1	0.174 E-03	0.169 E-03	0.168 E-03	0.165 E-03	0.157 E-03
ε%		2.88	3.40	5.17	9.77
0.28	1.82 E-03	1.83 E-03	1.83 E-03	1.835 E-03	1.84 E-03
ε%		0.55	0.55	0.82	1.1
0.41	4.7 E-03	4.31 E-03	4.28 E-03	4.16 E-03	4.15 E-03
ε%		8.29	8.9	11.4	11.7
Trim					
0.1	0.018	0.0176	0.0175	0.017	0.0163
ε%		2.22	2.8	7.7	9.4
0.28	0.108	0.110	0.1107	0.113	0.113
ε%		1.85	2.5	4.63	4.63
0.41	0.421	0.416	0.416	0.415	0.396
ε%		1.18	1.18	1.42	5.94

4.3.1.5 Free-Surface Results

Comparing the computed free-surface results against the EFD data, the non-dimensional free-surface topology is represented in in Fig. 4.24 showing the comparison between the CFD results for the medium speed *F*r=0.28 and the corresponding EFD data reported in [130]. The comparison shows that the CFD results have a close resemblance with the EFD data. The estimated error for the near-field free-surface measured for the average wave height at various 10 points near the hull is within 0.5% compared to the EFD. On the other hand, the far-field wave height was slightly under predicted with 1.1%. Two sections were selected at distances y/L_{pp}=0.082 and y/L_{pp}=0.172 corresponding to the available EFD results were the wave profile could be compared. This comparison also shows a phase shift between the predicted free-surface and the EFD data, as Fig. 4.24 bears out.

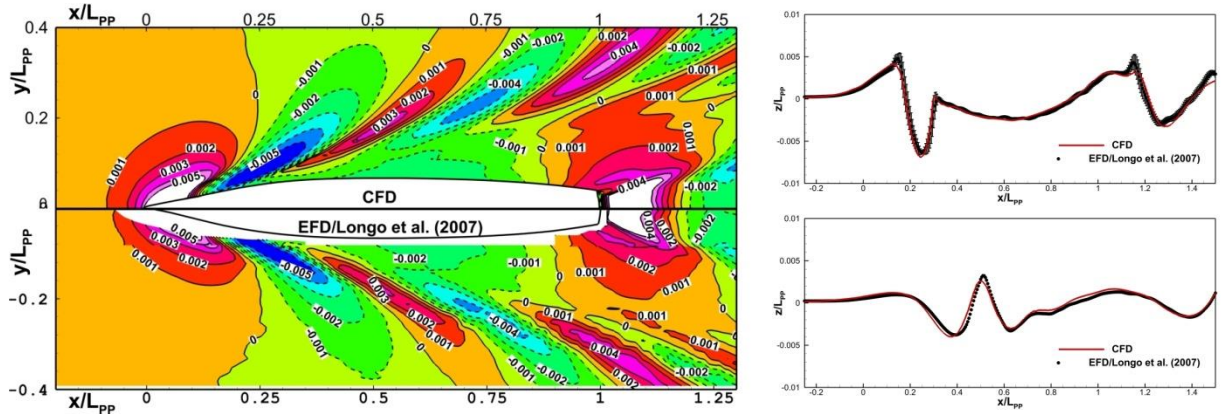

Figure 4.24 Free-surface profile (left), and wave cuts at y/L_{pp}=0.082 and y/L_{pp}=0.172 (right)

4.3.1.6 Local Flow Results

The local flow of the DTMB ship model is challenging to capture and requires special treatment for the grid in the vicinity of the hull in order to capture the possible flow separation and the developed vortices from the sonar dome, the appendages, when they exist, and the bottom rise in the stern. For this purpose, an isotropic refinement intended to capture the flow configuration is introduced in the underwater zone. Fig. 4.25 shows a comparison of different sections positioned at relative distances x/L_{pp}=0.1, 0.6, 0.935 and finally 1.1 from the forward perpendicular. These positions represent main checkpoint locations after the sonar dome, after the bottom rise, at the propeller position and the ship downstream, respectively.

The comparison shows that the CFD results resemble well compared to the available EFD data. The only difference is that the streamwise velocity contours at x/L_{pp}=0.935 and 1.1 tend to expand the boundary layer outward. This might have an influence from the vertical ship motions as it was introduced before that the error estimated in that was slightly considerable. Nevertheless, the qualitative and quantitative resemblance between both CFD and EFD results are within an acceptable range. Besides, the results are matching some of the obtained in the G2010 workshop as it can be verified in [47].

Concluding the results obtained for the bare hull DTMB ship model, it can be said that the simulation was successful in predicting at a very encouraging limit the total resistance, the free-surface and local flow. Unfortunately, some discrepancies were observed for the ship motions; yet, the error range is still within an acceptable level.

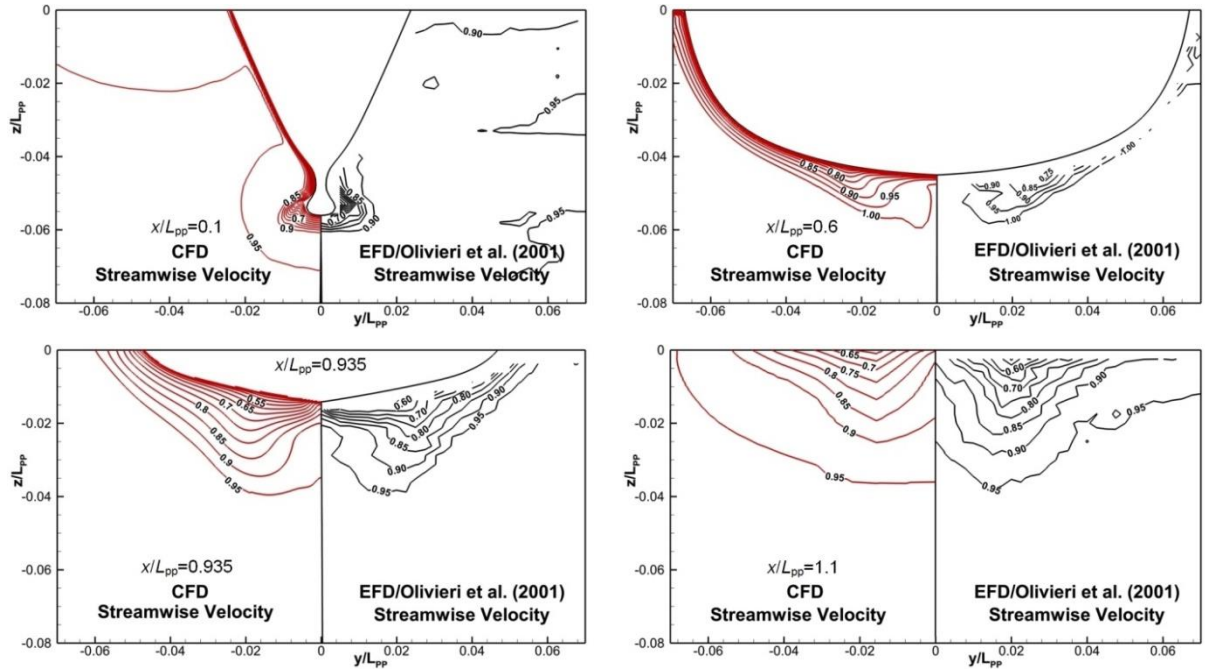

Figure 4.25 CFD vs. EFD streamwise velocity contours at different sections

4.3.2 Appended Hull Ship Model

One of the major challenges in the ship hull design process is the decisions made for the appendages regarding their shapes, orientations, positions, etc. It is very important to have a quick and reliable tool to help assessing this process with low cost, as the experimental method is by far not feasible in this condition. This is the purpose of this analysis, to investigate the capability of the CFD method to assess accurately the total resistance and the local flow of the fully appended DTMB ship model with bilge keels, shafts, shaft brackets and tow rudders. This aim is achieved by performing an investigation for the appended ship and comparing the results with the bare hull ship, since the fully appended ship data are not widely available. The same simulation cases performed for the bare hull is repeated for the appended ship and the resistance, motion and local flow results will be compared to highlight the influence of the appendages on each parameter from the proposed analysis.

4.3.2.1 Analysis Conditions

The same analysis conditions regarding the ship speed are repeated in this case in order to maintain the comparison consistency. Only in this case, the INSEAN model with L_{pp}=5.72 m is used in this simulation and compared with the same model results from the bare hull analysis.

4.3.2.2 Domain & Boundary Conditions

The same domain configurations and boundary conditions for the bare hull are maintained unchanged in this analysis.

4.3.2.3 Computational Grids

Same concept for grid generation is kept for this study, except for some special considerations regarding the appendages special refinements in the zones of flow separation and

the appendage-hull intersection zones. Four grids were generated to perform a grid dependent study and their density in millions of cells is summarized in Table 4.17, while the grid discretization is plotted in Fig. 4.26 showing the ship and the appendages refinements.

Table 4.17 Computational grids for ship based on the wall treatment modeling

Wall Condition	Number of grid cells (M)			
	M1	M2	M3	M4
WM	19.943	8.958	5.667	2.669
WR	26.757	16.605	9.022	3.634

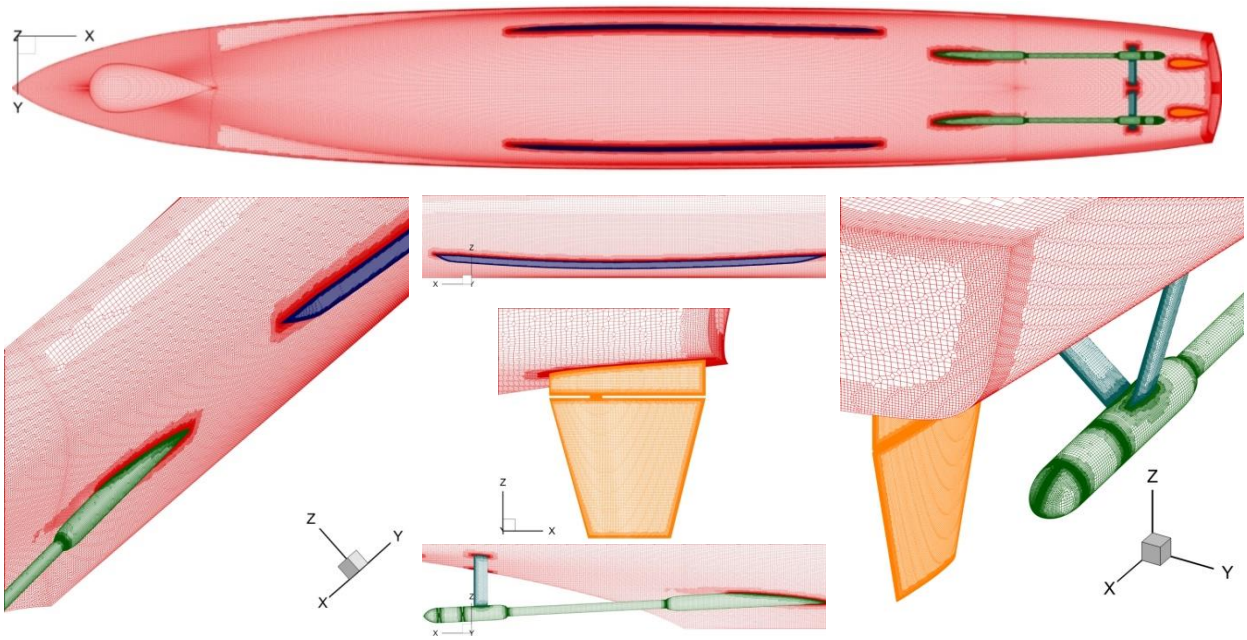

Figure 4.26 Discretization grid highlighting the appendages refinement

4.3.2.4 Resistance and Motion Results

The total resistance is obtained for the ship model with the appendages and represented in Table 4.18. One of the flexible features in the CFD modeling is regarding the fact that the solver can provide the drag on each appendage to highlight its influence on the total hull drag. This was introduced and compared for the different ship speed conditions and plotted in the pie chart represented in Fig. 4.27 in order to highlight the impact of each appendage on the total resistance computed.

Table 4.18 Total resistance computed for the appended hull and appendages drag force

Fr	Hull Component Force [N]					
	Shaft	Shaft Brackets	Bilge Keel	Rudder	Bare Hull	Fully Appended
0.10	0.30	0.15	0.11	0.21	5.40	7.18
0.28	3.56	2.02	1.66	3.04	45.46	55.73
0.41	5.65	5.75	4.59	8.38	154.16	178.53

On the other hand, the total resistance coefficient extracted from the bare hull component reported earlier in Table 4.18 is used for assessing the numerical results against the EFD data

provided in [129]. Two turbulence models *SST k-ω* and EASM were used to calculate the total resistance and wake flow of the ship model. The both models successfully predicted the total resistance coefficient with a maximum error of 7.82% and minimum of 1.49% for the *SST k-ω*, while the maximum and minimum error for EASM models are 7.44% and 1.06%, respectively.

It is worth mentioning that the results obtained and presented in Table 4.19 show an oscillatory convergence with respect to the total resistance value for the EASM model, because the coarse grid M3 shows better agreement with the EFD data for the wall resolved model. Nevertheless, the solution has a monotonic propensity taking into consideration the fact that the value is reduced consequently as the grid density increases, which tends to deviate the total resistance coefficient far from the recorded EFD value. Overall, the agreement between CFD and EFD data is satisfying.

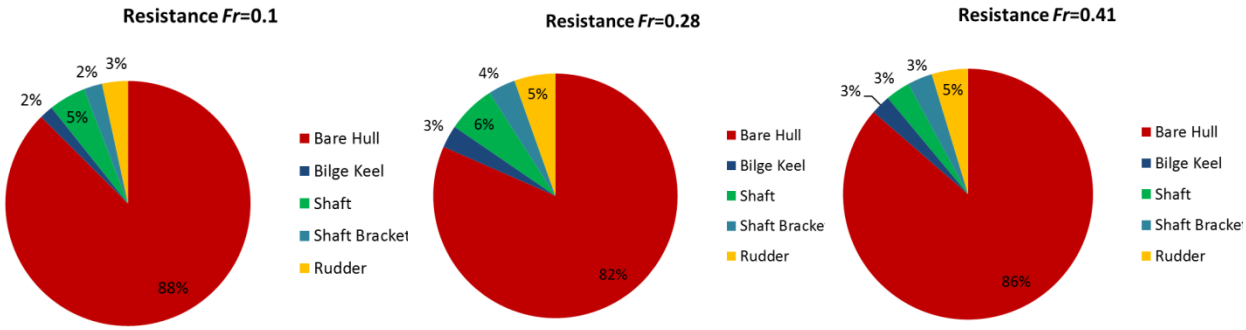

Figure 4.27 Resistance results for the fully appended ship and hull components individually

Table 4.19 Total resistance coefficient C_T computed for the bare hull component compared to EFD data [129]

Results	C_T EFD	C_T (WM), CFD		C_T (WR), CFD	
		SST k-ω	EASM	*SST k-ω*	EASM
M1	4.23×10^{-3}	4.361	4.334	4.049	4.092
ε%		3.10	2.49	-4.28	-3.26
M2		4.415×10^{-3}	4.359×10^{-3}	4.057×10^{-3}	4.098×10^{-3}
ε%		4.37	3.05	-4.09	-3.12
M3		4.545×10^{-3}	4.513×10^{-3}	4.293×10^{-3}	4.275×10^{-3}
ε%		7.44	6.69	1.49	1.06
M4		4.561	4.551×10^{-3}	4.363×10^{-3}	4.334×10^{-3}
ε%		7.82	7.59	3.14	2.45

The theoretical perspective for the ship motion in this simulation is not expected to be significantly affected by the presence of the appendages. For this purpose, the sinkage and trim values were computed and compared to the EFD data in order to investigate the influence of the appendages on ship motions. This comparison is brought to attention in Table 4.20 showing that the obtained CFD results are within a close agreement with the measured data in the tank test for the bare hull. This complies with the principle settled in the aforementioned proposition. Likewise, the error range for the predicted CFD results is within a reasonable range lies between 0.65% and 14.9% for minimum and maximum, values, respectively. The highest value is recorded for the slowest speed which is theoretically expected to have some discrepancies resulting from the

simulation setup, as previously explained. From this point of view, a final conclusion may be withdrawn regarding the obtained results for the total ship resistance and ship motions that they are within a reasonable level of accuracy, which indicates the capability of the CFD modeling in predicting the fully appended ship hydrodynamic in this standpoint.

Table 4.20 Sinkage and trim values computed for the fully appended hull compared to the measured value in [129]

Fr	Sinkage EFD	CFD		Trim EFD	CFD	
		SST k-ω	EASM		*SST k-ω*	EASM
0.1	0.174 x10^{-3}	0.148 x10^{-3}	0.149 x10^{-3}	0.018	0.0192	0.0192
ε%		14.9	14.32		6.67	6.67
0.28	1.82 x10^{-3}	1.892 x10^{-3}	1.891 x10^{-3}	0.108	0.1073	0.1107
ε%		3.96	3.95		0.65	2.5
0.41	4.7 x10^{-3}	4.635 x10^{-3}	4.642 x10^{-3}	0.421	0.441	0.439
ε%		1.38	1.23		4.75	4.27

4.3.2.5 Free-Surface Results

The comparison between the bare hull appended ship is represented in Fig. 4.28 showing that both results are almost the same except a slight difference in the downstream concentrated in the vicinity of the stern and the far field waves. However, this difference is scarcely noticeable.

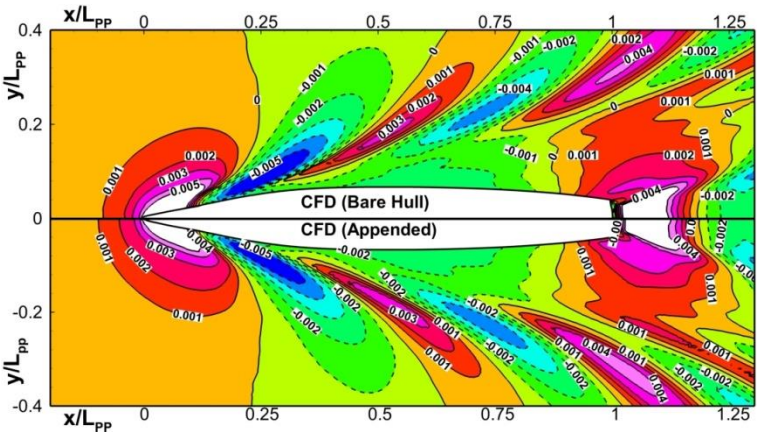

Figure 4.28 Free-surface profiles for bare and appended hull

4.3.2.6 Local Flow Results

The flow around the DTMB is dominated by a strong combination of vortices starting from the flow separation at the sonar dome, where two layers of vortex tubes are generated, as it can be observed in Fig. 4.29 and 4.30; where the velocity contours at 11 equidistance sections at $\Delta x/L_{pp}$=0.1 starting from the A.P. and heading downstream. Figure 4.29 represents the axial velocity contours and turbulent kinetic energy (TKE), while Fig. 4.30 shows the second Q invariant iso-surface Q^*=10 colored by non-dimensional helicity for ship bottom and profile, comparing the bare and appended hull cases. From both pictures, nine main vortical formations can be observed and arranged as numbered on the figure as follows:

1. Sonar Dome vortices (SDV); which results from the flow separation at the sonar dome. This form two strong vortex tubes on both sides of the ship that continue downstream until they are dissipated due to viscous effect or combined with other vortices that will form further downstream;
2. Fore-Body Keel Vortices (FBKV); these are generated at the intersection of the keel and sonar dome. Formed from two les intense vortex tubes that tend to open outward and vanishes faster than the SDV due to viscous dissipation;
3. Aft-Body Keel Vortices (ABKV); these are two vortices generated due to the flow separation from the bottom rise in the stern zone;
4. Bottom-Shaft Vortices (BSV); which are generated from the flow separation at the intersection between the shaft and the hull. This is kind of flow disturbance that is combined with other vortices such as SDV, as it can be observed in Fig. 4.30 b;
5. Bilge Keel Vortices (BKV); this has two vortical tubes generated as the flow separates from the leading edge of the bilge keel and travelled downstream forming the vortical tube as the flow leaves the trailing edge of the bilge keel. These vortices have an important role in damping the roll motion, as it will be covered in Chapter VI;
6. Shaft Vortices (SV); two separate vortical tubes are generated on each side of the propeller shaft, the vortex starts at the beginning of the shaft and separates at the shaft boss forming the vortical tubes that dissipate downstream. These are relatively intense vortices;
7. Rudder Tip Vortices (RTV); one vortex tube is generated at the lower tip of the rudder as the flow separates from the lowest point of the rudder trailing edge. One vortical structure is generated for each rudder. Usually, this vortical tube is merged with the propeller vortices as a result for the high momentum flow generated by the propeller. In this case, it is not combined with the propeller shaft vortices, since the rudder and propeller shaft are slightly out of position;
8. Flow separation at the bottom-bracket intersection; this is mainly a significant flow disturbance that results from the flow separation at the intersection of the shaft brackets and the bottom of the ship. The strength of these vortices depends mainly on the brackets configuration;
9. Flow separation at the Rudder-Hull intersection; this results as the flow interacts with the hull-rudder intersection. In this case, due to the fact that the rudder is split in two segments connected with the rudder stock, significant separation results at the lower tip of the top rudder piece and the rudder stock. These vortices are combined with the flow exiting the stern because the transom remains dry in the medium and high speed sailing conditions, causing a rooster-tail like breaking wave directly after the transom.

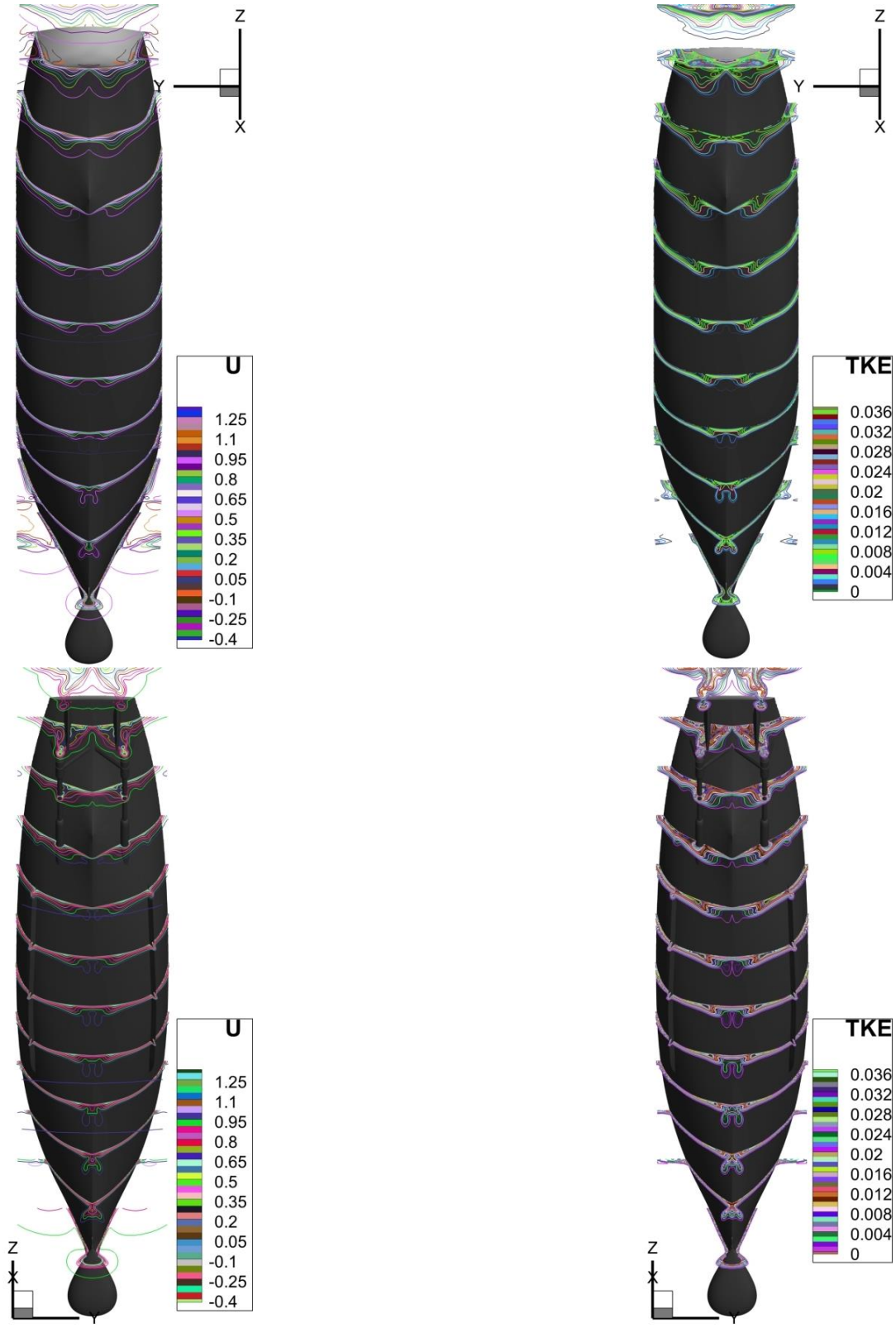

Figure 4.29 Comparison between bare and appended hull for axial velocity contours (U) and Turbulent Kinetic Energy (TKE)

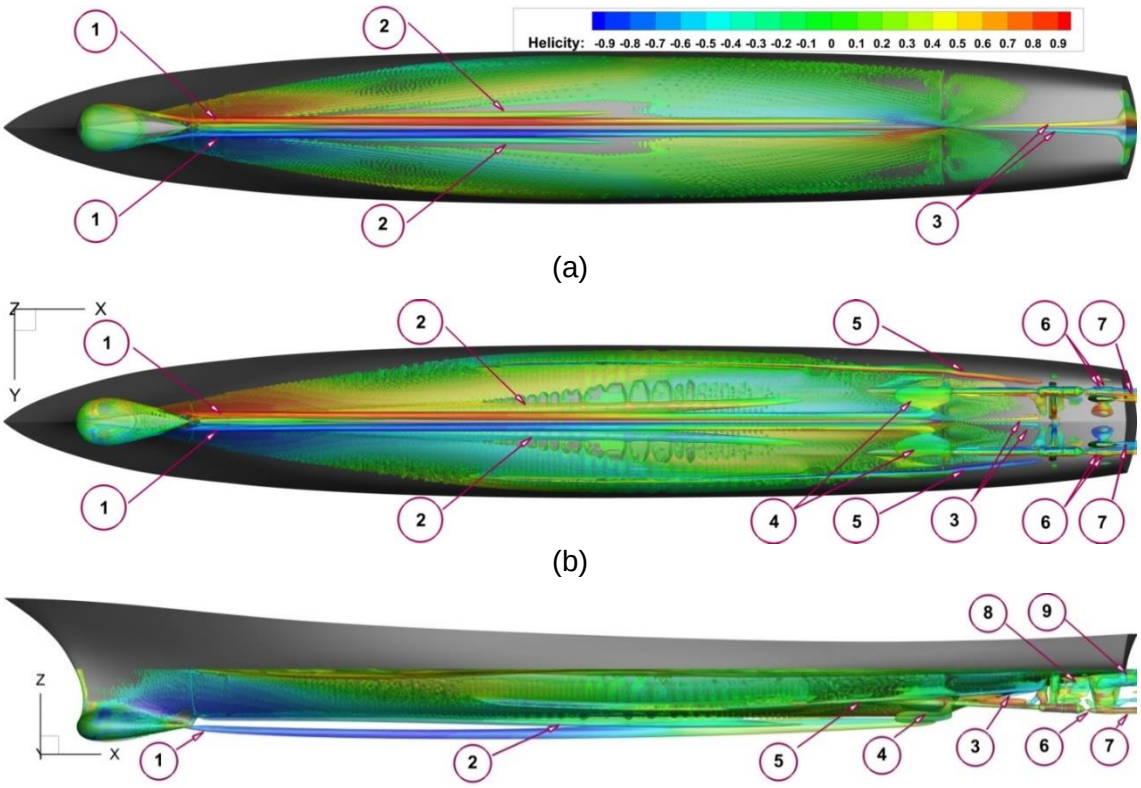

Figure 4.30 Second invariant iso-surface Q^*=10 colored by non-dimensional helicity bottom view: (a) Bare hull, (b) appended hull, and (c) appended hull profile

The results obtained for the bare hull ship model have been published in [135], while the simulation and results for the appended hull model are published in [136].

4.3.3 Experimental Test

Despite the fact that CFD method proved to be very reliable in predicting the hydrodynamic features of a classic resistance estimation process regarding the total resistance, vertical motions, free-surface and local flow; as presented in the preceded sections; yet, the experimental test remains as the most important tool in ship hydrodynamics and will always persist as the most accurate method to predict the hydrodynamic aspects of a ship. From this point of view, it was necessary to judge the numerically obtained result in this study based on the experimental results that were obtained for similar analysis conditions. Nevertheless, it is also important to have our own insight on the CFD capabilities compared to the available resources in the towing tank facility existing in the "Dunarea de Jos" University of Galati, which has principle dimensions of 45.0m length, 4.0m and 3.0m depth. For this reason, an experimental test was planned and performed in the towing tank, on January, 16th 2019, aimed at predicting the total resistance, and free-surface configuration of the DTMB ship model. To make the problem more challenging, the speed range was selected to cover the medium-high speed range, starting from Froude number Fr=0.2 up to Fr=0.44 with a step ΔFr=0.04 in every case. The reason behind choosing this range is to highlight the banking effect on the total resistance and the free-surface flow topology and wave height. To make this test possible, a geometrically similar model for the DTMB hull called "DTMB-UGAL" model with a scale of 1/44, which results in a reference length of L_{PP}=3.232 m and design draft of 0.14 m, full characteristics can be found in Table 4.12. The speed range plan resulted in seven test cases based on the ship speed as listed in Table 4.21 showing the corresponding Froude and Reynolds numbers for every case.

Table 4.21 Test cases and corresponding ship speed parameters

Case Number	C1	C2	C3	C4	C5	C6	C7
U [m/s]	1.126	1.351	1.577	1.802	2.027	2.252	2.477
Fr [-]	0.20	0.24	0.28	0.32	0.36	0.40	0.44
Re [-] x10^6	3.46	4.15	4.84	5.53	6.22	6.91	7.60

4.3.3.1 Experiment Setup

Prior to performing the experiment, many aspects have to be taken into consideration in order to ensure a successful experiment and highly reliable measurements. These aspects include crucially important points such as: model fabrication, which in this case should comply with the recommended procedures proposed by the ITTC as a principal reference in this scope [131]; another aspect stands for choosing the main dimensions of the model, which should comply with the Froude similarity concept and with respect to the basin dimensions to reduce the blockage effect as much as possible; calibration of the measuring instruments is also very important to ensure the accuracy of the results. As for the experiment execution, general procedures are followed for the test preparation comprising, for example, marking the draft lines; measuring the weight of the model to compare the theoretical weight with the actual one; preparing and mounting any necessary outfits that will help fixing the model to the carriage (in this test here, a specially designed wooden outfit was fabricated and mounted on the hull; and finally, measuring the temperature of the water in the tank. All the aforementioned procedures were planned and executed consistently to reduce the errors. The measured weight of the model had a deviation of 2.5% less than the theoretical weight. This problem was later managed by distributing extra weights to adjust the draft of the ship after the model was connected to the carriage. The measured water temperature before the first test was recorded as 15 ºC and, later it was continuously monitored during the following stages of the test. Two cameras are installed fore and aft the model

to capture the free-surface flow and to monitor the greening effect if it occurs. A general overview for the ship model and the carriage arrangement is represented in Fig. 4.31 showing the model arrangement and the added weights.

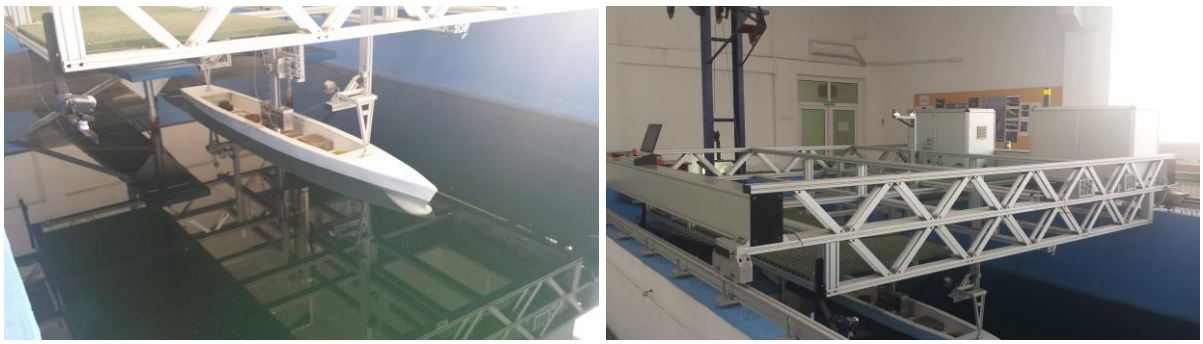

Figure 4.31 Ship model and the towing carriage arrangement

4.3.3.2 Resistance Measurements

As Table 4.20 bears out, there are seven test cases with respect to the ship speed. All the experimental results were measured for every case and represented in Table 4.22 for the total ship resistance. The total, frictional and residual resistance coefficients are estimated based on the ITTC 57 method, according to the equations

$$R_{\mathrm{T}} = R_{\mathrm{F}} + R_{\mathrm{R}}$$
$$C_{\mathrm{T}} = \frac{R_{\mathrm{T}}}{0.5\rho U^2 S} \tag{4.1}$$

$$C_{\mathrm{T}} = C_{\mathrm{F}} + C_{\mathrm{R}}$$
$$C_{\mathrm{R}} = C_{\mathrm{T}} - C_{\mathrm{F}} \tag{4.2}$$
$$C_{\mathrm{F}} = \frac{0.075}{(\log Rn - 2)^2}$$

where R_{T} refers to the total ship resistance, R_{F} stands for the frictional resistance and R_{R} being the residuary resistance; similarly for the resistance coeeficients C_{T}, C_{F} and C_{R}represents, total, frictional and residuary resistance coefficients, respectively.

Table 4.22. Measured total resistance and corresponding resistance coefficients

Test	Time	*U* [m/s]	R_{T} [N]	*Fr*	C_{T}	C_{F}	C_{R}
1	10:40	1.126	5.177	0.200	5.308	3.640	1.667
2	11:30	1.351	7.357	0.240	5.240	3.517	1.723
3	12:30	1.577	10.379	0.280	5.425	3.417	2.008
4	13:30	1.802	13.580	0.320	5.436	3.334	2.102
5	14:30	2.027	17.534	0.360	5.547	3.264	2.284
6	16:35	2.252	25.668	0.400	6.579	3.202	3.377
7	17:40	2.477	35.109	0.440	7.438	3.148	4.290

4.3.3.3 Free-Surface Measurements

The wave profile at the ship extremities is continuously monitored by the means of two cameras to capture the wave profile in the vicinity of model and any possible green-water effect, as previously indicated. Several snapshots are captured for the wave profiles near the ship hull during the test and are brought to attention in in figure 4.32. The wave amplitude of the generated in the vicinity of the forepeak is increasing as the ship speed increases, which in the high-speed cases starts cover the bow area of the model as the ship vertical motion oscillates; nevertheless, no greening effect could be observed during the experiment, thanks to the flare configuration which tends to drive the water outward far from the hull. It is worth stating that to simplify the model construction process, the rise of flare was ignored; hitherto, this did not result in any green-water effect on the deck. At the ship stern, the transom remained almost dry during the test regardless of the ship speed. The flow was forced in the downstream from underneath the transom, causing a rooster-tail-like wave breaking formations behind the hull.

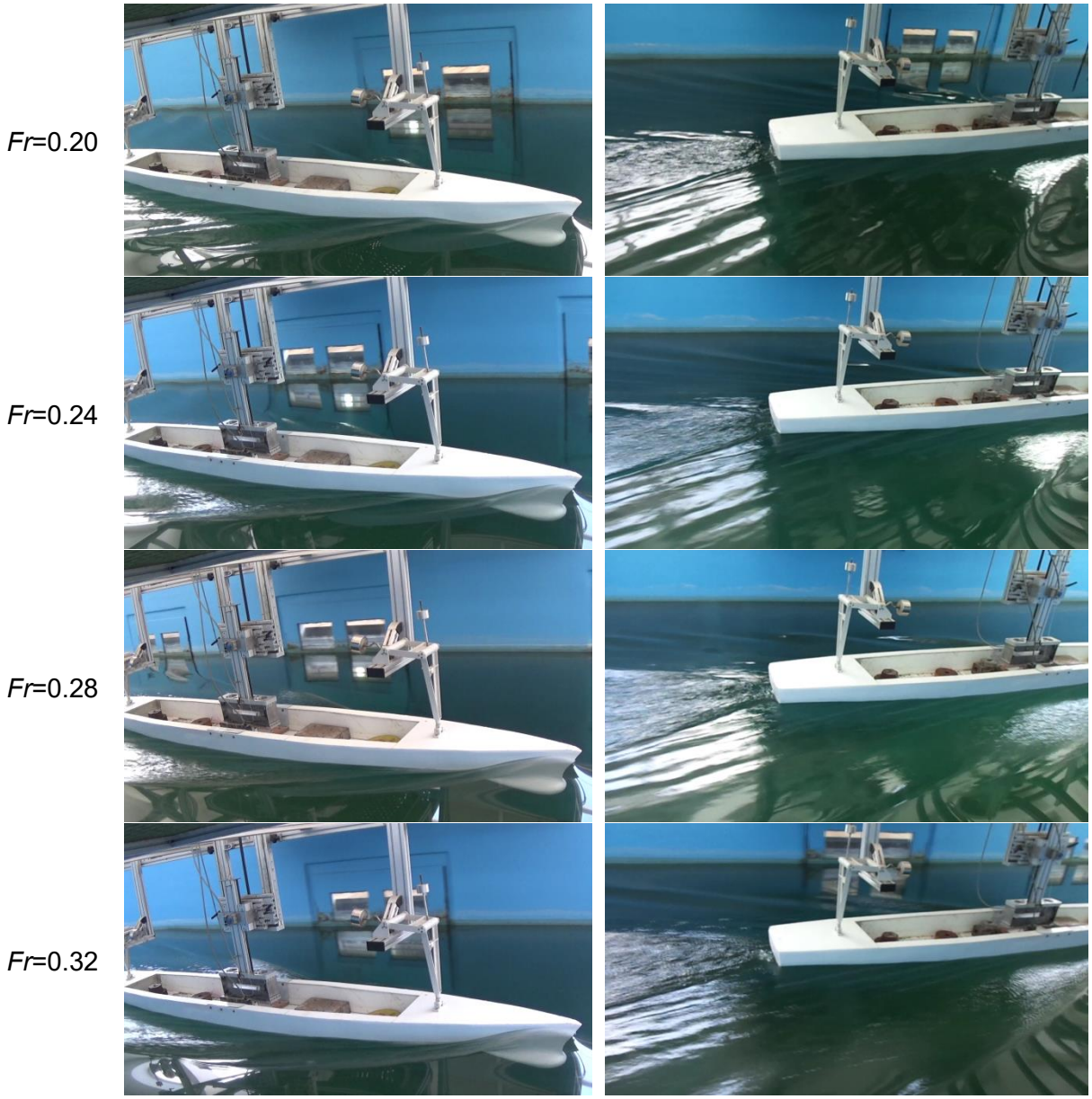

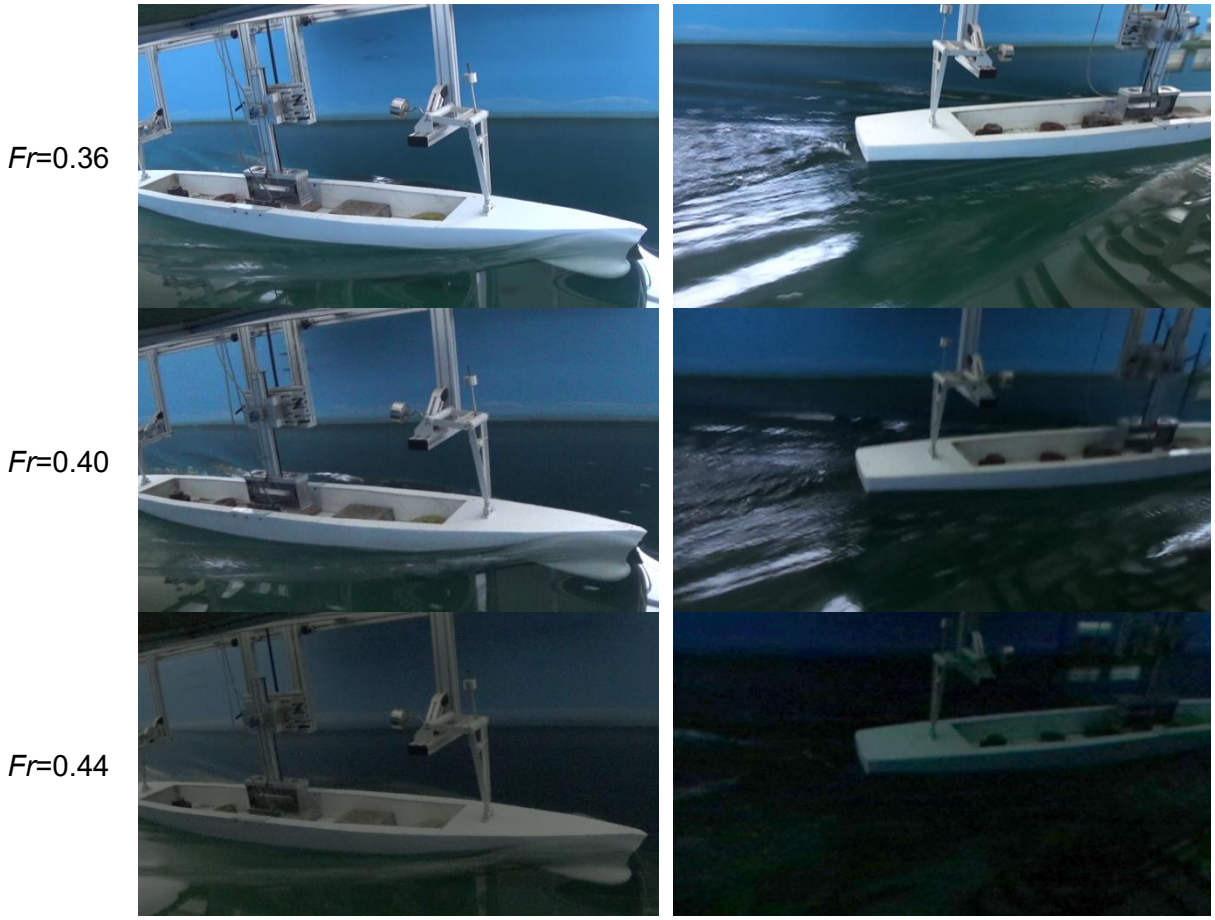

Figure 4.32 Free-surface topology at ship extremities during the test: bow (left), stern (right)

4.3.3.4 Measurements Validation

In order to investigate the accuracy of the measured results in the experiment, a simple comparison between the measured resistance in the towing tank for Model – UGAL and Model – INSEAN was performed after the data extrapolation procedure corresponding to the ITTC57 recommended procedures. This comparison is presented in Table 4.23 which shows that the tank experiment complies from the total force perspective, especially for the higher speed conditions, while for the lowest speeds, the error range is recognizable.

Table 4.23 Extrapolated data from the UGAL model to the INSEAN model scale

Fr	Total Resistance R_T [N]		ε%
	Model – UGAL	Model – INSEAN	
0.2	25.39	22.58	-12.45
0.24	36.24	33.76	-7.36
0.28	51.61	48.82	-5.71
0.32	67.81	65.88	-2.93
0.36	88.04	88.70	0.75
0.4	131.28	136.35	3.72
0.44	181.58	191.23	5.05
		Average $\lvert\varepsilon\%\rvert$	**5.42**

There are several factors that can contribute in this discrepancy, which may be related to the data sampling errors, the blockage effect did not exist in the corresponding experiment, the aforementioned volumetric error, and finally, the extrapolation process itself, which is basically a theoretical procedure that contains some assumptions. Overall, the average error obtained in this comparison is still within 5.42%, which may be considered acceptable in the view of the aforementioned factors.

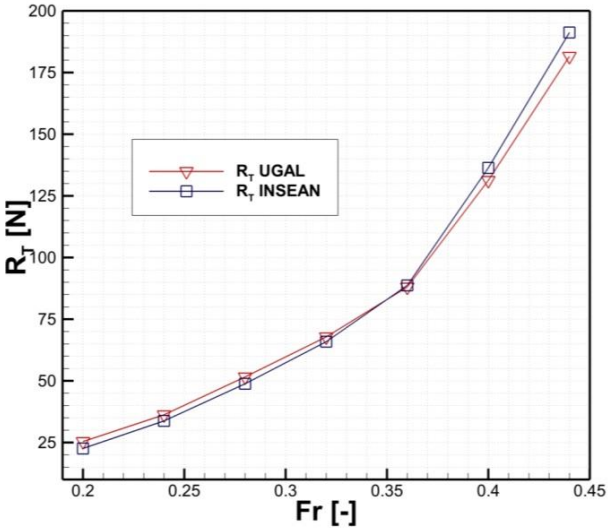

Figure 4.33 Extrapolated data of the UGAL – Model compared to INSEAN – Model [129]

4.3.3.5 CFD Approach

Since the scope of this study is to validate the CFD approach against the experimental data, this part has no difference to highlight the CFD results for the numerical simulation performed to imitate the same experimental conditions. In this scope, a consistent study is performed taking into consideration the model dimensions, running speed and tank conditions, to reproduce the experimental tank into a numerical tank. A full case study was presented and published by the author in this regard in [132], from which the main highlights are summarized in the following sections, while the full details can be found in Appendix A.

The main scope is to cover the problem as a general case simulation from one perspective, and to account for the tank banking effect by controlling the boundary conditions and tank-like domain configuration. This resulted in three cases, the General Domain (GD) analysis, where the main setup for CFD analysis, as described in the previous sections remain unchanged; On the other hand, two different conditions are created for the tank-like concept having the same tank dimensions and the boundary condition on the side tank wall is either active (AW) or disabled (DW) to account for banking effect. The following sections will highlight the CFD results from the total resistance and the free-surface viewpoints.

- ***Resistance Comparison***

The total resistance force is numerically predicted and compared to the EFD data obtained from the experiment. This comparison is qualitatively described in Table 4.24 for the three simulation conditions. The comparison shows that the agreement between the EFD data and the CFD results is reasonable as the average error for the three simulation cases is slightly above

4.0%, which makes it more than acceptable. And also, it remains within the error range obtained for the comparison made after results extrapolation that was presented in Table 4.23.

Table 4.24 Total resistance comparison between CFD and EFD results

U [m/s]	Total Resistance R_T [N]				Error		
	CFD (GD)	CFD (DW)	CFD (AW)	EFD	$\varepsilon_{GD-EFD}\%$	$\varepsilon_{DW-EFD}\%$	$\varepsilon_{AW-EFD}\%$
1.126	4.910	4.947	4.950	5.177	5.157	4.443	4.385
1.351	6.850	6.881	6.941	7.357	6.891	6.470	5.654
1.577	9.696	9.814	9.830	10.379	6.581	5.444	5.290
1.802	12.973	13.176	13.164	13.580	4.470	2.975	3.063
2.027	17.194	17.458	17.468	17.534	1.939	0.433	0.376
2.252	25.846	26.492	26.528	25.668	-0.693	-3.210	-3.350
2.477	36.308	37.292	37.422	35.109	-3.415	-6.218	-6.588
				Average $\|\varepsilon\%\|$	**4.164**	**4.170**	**4.101**

- ***Free-Surface Results***

The free-surface configuration that was captured in the towing tank showed different aspects regarding the free-surface topology, the absence of the green-water on the deck and the transom breaking rooster-tail wave breaking formations. All these aspects were taken into consideration during the numerical simulation to ensure that the free-surface was captured properly. For this reason, the free-surface configuration corresponding to the different simulation conditions are presented in Fig. 4.34 for the seven simulation cases based on the Froude number. It can be clearly observed the wave reflection at the side walls of the tank resulted from the ship speed increment.

Fr=0.20

Fr=0.24

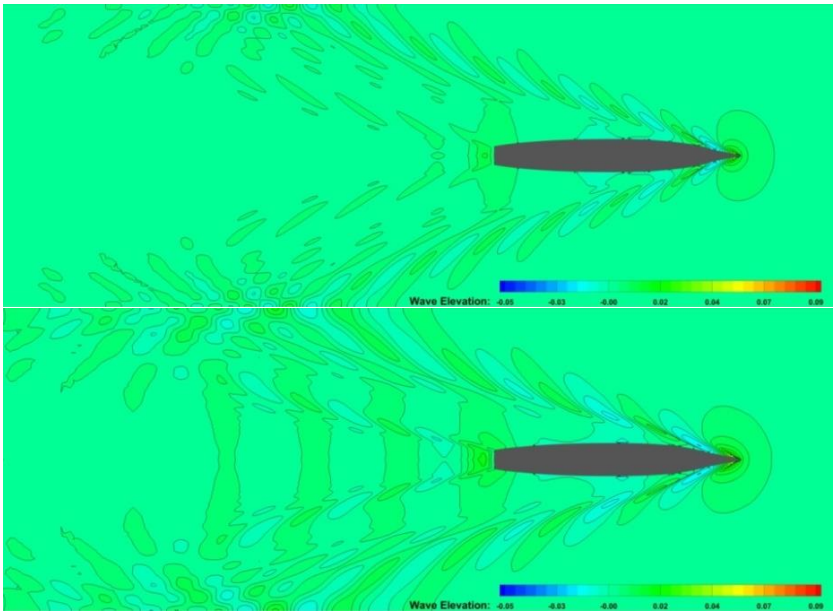

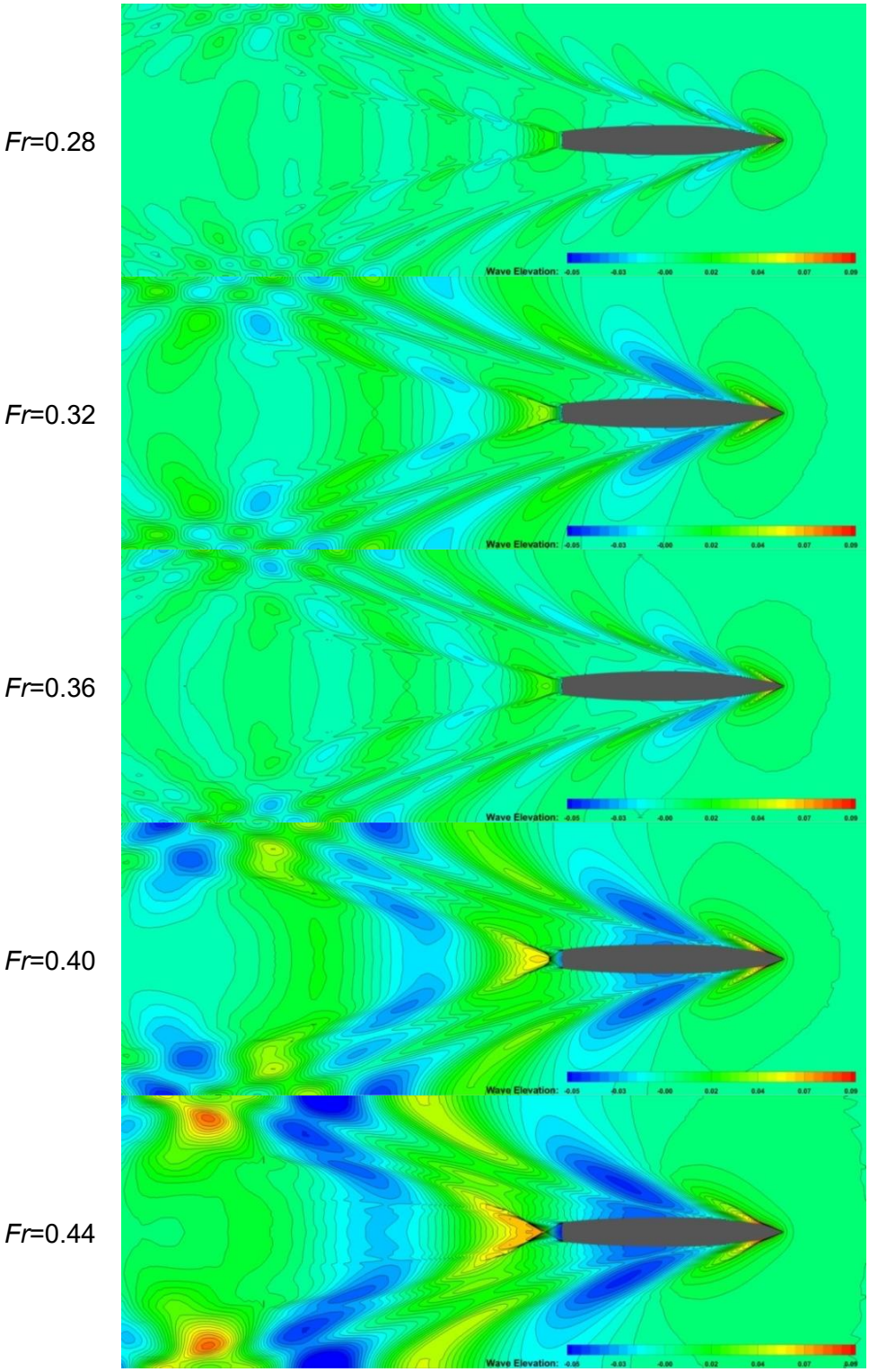

Figure 4.34 Wave pattern for active tank walls domain showing wave reflection at the wall

The wave elevation diagram can also be visualized in Fig. 4.35 for the simulation cases combining the wave profile at the hull and at the side boundary. Evidently, due to the water reflection at the tank walls, another wave is generated.

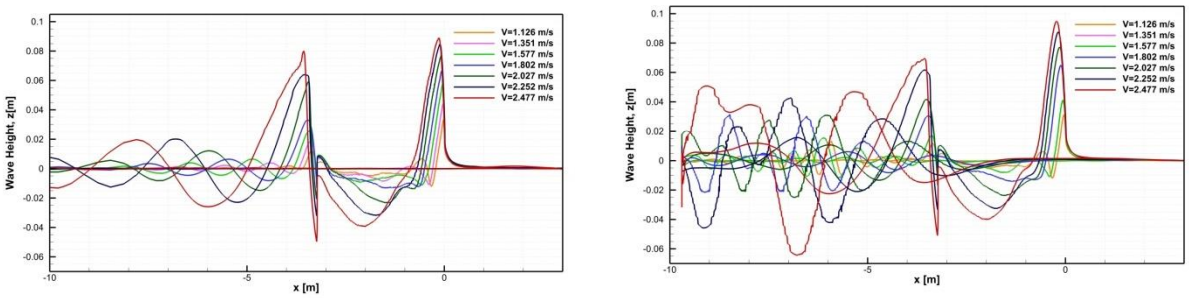

(a) (b)

Figure 4.35 Wave elevation diagram: (a) general domain, (b) active walls domain

Finally, the comparison represented in Fig. 4.36 shows the computed and the measured free-surface at the bow and the stern of the model. The CFD results resemble qualitatively well compared to the EFD data.

Figure 4.36 The numerically predicted against the measured free-surface profile at model extremities

Finally, it is important to mention that all the results reported earlier for the experimental and numerical approach for this study have been fully published in [137].

After finishing the hydrodynamic performance of the ship resistance, the following stage is to stand for the propulsion performance or powering performance of the ship. In this stage, the propeller is the main subject of concern in both, open water and behind the ship. This is the main subject of the following chapter that will cover the hydrodynamic performance of the marine propeller for two propeller model of two different types of ships.

Chapter V
Ship Propulsion Performance

Ship propulsion performance, also referred to as ship powering performance, is one of the most important aspects considered in ship hydrodynamics in the initial design stage of a ship. It comes directly after ship resistance prediction in order to establish the powering arrangement of the ship. Two vital decisions are made based on the estimated power; the first is related to the main engine selection to derive the ship and overcome the drag, while the second is concerned with the selection of the propulsion system itself. Most of the existing ships in the international fleets nowadays rely on the screw propeller working in the wake field of the hull. It is crucially important, from the hydrodynamic performance point of view, to analyze and investigate the working medium for the propeller before and after it is attached to the ship. This step is crucially important to avoid any undesired drawbacks that may directly or indirectly affect the propeller performance, such as flow separations, loss of propulsion, cavitation, noise and vibrations. Looking at the problem from a completely different perspective, the challenge does not stop at this point since the latest regulations imposed by the IMO to control the Green-House Gases (GHG) emissions from marine activities proposed new criteria to judge the powering performance of a ship based on the Energy Efficiency Design Index (EEDI). This increases the design challenges, as the problem now is not just dominated by the efficiency and economy gained from the propulsion system, but it is also controlled by the potential environmental impact. In such circumstances, traditional methods such as experimental and statistical methods can be very inappropriate; since the first requires complex operations and significant overhead costs, while the second cannot stand for the new parameters proposed by the IMO because the method itself was proposed few decades in past.

The latest development recorded for the CFD applications in the past two decades in predicting propulsion hydrodynamic performance is highly recognized. Increasing success in predicting mostly all the associated characteristics of the propeller, whether in open water or behind the ship condition, has been recorded in various research worldwide. Level of accuracy for the predicted solution, as well as the propulsion characteristics, blade loading, vortex formations, cavitation inception and hull-propeller interaction has reached a remarkable level of maturity. The latest techniques in modeling the rotating propeller, such as the sliding and overset grid reduced the physical modeling assumptions and made it possible, not just to estimate the thrust, torque and propulsion efficiency parameters, but it can be further extended to predict flow features near both, hull and propeller. Two possible methods can predict the propulsion performance of a ship based on the purpose of the simulation, as it was formerly discussed in Chapter I. If the target is only the propulsion characteristics, the body force method is used to calculate the acting forces and propulsion parameters. However, the fully discretized propeller model is necessary in case of more details of the flow are required to be investigated. Both methods are examined and reported in this chapter for two types of ships: the JBC and KVLCC2 ship models. Qualitative and quantitative assessments of the numerical results are reported in the following sections, along with the simulation strategy, computational aspects, results verification and validation. The analysis is aimed at covering the propulsion performance in the nominal, effective and open water conditions.

5.1 Propulsion Performance of the JBC

The JBC ship model continues for this simulation, taking advantage of the available EFD data in the public domain in order to validate the numerical results compared to the available experimental data provided by the NMRI from the Tokyo 2015 Workshop [48]. The analysis is covering three main aspects regarding the propulsion performance, which are: the propeller performance in open water (POW), the nominal flow analysis and finally, the self-propulsion performance for the propeller working in the wake domain behind the ship.

5.1.1 Propulsion Performance in Open Water

The JBC ship model is equipped with five-blade conventional screw propeller with a diameter of 0.203 m. The propeller configuration was presented in Chapter IV in Fig. 4.1. The characteristic dimensions of the propeller are tabulated in Table 5.1.

Table 5.1 Principal characteristics and parameters of the JBC propeller

Parameter	Value
Diameter, D_p [m]	0.203
Boss ratio, D_h/D_p	0.18
Pitch ratio, P/D_p	0.75
Expanded area ratio, A_E/A_0	0.5
Number of blades, Z	5
Blade section	AU
Direction of rotation	Clockwise
Angle of rake	5º
Maximum blade width ratio	0.2262
Blade thickness ratio	0.05
Propeller Location from A.P., x/L_{pp}	0.014497
Propeller Location from base line, z/L_{pp}	0.018507

5.1.1.1 Analysis Conditions

The open water simulation in this study of the JBC propeller corresponds to the tank test performed in the NMRI and reported on the Tokyo Workshop network [48] for 15 different values of the advance ratio J=0.1~0.8 increasing with 0.05 in every test, such that $J = U/nD_P$, where U stands for the flow velocity in [m/s], D_P is the propeller diameter in [m] and n refers to the propeller rotation in [rotation/s]. In order to maintain the simulation within a reasonable range, only eight simulations are performed for advance ratio J=0.1~0.8 increasing with 0.1 in every simulation. In order to control the advance ratio, there are two methods which come from the definition of the ratio itself, depending on changing one of the variables involved in the advance ratio equation, which are the flow velocity U or the propeller rotation rate n. Both concepts are accepted and have no influence on the result accuracy. In this study, the flow velocity was maintained constant, similar like the ship speed of U=1.179 m/s, while the n is adapted accordingly to provide the corresponding advance ratio J. The simulation conditions and analysis cases are summarized in Table 5.2.

The propeller is analyzed in a mono-fluid condition with only water flow is considered in the simulation. All the eight speeds are investigated using the EASM for turbulent flow treatment to

ensure better flow characteristics; however, two speeds are analyzed using an advanced turbulence model such as the DES model for comparison.

Table 5.2 POW simulation cases and flow parameters

Simulation Case	C1	C2	C3	C4	C5	C6	C7	C8
J	0.1	0.2	0.3	0.4	0.5	0.6	0.7	0.8
n [rpm]	3485.0	1742.0	1162.0	871.0	697.0	581.0	489.0	436.0
Equivalent Speed, U_{eq} *[m/s]*	25.96	13.01	8.72	6.59	5.32	4.48	3.89	3.45
*Re *10^5*	23.82	11.94	8.01	6.04	4.88	4.11	3.57	3.17

5.1.1.2 Domain & Boundary Conditions

The domain is represented in a cylindrical form whose dimensions in the circumferential direction are 6.0 times the propeller diameter D_P and 8.0 times the propeller diameter in the longitudinal direction as depicted in Fig 5.1. A global reference frame is assigned at the point (0, 0 and 0) which represents the intersection point of the generator line of the propeller and the shaft centreline. The inflow boundary is at 2.0D_P upstream, where a velocity inlet boundary condition is set for the inlet. The outlet boundary is placed at 6.0D_P downstream with a frozen pressure boundary condition. Similarly, the inlet velocity condition is chosen for the cylindrical wall of the domain. Since the local flow wake is of an extreme importance in this case to understand the flow mechanism in the wake, an isotropic cylindrical refinement zone is imposed in the vicinity of the propeller with a diameter about 1.5D_P distributed equally above and beneath the propeller shaft axis line. This cylindrical refinement is extended in the longitudinal direction starting from 0.25D_P upstream and 4.0D_P downstream. No slip condition is applied on the propeller tip, blades, cap and boss, while the slip condition is imposed for the propeller shaft, considering that it remains in the upstream with no significance in its local flow. The boundary layer is considered in this simulation, maintaining the y^+ values for all the no slip walls less than unity.

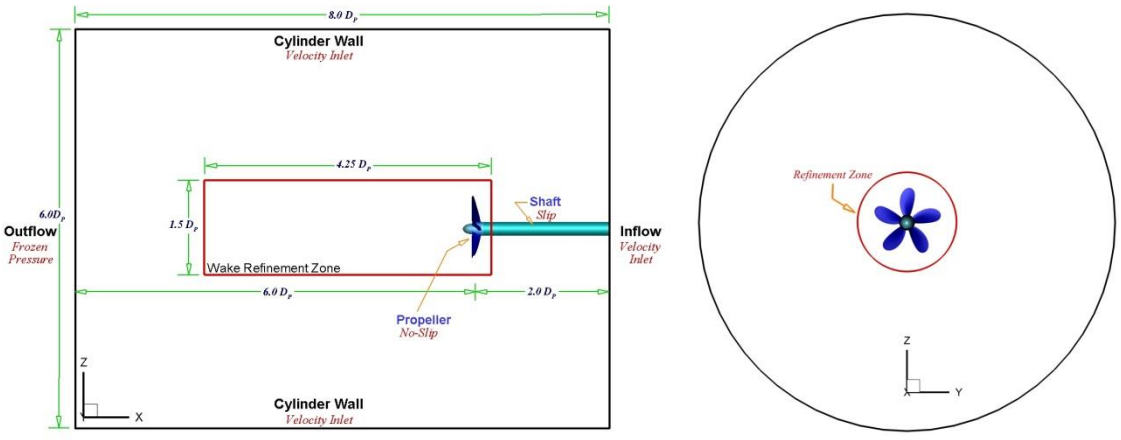

Figure 5.1 Simulation domain dimensions and boundary conditions in *x-z* and *y-z* view

5.1.1.3 Computational Grids

As the resistance grids were generated, the automatic Hexpress module available in the solve package is used for generating the discretization grids in this simulation. Four grids are generated to study the influence of the grid on the solution accuracy through a grid convergence

study. The grid details are listed in Table 5.3, while the discretization grid configuration can be visualized in Fig. 5.2, showing the propeller blades, shaft and refinement zone.

Table 5.3 Computational grids

	Grid Size (Million Cells)			
Propeller Grid	M1	M2	M3	M4
	3.05	7.5	19.7	34.63
y^+	1.26	0.92	0.68	0.46

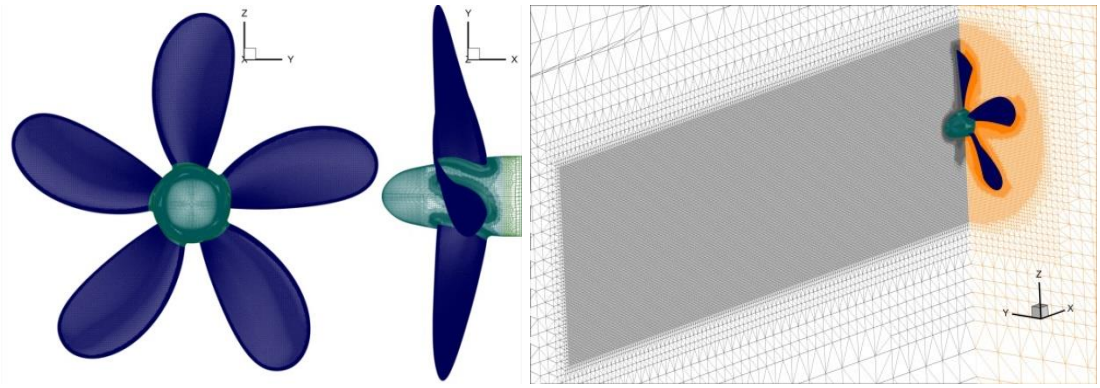

Figure 5.2 Discretization grids for the finest grid illustrating blades grid and refinement zone

5.1.1.4 Simulation Strategy

The simulation is performed for 5 seconds in each simulation case to ensure a sufficient convergence for the thrust and torque. The flow is accelerated in a quarter-sinusoidal wave pattern based on an unsteady approach for 1~2 minutes depending on the propeller rotational speed. Second order convergence criteria is applied with 5 nonlinear iterations, while the time step Δt is decided to provide 100 time-steps per propeller rotation according to the common practice from previous simulations based on the rotating frame approach, as proposed in the theoretical manual for the solver [110]. Once the convergence is achieved, the thrust and torque are recorded for every case and compared with the available EFD data [48].

5.1.1.5 Thrust and Torque Results

The numerically obtained results for the thrust coefficient K_T, torque coefficients K_Q and the propeller open water efficiency η_o are computed for each advance coefficient based on the equations:

$$K_T = \frac{T}{\rho n^2 {D_p}^4} \tag{5.1}$$

$$K_Q = \frac{Q}{\rho n^2 {D_p}^5} \tag{5.2}$$

$$\eta_o = \frac{1}{2\pi}\frac{K_T}{K_Q}J \tag{5.3}$$

The results obtained for the propulsion coefficients are compared with the EFD data provided in [48,] as plotted in Fig. 5.3; showing a reasonable agreement for the coarse grids and good agreement for the fines grids. The average error estimated for the thrust coefficient K_T ranges

between 0.68 and 2.81; where the lowest value is the average error for finest grid M1and the maximum is estimated for the coarsest grid. The average error for the torque coefficients K_Q is limited within 1.12 and 4.96, for finest and coarsest grids, respectively. Unfortunately, the error estimated for the open water propulsion efficiency η_o is ranging between 1.82 and 4.87 for finest and coarsest grids, respectively. It can also be observed that the error for the light loaded propeller, i.e., for higher values of *J* is higher than the error estimated for the heavy loaded, i.e., for lower values of *J*, especially for the coarsest grids. This might result from the grid uncertainties at low speed, which possible to occur in this type of simulations as a consequence for the underestimated pressure field on the propeller blade, which subsequently leads to an underestimated forces and moments. On the other hand, the average error for all the three parameters is within a controlled level of accuracy beneath the 5%, even for the coarsest grid M4, which is considered more than sufficient for this type of simulations.

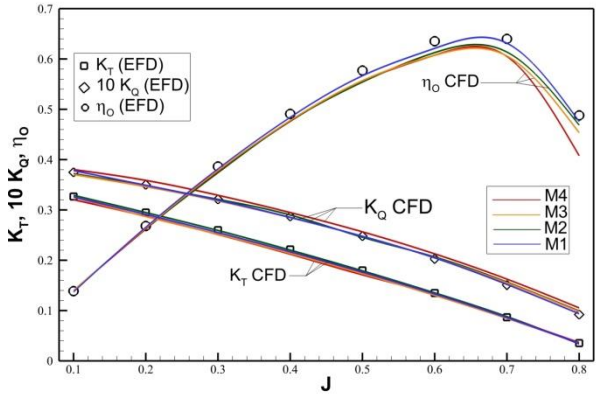

Figure 5.3 Thrust coefficient K_T, torque coefficient K_Q and propeller open water efficiency η_o curves compared to EFD data [48, 125]

One of the most important aspects to be considered in propeller simulations is the pressure field on both sides of the propeller, suction and pressure sides. For this reason, the pressure distribution on the propeller blades suction and pressure sides represented in the non-dimensional pressure coefficient C_P is depicted in Fig. 5.4.

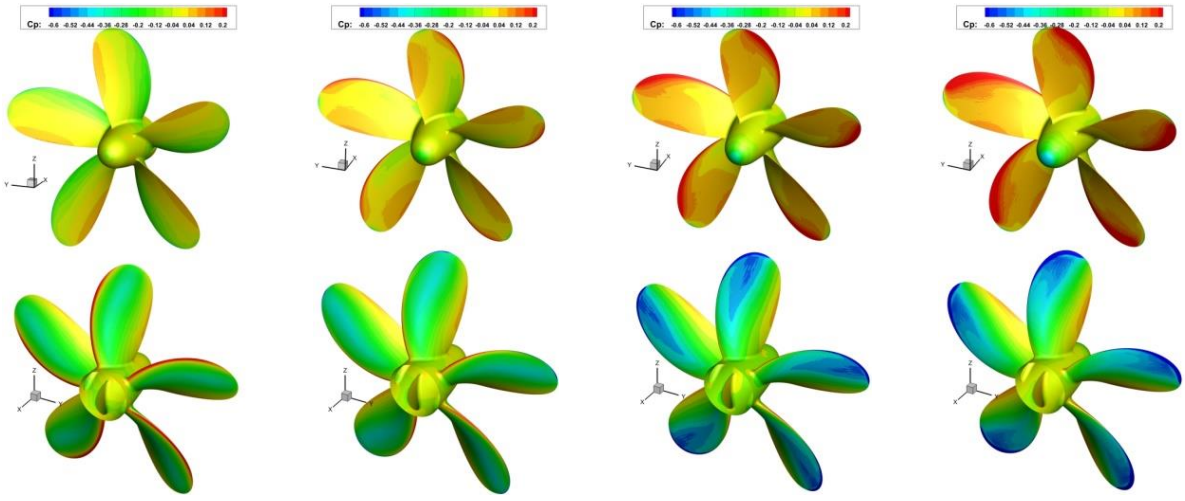

(a) (b) (c) (d)

Figure 5.4 Pressure distribution on the suction and pressure sides of the propeller at different advance ratios *J*: a) *J*=0.7, b) *J*=0.5, c) *J*=0.3 and d) *J*=0.1

The pressure distribution corresponds positively with the theoretical flow principles, where the stagnation effect is observed on the leading edge resulting in high pressure region and reduced closer to the propeller tips. When the propeller is lightly loaded, a slight change in pressure can be observed between the leading and trailing edge as Fig. 5.4 (a) and (b) bears out. On the other hand, when the propeller loading is increased, the low pressure tends to move significantly to be concentrated near the propeller tip; as it can be observed in Fig. 5.4 (c) and (d). This pressure concentration, especially at this high rotation rate, might be a possible reason for cavitation inception. Similar pressure distribution on the propeller blade suction and pressure sides was presented in [138].

5.1.1.6 Wake Flow Analysis

The wake flow of the propeller is analyzed using two different turbulence models; the EASM and the DES models. One of the most important characteristics of the flow downstream of the propeller is the vortex formations, which should be well understood to get an insight into the flow development in the wake zone. In order to have a proper look at the flow development, four parameters are used to describe the flow in Fig. 5.5. The streamwise velocity shows that the flow is accelerated by the propeller momentum and pushed downstream the propulsion domain. The corresponding pressure is showing fluctuation points at the propeller wake in the vicinity of the propeller blade and soon after about 1.5 times the D_P. Similarly, the turbulent viscosity and turbulent kinetic energy produce similar disturbance and fluctuations. The reason for those formations is because of the development of the propeller vortices rising from the tip, root and hub of the propeller.

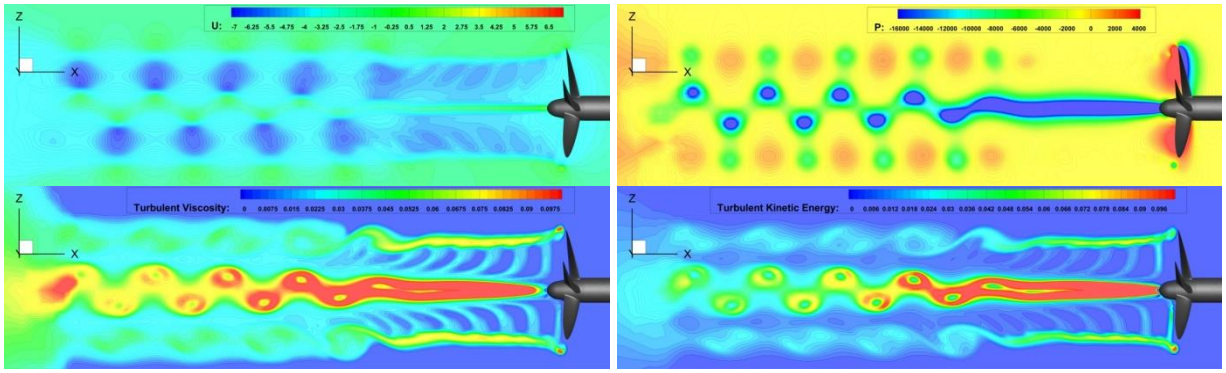

J=0.3

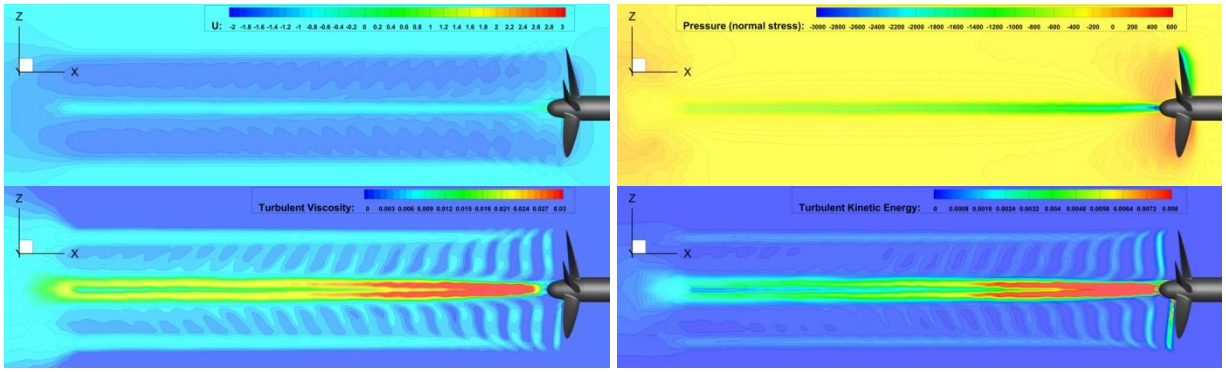

J=0.6

Figure 5.5 Axial flow velocity, pressure distribution, turbulent viscosity and TKE in the propeller wake for *J*=0.3 and *J*=0.6

The vortices formation can be expressed by the second invariant *Q* criterion, as previously described in Chapter IV, as it is illustrated in Fig. 5.6 and 5.7 showing that the vortical tubes are starting due to the propeller rotation as the flow leaves the propeller tip causing the tip vortices. Correlating the flow characteristics in Fig. 5.5 and 5.6 makes it easy to understand the pressure and velocity fluctuations downstream. The tip vortices are generated in two sets; one from the leading edge and the second is from the trailing edge, with a slight phase shift from the first vortical tube on the leading edge. Close at the root of the blade, another helical tube formation can be observed resulting from the propeller rotation and flow separation at the blade root, as it can be noticed in Fig. 5.6. And finally, the hub vortices are configuring a longitudinal tube starting soon at the propeller hub centerline washed downstream. The helical structure of the vortices is dependent on the advance ratio as it can be observed, where the light loaded propeller results in well-constructed vortices that continues downstream in the wake about two times D_P and then vanishes because of the viscous dissipation. On the other hand, for heavy loaded propeller, the vortices are combined resulting in a thicker vortical tube and a significant distortion of the hub vortices can be observed downstream. Again, comparing the Fig. 5.5 and 5.6 can give an understanding for the reason behind this, which is influenced by the viscous dissipation between the low momentum and high momentum flow accelerated downstream by the propeller rotation.

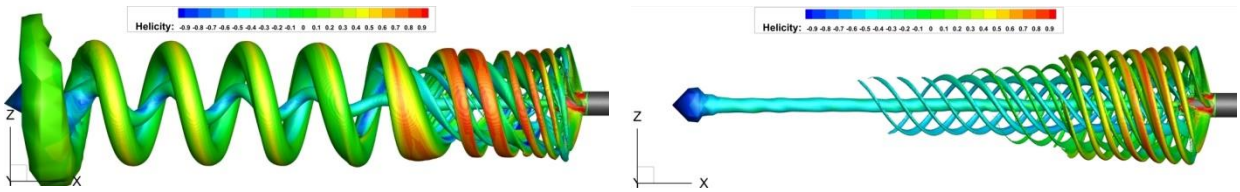

(a) (b)

Figure 5.6 Vortical structure of the wake flow computed at T=5 sec. for: (a) *J*=0.3, (b) *J*=0.6

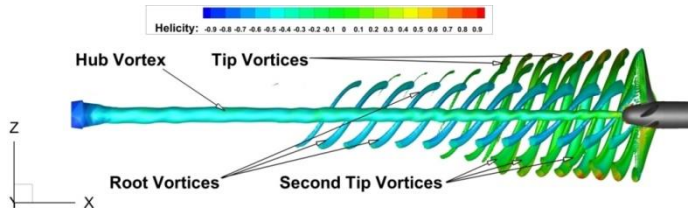

Figure 5.7 Longitudinal cut in the vortical structure of the wake flow at *J*=0.6

Analyzing the obtained results for TKE, turbulent viscosity and the vortices formation, it seems that the grid density is not sufficient to capture properly the flow details, because the flow is dissipated faster in the downstream. This may indicate that the grid size in the wake refinement zone should be improved.

Although there is no validation data for the wake flow of this propeller provided in the Workshop, the results are compared with other similar research outcomes from experimental and numerical studies that were reported in [139-141] and showed to within a good correlation.

Finally, it is worth mentioning that the results reported in the previous sections have been partially or fully published in the conference paper by the author reported in [142].

The next sections are covering the study of the propeller working the ship wake based on the body force method and the fully discretized propeller using the sliding grid technique.

5.1.2 Self-Propulsion Simulation

The self-propulsion simulation in this study is aimed at predicting the self-propulsion point for the propeller, which can be defined as the propulsion condition when the propeller thrust is equal to the total ship drag obtained in the simple resistance test, a relation that can be mathematically expressed as $T=R_T$. Because the ship is usually towed in the tank by the carriage, as presented in Chapter IV, sometimes the propeller thrust is not sufficient to provide the required thrust to overcome the total resistance of the model in the self-propulsion test. Thus, an extra force is added to help the propeller to overcome the total drag of the ship. This force is called the Shear Force correction (*SFC)*, and can be estimated based on the formula; $SFC=R_T-T$. The data provided from the Tokyo Workshop 2015 reported the *SFC*, thrust and resistance values for both cases with and without the ESD. These results are used as a validation reference for the following numerical studies.

Two approaches can be applied in this concern; the first is based on the body force method using an actuator disc approach, while the second stands for introducing the actual propeller in the simulation based on sliding or overset grids. In this study, only the sliding grid technique is used for propeller modeling because it simpler and easier to model.

5.1.2.1 Analysis Conditions

The analysis conditions correspond to cases 1.5~1.8 in the Tokyo 2015 Workshop for ship with and without the ESD sailing in calm water similar like resistance simulation with speed of U=1.179 m/s that corresponds to the Froude number Fr=0.142 and Reynolds number Re=4.6x10^6. Both cases are investigated and reported in the following sections for propulsion parameters and local flow analysis.

5.1.2.2 Domain & Boundary Conditions

Regardless of the approach applied, the computational domain and boundary conditions are perfectly matching the same configuration for a classic resistance test domain from the dimensions and boundary condition perspective, except that the symmetry condition is not applicable in this case; thus, the full hull is introduced in the domain. Same refinement parameters for hull, duct, free-surface and refinement zones still persist. However, the difference between the body force method and propeller modeling based on sliding grid is that the shaft and boss of the propeller are set to slip condition, in order to avoid numerical errors at the inlet and of the sliding grid. A general computation domain for the self-propulsion simulation is represented in Fig. 5.8 showing the domain dimensions and boundary conditions.

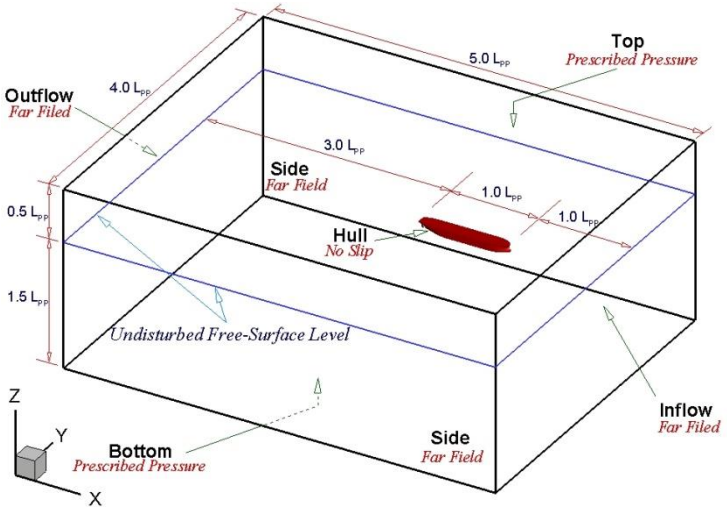

Figure 5.8 Computational domain and boundary conditions for self-propulsion simulation

5.1.2.3 Computational Grids

Computational grid in this study is more complex compared to a simple resistance case. If the actuator disk method is applied, a special focus is necessary to represent properly the actuator disk refinement such that, the actuator disk refinement should be made fine enough to ensure at least 35 grid cells in the disk circumferential direction and 25 cells at the disk thickness. On the other hand, if the sliding grid approach is applied, the consistency between the sliding grid for both domains (Ship and propeller domains) is crucially important to avoid divergence and other numerical problems. Particularly in this study, where the sliding grid approach was performed, there was no problem in inserting the sliding grid between the two domains in case without the ESD being present in the CAD model. Once the duct is present, it is very difficult to select the sliding grid similarly like the bare hull ship without the duct. For this reason, a transitional unconventional cylindrical sliding grid comprises two segments is proposed by the author to avoid cutting apart from the duct to rotate with the propeller during the simulation, which will cause unrealistic simulation. The configuration of the sliding grid can be observed in Fig. 5.9.

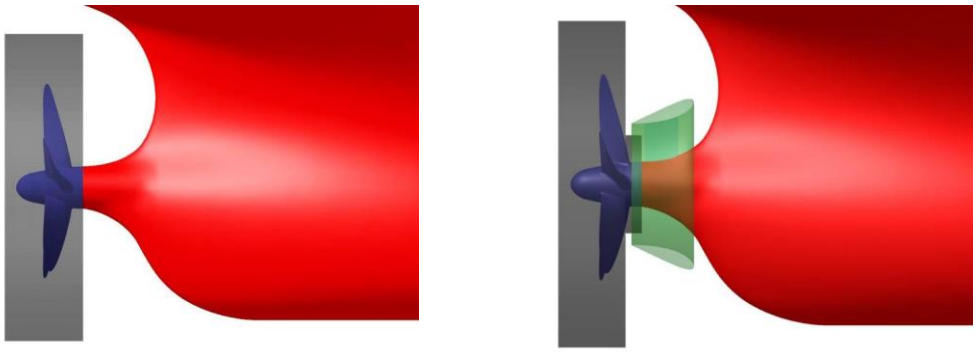

Figure 5.9 Sliding grid arrangement for JBC without ESD (left) and with ESD (right)

The generated grids for both approaches are listed in Table 5.4 showing the total number of cells based on the grid density. Three grids are generated for every simulation to investigate the influence of the grid density on the solution accuracy, while the grid arrangement for the actuator disk and the sliding grid approach are presented in Fig. 5.10 for the ship equipped with the ESD.

Table 5.4 Number of grid cells based on simulation conditions and grid density

	Simulation	Actuator Disk Approach		Fully Discretized Propeller	
		Without ESD	With ESD	Without ESD	With ESD
Number of Grid Cells (x 10^6)	Coarse (M3)	5.15	5.32	6.33	6.87
	Medium (M2)	10.29	11.52	11.05	12.48
	Fine (M1)	19.883	21.750	24.846	27.353

5.1.2.4 Simulation Strategy

For the actuator disk method, the simulation is performed on two levels; the first is identical to the resistance simulation, which is aimed at predicting of the nominal performance of the hull without the propeller including the prediction of nominal wake; the second is dedicated to the analysis of the propeller performance based on infinite-blade actuator disk approach that is used simulate the propeller performance based on the resistance results obtained in the first simulation combined with the data from open water propeller, either measured from a tank test or even

computed based on the CFD method. Both simulations are similar to the resistance simulation explained in Chapter IV with a quasi-static simulation, with the same time step and solution principles.

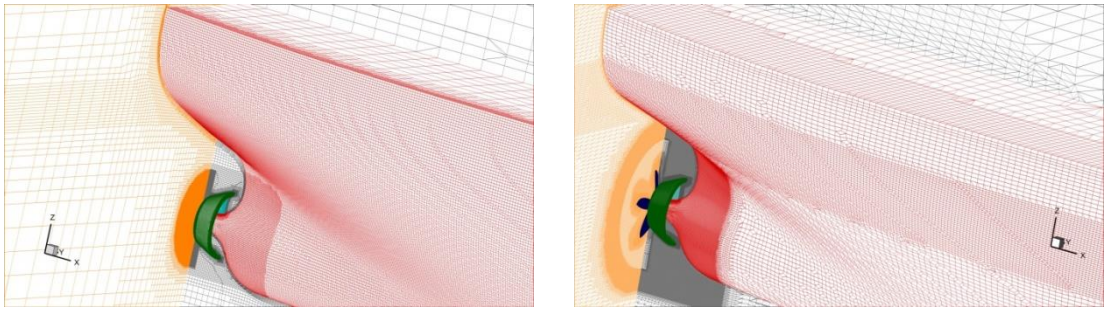

Figure 5.10 Grid arrangement for: actuator disk(left) and sliding grid (right) approches

For the self-propulsion prediction based on the sliding grid technique, two steps are used to perform the simulation; the first is also to estimate the nominal performance and to stabilize the resistance forces and vertical motions of the ship, while the other is used to stabilize the propeller thrust in the effective propeller performance of the propeller after connected to the hull. The first simulation corresponds perfectly with any similar resistance simulation; however, the second simulation is an unsteady simulation with a reduced time step to balance the propeller thrust and torque. The time step for the second simulation, as it is advised in the solve manual, is chosen to provide 200 time-steps per propeller rotation. High performance computer is used for this simulation to ensure a quick and enough memory for the sliding grid approach, since the sliding grid technique requires a significant memory for the simulation.

5.1.2.5 Self-Propulsion Results

The results obtained for the self-propulsion parameters are validated against the EFD data reported in [125, 126] and presented for both methods. The numerical simulation based on the actuator disk method showed to be faster from the physical simulation time point of view. Besides, the obtained results are sufficiently accurate and reliable. The simulation based on the sliding grid can be held in two approaches to predict the self-propulsion points of the propeller; the first is to run the simulation with the same parameters obtained from a tank test and compare the errors for the self-propulsion coefficients; while the other is to predict the propeller rotation using trial computations that may help in generating a diagram line at different propeller rotations, then the propeller rotation is estimated by introducing the thrust-resistance equivalent relation to estimate the self-propulsion point. Both methods are applied in this study. The first is faster and straightforward; unfortunately, it depends on the data from the tank test. If there are no tank test results for the studied ship, the second method must be applied.

- ***Actuator Disk Method***

The self-propulsion parameters computed based on the actuator disk method are listed for the three grids in Table 5.5 showing a good agreement with the EFD data. The results show a good agreement with an average error for the total resistance coefficient within 4.2% and 5.27% for ship with and without ESD. The results obtained for the ship with ESD is having a better accuracy compared to the results without ESD. The same case is repeated for estimated advance, thrust, torque, and wake fraction coefficients; however, for the thrust deduction fraction and

relative rotative efficiency, the error for the ship with ESD is higher than that case when the ship is not equipped with the ESD. Overall, the maximum error is estimated for the wake fraction with about 6.28% for the ship without ESD, while the minimum error is recorded for the thrust coefficient for the ship with ESD with an error value of 0.2%.

Table 5.5 Self-propulsion results for ship with and without ESD based on actuator disk method

Coefficient	Without ESD						With ESD			
	EFD	M1	M2	M3	$\|\varepsilon_{av}\|$%	EFD	M2	M3	CFD	$\|\varepsilon_{av}\|$%
Total resistance, C_T x10^3	4.81	4.61	4.57	4.49	5.27	4.76	4.62	4.56	4.50	4.20
Thrust, K_T	0.217	0.2181	0.2184	0.2191	0.71	0.233	0.2332	0.2332	0.234	0.20
Torque, $10K_Q$	0.279	0.283	0.284	0.288	2.15	0.295	0.297	0.298	0.303	1.47
Advance, J	0.410	0.407	0.407	0.411	0.417	0.36	0.37	0.37	0.374	3.15
Thrust deduction, (1-t)	0.803	0.795	0.794	0.79	1.25	0.810	0.796	0.794	0.789	2.10
Wake fraction, (1-w)	0.552	0.524	0.517	0.511	6.28	0.471	0.461	0.457	0.459	2.55
Relative rotative, η_r	1.011	1.0	1.0	1.0	1.09	1.014	1.0	1.0	1.0	1.38
Hull efficiency, η_H	N. A	1.517	1.535	1.545	-	N. A	1.727	1.739	1.719	-

In order to have a closer look to the local flow analysis based on the actuator disc method, the EFD data [Hirata] for the axial velocity contours measured at the section located in the propeller reference plan is plotted in Fig. 5.11 for the ship with and without the ESD at the nominal and effective wake condition, along with the computed results for the three relative velocity components V_a, V_r, V_{theta} for the actuator disk also located at the propeller reference plan at a distance 0.10148 m from the A.P. The comparison shows that the obtained results have a well congruence with the EFD data as Fig. 5.11 bears out. The measured and the computed results show the effect of the ESD on the flow configuration at the propeller vicinity, which indicate that the axial velocity contours are having more circular configuration compared to the ship without ESD. This means that the flow entering the propeller is more uniform, which can positively enhance the propulsion efficiency. At the core of the velocity contours, a slight discrepancy can be observed which is resulting from the absence of the propeller hub because it was not included in this simulation. Nevertheless, the effect is insignificant and the computed velocity contours resembles well with EFD data.

- ***Sliding Grid Method***

In order to generate the trend line of the propeller rotation versus the thrust, at least three simulations are required. In each simulation, the resistance and thrust are recorded and compared. In case when there is SFC, the self-propulsion point is obtained when the thrust is equal to the resistance. If the SFC exists, the difference between resistance and thrust should be equal to the SFC, and the propeller rotation rate can be predicted. In the current study, the SFC was given for the ship with and without the ESD as 18.1 and 18.2 N, respectively. And the propeller rotation rate was recorded for both cases, with and without the duct as 7.5 and 7.8 rps, respectively. The numerical simulation started with closer values to the data and the trend line was constructed for every case and the propeller rotation was reported for the self-propulsion condition as it can be observed in Fig. 5.12.

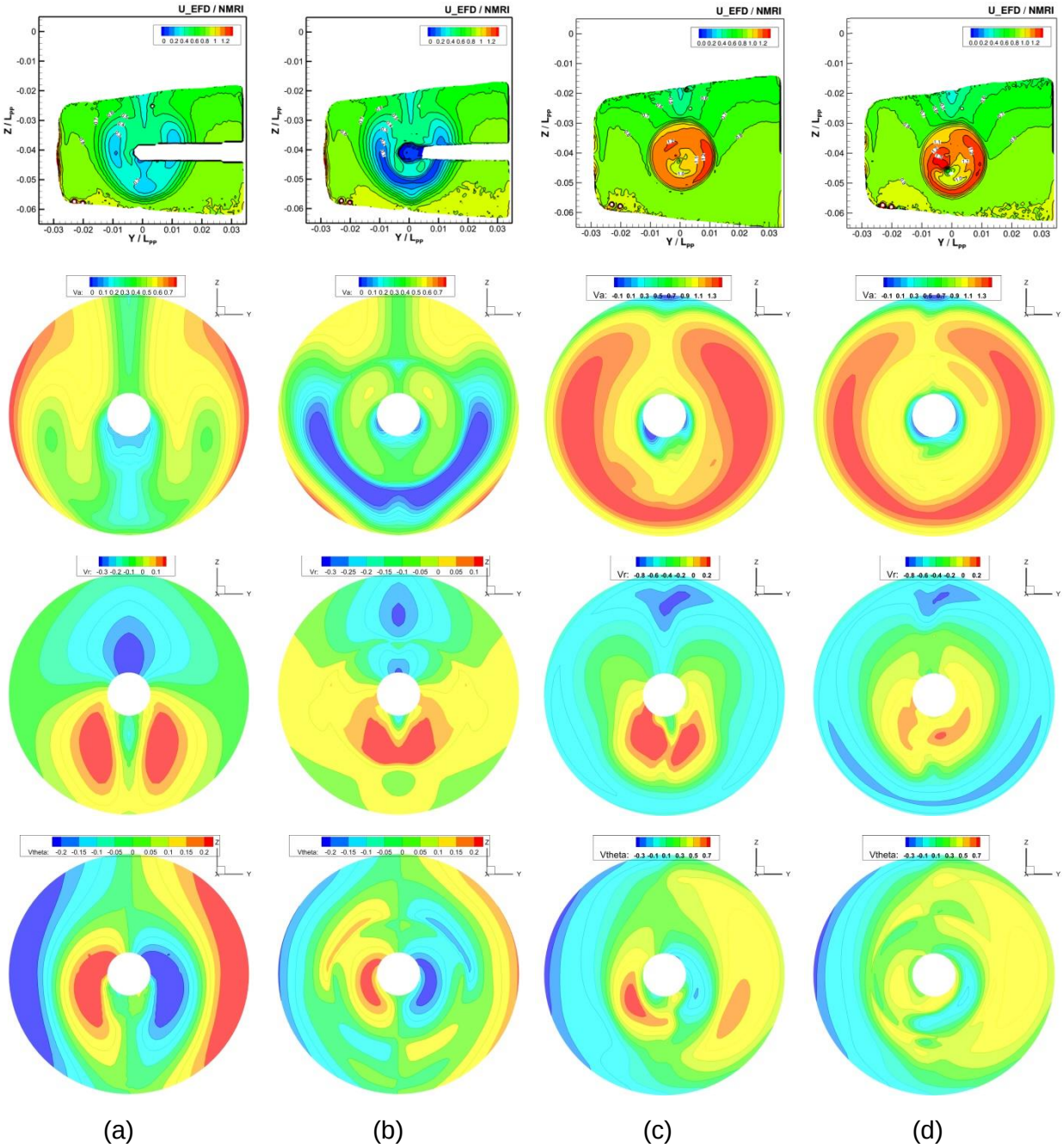

(a) (b) (c) (d)

Figure 5.11 CFD results for nominal (a and b) and effective (c and d) velocity contours computed for ship without and with ESD, respectively, using actuator disk method

The numerical results obtained for the propeller rotation resembles very well with the experimental data. The obtained rotation for the ship without the duct is n=7.7223 rps, compared to the experimental value of n=7.8 rps, with an error within 0.99%; while for the ship with the duct, the calculated propeller rotation is n=7.3852 rps, compared to the experimental value of n=7.5 rps, with an error 1.53%. Both values show the capability of the CFD method to predict accurately the self-propulsion point of the ship. The medium grid is used for this simulation to ensure a proper balance between the simulation time and accuracy. The numerical results are within a satisfying level of accuracy that can encourage for further investigation on different types of ships.

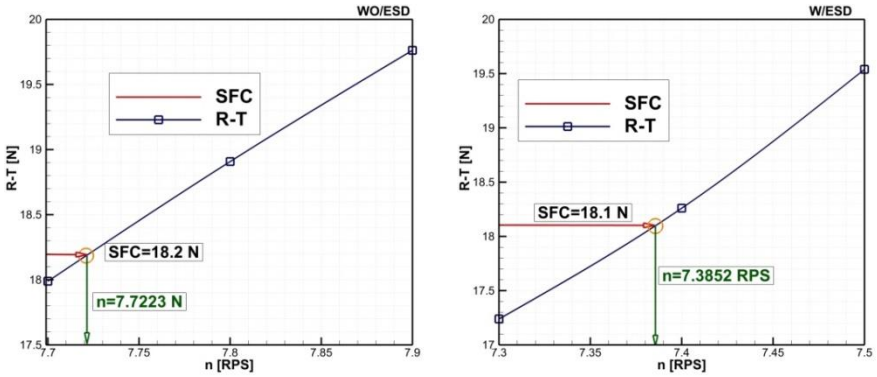

Figure 5.12 Results interpolation to predict the propeller rotation rate

Similar to the results obtained in the actuator disk simulation, the resistance, thrust, torque and advance coefficients are tabulated in Table 5.6. The results show a good agreement with the experimental data, the only deviation is observed for the thrust coefficient with an error within 6.9%, which can be considered slightly significant; nevertheless, this error can be enhanced by modifying the grid density. The other coefficients are constrained within a reasonable error range for both ship conditions with and without ESD.

Table 5.6 Self-propulsion coefficient for ship with and without ESD using sliding grid method

Coefficient	Without ESD			With ESD		
	EFD	CFD	|ε|%	EFD	CFD	|ε|%
Total resistance, C_T x10^3	4.811	4.913	2.12%	4.76	4.69	1.58%
Thrust, K_T	0.217	0.232	6.91%	0.233	0.243	4.16%
Torque, $10K_Q$	0.279	0.291	4.30%	0.295	0.306	3.72%
Advance ratio, J	0.410	0.414	0.98%	0.36	0.366	1.67%
Propeller rotation at self-propulsion point, n [rps]	7.8	7.7223	0.99%	7.5	7.3852	1.53%

The finest grid is used for the classic type of simulation, where the propeller rotation obtained in the tank is imposed in the simulation and the resistance, thrust and torque are recorded and compared to the EFD data. In addition to the simulation without rudder, in 2017 the rudder geometry was presented on the Workshop website [48]. This encouraged a further analysis to study the self-propulsion condition with the rudder for the ship without ESD, for simplification purposes. A special grid was generated for the rudder similar to the one for the ship without ESD to maintain the consistency if the results are to be compared. The number of grid cells for the ship with rudder case is 25.85 M cells, while the one without rudder is 24.846 M cells. Of course, the difference results from the rudder insertion in the domain.

To maintain the study within the same validation concept, the resistance, thrust and SFC factor are calculated for ship without rudder and compared to the EFD data. Then another comparison is made for the ship without and with rudder to study the influence of rudder on the self-propulsion simulation. The results obtained for ship without and with rudder are summarized in Table 5.7 showing that the results are in a good agreement with the EFD data with slightly over predicted forces and torque. Taking an insight to the influence of the rudder on the simulation, we can observe that the thrust in the case for ship with rudder is increased to 23.71 N compared to 23.09 for case without rudder, with a total gain in the propeller thrust within 2.68%. Similarly, the

torque in case with rudder is 0.608 N.m compared to 0.599 in case without rudder, with a total gain in propeller torque about 1.5%. Also, the hull resistance has increased with about 1.18%. This means that the rudder presence in the propeller wake is enhancing the propeller performance, since the gain in thrust is higher than the increase in resistance. Probably the reason behind this is that the rudder presence in the propeller wake tends to transfer a part of the tangential velocity component resulting from the propeller rotation into an axial component, which participates in the thrust increment. A further investigation could be useful here, taking into consideration the change in rudder geometry.

Table 5.7 Self-propulsion results for ship with and without rudder

Parameter		Without Rudder	With Rudder
Resistance, *R* [N]	EFD	40.83	N.A.
	CFD	41.47	41.96
	|ε|%	1.57	-
Thrust, *T* [N]	EFD	22.39	N.A.
	CFD	23.09	23.71
	|ε|%	3.18	-
SFC (*R*-*T*) [N]	EFD	18.2	N.A.
	CFD	17.88	18.25
	|ε|%	1.75	-
Torque, *Q* [N.m]	EFD	0.584	N.A.
	CFD	0.599	0.608
	|ε|%	2.57	-

To have a closer look on the flow in the propeller wake, two sections are proposed to compare the flow in the stern region at stations S4 and S7, as described earlier in Chapter IV. The streamwise velocity contours are compared with the EFD data and presented in Fig. 5.13, the comparison shows that the computed streamwise velocity contours are within a good correspondence with the experimental data.

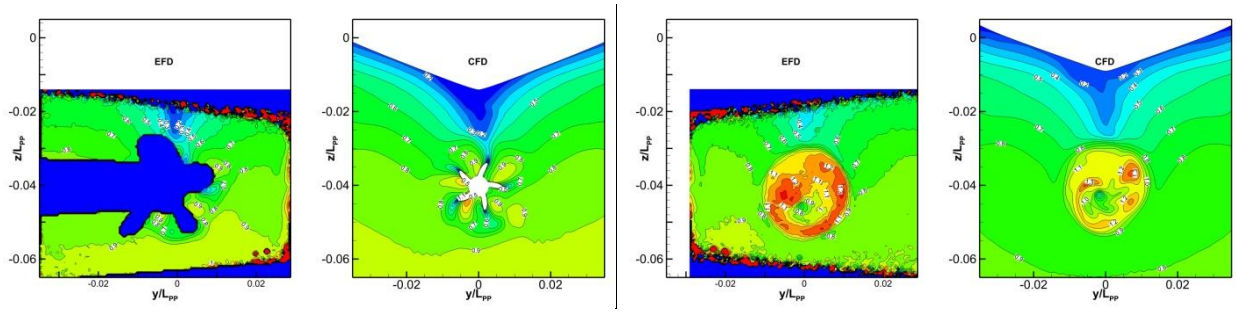

Figure 5.13 Comparison between the streamwise velocity contours measured and ship without ESD for sections S4 and S7

The contours also show the behavior of the flow in the wake, which reveals the vortices cores formation as they are originated from the propeller tip, root and hub; a fact that complies well with the description given in section 5.1.1.6. The symmetry of the flow downstream is not maintained around the ship centerline axis as a consequence for the propeller rotation. The cores of the vortices are dissipated slightly towards the ship portside, because the propeller is having a clockwise direction of rotation when visualized from stern to bow; i.e., the propeller rotates from

port to starboard direction. More details of the velocity contours at different section for ship with and without rudder is plotted Fig 5.14 along with the second invariant iso-contours of the vortices, in order to understand the mechanism of the generated vortices. The vortices formation is similar to the open water configuration.

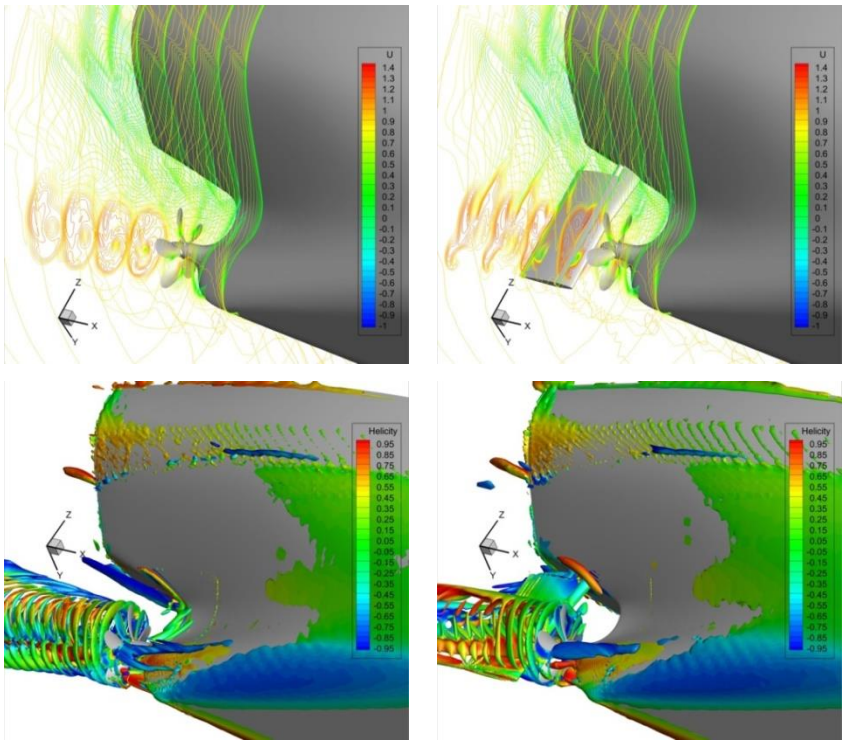

Figure 5.14 Comparison between the streamwise velocity contours for ship without ESD and the second invariant Q^*=50 for ship with and without rudder, computed using DES turbulence model

Having in sight the obtained results from the numerical simulation and the direct comparisons with the experimental data, it can be concluded that the CFD simulation can stand successfully for the propulsion simulation, whether for open water propeller simulation, nominal propeller flow prediction or when the propeller is connected to the hull. The body force and the discretized propeller methods both could predict accurately the propulsion performance from both, propulsion parameters and local flow analysis points of view. The body force method based on the actuator disk is simpler in implementation and faster in execution; however, it has some limitations regarding the absence of propeller blade loading and cavitation occurrence analysis. Despite all that, it is sufficiently accurate to stand for initial design purposes as a quick judgment tool, especially for optimization purposes. The fully discretized propeller can provide a proper solution for studying all the propulsion aspects; nevertheless, it comes with a significant cost and some complications in modeling and execution.

Finally, it is worth mentioning that the results reported in the previous sections have been partially or fully published in the conference paper by the author reported in [143, 144].

The next sections are covering the same simulation concept for open water propeller and self-propulsion simulation of the KVLCC2 ship model.

5.2 Propulsion Performance of the KVLCC2

Following the same principle in the previous study related to the propulsion performance of the JBC ship model, this continuous study is concerned with applying the same principles for predicting the propulsion performance of another ship type, though both hulls are within he category of large block coefficient ships. The KVLCC2 ship model as it was presented in the resistance simulation in Chapter IV is also investigated from the propulsion performance point of view. The open water simulation and self-propulsion is also assessed for ship with and without rudder, the difference in this case that there are available EFD data for the ship with rudder, which was retrieved and extracted from both; the Gothenburg 2010 Workshop [47] and the rigorous study reported in the thesis work in [145]. A comprehensive analysis is brought into focus for clarifying more details in the wake flow prediction, analysis of propeller performance in open water and behind the ship, in order to clarify the viscous flow mechanism in the propeller wake by imposing more complex turbulence models for open water condition and trying to the interaction between the ship hull, propeller and rudder.

5.2.1 Propulsion Performance in Open Water

The KVLCC2 model proposed by the INSEAN institute in Italy is equipped with four-blade conventional screw propeller known as E698 model with a diameter of 0.204 m. Comparing this propeller to the one analyzed for JBC ship model, this propeller is more skewed and has a symmetrical configuration, which make it easier to analyze from the symmetry point of view, and more complex from its steep skew perspective. The propeller and rudder details are tabulated in Table 5.8, while the propeller and rudder geometry were presented in Fig. 4.12 Chapter IV.

Table 5.8 Principal particulars of KVLCC2 E698 propeller model

Parameter	Value
Diameter, D_p [m]	0.204
Boss ratio, D_h/D_p	0.165
Pitch ratio, P/D_p	0.808
Expanded area ratio, A_E/A_0	0.448
Number of blades, Z	4
Direction of rotation	clockwise

5.2.1.1 Analysis Conditions

The open water simulation of the E698 propeller model corresponds to a tank test reported in the SIMMAN Workshop [146]. Similar approach like the one performed in the JBC propeller simulation is also repeated here. The flow velocity is kept constant at U=1.0 m/s, while the n is adapted accordingly to provide the corresponding advance ratio J within the range of 0.1~0.7 with step 0.1 in every simulation, resulting in total seven simulation cases.

5.2.1.2 Domain & Boundary Conditions

The domain and boundary conditions reported in the same simulation for the JBC hull still persist in this simulation, with the same dimensions and conditions on the boundaries and surfaces.

5.2.1.3 Computational Grids

Two grids were tested for simulation convergence and solution accuracy, the first has number of grid cells within 10.67 M and the second has 36.33 M cells, which is dedicated for the local flow assessment based on 5 turbulence models: the *SST k-ω*, EASM, DES, DDES and IDDES. The fine discretization grid is plotted in Fig 5.15.

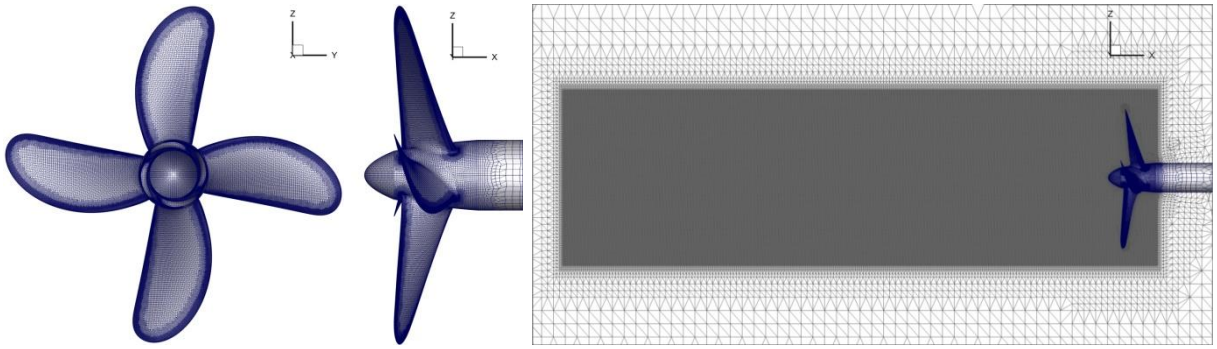

Figure 5.15 Mesh arrangement of the fine grid

5.2.1.4 Simulation Strategy

The simulation is performed for 8 seconds in each simulation case to ensure a sufficient convergence for the thrust and torque. The flow is accelerated in a quarter-sinusoidal wave pattern based on an unsteady approach for 2 minutes depending on the propeller rotational speed. Second order convergence criteria is applied with 5 nonlinear iterations, while the time step Δt is decided to provide 100 time-steps per propeller rotation according to the common practice from previous simulations based on the rotating frame approach, as proposed in the theoretical manual for the solver [110]. For the hybrid DES, DDES and IDDES, the simulation is performed based on the *SST k-ω* turbulence model for 6 seconds and then the turbulence model is switched to the hybrid models for 2 seconds. For IDDES, it was observed that the *k-ω SST*-2003 was also used to ensure better representation of the wake flow.

5.2.1.5 Thrust and Torque Results

The numerically obtained results for the thrust coefficient K_T and torque coefficients K_Q are plotted in Fig. 5.16 compared to the available EFD data. The obtained results show a good agreement with the experimental data, especially for the light loaded propeller condition when *J* value increases. The average error computed for all the thrust coefficient K_T divided on the seven simulation cases is within 0.87%, while the average error for the torque coefficients K_Q is within 1.42%. This again ensures the accuracy of the numerical simulation as it was concluded for the JBC propeller. The results presented are the one computed based on the EASM turbulence model, since it is the initial case simulation that was performed in the beginning of this study. The results for the other turbulence models are omitted since only three cases per each turbulent model were analyzed.

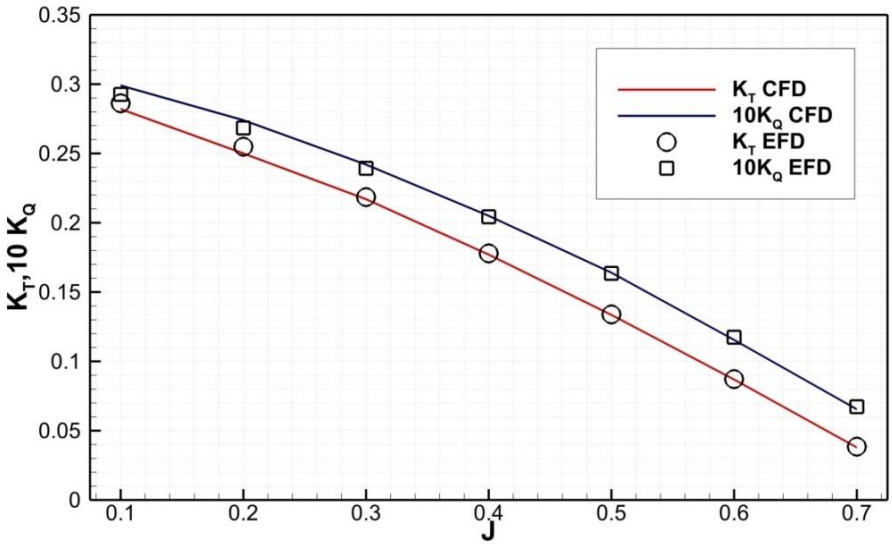

Figure 5.16 Open water propeller performance curves CFD results against EFD data

5.2.1.6 Local Flow Results

The local flow is computed for each advance speed only based on the EASM turbulence model. Three cases are calculated for comparison purpose based on the *SST k-ω* two equation model and the hybrid RANS/LES models DES, DDES and IDDES. The results are presented in the following section to have a close insight in the propeller wake, though it was neatly described in section 5.1.1.5 for the JBC propeller; yet, the flow is better captured in this case taking into consideration that the grid resolution for this simulation was enhanced to avoid the defects appeared in the previous simulation. The results are presented in the streamwise direction for the velocity and pressure distribution, turbulent kinetic energy, turbulent viscosity, vorticity and the second invariant. Confirming the vortical structure formation in the propeller wake, as described for the JBC propeller, Fig. 5.17 shows the magnitude of the vorticity computed for J=0.2 based on the IDDES turbulence model for the downstream flow. Both vector form and streamwise contours reveals the vortices cores that are originated at the propeller tip, root and hub. Those vortices concentration nodes are the traces of the helical formations crossing the symmetric plan y=0.

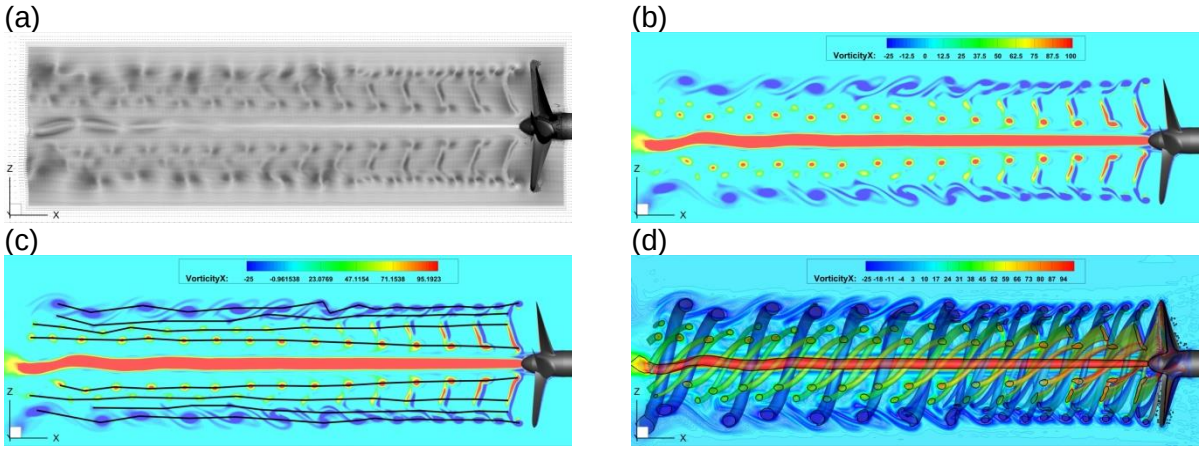

Figure 5.17 Vorticity at J=0.2: (a) vector form, (b) magnitude, (c) trajectory and (d) vortex cores

Similarly, the second invariant is presented in Fig. 5.18 for *J*=0.2 computed based on 5 turbulence models.

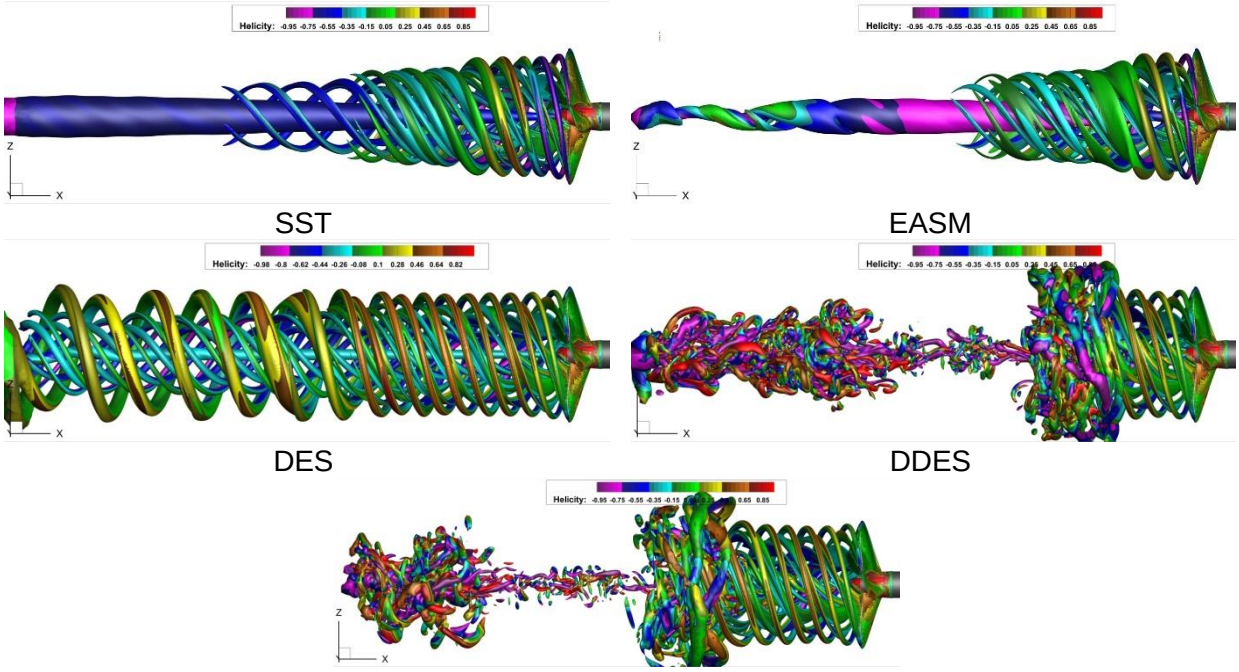

Figure 5.18 Second invariant computed for J=0.2 based on different turbulence models for iso-surface=500

Fig. 5.19 represent the velocity, pressure, turbulent viscosity and TKE distribution computed for *J*=0.2.

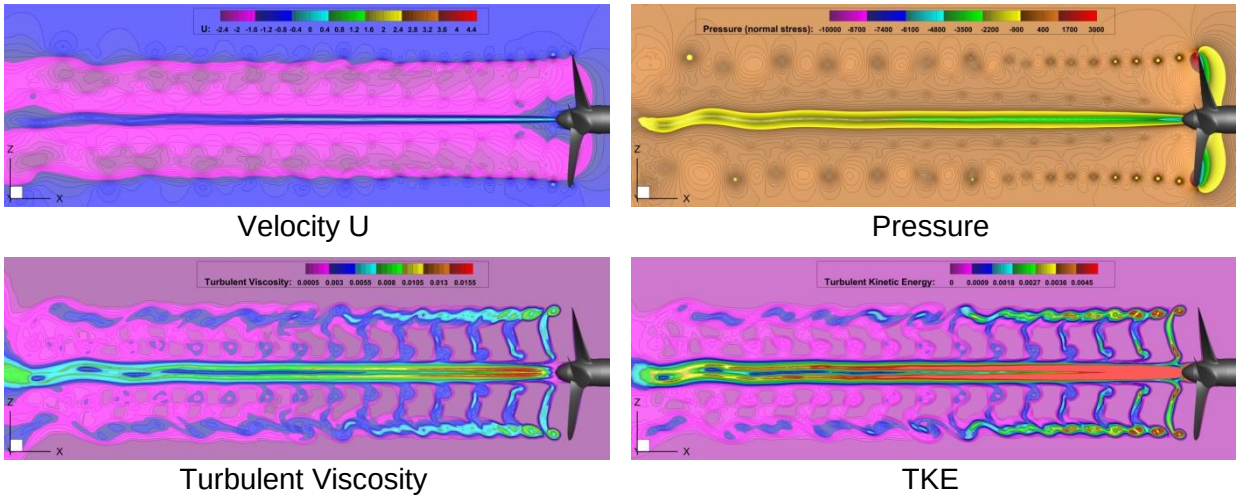

Figure 5.19 Flow characteristics computed for J=0.2 based on DDES turbulence model

Similarly, the second invariant is presented in Fig. 5.20 for *J*=0.4 computed based on 5 turbulence models.

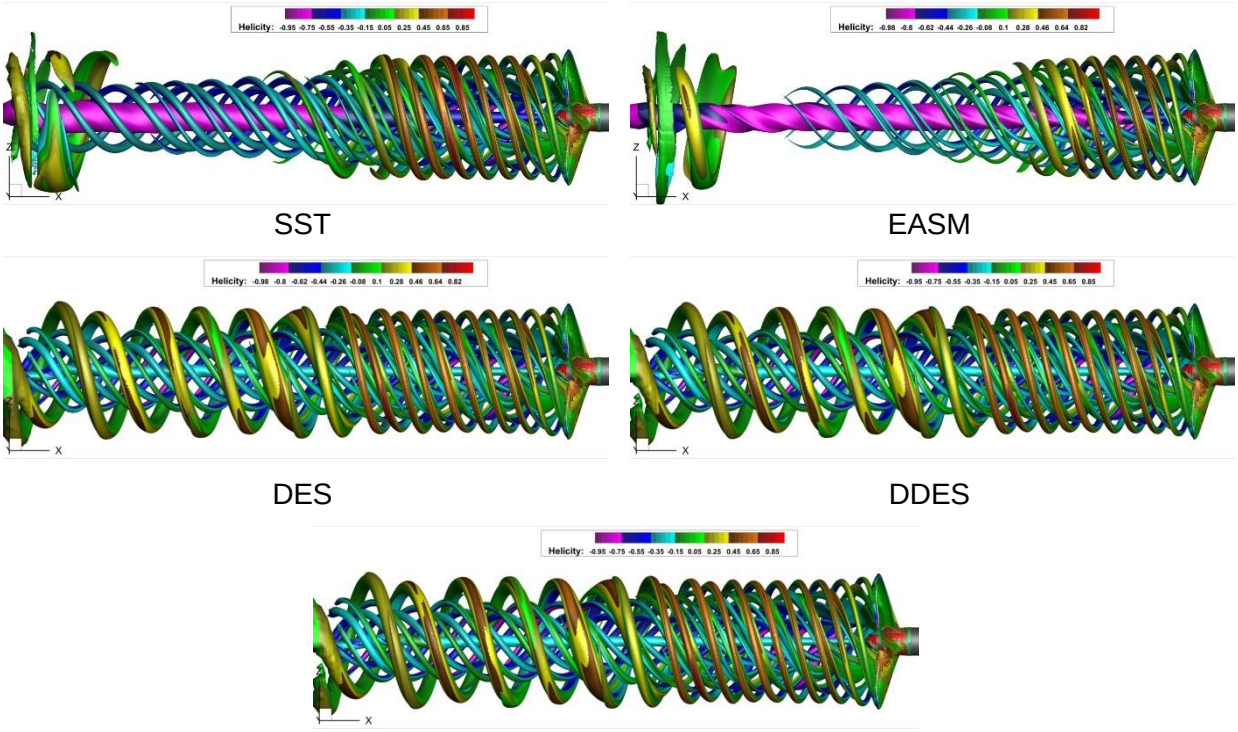

Figure 5.20 Second invariant computed for J=0.4 based on different turbulence models for iso-surface=250

Fig. 5.21 represent the velocity, pressure, turbulent viscosity and TKE distribution computed for *J*=0.4.

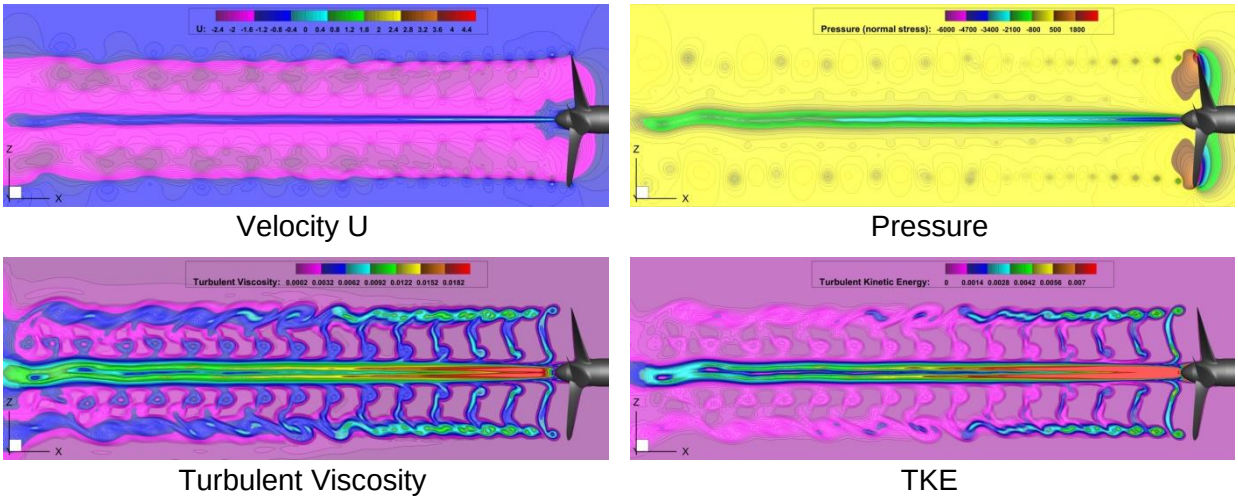

Figure 5.21 Flow characteristics computed for J=0.4 based on DDES turbulence model

Finally, the second invariant is presented in Fig. 5.22 for *J*=0.6 computed based on 5 turbulence models.

Fig. 5.23 represent the velocity, pressure, turbulent viscosity and TKE distribution computed for *J*=0.4.

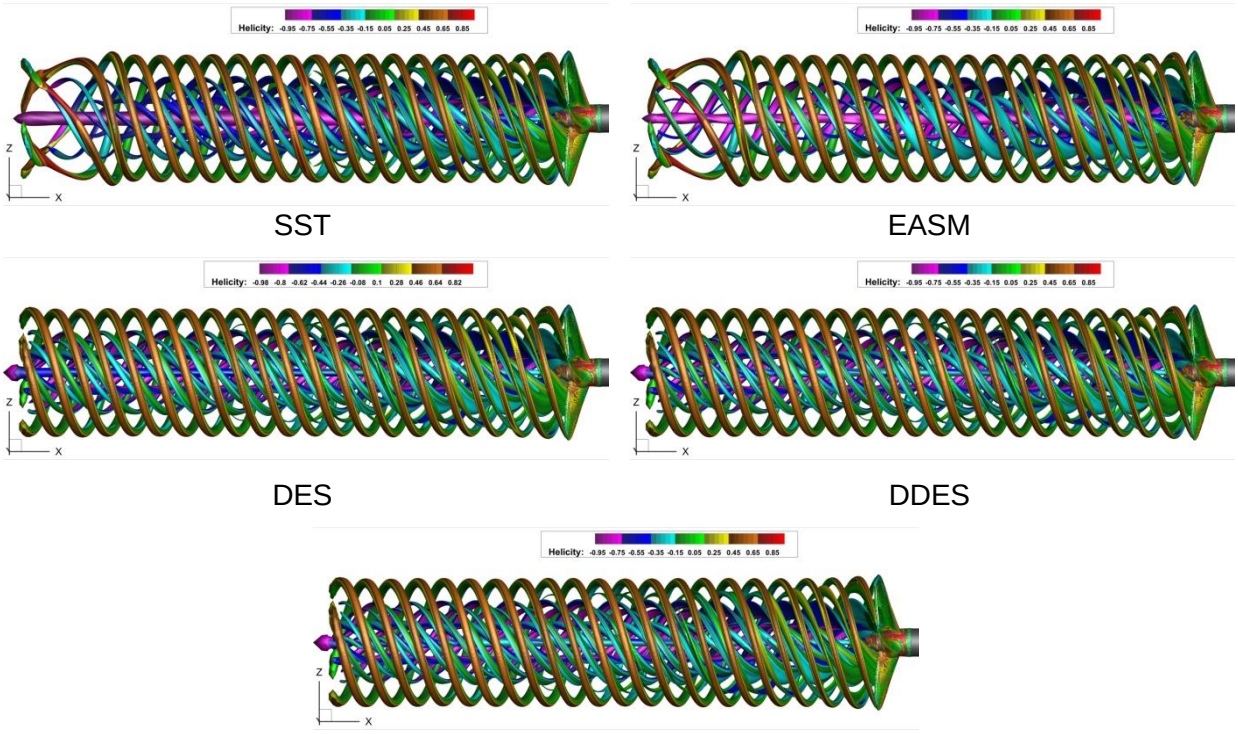

Figure 5.22 Second invariant computed for J=0.6 based on different turbulence models for iso-surface=125

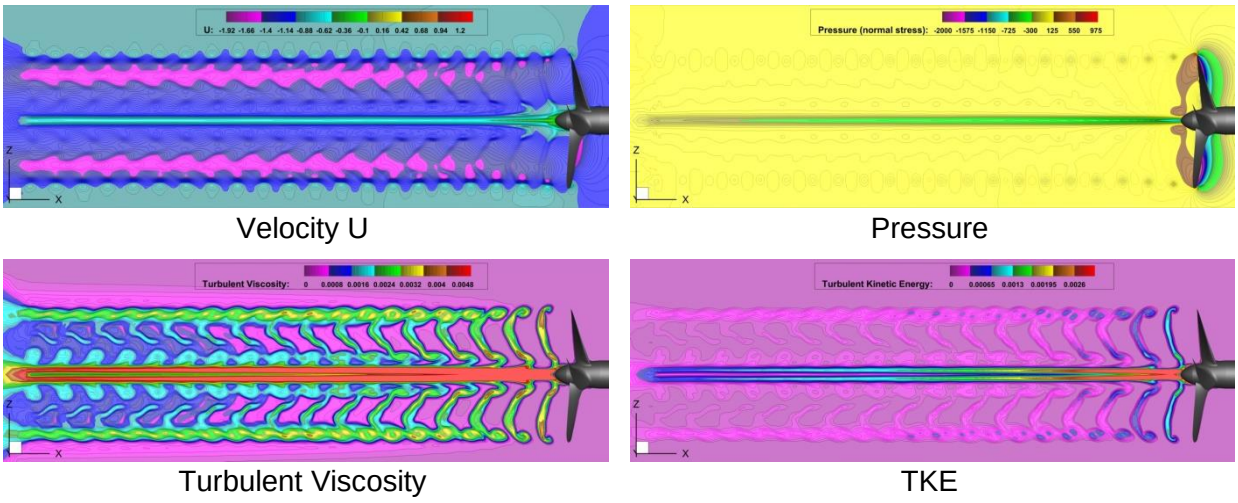

Figure 5.23 Flow characteristics computed for J=0.4 based on DDES turbulence model

Summing up, the results obtained for the open water performance of the KVLCC2 propeller model E698 are compatible with the same outcomes from the JBC propeller model, which was compared successfully against EFD results for both, propulsion coefficients and local flow analysis. The results here are more consistent since the problem with the grid that was highlighted in the JBC propeller simulation was resolved in this case. Similarly, the following sections will cover the self-propulsion performance of the KVLCC2 propeller.

Last but not the least, the results from this study were partially published in [135].

5.2.2 Self-Propulsion Performance

The same principle applied for the JBC ship is repeated here for the KVLCC2 ship model in order to compute the self-propulsion performance characteristics and local flow. The solution is achieved also by applying the body force method based on the actuator disk approach and the second is dedicated for the self-propulsion using a fully discretized propeller modeling based on the sliding grid technique.

5.2.2.1 Analysis Conditions

The ship is sailing in calm water at ship model speed U=1.179 m/s. corresponding to Froude number Fr=0.142. Both actuator disk and sliding grids approaches are applied similar to the previously mentioned simulation for the JBC.

5.2.2.2 Domain & Boundary Conditions

The domain and boundary conditions are identical to the same simulation performed for the JBC ship model.

5.2.2.3 Computational Grids

The analysis is performed for actuator disk approach based two different cases with respect to the rudder geometry as previously stated in Chapter IV; the rudder is either presented in a real form or simplified form. Both cases are tested to study its influence on the solution accuracy. For the fully discretized propeller, only the real rudder was used. It is also important to highlight the fact that the cad model for the propeller was modified to fit with the ship boss, because the reported propeller diameter from the INSEAN model was causing a gap between the propeller boss and ship boss. For this reason, the propeller diameter was reduced to eliminate the gap. This definitely may affect seriously the self-propulsion point prediction for the hull. However, as a principle, the simulation was performed regardless of the expected discrepancy. The details for the simulation grids are tabulated in Table 5.9. While the grid configuration for both approaches is depicted in Fig. 5.24.

Table 5.9 Computational grids for the self-propulsion simulation

Computational Grid	Actuator Disk Method			Sliding Grid Method	
	Without Rudder	Simplified rudder	Actual Rudder	Without Rudder	With Rudder
Number of grid cells x10^6	17.78	20.21	21.58	23.70	27.82

5.2.2.4 Simulation Strategy

Both methods are performed corresponding to the same details explained for the JBC ship model. For the actuator disk model, two simulations are performed to obtain the nominal ship wake, and then the effective ship wake is computed based on the open water data that was provided from the test results reported in [146]. For the sliding grid technique, five simulations with different propeller rotation starting from n=8, then increased to 10, 13, 14 and finally 15 rps to achieve the self-propulsion conditions for the ship where the thrust equals the resistance. The simulation with rudder, only three propeller rotations were used n=13, 14 and 15 rps.

5.2.2.5 Thrust and Torque Results

The thrust and torque coefficients are calculated based on the actuator disk approach are summarized in Table 5.10 compared to the EFD data extracted from the data reported in [145].

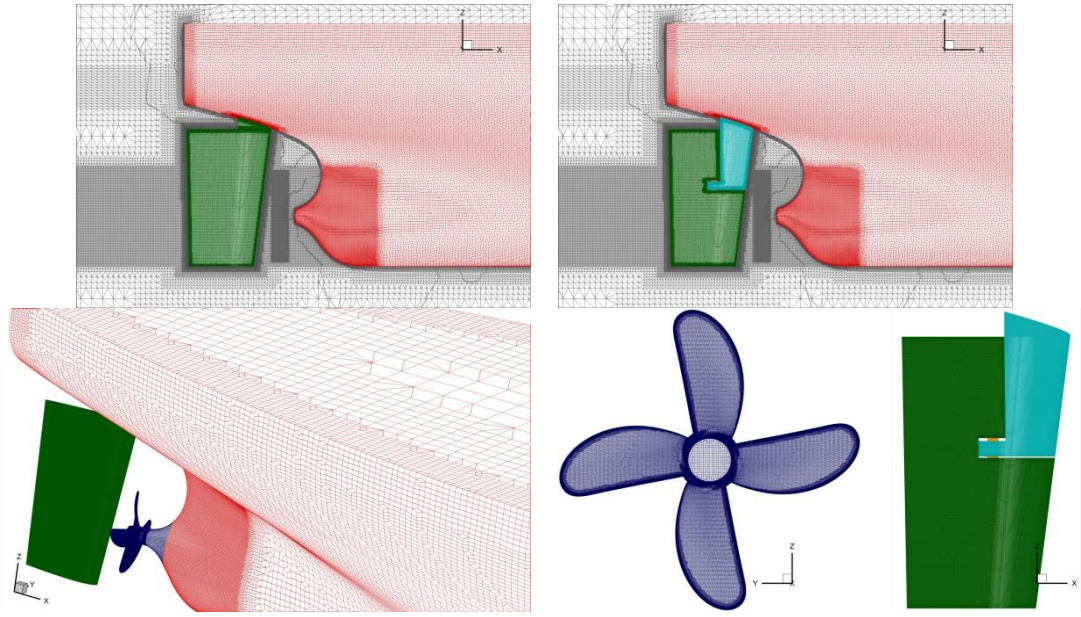

Figure 5.24 Grid geometry for actuator disk approach (top) and fully discretized propeller (bottom) highlighting the propeller and rudder

The results show a good agreement with the experimental data with an error range between 1.61% and 13.27%. The maximum error is recorded for the torque coefficient of the bare hull ship. Similar significant error for the same case was reported in the study reported in [145] where the EFD data are imported from. The solver was used in that study was the CFDShip-Iowa, which is considered as one of the strongest solvers in the ship hydrodynamics field. For this reason, apparently the error is related to the EFD data provided for the open water test that was used for comparing the nominal and effective wake in the actuator disk model.

Table 5.10 Thrust and torque coefficients computed using the actuator disk method compared to the EFD data extracted from [145]

Parameter	Bare hull			With simplified rudder			With actual rudder		
	EFD	CFD	$\|\varepsilon\|$%	EFD	CFD	$\|\varepsilon\|$%	EFD	CFD	$\|\varepsilon\|$%
Thrust coefficient, K_T	0.195	0.1983	1.69	0.198	0.208	5.05	0.198	0.2022	2.12
Torque coefficient, $10K_Q$	0.266	0.2307	13.27	0.228	0.2357	3.37	0.228	0.2307	1.18

The quantitative assessment of the resistance and thrust forces obtained with the sliding grid technique is summarized in Table 5.11 and plotted in Fig. 5.25 showing the different simulations performed based on changing the propeller rotation and the corresponding thrust and drag. The interpolation is performed to achieve the self-propulsion point of the hull without and with rudder. The rotation rate from the experiment for the bare hull is reported as n=10 rps; however the obtained results from the numerical simulations for both cases with and without

rudder are slightly ove 14 rps. The reason behind this deviation is related to the change in the propeller dimensions such that it can fit in place with the ship boss.

Table 5.11 Interpolation of the propeller rotation based on resistance and thrust results

Parameter		Rotation rate, *n* [rps]	Resistance, *R* [N]	Thrust, *T* [N]
Without Rudder	Computed	13	41.874	33.789
		14	41.931	40.291
		15	43.09	46.938
	Interpolated	14.27	42.44	42.44
With Rudder	Computed	13	45.084	36.612
		14	46.116	42.948
		15	47.244	49.907
	Interpolated	14.55	46.79	46.79

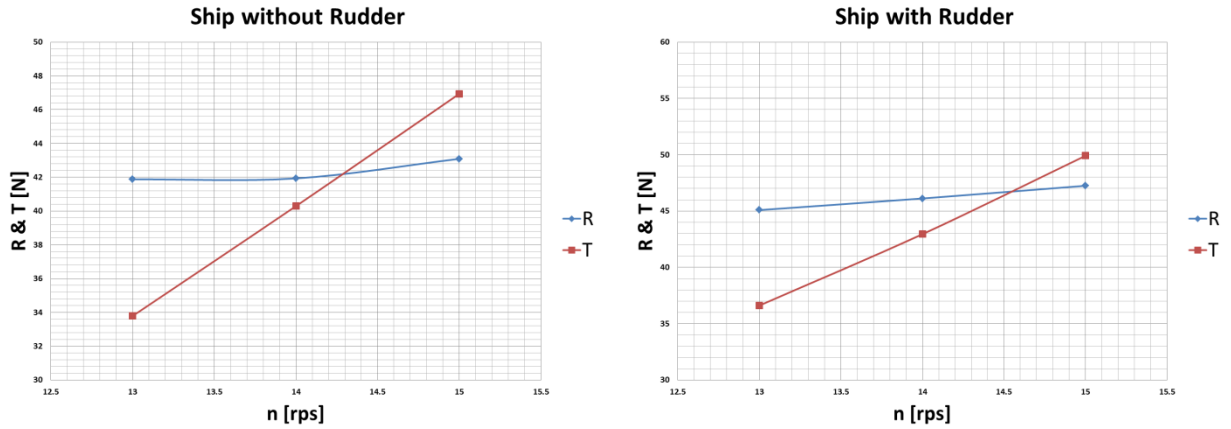

Figure 5.25 Prediction of the self-propulsion point using interpolation method

5.2.2.6 Local Flow Results

To ensure a proper prediction of the effective wake in the self-propulsion simulation, the predicted flow in the downstream is presented for two sections located at the aft perpendicular where x/L_{pp}=1.0 and slightly further downstream at x/L_{pp}=1.025. The CFD results compared to the EFD data at both section are represented in Fig. 5.26. The obtained results as well as the EFD measures can give an indication about the hull, propeller and rudder interaction where the flow is divided in two segments due to the presence of the rudder. Looking from the stern towards the bow, it is known that the propeller rotates in the clockwise direction; this results in position change in the velocity contours, pushing the portside contours upwards and the starboard side contours downward. This was also observed for the JBC ship model; nevertheless, there were no validation data to extract a solid conclusion regarding this flow behavior.

Finally, the interaction between hull and propeller from the vortical formation point of view is shown in Fig 5.27 showing strong vortices that rise from the actuator disk rotation at the disk tip. The flow separation from the bilge also persists in the wake forming the two flow separations, which are transferred downstream due to the actuator disk suction effect. As the flow is accelerated by the actuator disk rotation, the rudder tip causes strong vortex formation originated at the lower tip of the rudder leading edge, resulting in two vortices, a short and less intense one on top of the rudder lower tip, and another stronger one underneath.

These results have been published in [135].

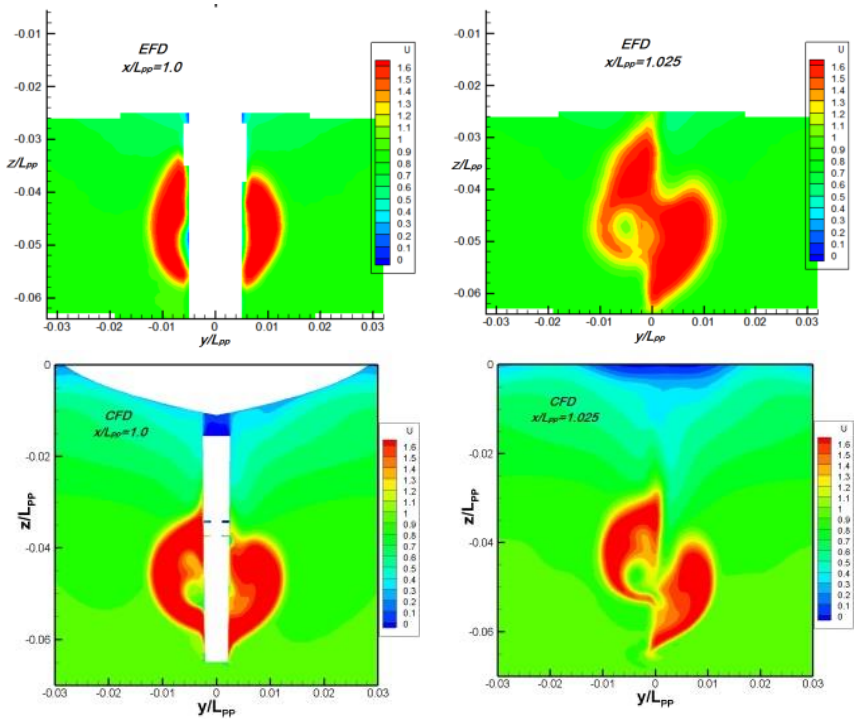

Figure 5.26 Streamwise velocity contours comparison between CFD and EFD [22]

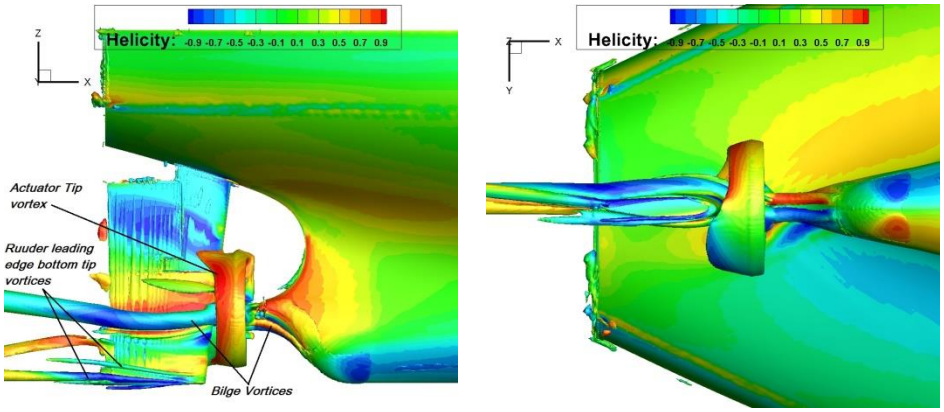

Figure 5.27 Vortices formation in the wake showing the profile and bottom view

Reviewing the scope of this study and the results discussed in this chapter, it can be said that the CFD method for self-propulsion simulation performed reliably, and the results obtained are very promising to be used for further simulation regarding powering estimation and hull, propeller rudder interaction investigations. Both actuator disk method and fully discretized propeller can be applied successfully in this domain to predict accurately ship propulsion performance.

The following chapter is concerned with the study of ship seakeeping performance in waves with special focus on regular waves, from the physical modeling point of view, and the target is as usual to predict ship motions, free-surface and local flow in different seakeeping aspects.

This page is intentionally left blank.

Chapter VI
Ship Seakeeping Performance

Studying ship hydrodynamic performance in wave comes with great importance from multiple perspectives. For example, considering ship motions in waves, potential hazards can result from severe motions, which may have negative effects on the ship stability, safety, survivability and finally working operations on board, if green water phenomena occur. Handling the problem from the ship powering point of view, it is very important to estimate the added resistance in waves to provide sufficient power margin to overcome the drag resulting from sailing in waves.

The most popular methods for predicting the seakeeping performance include the experimental method, potential methods and most recently, the CFD method. Like all the other fields in ship hydrodynamics, the experimental method stands as the most accurate and reliable, yet it is very complex and expensive to perform. Potential methods have always been and basically still the workhorse of seakeeping performance prediction method; nevertheless, the absence of viscous effect imposes several problems, especially for roll motion, for example. CFD recently took the lead in ship hydrodynamic performance for seakeeping applications, thanks to the significant development in computational resources; because it is well known that CFD method in seakeeping applications requires significant simulation time. Beside its capability in predicting the forces acting on the hull and calculating accurately ship responses in waves, CFD can provide more details regarding the local flow in the vicinity of the ship especially in the propeller wake zone, which may have a consequence on the propulsion performance, as described in Chapter V. In general, seakeeping problems can be handled either in regular waves or in a seaway with irregular waves. The first is the most common, as it is easier to execute, while the latter is more complex and requires very significant simulation resources and time. That is why it is still within the development stage in CFD applications that can be found nowadays.

From this perspective, the study proposed in this section is concerned with predicting the seakeeping performance of the DTMB ship model in regular waves, more specifically, regular head waves to study the ship responses in waves from two major aspects. The first is to cover the diffraction condition when the ship is sailing in waves with all the degrees of freedom blocked. The target is to capture the acting forces and moments on the hull. The second is when the ship is in a diffraction condition with two degrees of freedom regarding the vertical motions, i.e., heave and pitch. Taking into consideration the aforementioned aspects concerning the capability of the CFD to predict the viscous flow configuration in roll motion, a special study dedicated for the ship performance in roll decay case is presented in the last section of this chapter. Both studies for ship vertical motions assessment in waves and roll decay prediction will include a thorough analysis for the free-surface prediction and local flow analysis, as it was presented for resistance and propulsion performance prediction in Chapters IV and V. The results for both simulations are computed and validated against the experimental data available in the public domain, in order to highlight the efficiency of the numerical simulation performed in each case.

6.1 Seakeeping Performance in Regular Head Waves

The seakeeping performance of the DTMB ship model in head waves is analyzed and presented for two cases; wave diffraction and wave radiation. All the numerical results obtained in both cases are validated compared to the experimental results reported in [87, 130].

6.1.1 Seakeeping in Wave Diffraction Condition

In this simulation, the ship is sailing in regular sinusoidal head waves with no degrees of freedom, i. e. all the motions are restricted. The main scope is to analyze the forces, free-surface and flow features in the ship domain. The ship model used in this simulation is the DTMB surface combatant whose geometry and principal dimensions were presented in Chapter IV.

6.1.1.1 Analysis Conditions

The simulation conditions correspond to the test case proposed in the G2010 Workshop under the case number 3.5, where the ship is sailing in regular head wave. Prior to describing the main simulation parameters, the wave theory and formulation should be introduced first.

In order describe a wave, some parameters have to be explained such as; wave length λ, period *T*, amplitude A, wave number *k* such that $k = 2\pi/\lambda$, circular frequency ω, where $\omega = 2\pi/T$. Also, the wave steepness *Ak* is used to describe the wave, since it represents a ratio between t wave amplitude and wavelength according to the formula

$$Ak = 2\pi A/\lambda \tag{6.1}$$

Wave frequency and ship encounter frequency can be, respectively, expressed as

$$\begin{aligned} f_w &= \sqrt{g/2\pi\lambda} \\ f_e &= f_w + U/\lambda \end{aligned} \tag{6.2}$$

where *U* represents the ship velocity. Correspondingly, encounter time is defined as $T_e = 1/\ f_e$. For an incident wave height ζ_I, considering a time reference marked at the ship F.P., wave height can be expressed according to the formula

$$\zeta_I(t) = \frac{A}{L_{PP}}\cos(2\pi f_e t + \gamma_I) \tag{6.3}$$

where γ_I stands for the initial phase, such that, $\gamma_I = 0$ when wave crest coincides with the F.P.

Since all the results in waves are expected to gain the same response from the initial source as a sinusoidal behaviour with respect to time, the estimated parameters should be subjected to a Fourier series to analyse the time history of the simulation parameter, such as total resistance coefficient C_T, heave coefficient C_H and pitch moment coefficient C_M. For this reason, the Fourier series representation of a general $P(t)$ is given by the equaions

$$\begin{aligned} P(t) &= \frac{P_0}{2} + \sum_{n=1}^{N}\cos(2\pi f_e t + \Delta\gamma_n) \\ \Delta\gamma_n &= \gamma_n - \gamma_I \\ a_n &= \frac{2}{T}\int_0^T P(t)\cos(2\pi f_e t)\,dt \\ b_n &= \frac{2}{T}\int_0^T P(t)\sin(2\pi f_e t)\,dt \\ P_n &= \sqrt{a^2 + b^2} \end{aligned} \tag{6.4}$$

$$\gamma_n = \tan^{-1}\left(-\frac{b_n}{a_n}\right)$$

Where P_n represents the nth harmonic amplitude, while γ_n stands for the nth phase.

Correlating the simulation conditions as described in case 3.5 from G2010 [47] with respect to the wave steepness *Ak.* Table 6.1 summarises simulation conditions and corresponding wave characteristics.

Table 6.1 Simulation conditions and corresponding wave parameters

Wave Parameter	*Ak* [-]	λ [m]	H_w [m]	*T* [s]	f_w [Hz]	T_e [s]	f_e [Hz]
Value	0.025 0.050 0.075	4.572	0.03638 0.07276 0.10914	1.711	0.584	1.088	0.919

6.1.1.2 Domain & Boundary Conditions

The domain has a prism geometry whose length in *x*-direction is 7.0L_{ref}, where L_{ref} is selected as the maximum value between wavelength and L_{PP}. The domain section is extended in *y*-direction for 2.0L_{ref} and 6.0L_{ref} in *z*-direction, as it can be observed in Fig. 6.1. Since the ship is sailing in head waves with only the heave and pitch considered in the simulation, A symmetry boundary condition is applied at the centerline plane of the ship, with only half ship introduced in the simulation to reduce the simulation cost and effort. At the upstream, the wave generator is applied two times away from the F.P. at the inlet boundary. A second order Stokes wave with the simulation parameters is introduced. It is advised that the distance between the inlet boundary and forward perpendicular should be sufficient to provide be at least two wave lengths before encountering the ship.

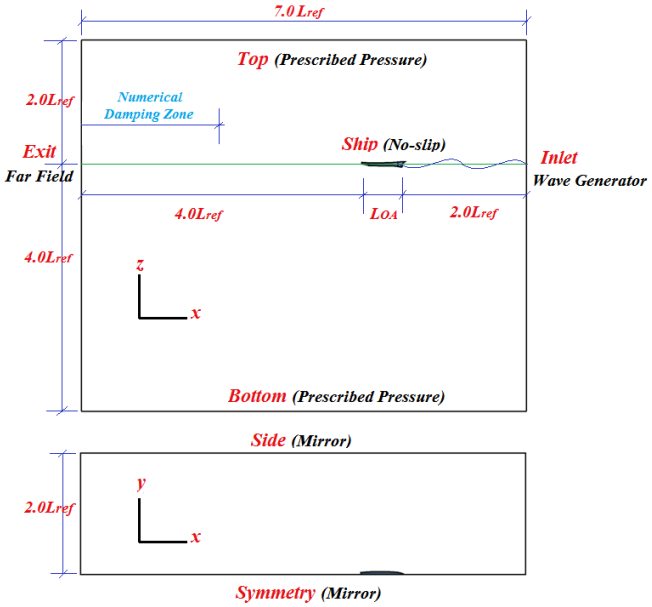

Figure 6.1 Domain geometry, dimensions and boundary conditions

The top boundary is above the none-disturbed free-surface level with 2.0L_{ref}, while the bottom boundary is 4.0L_{ref} below that level. Side boundary is also located at 2.0L_{ref} from the ship centerline. A symmetry condition is also chosen for the side boundary to mitigate the wave reflections. Downstream, the outlet boundary is located at a distance 4.0L_{ref}; the first half of that

distance is used for wave capturing, while the last half is called the numerical damping zone which is divided in two zones. In the first zone, the grid size in x and y-directions is increased by a factor of 4, while the cell size in the last zone close to exit is increased with a factor of 8 to provide sufficient damping for the wave to not reflect from the exit boundary.

6.1.1.3 Computational Grids

The grid in seakeeping simulations requires special treatment especially at the free-surface zone, to ensure a good quality of the obtained results. Here, the whole free-surface is refined with a refinement box extended in the entire domain and its height is $3.0H_w$. This refinement box is split into four zones; the first starts at the inlet and is extended at $1.0L_{ref}$ behind the ship to capture the wave correctly, and the hull-wave interaction. The cell size in that zone should provide sufficient density to capture the wave details, theoretically in x- and y-directions, the cell size should be chosen to provide at least 60 cells/wave length. An extra Kelvin pattern refinement zone was added at the free-surface region close to the hull with cell size refinement criteria that provides 100 cells / λ, to capture the sharpness of the free-surface and wave breaking effect if it happens. The second zone is called the damping relaxation zone which is extended between 1.0 and $2.0L_{ref}$ astern the ship, cell size in this case is two times the initial cell size in x- and y-directions. The third and fourth have been described earlier for the numerical damping zone, with cell size in in x- and y-directions is 4 and 8 times the initial cell size in the horizontal direction. For a consistency purpose, the cell size in the vertical direction is chosen to be $H_w/20$ for all the 4 zones. Special box refinements are added at the bow and stern to capture the interaction with the wave and possible greening effect, if exists. The grid configuration for fore, aft regions and a longitudinal section are presented in Fig. 6.2.

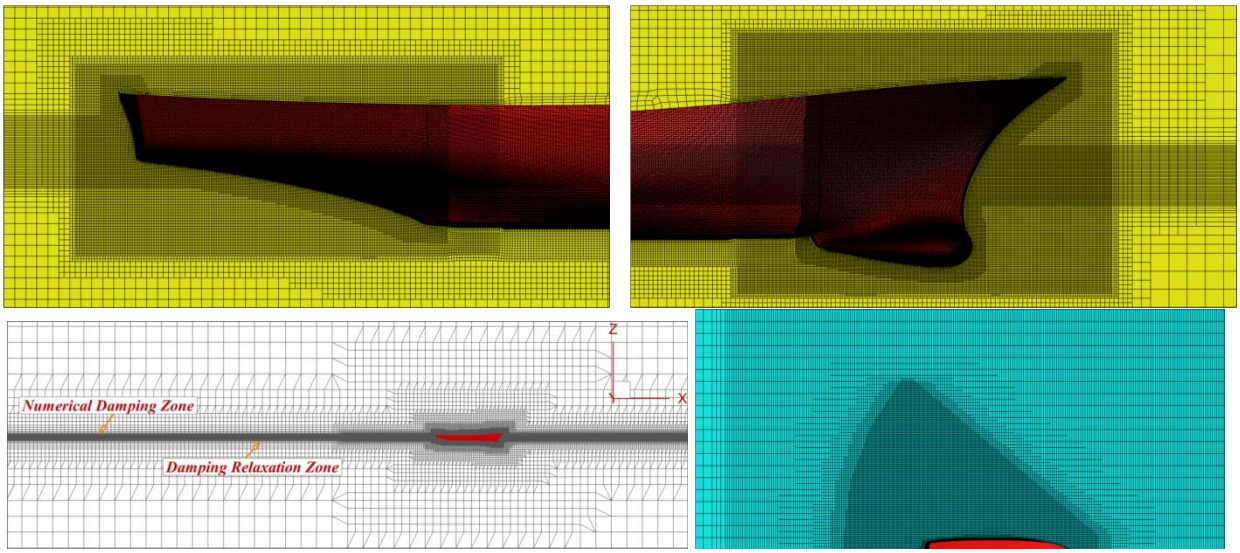

Figure 6.2 Grid configuration showing: stern, bow, longitudinal section free-surface top view

Three grids are generated to study the effect of the grids on the accuracy of the numerical results. The numbers of grid cells are 6.21, 8.186 and 14.39 M cells. The first two grids are chosen for the forces comparison, while the finest one is chosen for local flow and free-surface prediction to ensure sufficient resolution to capture the flow details.

6.1.1.4 Simulation Strategy

Unsteady simulations are performed until the ship encounters 15 consecutive waves to ensure sufficient convergence, or until the numerical residuals are sufficiently reduced. The discretization in time is made to provide 150 time-steps/ wave period for wave fixed ship condition, and 200~250 time-steps for motion condition. Integration in time is imposed with fourth order convergence criteria, combined upwind and central schemes with 12~20 nonlinear iterations are used. All the simulations are performed on HPC concept with available resources for this simulation of 120 cores and 128 GB of RAM at1.6 GHz. Physical simulation time is recorded within 28 and 268 hours, depending on the grid resolution and simulation time.

6.1.1.5 Resistance, Forces and Moments Results

Case 3.5 proposed in the G2010 Workshop was basically a speed diffraction problem with no degrees of freedom available for the ship. In this case, the results are concerned with the forces acting on the hull for resistance, heave and pitch. For this reason, the results obtained in the CFD simulation is compared with the EFD data provided from the workshop in [47] and represented in Table 6.2 and Fig. 6.3.

Table 6.2 Computed versus measured C_T, C_H, C_M coefficients

Variables	*Resistance (C_T)*		*Heave (C_H)*		Pitch (C_M)	
	0^{th} Amplitude	1^{st} Amplitude	0^{th} Amplitude	1^{st} Amplitude	0^{th} Amplitude	1^{st} Amplitude
EFD [47]	0.00462	0.00608	-0.0334	0.0357	-6.08×10^{-4}	0.0108
CFD	0.00447	0.00664	-0.0242	0.0422	-6.84×10^{-4}	0.0119
$\|\varepsilon\|$%	3.25	9.21	27.55	18.21	12.50	10.19

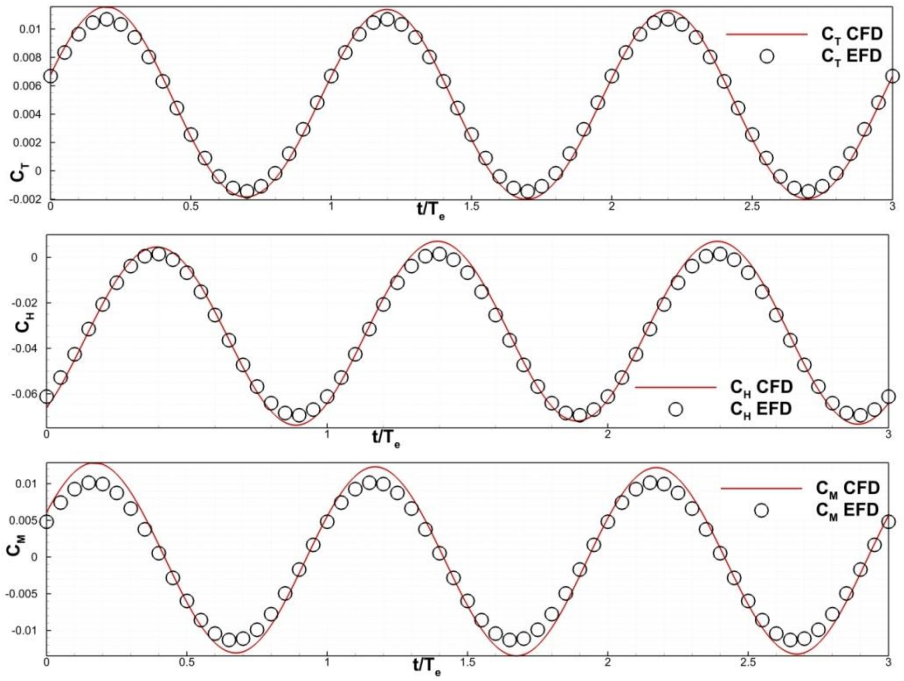

Figure 6.3 Resistance C_T, Heave C_H and Pitch C_M coefficients compared to EFD [47]

For the 0th harmonic, the results resemble well for the resistance coefficient. On the other hand, the results for heave and pitch coefficients recorded a significant deviation compared the EFD dat. The error is up to 27.5% for heave 0th amplitude and 12.5 for pitch moment coefficient. However, it is worth mentioning that in the Workshop, the results had also significant discrepancies for heave and pitch coefficients similar like the values obtained in this study, so the results are within the Workshop range.

In order to study the effect of the grid on the numerical results, a comparison between the three grids is performed and presented in Fig. 6.4 showing that the coarser grid tends to slightly over predict the resistance coefficient compared to the finest grid. The difference in resistance amplitude between the coarse and fine grid is about 1.64% while between the medium and fine is about 1.07%.

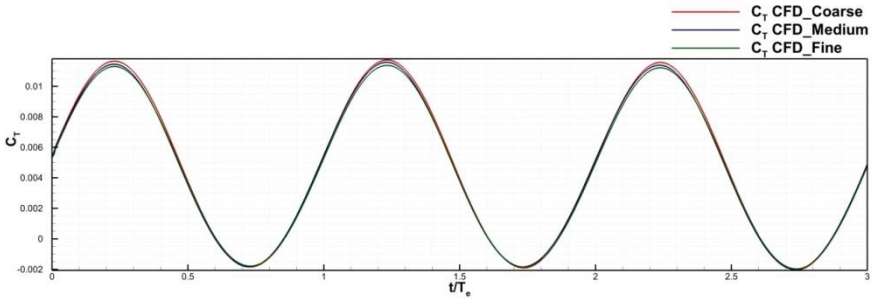

Figure 6.4 Grid resolution effect on the total resistance coefficient

The effect of wave height shows that the resistance average value is changing according to the wave steepness can be observed in Fig. 6.5; where at wave steepness *Ak*=0.025, the C_T=0.00454, while in case when *Ak*=0.050, the C_T=0.00506, and finally at *Ak* = 0.075, C_T = 0.005903, with a total increase of the resistance within 11 and 30%, respectively. This might give a clue about the added resistance in wave which might vary according to these values up to 20%, which is a significant value that should be taken into consideration.

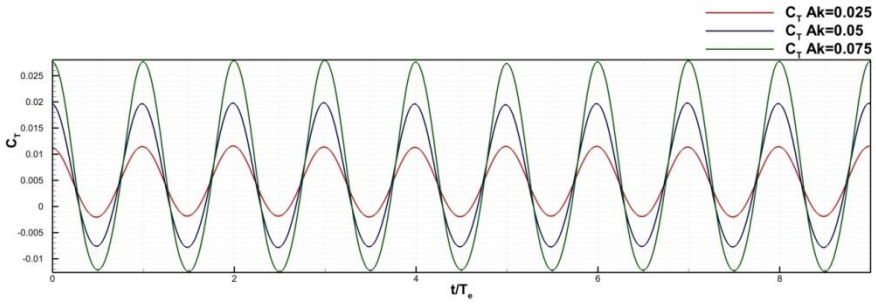

Figure 6.5 Comparison between the time history of the total resistance based on wave steepness for *Ak* = 0.025, 0.050 and 0.075

6.1.1.6 Free-Surface Results

The free-surface prediction is performed and compared with the available EFD results in [86, 87] only for the speed diffraction problem at *Ak*=0.025. The results are given at the wave quartering period as it is illustrated in Fig. 6.6. Four different instants of wave encounter are denoted with t/T=0 when the wave crest coincides with the F.P., t/T=0.25 when the wave point between crest and trough is at the F.P., t/T=0.5 when the trough is positioned at the F.P, and finally, t/T=0.75 at the mid-distance between trough and crest in the following wave profile, as it can be observed in Fig. 6.6.

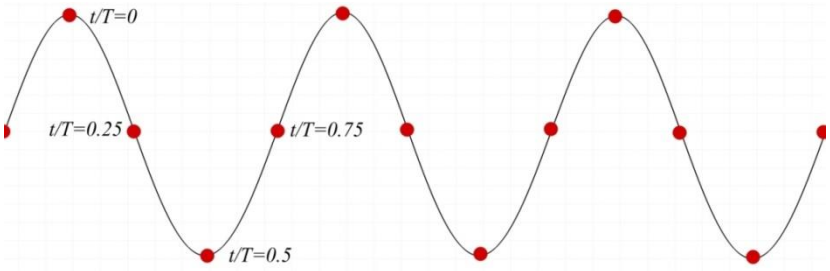

Figure 6.6 Schematic diagram for the quartering wave instants corresponding to the encountering moment with the F.P. of the ship

The free-surface comparison presented in Fig. 6.7 shows that qualitatively and quantitatively, the computed free-surface is within a good agreement with the experimental results. However, it is worth mentioning that the free-surface elevation is slightly under predicted in the region away from the hull. Near to the hull region, the agreement between CFD and EFD is encouraging. This is related to the existence of the Kelvin batter refinement, which seems to be sufficient with 100 cell/wave length. Yet, for coarser grids, the free-surface was under predicted.

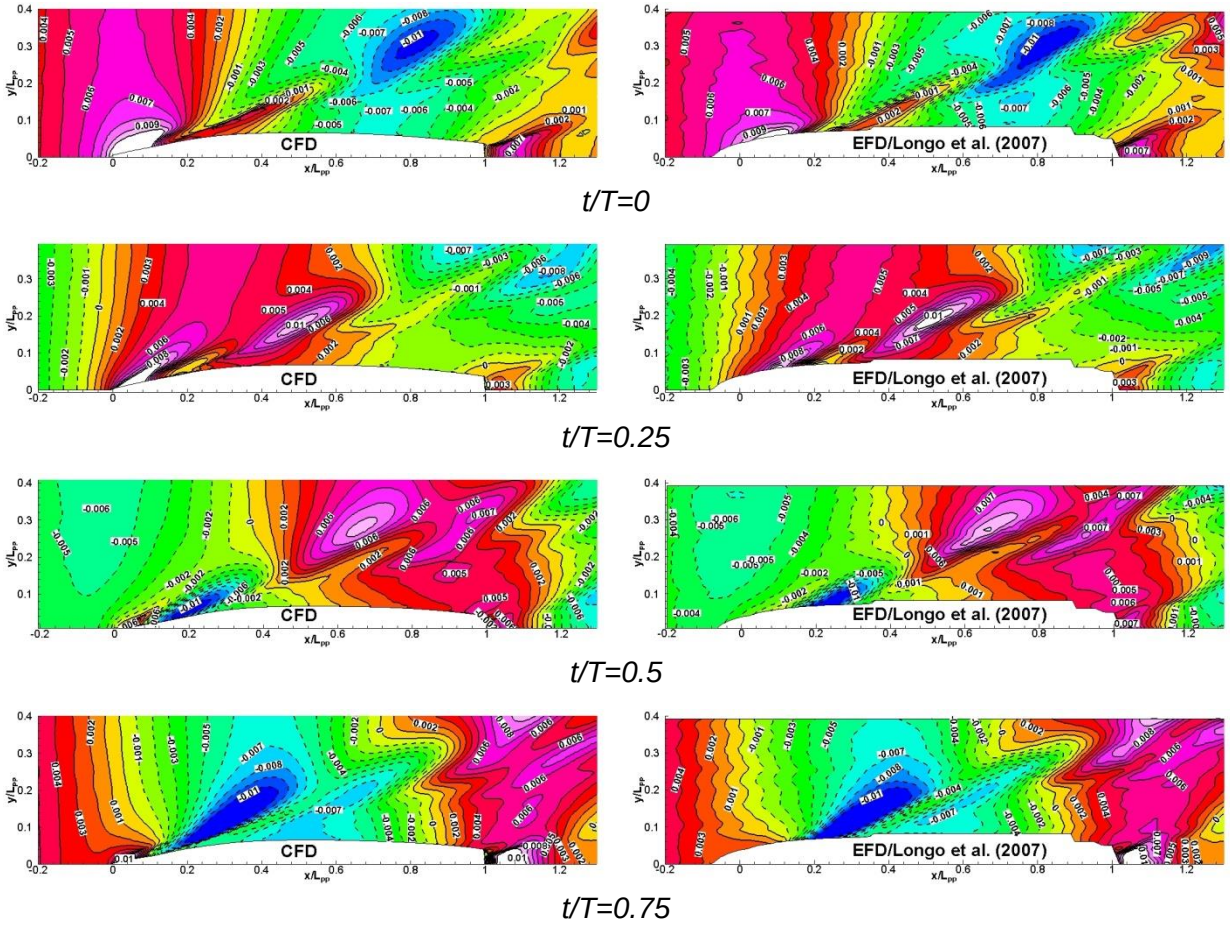

Figure 6.7 Computed free-surface at four wave quarters compared EFD [47, 87]

Taking advantage of the VOF method, which is famous to capture the breaking wave effect, the wave breaking is analyzed for the maximum wave steepness *Ak*=0.075. This analysis is crucially important, from one perspective; it is well known that the breaking waves can influence significantly the added resistance in waves. Also, it is necessary to understand the hull-wave

interaction during the breaking effect. Another important reason is also to visualize the greening effect to keep the problem under control by increasing the flare height, or imposing any other design aspect that can prevent this phenomenon from happening. The wave-hull interaction is investigated at the four quarters of the wave encounters as noticed Fig. 6.8. The breaking phenomenon is well illustrated at the fore and aft of the ship, especially at *t/T*=0, when the hull is encountering the wave crest. The separation effect is happening at the fore peak, while a rooster-tail separating takes place immediately after the transom stern. This separating effect at the stern differs slightly at various moments for wave encounter; yet, it can be observed, as it was also the case in calm water, that the transom remains dry during all the wave encounter moments.

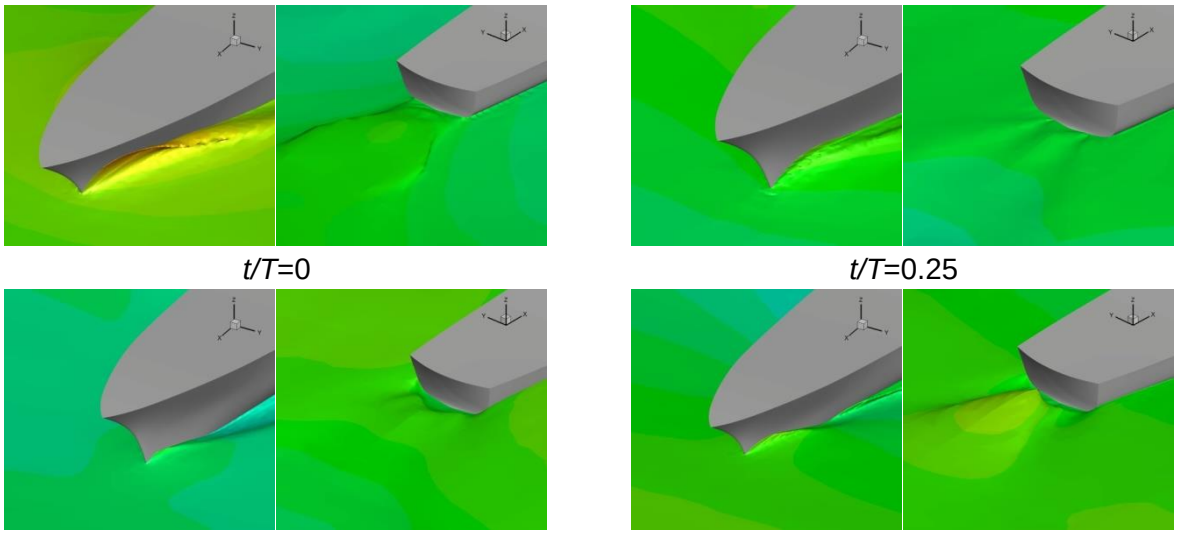

t/T=0 *t/T*=0.25

t/T=0.5 *t/T*=0.75

Figure 6.8 Wave visualisation at the bow and stern of the ship for *Ak=0.075* at different encountering instants

The free-surface configuration and also the mass fraction are illustrated in Fig. 6.9 showing the interaction between the hull and wave. The mass fraction for the highest wave shows that the wave height at the fore peak is very close to green the deck. Increasing the wave height more than this value might cause a green water phenomenon on the deck. The aforementioned dry transom can also be observed in the mass fraction representation.

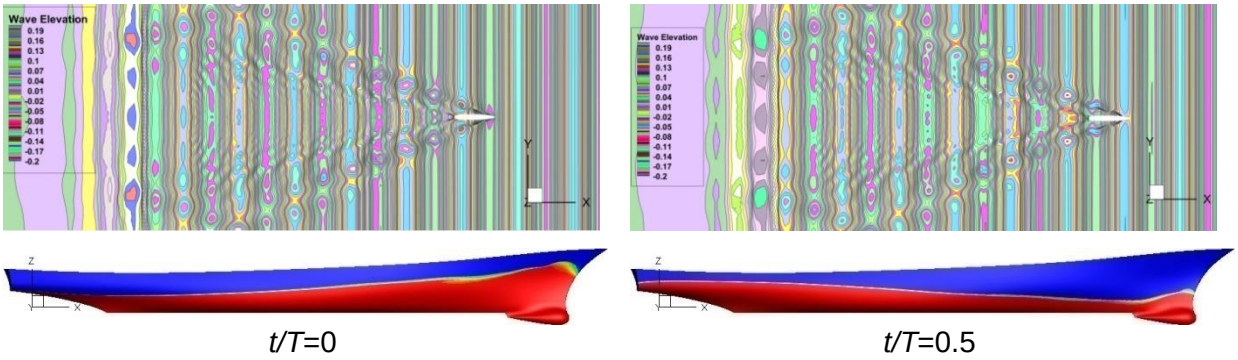

t/T=0 *t/T*=0.5

Figure 6.9 Wave profile and mass fraction for *Ak=0.075* when the peak and trough encounter F.P., from left to right, respectively

6.1.1.7 Local Flow prediction

Although it is more important to investigate the local flow in the free motion condition, it is important to investigate the accuracy of the solver in predicting the local flow in seakeeping simulation. Thus, the result obtained in the numerical simulation is compared with the available EFD data at the propeller lateral section positioned at x/L_{PP}=0.935 from the F.P. The streamwise velocity contours in x-direction is plotted against the EFD data in Fig. 6.10, showing that the results resemble well compared to the EFD data. The only thing to notice is that the boundary layer seems to be slightly contracted towards the ship hull closer to the centerline and expanded on the ship side. The CFD results obtained in this study are similar to the results obtained in the G2010 workshop.

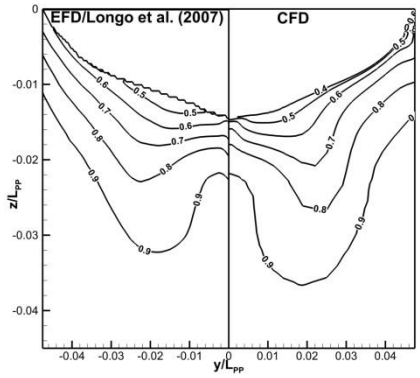

Figure 6.10 Relative velocity contours at x/L_{PP}=0.935 and t t/T=0 compared to EFD [47, 130]

The development of the flow around the hull based on the previously mentioned comparison is depicted in Fig. 6.11 for Ak=0.025, 0.050 and 0.075, respectively.

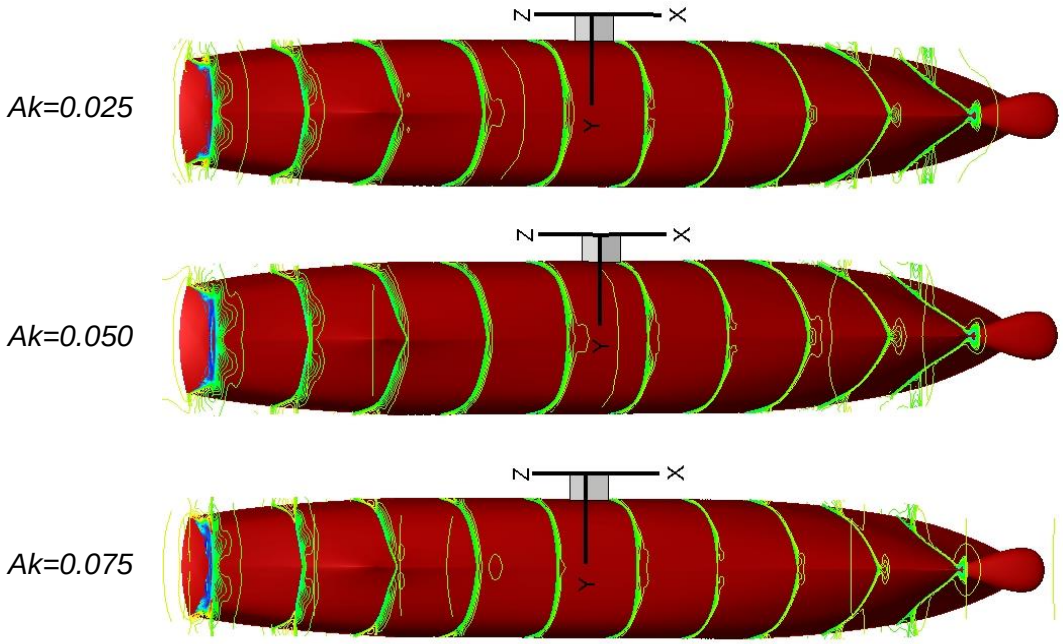

Figure 6.11 Streamwise velocity contours for different wave steepness

Ten different sections are selected at distance $\Delta x/L_{pp}$=0.1 to study the development of the streamwise velocity along the entire hull. The streamwise velocity contours shows the

development of the axial velocity distribution along the hull revealing the formation of the vortices. The initiation of the vortices starts at sonar dome, which is similar to the vortices generated in the calm water condition. This vortex vanishes downstream due to the viscous dissipation. Two different vortices are generated due to the separation at the rise of the stern having a symmetrical pattern port and starboard. The flow separation at the stern causes three different set of vortices, the one developed by the stern rise, the transom wave interaction and finally the shoulders interaction with the free-surface. It is worth mentioning that the intensity of the vortices is varying according to the wave height as it can be observed in Fig. 6.10. More discussion regarding the vortices formations is covered in local flow analysis in the motion condition.

6.1.2 Seakeeping in Wave Radiation Condition

In this simulation condition, the ship is free to heave and pitch. Total resistance and ship responses are important to be taken into consideration is this study. The target is to analyse the total resistance in wave and to attempt to correlate it to the total resistance in the calm water condition to extract the added resistance in wave. As for the ship motions, ship responses have very significant importance, because it might impose a direct or indirect impact on ship safety and operability.

6.1.2.1 Analysis Conditions

The simulation conditions are divided in this case into four major categories, as it is listed in Table 6.3. The first is dedicated for the Verification and Validation (V&V) of the obtained results to study the numerical uncertainties from the grid and time step influence point of view. For this purpose, four geometrically similar discretization grids are generated with a grid refinement ratio $r_G \cong 1.5$.

Table 6.3 Simulation cases parameters and corresponding grid density

Simulation cases	λ/L_{PP}	*Ak*	*Fr*	Grid density (x10^6)
a. V&V study				
C1	1.5	0.025	0.28	3.1, 4.8,7.2, 10.3
b. Response and added resistance in waves based on λ				
C2-C8	0.50	0.025	0.28	6.5
	0.75			6.3
	1.00			2.9
	1.25			2.6
	1.50			3.1
	1.75			3.9
	2.00			2.9
c. Zero Speed				
C9-C10	1.5	0.025 & 0.050	0	2.6
d. Free-surface & Wake Flow				
C11-C12	1.50	0.025	0.28 & 0.41	14.4

The second simulation cases category is concerned with ship responses, represented by Response Amplitude Operator (RAO) and added resistance C_{aw}, corresponding to the change in wavelength. The third is more like a station keeping simulation, where the ship velocity is set to

zero. This study is crucially important for some applications, such as in offshore activities and floating units in general. The last case is focusing on the free-surface and local flow analysis.

6.1.2.2 Domain & Boundary Conditions

The domain dimensions, configuration, boundary conditions are the same like the one used for diffraction condition.

6.1.2.3 Computational Grids

To keep the consistency of the numerical solution at different simulation conditions, same grid generation parameters are maintained for the spatial discretization of the simulation of each case. The resulting difference in the simulation grid is influenced by the length and amplitude of the wave. The full details of the grid resolution have been represented in Table 6.3.

6.1.2.4 Simulation Strategy

The same criteria used for the fixed ship condition is repeated in this case, except for the number of nonlinear iterations are increased to 20 iterations/time step. For the grid convergence study, two conditions applied to control the influence of grid and time step on the numerical solution. The first is to simulate all the computational grids with the same time step, to study only the influence of the grid on the ultimate solution. The second is dedicated for changing the time step consequently by reducing the time step in half for every simulation.

6.1.2.5 Results

Depending on the simulation case scope, the results are obtained for every case and validated with the experimental results, if exist. The following subsections will cover every case individually focusing on the obtained results and their validation outcomes.

- ***Case1: Verification and Validation***

The Richardson Extrapolation method is used to assess the numerical uncertainties for the grid and time step influence on the solution accuracy. For this purpose, four systematically refined grids with a grid refinement ratio $r_G \cong 1.5$, while for the time step, a time step refinement ratio is chosen as $r_T=2.0$, starting with a time step $\Delta t=0.006845$ s, which corresponds to 250 time-steps/wave period. This value is reduced by half gradually until it reached $\Delta t=0.000856$ s, which corresponds to 2000 time-steps/wave period. It is worth mentioning that this simulation is very time consuming, especially for the finest time step; thus, after the solution became periodic, which is usually reached after 5~8 wave encounters, only 3 encounters were recorded and presented to reduce the simulation time.

The results for the total ship resistance coefficient computed in waves based on the grid convergence study is plotted in Fig. 6.12, where M1 is used to define the fines grid and M4 is used to define the coarsest.

On the other hand, the quantitative representation of the numerical results based on the grid convergence study is presented in Table 6.4. The results obtained for the four grids have a monotonic convergence. The estimated error compared with the EFD data extracted from [86] is within 2.76 and 6.1% for the finest and coarsest grids, respectively. Comparing the obtained data in this study with the one reported in [86], the correspondence between the values obtained in this study compared to the reported results in their research is very close, even though the solver they

used is different and the grid resolution is also not the same. This reveals that the simulation performed in this study is correct.

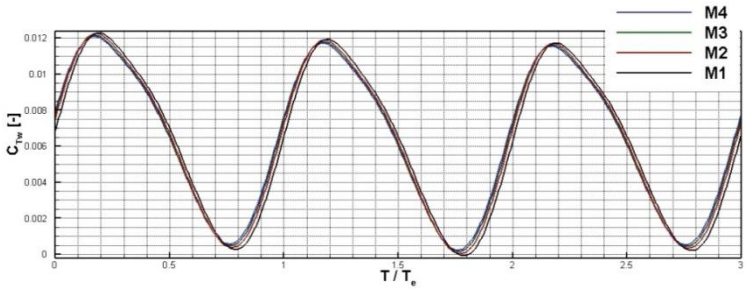

Figure 6.12 Total resistance coefficient C_{TW} computed based on grid convergence study for C1

Table 6.4 Grid convergence parameter for the total resistance coefficient in wave $C_{Tw\text{-}G}$

Grid Convergence	EFD C_{Tw} (x10^{-3}) [86]	C_{TwG} (x10^{-3})	$\|\varepsilon\|$%D	R_G	p_G	U_G (%S1)
M1	5.78	5.62	2.76	0.75	1.26	1.26
M2		5.59	3.28			
M3		5.54	4.15	0.03	4.01	
M4		5.28	6.10			

As for the time step convergence study the results are tabulated in Table 6.5, showing that the results seem to dissipate far from the as the time step is refined, but the solution is still having a monotonic trend. Besides, an asymptotic range is reached for the time step $T1$, $T2$ and $T3$, so the excess refinement is unnecessary, since the solution is time independent in that range of time-steps/wave period. This also could be observed in the uncertainty for the time step analysis as it is within 0.06, thus it has minor influence.

Table 6.5 Time step convergence parameter for the total resistance coefficient in wave $C_{Tw\text{-}T}$

Time Step Convergence	EFD C_{Tw} (x10^{-3}) [86]	C_{TwT} (x10^{-3})	$\|\varepsilon\|$%D	R_T	p_T	U_T (%S1)
$T1$	5.78	5.286	8.55	0.75	0.42	0.06
$T2$		5.289	8.49			
$T3$		5.293	8.42	0.30	5.09	
$T4$		5.429	6.1			

In order to analyze the heave and pitch results in the non-dimensional form, the transfer function (TF) or Response Amplitude Operator (RAO), which represent the ratio between the amplitude of the ship response to the wave amplitude. The TF terms can be defined for heave and pitch motion according to the following equations

$$TF_{x_3} = \frac{A_{x_3}}{A}$$
$$TF_{x_5} = \frac{A_{x_5}}{Ak} \quad (6.5)$$

where A_{x_3} and A_{x_5} represent respectively, the heave and pitch amplitudes.

The time history for the heave response is represented in Fig. 6.13 showing the change in heave amplitude based on the change of the grid density. As it can be observed that for the coarsest grids the amplitude is higher than the amplitude for the finest grid.

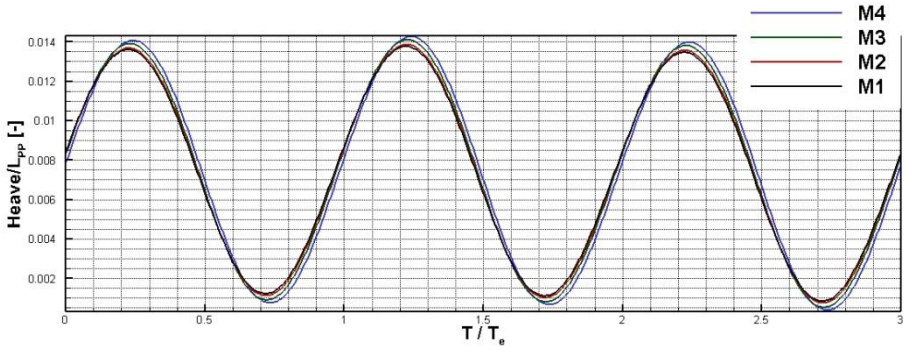

Figure 6.13 Heave response computed based on the grid convergence study for C1

The heave convergence parameters computed based on grid and time step are represented in Tables 6.6 and 6.7, respectively. Both tables reveal that the as the grid or time step are refined, the solution is having a descending trend. Monotonic convergence is achieved for all the simulation, whether based on grid or time step convergence criteria.

Table 6.6 Grid convergence parameter for the heave response

Grid Convergence	EFD Heave *TF* [87]	*TF* Heave	$\|\varepsilon\|\%D$	R_G	p_G	U_G *(%S1)*
M1	0.966	0.983	1.80	0.4	2.26	0.75
M2		0.987	2.25			
M3		0.999	3.39	0.48	1.83	
M4		1.022	5.78			

For the heave time step convergence study, it is observed that the closest solution to the EFD results is at the third time step *T*3, which is closer to the coarsest one. Though it sounds contradictory; yet the descending trend of the solution makes it logic from that perspective, as the solution is monotonic and is reduced as the time step is refined. Finally, the difference between the heave responses for the two finest grids is inconsiderable; apparently the solution is time independent after 500 time-steps/wave period. It is also very important to notice that the combination between grid and time step can really enhance the numerical results.

Table 6.7 Time step convergence parameter for the heave response

Time Step Convergence	EFD Heave *TF* [87]	*TF* Heave	$\|\varepsilon\|\%D$	R_T	p_T	U_T *(%S1)*
*T*1	0.966	0.959	0.70	0.67	0.58	-0.35
*T*2		0.961	0.47			
*T*3		0.965	0.13	0.06	4.11	
*T*4		1.022	5.78			

Similarly, the pitch time history is plotted in Fig. 6.14 and the convergence parameters for the pitch response are tabulated in Tables 6.8 and 6.9. Conflicting with the results obtained for heave response, the coarser grid gets the lowest value while the finest grid results in the highest value for the pitch amplitude. This might result from the grid density nearby the fore and aft regions

in the ship, since it is known theoretic that a coarser grid damps the wave amplitude, which results under predicted.

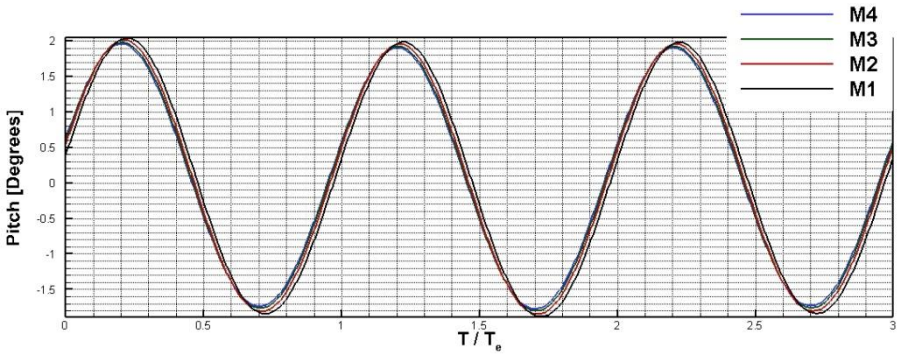

Figure 6.14 Pitch response computed based on the grid convergence study for C1

The qualitative results for the grid and time step convergence study reveal a significant error close to 11%, which is considered quite significant for this simulation. It is necessary to study the behavior of the pitch response maybe with other ship to understand the reason behind this deviation.

Table 6.8 Grid convergence parameter for the pitch response

Grid Convergence	EFD Pitch *TF* [87]	*TF* Pitch	$\|\varepsilon\|\%D$	R_G	p_G	U_G *(%S1)*
M1	1.05	1.164	10.89	0.52	1.63	0.6
M2		1.161	10.64			
M3		1.157	10.15	0.63	1.14	
M4		1.148	9.24			

The same conclusions regarding the time step effect for the total ship resistance coefficient in wave and heave response is still applicable here for the pitch response dependence on the time step change. The results seem to reach an asymptotic range after a certain range of time step/wave period.

Table 6.9 Time step convergence parameter for the pitch response

Time Step Convergence	EFD Pitch *TF* [87]	*TF* Pitch	$\|\varepsilon\|\%D$	R_T	p_T	U_T *(%S1)*
*T*1	0.966	1.1501	9.53	0.61	0.72	0.06
*T*2		1.1497	9.50			
*T*3		1.1492	9.45	0.82	0.28	
*T*4		1.148	9.24			

For all the convergence studies, whether grid or time step, the variation between the finest three solutions is considerably insignificant; this consequently reduces the estimated uncertainty values for grid and time step U_G and U_T, respectively. Validation results are summarized in Table 6.10, which shows that the average error computed for the four grids or time-steps exceeds significantly the U_V level, i.e., $|\varepsilon|_{av} >> U_V$, this means that validation is not achieved.

Overall, the results for the computed resistance in waves and heave response are within a very encouraging agreement with the experimental results. Nevertheless, the pitch response is having a significant discrepancy compared to the measured values in the experiment. This

requires a special investigation, preferably on a different ship type, to understand the reason for this deviation. One possible cause for this significant discrepancy might be correlated to an error in computing inertia matrix, which is made automatically by the solver. This investigation was performed by the author for the KVLCC2 ship model at different wave lengths and published in [147]. The results from this study are presented in Appendix c to keep this chapter in control from the contents point of view.

Table 6.10 Validation parameter for resistance in wave, heave and pitch in C1

Parameter	*EFD*	$\|\varepsilon\|_{av}$ *%D*	U_D	U_{SN} *%D*	U_V *%D*
C_{Tw}	5.76	5.98	1.02	1.25	1.62
TF Heave	0.966	2.54	1.02	0.75	1.32
TF Pitch	1.05	9.83	1.02	0.64	1.20

- ***Case 2–8: Ship Responses and Added Resistance In Waves C_{aw} Based On Wave Length λ***

To have a deeper insight in the influence of the wave parameters on the added resistance and ship responses, the wavelength is adapted to create seven simulation cases C2~C8 with a wavelength starting from λ=0.5 L_{pp} up to 2.0 L_{pp} with a change in step in every case Δλ=0.25 L_{pp}, whereas the wave steepness *Ak* is kept unchanged at *Ak*=0.025.

Added resistance plays a particularly important role in predicting the powering performance of the ship, as previously explained in the chapter preface. For this reason, it is very important to be investigated and analysed in this study. For this reason, the total resistance coefficient in wave C_{Tw} is computed for every case to be used in comparison with the total resistance coefficient in calm water C_{Tcw}. Having both information in hand, the added resistance coefficient in wave can simply be extracted from both values as it is proposed in [148] by subtracting the 0th harmonic of the total drag in wave C_{Tw}, then subtracting the calm water drag C_{Tcw}, and the resulting value is the added resistance in wave C_{AW}. A similar representation for the procedure is presented in Fig. 6.15.

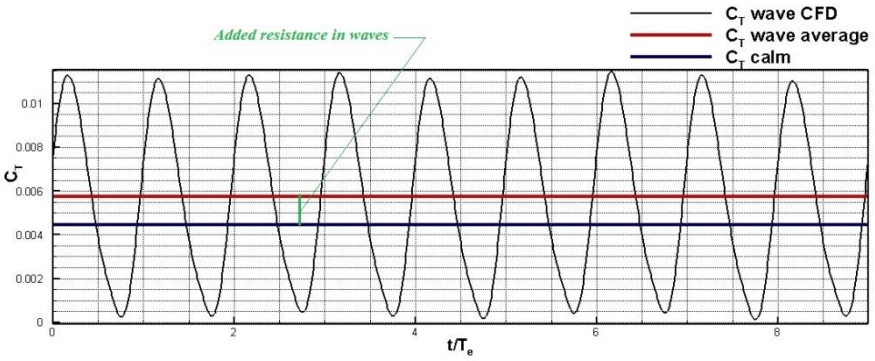

Figure 6.15 Added resistance in wave schematic representation

The calculations for the added resistance coefficient in waves C_{AW} are presented in Table 6.11. The computed calm water resistance coefficient C_{Tcw}=0.00425, which can be subtracted from the values of the total resistance coefficient in calm water C_{AW} to give the added resistance in waves C_{aw}, as previously explained. This has resulted in an increase of total resistance in waves compared to that computed in calm water with a range between 8.1% and 39.2%. This range is very considerable, and now it can be clear the fact that this value might impose a substantial change in the powering prediction. As expected, results obtained near the resonance condition impose the highest resistance addition. There is also a recognised

unsteady behaviour that may occur when the ship is sailing in a wavelength that is close to the ship length. This behaviour was recorded and presented for two cases when λ=1.0 L_{pp} and λ=1.25 L_{pp}. This unsteady behaviour can be observed clearly in the distorted signal for the predicted total resistance in waves, as Fig. 6.16 bears out.

Table 6.11 Added resistance in waves for cases C2~C8

λ/L_{PP}	Total Resistance Coefficients		Added Resistance in Waves	Ratio
	In Waves C_{Tw}	In Calm Water C_{Tcw}	C_{AW}	C_{AW} % C_{Tcw}
0.50	0.00459	0.00425	0.00034	8.1
0.75	0.00473		0.00048	11.2
1.00	0.00527		0.00102	24.0
1.25	0.00592		0.00167	39.2
1.50	0.00528		0.00113	24.2
1.75	0.00521		0.00096	22.6
2.00	0.00498		0.00073	17.3

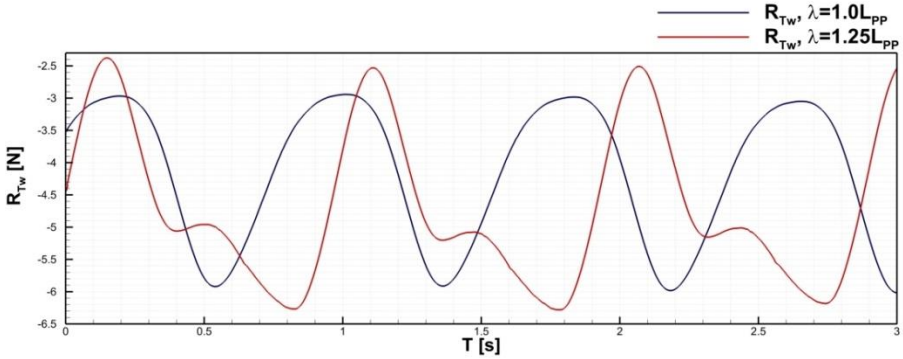

Figure 6.16 Unsteady signal of the total resistance time history at λ=1.0 L_{pp} and λ=1.25 L_{pp}

Taking a closer look at the results for heave and pitch responses which are presented in Fig. 6.17, a reasonable agreement with the experimental data can be observed for the heave response with an average error for the seven points within 5.6%.

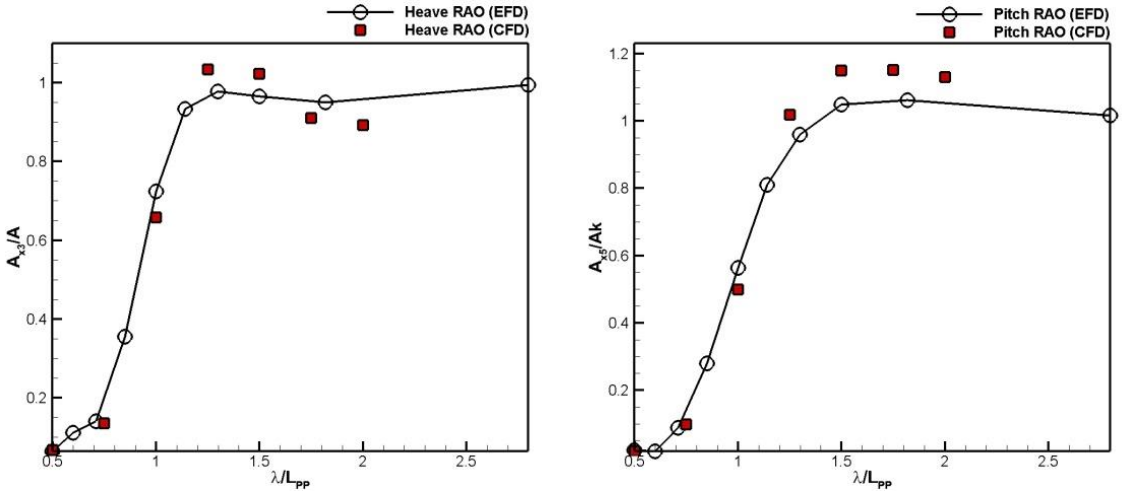

(a) (b)

Figure 6.17 RAO for: (a) heave and (b) pitch compared to EFD data [87] at cases2~8

For small wavelength λ<1.0 L_{pp}, the CFD results are under predicted, also similar when λ>1.5 L_{pp}. Only two values are over predicted for λ=1.25 and 1.5L_{PP}. This might be related to the fact that this range is very close to the resonance range of the ship, which was recorded in [86] at λ≅1.33 L_{pp}. theoretically and practically, the response of the ship in this case is expected to be significant.

For the pitch response, also the error range for the average value of the seven points is within 11.2%, which is significant as it was presented earlier in Case1. However, it can be said that the computed RAO curve is behaving similar like the EFD, despite the discrepancies between CFD and EFD values.

- ***Case 9-10: Zero Speed***

The zero-speed case is performed exactly as the other cases are performed, except that the computational domain is slightly modified. The domain is extended 2.0L_{ref} in the upstream in front of the classic inflow boundary. This means that the distance between the inflow boundary and the F.P. becomes 4.0L_{ref}. The reason behind that is that the wave cannot be generated exactly at the boundary, since it cannot oscillate downstream with zero speed, for this reason, the solver developers provided a new feature called the Internal Wave Generator (IWG) to be suitable for this type of simulation.

Analysing the results for zero speed case, which are summarised in table 6.12, for cases C9 and C10, the absolute average error range for heave response is within 4.1 and 4.3%, which is considered reasonable. On the other hand, the pitch response has an error that is still considerably significant at 11.4%. The heave values are under predicted, while the pitch values are over predicted. Yet, the range complies with the previous results in other simulation cases, which can give a good sign about the consistency of the solution despite the high error reported for the pitch responses.

Table 6.12 Heave and pitch responses in at different *Ak* from C9

Ak	*TF* Motion	EFD [87]	CFD	|ε|%
0.025	Heave	0.604	0.580	4.1
	Pitch	0.780	0.869	11.4
0.05	Heave	0.607	0.581	4.3
	Pitch	0.788	0.878	11.4

- ***Case 11: Free surface and Local flow Analysis***

The free-surface analysis includes two cases based on the ship speeds corresponding to *Fr*=0.28 and 0.41, while the wave conditions remain the same λ=1.5L_{PP} and *Ak*=0.025. The study is aimed at predicting the ship-wave interaction at different conditions to oversee the existence of any non-linear phenomena, such as breaking, separation, overturning or green water on deck. The free-surface analysis made for the speed diffraction problem showed that the free-surface is well computed, qualitatively, and quantitatively. For that purpose, results for free-surface in motion can be correlated to those predicted for fixed ship to understand the difference between the two conditions. Figure 6.18 shows a comparison between the wave elevations computed for both fixed and free ship conditions. The comparison shows that the obtained wave elevation results for free ship is more significant than that computed for the fixed ship case. This is reasonable since the ship vertical motion can impose a vertical pressure component that increases or decreases the motion depending on the direction of ship motion regarding the wave crest and trough. The general overview shows that both wave profiles are almost the same, except some perturbations nearby the hull generated by the vertical motions of the ship. This observation was also stated in the study presented in [86].

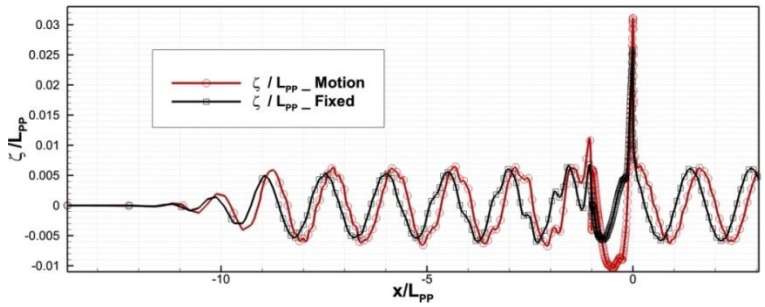

Figure 6.18 Relative wave elevation computed for free and fixed ship conditions

Since the most critical case should result with the high-speed simulation condition, a closer look at the hull-wave interaction is brought to attention in Fig. 6.19 highlighting the two most critical moments, when F.P. encounters the crest and the trough. An intense interaction can be observed between as the wave crests encounter the bow that results in a significant separation. This was also observed for the fixed ship condition; however, now that the ship is free to move vertically, the situation is more severe and even getting worse as the ship speed increase. The water level, as observed in the mass fraction, causes a green water effect; however, the flare design shape separates the flow outwards as the ship is moving downward, keeping the deck dry.

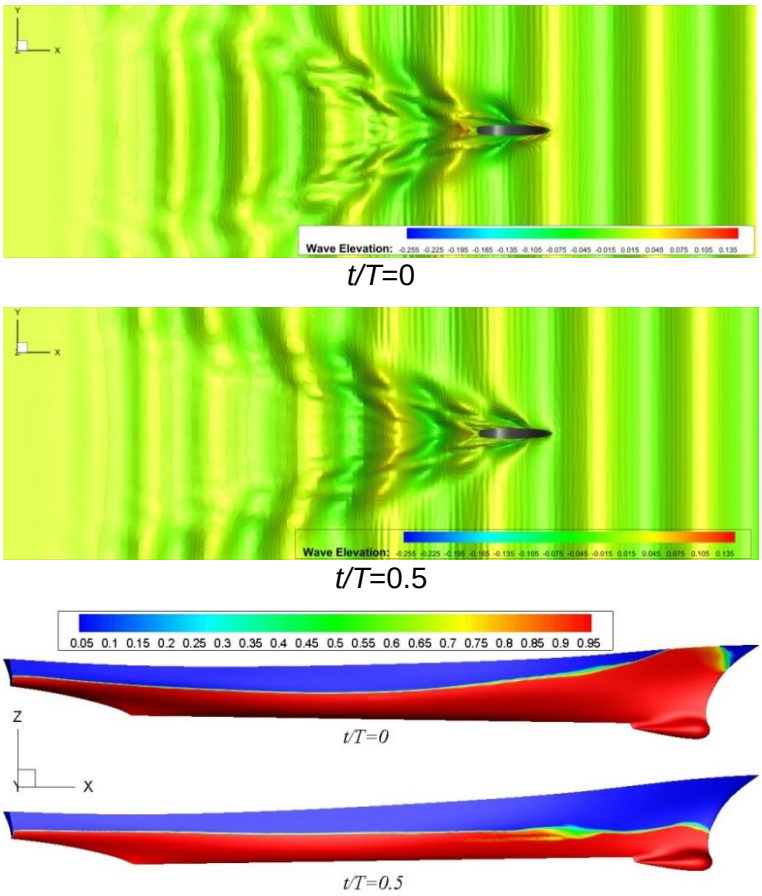

Figure 6.19 Free surface profile and mass fraction computed for case C11 at *Fr*=0.41

The interaction between wave and hull is spotted and presented in Fig. 6.20 in the hull vicinity at the previously reported moments to get a closer look at the wave separation and any breaking effect during the simulation. The figures ensure the aforementioned separation at the

flare on one side, whereas on the other side closer to the ship stern, the rooster-tail separation and breaking effect seems to be more obvious compared to the fixed case. The same conclusion remains for the reason behind this effect, which returns to the interaction that occurs as the ship encounters the wave.

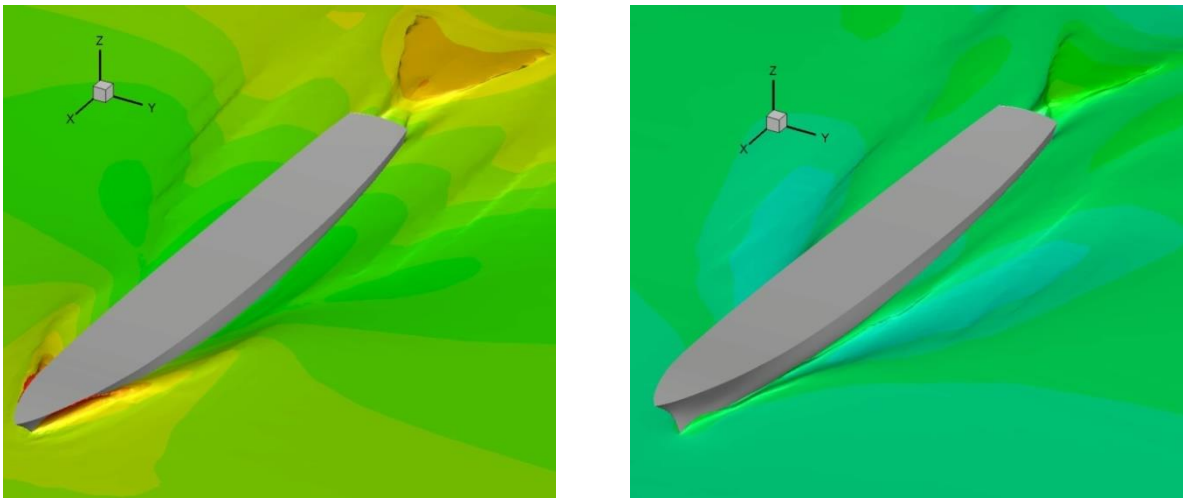

t/T=0 *t/T*=0.5

Figure 6.20 Hull wave interaction at *t/T*=0 and *t/T*=0.5

The free-surface analysis for both fixed and free conditions reveals that the achieved results for both cases are successful from the accuracy point of view, based on the comparison between the CFD results and the available EFD data; and from achieving the initially proposed aim to study the hull-wave interaction and trying to visualise any unsteady phenomena or any breaking wave occurrence.

- ***Case 12: Wake Flow Assessment***

Heading to the wake flow analysis, similar comparison as the one proposed for the free-surface is repeated to compare the achieved results in the motion condition with the fixed ship condition. This comparison is brought to attention in Fig. 6.21 for the axial velocity contours computed for the cross section at x/L_{pp}=0.935 at t/T=0. The resulting streamwise velocity contours at the moving ship differs slightly from the fixed ship condition, where the ship position is already changing because of the ship trim as the ship sinks, which results in a contracted boundary layer towards the hull due to the viscous effect. Similar observation is reported in [86].

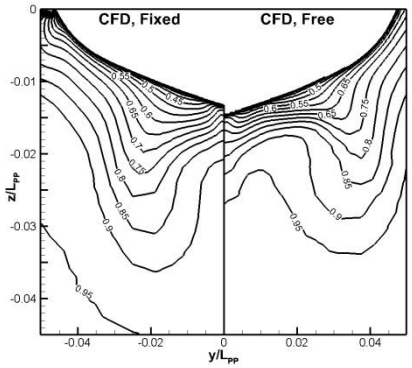

Figure 6.21 Relative velocity contours at x/L_{PP}=0.935 and *t/T*=0 compared to EFD [47, 130]

The development of the flow around the hull at ten different sections located at equal distance $\Delta x/L_{pp}$=0.1 is presented for the current simulation compared to the calm water condition. The streamwise velocity contours and the second invariant iso-surface=50 are

plotted in Fig. 6.22, showing the development of the axial velocity distribution along the hull and revealing the formation of the vortices. As described in Chapter IV regarding the vortices formation of the ship in calm water, two main vortices are observed in the fore part of the ship; the SDV and FBKV. Those vortices are uniformly transported downstream with no noticeable distortion. But, when the ship is sailing in waves, these two vortices remain in the simulation, however, because of the ship motion in wave, the interaction between hull and wave causes a deformation in the helical tube of the vortices causing a lateral deformation in the helical structure of the vortices. A side of that, the intensity of the vortices is changing almost after 0.25 L_{pp} from the F.P. revealing almost a nodal point where both tubes are like crossing from one ship side to another. After that nodal junction, the vortices are detached outwards toward the side and then recollected close to the centerline, where a coaxial distortion takes place and then the vortices are washed downstream close to the amidships because of viscous dissipation. Though the vortical structure vanishes in the amidships, the velocity contours still represent the lateral oscillation of the vortices downstream closer to the propeller plan and near the stern. This oscillation in the velocity contours and the boundary layer of the ship may cause a very significant impact on the propeller performance. Further investigation of the propeller existence in the wake could provide more understanding for this problem.

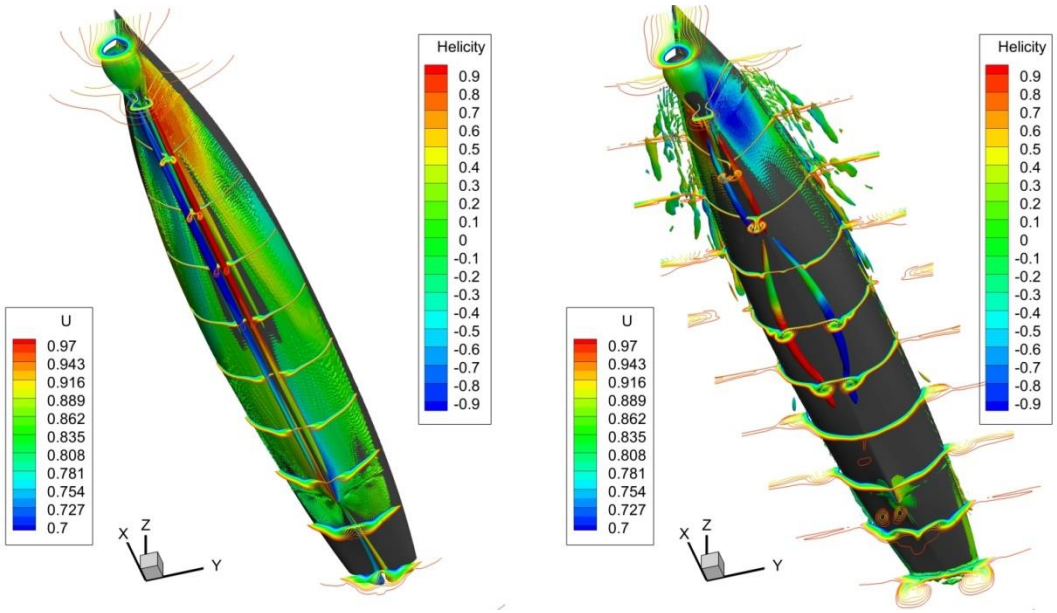

Figure 6.22 Axial velocity contours computed at equal distances Δx=0.1L_{pp}, and second invariant iso-surface=50 at a random moment during simulation

Since the results presented in Fig. 6.22 are for a random instantaneous moment during the simulation. The two main simulation moments t/T=0 and t/T=0.5 are plotted in Fig. 6.23 to grasp a proper understanding for the development of the vortices within the different instances of the wave encounters showing the ship profile and bottom view.

The vortices show similar behavior like the early described instantaneous vortices with an extra vortical tube that appears parallel to the propeller shaft close to the shaft domain, which means that the hull-wave interaction changes the vortices intensity causing them to be captured in this simulation only when the intensity is sufficient to make them visible at this iso-surface level, and maybe beyond that, using this turbulence model. Final suggestion is that a more complex turbulence model such as DES model will be very useful in capturing all these vortices and help

understanding more details regarding this boundary layer deformation. This could be a plan for future work.

Finally, it is worth mentioning that all the results presented in this study were partly published in [149].

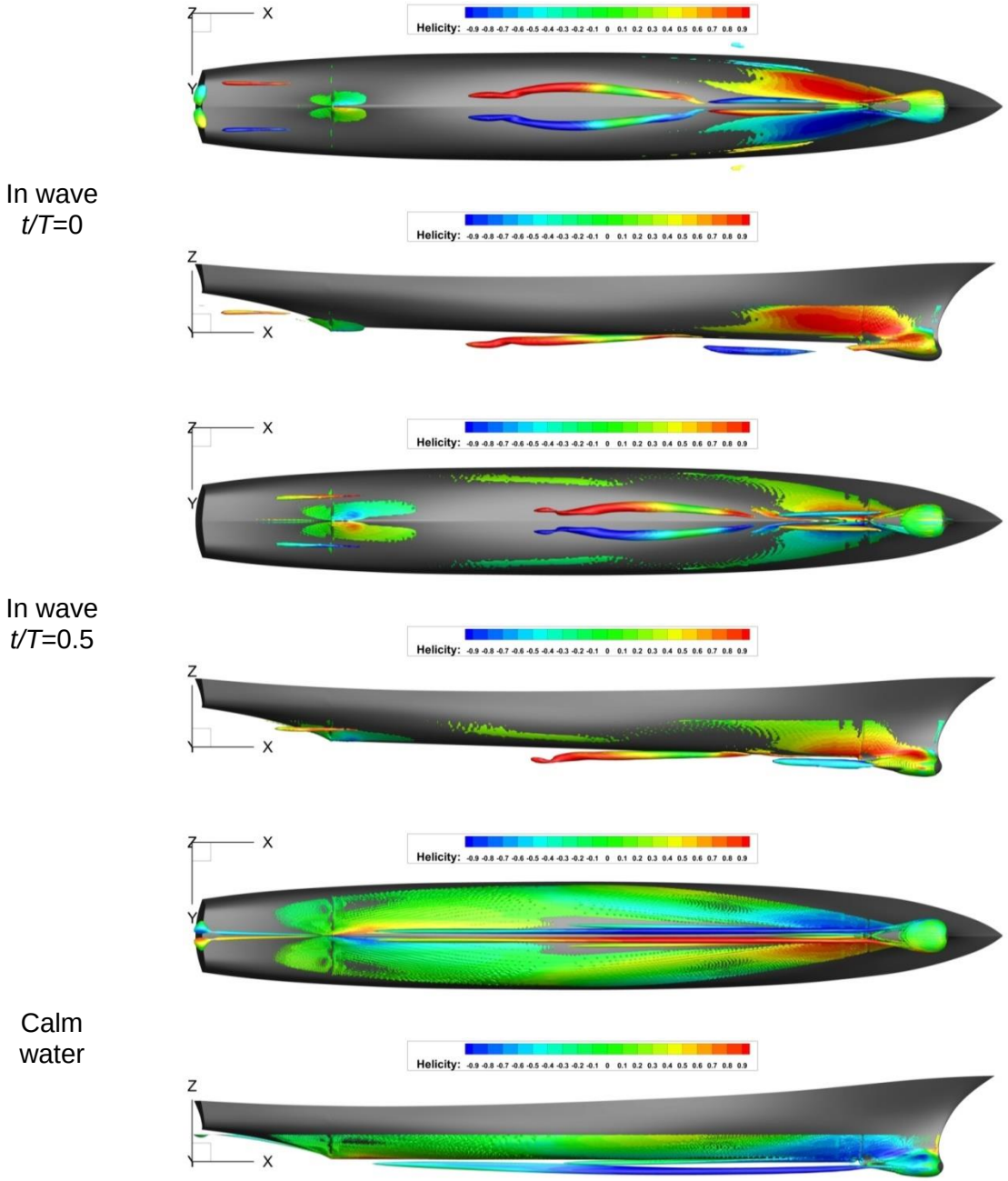

Figure 6.23 Vortices formation in wave at *t/T*=0 and 0.5 compared to calm water

6.2 Roll Decay Performance in Calm water

This study is concerned with the analysis of ship hydrodynamic performance in roll decay condition, so the ship is sailing in calm water and has only one degree of freedom to oscillate around its centerline axis, the motion that is known as roll. Conceptually, the ship is towed at an initial inclined angle then released to oscillate and the roll motion amplitudes are recorded. The resulting curve of oscillation is called the roll decay curve.

6.2.1 Simulation Conditions

The study performed in this section corresponds to the case 3.6, which was proposed for the DTMBT sip model appended with bilge keels in roll decay condition. The experimental results for this case can be found in [47, 150]. This numerical simulation has four major objectives; the first is concerned with the validation of the numerical results compared to the available EFD data to ensure the capability of the CFD solution to replicate the experimental study numerically. The second is aimed at assessing the numerical errors based on a verification and validation method. The third is focusing on the free-surface flow prediction. Finally, the last part is to analyze the local flow during the roll decay simulation in order to understand the flow mechanism during ship rolling.

6.2.2 Domain & Boundary Conditions

Full ship domain is used to represent the control volume of the numerical simulation because the half domain is not applicable in this case study. The domain has a parallelepiped geometry which is extended in x-direction with $5.0L_{PP}$, in y-direction with $4.0L_{PP}$ and in z-direction with $2.5L_{PP}$. The domain boundaries are distributed as follows: inflow boundary upstream is positioned at $1.0L_{PP}$ from F.P.; outflow boundary at $3.0L_{PP}$ downstream from A.P.; both side boundaries at $2.0L_{PP}$ the ship centerline; bottom and top boundaries at $1.5L_{PP}$ and $1.0L_{PP}$ on both direction from the undisturbed free-surface, respectively. Fig. 6.24 shows the simulation domain and the boundary conditions imposed on the exterior boundaries.

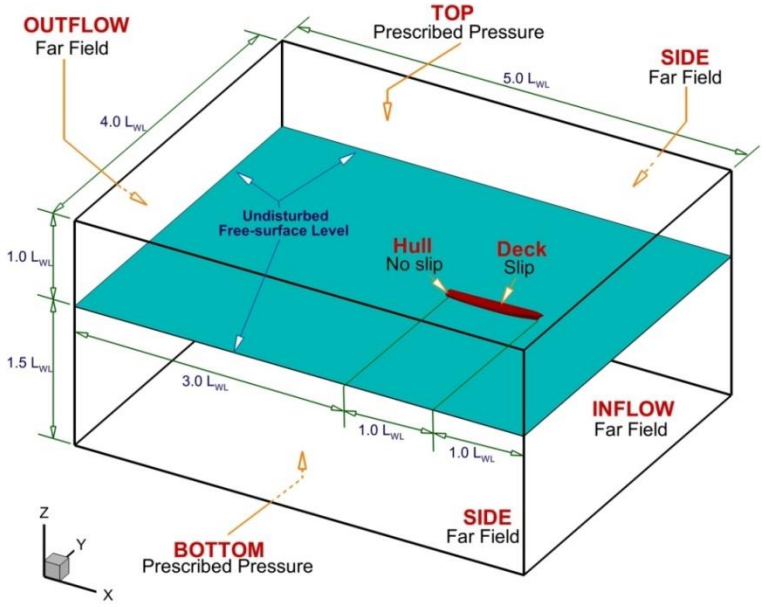

Figure 6.24 Simulation domain and boundary conditions

Ship hull has no slip boundary condition; slip condition is applied for the deck, knowing that it should remain in air during the simulation, where the effect of viscosity in the air may be ignored compared to that in water.

6.2.3 Computational Grids

The grid generation started corresponding to the main case parameters; the ship speed corresponds to *Fr*=0.138. Though the simulation is also performed for higher Froude number, it is well known that a grid density for slow speed ship can also handle the high-speed case from the grid resolution quality point of view. To maintain the grid quality and similarity on both sides, the grid is generated with no initial inclination angle, i.e., the upright position, or the initial roll angle is zero. The common techniques used for roll decay is to use the sliding or overset grids, especially when the initial roll angle is large; this usually come with some cost regarding the complexity of modeling, the larger memory required and finally longer simulation time. To evade this problem, a large isotropic refinement box is introduced in the domain containing the whole ship, extended longitudinally at 0.1 L_{PP} downstream the A.P., and slightly upstream the bow; laterally, box sides are set at 0.25 L_{PP} from the centerline; finally, in the vertical direction, the bottom and top faces of the box are positioned at 0.075 L_{PP} and 0.065 L_{PP} from the ship base line, respectively. In the vicinity of the keel, another isotropic refinement box is introduced to capture more flow details. Last but not the least; the free-surface is refined using a section refinement following the Kelvin-pattern, with a wider opening angle of 60˚, equally distributed from the ship centerline. This refinement section starts closely ahead the F.P. and extended longitudinally with about 2.0 L_{PP} downstream. 60 grid cells/hull propagated wavelength is the refinement criteria imposed in *x*- and *y*-directions; whereas in *z*-direction, the height of the refinement section is set to cover the stagnation wave amplitude corresponding to the equation $\zeta_{max}=0.5U^2/g$. In *z*-direction, the refinement criteria is set to $z= 0.001L_{PP}$. Fig. 6.25 represents the finest grid with longitudinal, transversal, and horizontal sections to show the box refinements close to the hull and bilge keels, with a top view showing the free-surface refinement.

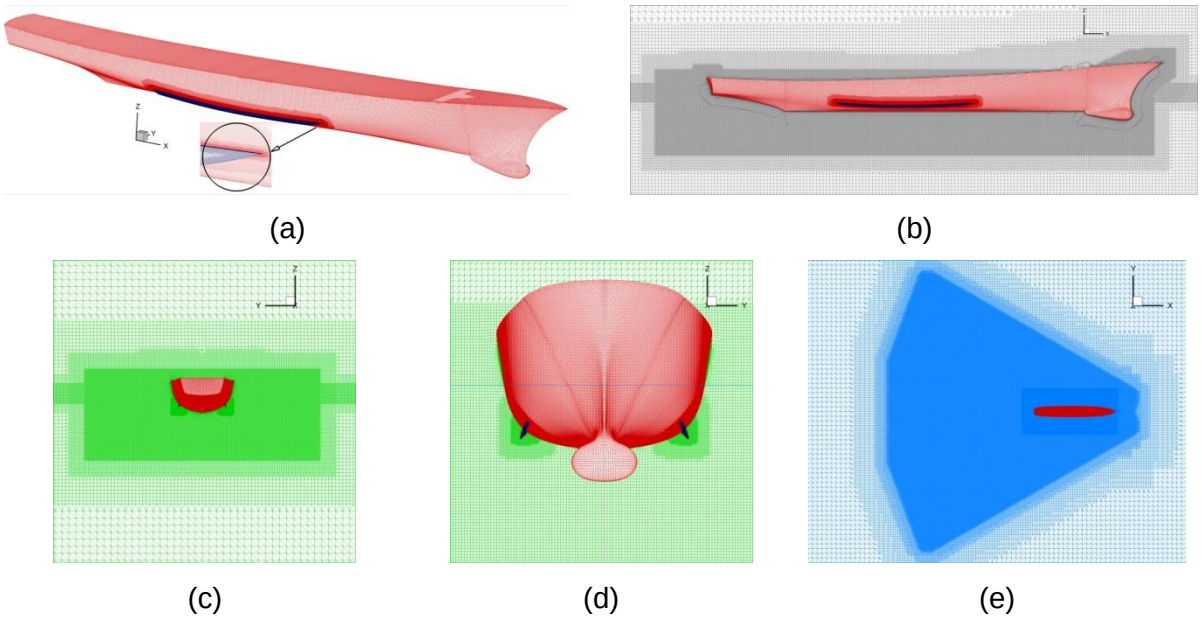

(a) (b)

(c) (d) (e)

Figure 6.25 Finest grid discretization, spotting: (a) 3D hull; (b): longitudinal section; (c,d): lateral section depicting the refinement boxes around the hull and bilge keels; (e): free-surface refinement section top view

To perform the verification and validation, four systematically refined grids are created to ensure a grid similarity for a successful application of Richardson Extrapolation method. The average grid refinement ratio of r_{Gav}=1.457. Table 6.13 summarizes the computational grids for the Grid convergence study, where M1 denotes the finest grid and M4 stands for the coarsest.

Table 6.13 Grid arrangement for the grid convergence study

Computational Grid	M4	M3	M2	M1
Number of cells (x10^6)	15.15	23.43	33.59	46.71
r_G	1.55	1.43	1.39	

6.2.4 Simulation Strategy

Two simulations are performed for every initial roll angle in an unsteady mode. The ship is towed ahead with an imposed target roll angle to generate the initial roll angle before the release. The acceleration period in the first simulation is set to 8 seconds, while the total simulation time is chosen to be 40 seconds to ensure sufficient convergence. The time step in the first simulation is similar to that of a resistance simulation, resulting in Δt=0.02s with 8 nonlinear iterations to keep the solution residuals under control.

In the second simulation, the time step is set at Δt = 0.005s with 20 nonlinear iterations, which are 3 times larger than the minimum recommendations for roll decay simulations proposed by the ITTC recommended procedures [123, 151]. The simulation is performed until it counts full six roll periods to be sufficient for results validation against EFD data. HPC is used for this simulation, with available 120 CPU nodes up to 3.3 GHz. Physical ccomputation time for first simulation needs about 13–38 hours, whereas the second free roll simulation needs 22–73 hours, depending on the grid density and time step choice during the simulation.

6.2.5 Roll Motion Results

The results are validated based on direct comparison with the EFD data provided for the similar test case reported in [47, 150] when the ship is sailing at medium speed with Fr=0.138. Various initial roll angles were tested starting from $Ø_0$=2.5˚ up to $Ø_0$=20˚, with a step $\Delta Ø_0$=2.5 in every simulation. The comparison between CFD and EFD is plotted in Fig. 6.26.

The computed roll period is T_{CFD}=1.572s, while the measured one is T_{EFD}=1.54s. This records an error value of 2.1% in the roll period. Considerably, this is considered within a reasonable range of accuracy. On the other side, regarding the roll peaks amplitudes, the results showed a good agreement between CFD and EFD, especially for the small roll angles. Unfortunately, for the large roll angles, the error seems to increase proportionally to the increment of the initial roll angle. The computed error for the maximum and minimum deviations between the CFD and EFD results is within 1.06 and 24.28%, respectively. The maximum errors for the computed roll amplitudes are recorded for the second peak of the roll oscillation. The reason behind that may be related to two factors; the first may be the turbulence model used, since it is theoretically and practically proven that the turbulence models suffer stability issues when the flow separation is significant. This is the case for the second period as the roll angle is still un-damped. The other reason might be related to the grid consistency after deformation during the ship rolling, which may cause this instability and large amplitude predicted. With all that said, the resemblance between CFD and EFD is sufficiently satisfying. The best results obtained are the ones computed for initial roll angle of $Ø_0$=2.5˚ and 5˚, while the most deviated results are the one computed for the maximum initial roll angles of $Ø_0$=15˚ and 20˚.

It is worth mentioning that the results obtained in this study corresponds well with the results predicted based on other simulation codes in the G2010 Workshop [47] and by other researchers, such as [96, 152].

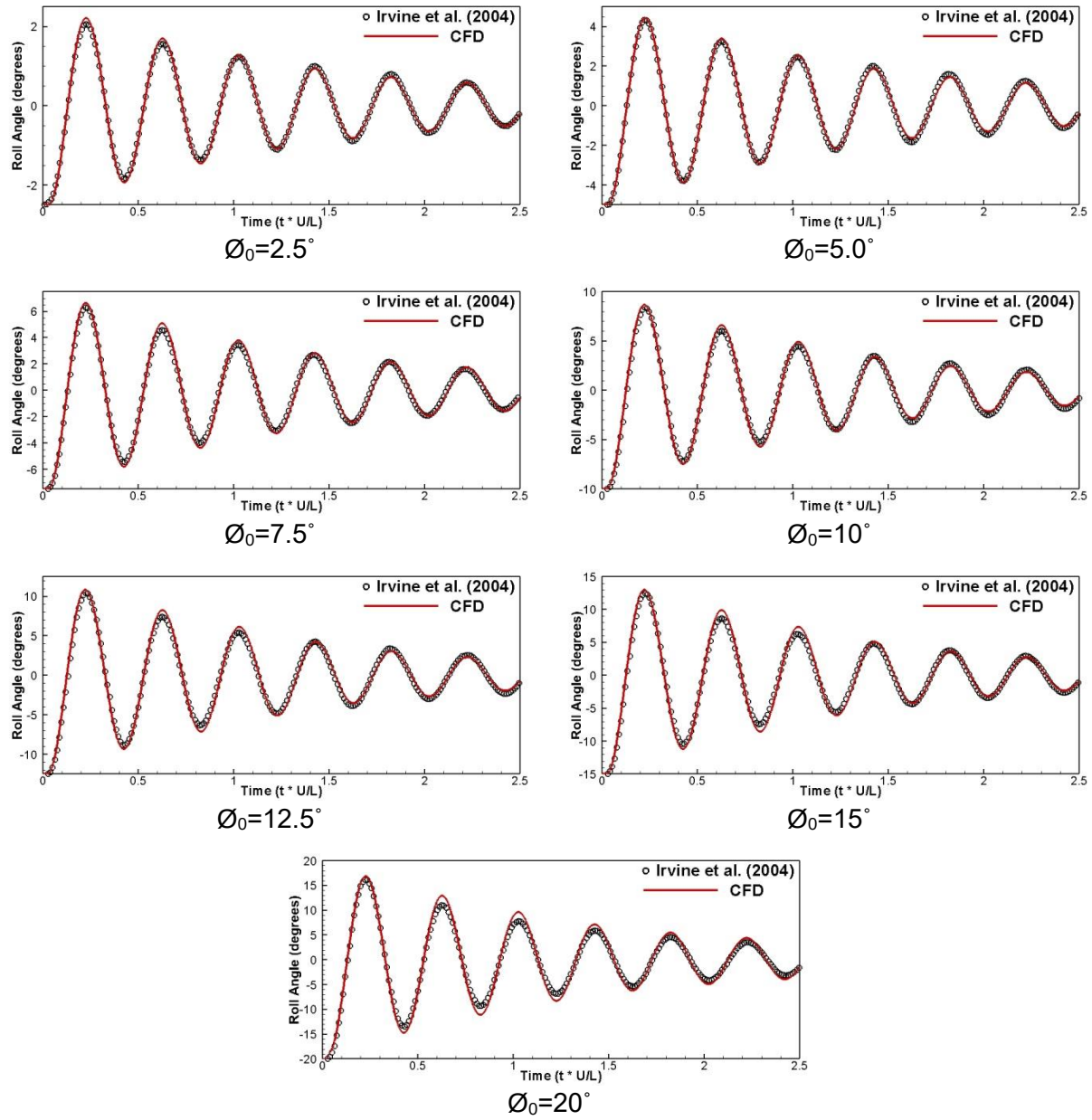

Figure 6.26 Time history for roll simulation at altered initial roll angles

- ***Validation with the fitted Decay Curve***

The validation process performed here corresponds to the main simulation case 3.6 from G2010 Workshop [47] where the ship is sailing at medium speed with *Fr*=0.138 and initial roll angle $Ø_0$=10˚. The time history of the roll peaks is recorded to plot the roll decay curve as function of the mean decay value $Ø_m$ from the decay response, which can be computed based on the formula proposed by ITTC in [151] as: $Ø_m = (Ø_{n-1} + Ø_n)/2$, while the other variable is the roll angle decrement computed based on the formula: $\Delta Ø = Ø_{n-1} - Ø_n$. A third-degree polynomial fitted curve should be drawn according to the equation

$$\Delta Ø = a Ø_m + b Ø_m{}^2 + c Ø_m{}^3 \quad (6.6)$$

where a, b and c represent the roll extinction coefficients, that can be estimated from the fitted curve on the decay curve.

The results for the decay extinction curve computed based on the roll amplitudes average and mean values are plotted in Fig. 6.27 while the quantitative representation of the computed results is given in Table 6.14. The maximum and minimum computed errors for the computed results is within 1.06% and 6.52%, with an average error of 4.22%, a value that is within an acceptable limit.

Table 6.14 Computed results for roll amplitudes compared to EFD data and corresponding average and mean values for decay fitting curves

t	CFD	EFD	ε%D	$\emptyset_{m_{CFD}}$	$\Delta\emptyset_{CFD}$	$\emptyset_{m_{EFD}}$	$\Delta\emptyset_{EFD}$
0.00	-10.00	-10.00	0.00	-	-	-	-
0.83	8.66	8.40	3.06	8.68	2.83	8.59	2.83
1.68	-7.36	-7.17	2.59	7.58	2.36	7.22	2.36
2.53	6.50	6.04	7.52	6.48	1.96	6.19	1.96
3.38	-5.60	-5.21	7.43	5.60	1.59	5.25	1.59
4.22	4.71	4.46	5.62	4.83	1.25	4.59	1.25
5.06	-4.06	-3.96	2.51	4.09	0.94	3.99	0.94
5.90	3.48	3.52	-1.06	3.54	0.77	3.58	0.76
6.73	-3.02	-3.20	-5.63	3.06	0.76	3.13	0.77
7.57	2.65	2.75	-3.82	2.67	0.72	2.84	0.72
8.41	-2.32	-2.48	-6.64	2.35	0.63	2.43	0.63
9.24	2.05	2.12	-2.95	2.03	0.61	2.18	0.61
10.07	-1.75	-1.87	-6.60	-	-	-	-

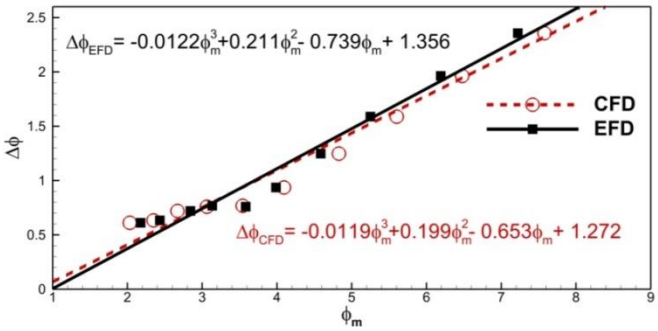

Figure 6.27 Fitted decay curves for computed results compared to EFD data [150]

- ***Verification & Validation of Numerical Errors***

Table 6.15 represents the main parameters for the grid convergence study performed on the four systematically varied meshes, knowing that M1 and M4 denote finest and coarsest grids, respectively. The general observation of the grid dependence test reveals that, for the coarser grids, the roll amplitude is over predict for the six roll periods, while for the finest grid, the amplitudes of the roll response resemble well compared to the EFD results. The grid study shows a descending behavior with a monotonic convergence. In addition, a minor phase shift can also be noticed between the four grids. The global behavior of the grid parameters represents a monotonic convergence for the roll amplitudes; however, it seems like between M1 and M2, a local oscillatory convergence can be observed near the peak of the 5th period of roll. Apparently,

at that limit of grid density, it can be said that the study is close to asymptotic range with limited dependency on the grid resolution.

Table 6.15 Grid convergence study parameters

Grid Convergence parameters	r_G	R_G	p_{th}	p_G	$U_G\%S_1$
Value	1.457	0.52	2.0	1.75	2.57

Looking at the time convergence parameters tabulated in Table 6.16, the change in time step showed very minor influence on the numerically obtained results, a fact that was concluded by other researchers in similar studies for the same ship, such as [94, 152]. This might be a proof of the good choice of initial time step; bearing in mind ITTC criteria recommended for the roll decay simulation time step proposes 100 time-steps/roll period. In this study, 325 time-steps were used instead, meaning over three times the recommended criteria by ITTC. For the time step convergence test, this value is reduced by half three times, resulting in 2600 time-steps/roll period. This value is very significant, which consequently resulted in a significant physical simulation time. Thus, to avoid the long simulation period, only the first signal was recorded for the two finest grids and compared with the other two coarsest ones, as it is illustrated in Fig. 6.25, along with the time history for the grid convergence results.

Table 6.16 Time step convergence study parameters

Time Convergence parameters	r_T	R_T	p_{th}	p_T	$U_T\%S_1$
Value	2.0	0.35	2.0	2.75	0.90

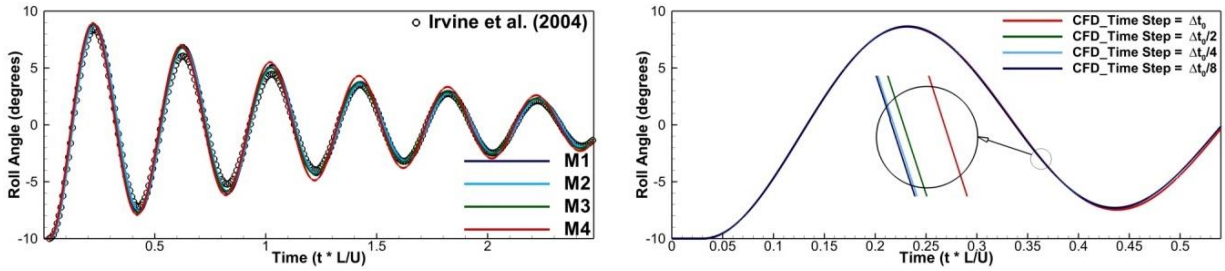

(a) (b)

Figure 6.28 Time history for roll decay based on: (a) grid & (b) time step convergence tests

Comparing the obtained values with the numerical errors after computing the numerical and validation uncertainties, validation parameters could be constructed as given in Table 6.17 showing that, average permissible computed error should be kept beneath 4.06%. This means that the validation uncertainty in this study exceeds the validation uncertainty level, since the average error is within 4.25%. Still, the results are in a reasonable level of accuracy, especially that the error for the finest grids does not exceed 5%, which is very reasonable.

Table 6.17 Results for validation test

Validation Results	U_{SN}	U_D	U_V	$\|E\|\%$
Value	2.57	2.0	3.38	4.06

6.2.6 Free-Surface Analysis

As previously stated, the main analysis is computed for the initial roll angle of $Ø_0$=10˚, to study the influence of the roll decay process on the free-surface, a consistent study is made for the ship design speed at *Fr*=0.28. The free-surface topology is recorded for this condition starting

from the second roll period at the foe quarters of the roll period, as previously explained for the seakeeping simulation, at t/T=0, 0.25, 0.5 and 0.75, respectively. The free-surface configuration at these four instances are represented in Fig. 6.29, showing that the pressure and viscous effect resulting from the roll motion have a noticeable influence on the free-surface of the ship during the roll motion. First, an asymmetrical free-surface configuration resulting from the ship heeling can be observed, even when the ship is returned to the upright position in the moments t/T=0.25 and t/T=0.75. Closer to the hull skin, the viscous effect imposed by the no slip condition on the hull induces a vertical velocity component that creates a trough or crest, depending on ship heeling position. This interacts with the regular Kelvin pattern generated by the hull, adding or subtracting from the generated wave hight. On the other hand, the pressure effect during the roll pushes or drags the flow laterally, resulting of an upstream propagation of the generated waves. This can be observed clearly closer to the forward shoulders of the ship.

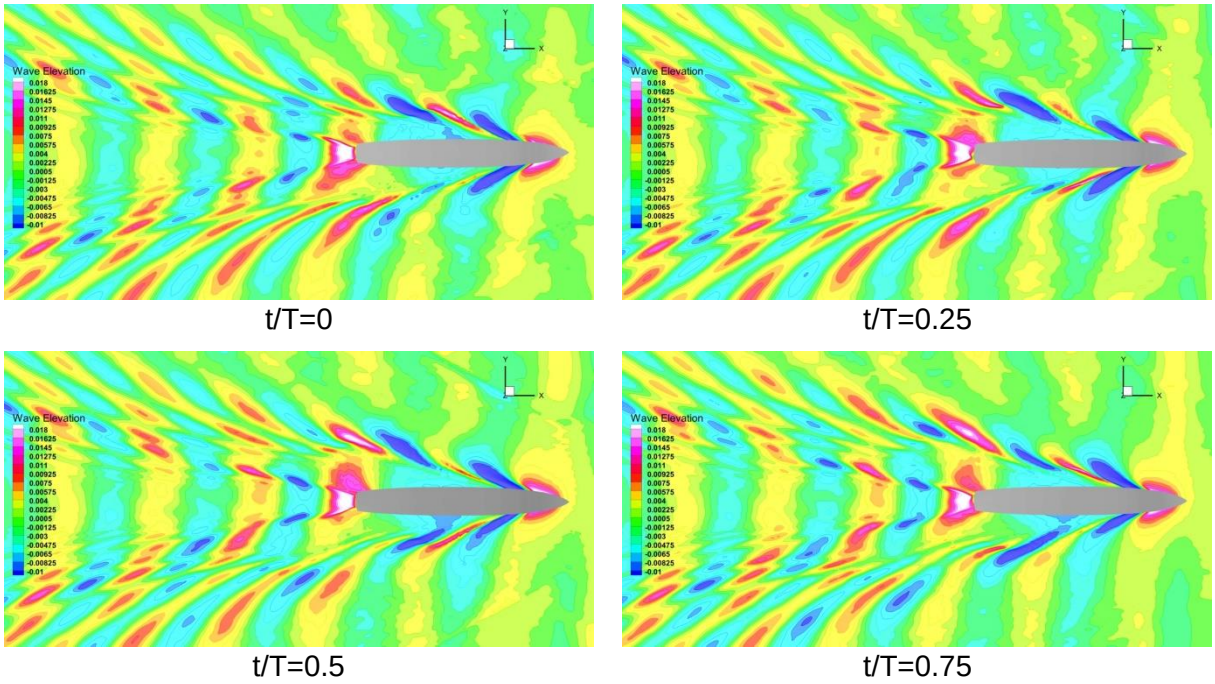

Figure 6.29 Free-surface topology recorded in the second roll period at the four quarters in case of initial roll angle $Ø_0$=10 and *Fr*=0.28

- ***Speed Effect on the Roll Damping***

At the same condition, with initial roll angle of $Ø_0$=10˚, five ship speeds are investigated to study the effect of changing the ship speed on the roll damping process and the free-surface configuration. Five ship speeds are tested corresponding to *Fr*=0, 0.138, 0.20, 0.28 & 0.41. The roll damping time history and the free-surface at the end of every simulation were recorded and presented in the results. It is important to highlight the assumption made to perform the roll damping simulation at *Fr*=0, since this condition is not applicable to the solver. To evade this problem, a very small ship speed was imposed *U*=0.001m/s, which results in approximate *Fr*≅ 0.0001, a value that is small enough to be considered as zero.

The computed results for the roll damping time history are plotted in Fig. 6.30, showing that the speed effect increases the damping effect on the hull, which diminishes the motion amplitude very fast at *Fr*=0.41 soon after the fourth damping period. This observation complies also with the similar observation reported in the tank test in [150, 153]. It is also noticed that the speed effect

has an influence on the roll damping period, which can be observed from the different in phase between the various ship velocities. Apparently, the periodicity of the roll is lost gradually as the ship speed increase.

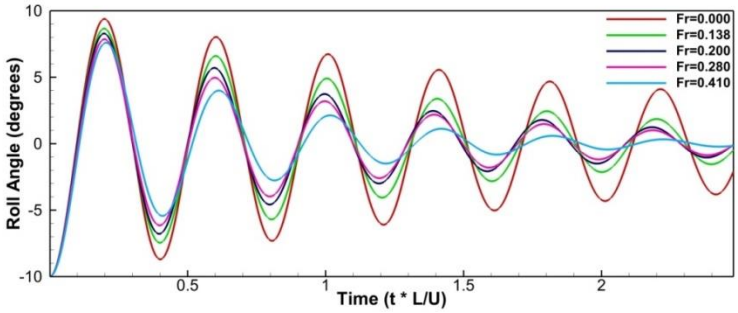

Figure 6.30 Time history for roll decay curves corresponding to various ship speeds

Studying the speed effect on the free surface, the five speeds cases are plotted for the free-surface configuration computed at the 6th period of roll, as presented in Fig. 6.31. It can be observed that for the zero speed, there are no waves generated; only the free-surface is laterally distorted because of the ship heeling. For the medium speeds, *Fr*=0.138 & 0.20, the free-surface configuration seems to be under predicted. This might be related to the grid density at the free-surface refinement, which indicates that 60 cells/wavelength in this study for slow speed is insufficient. Increasing the grid density may help capturing the free-surface more accurately, as it was proven in the seakeeping study. Despite all that, the pressure and viscous effect can be observed for the medium speed range; nevertheless, at the highest speed, seemingly this effect is less present.

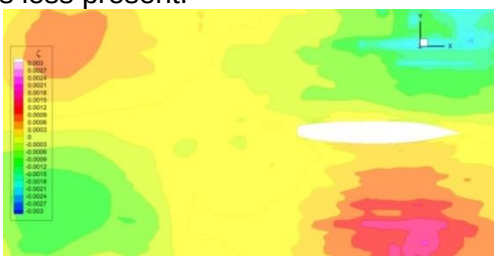

Fr=0.0

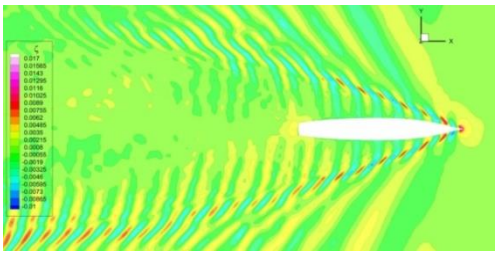

Fr=0.138

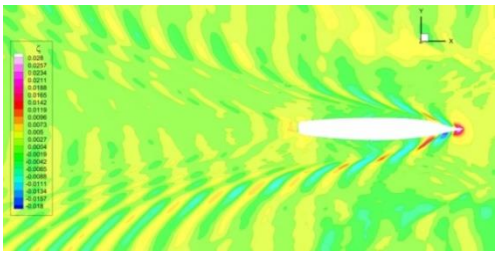

Fr=0.20

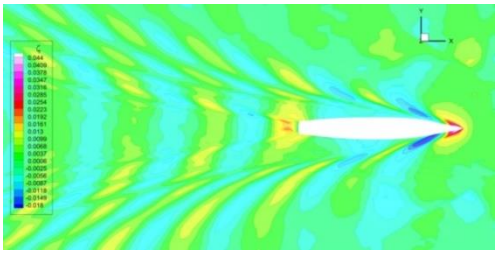

Fr=0.28

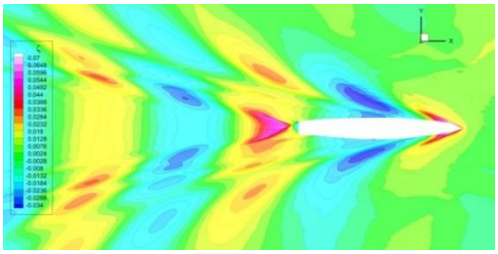

Fr=0.41

Figure 6.31 Computed free-surface at the 6th roll for various ship speeds

6.2.7 Local Flow Analysis during Roll Damping

Prior to studying the local flow during the damping simulation, it is very important to validate the accuracy of the turbulence models used in this study to capture the local flow. Hence, a comparison made for the local flow velocity contours at a transversal section located at x=0.675 L_{pp} from F.P. computed based on both turbulence models that provided good results in the previous simulations, such as *SST k-ω* and EASM turbulence models. This comparison is represented in Fig. 6.32 for ship sailing with Fr=0.138 and initial roll angle $Ø_0$=10˚. The results are plotted for the two instances t/T=0.5 and 0.75, i.e., when the ship is at the trough and in the zero position while heading back to the crest, respectively.

The comparison illustrates the accuracy of both turbulence models in capturing accurately the streamwise velocity contours, though the contours seem under predicted and contracted inward to the hull. The overall agreement is sufficient, with a better agreement observed for the EASM model compared to the *SST k-ω*.

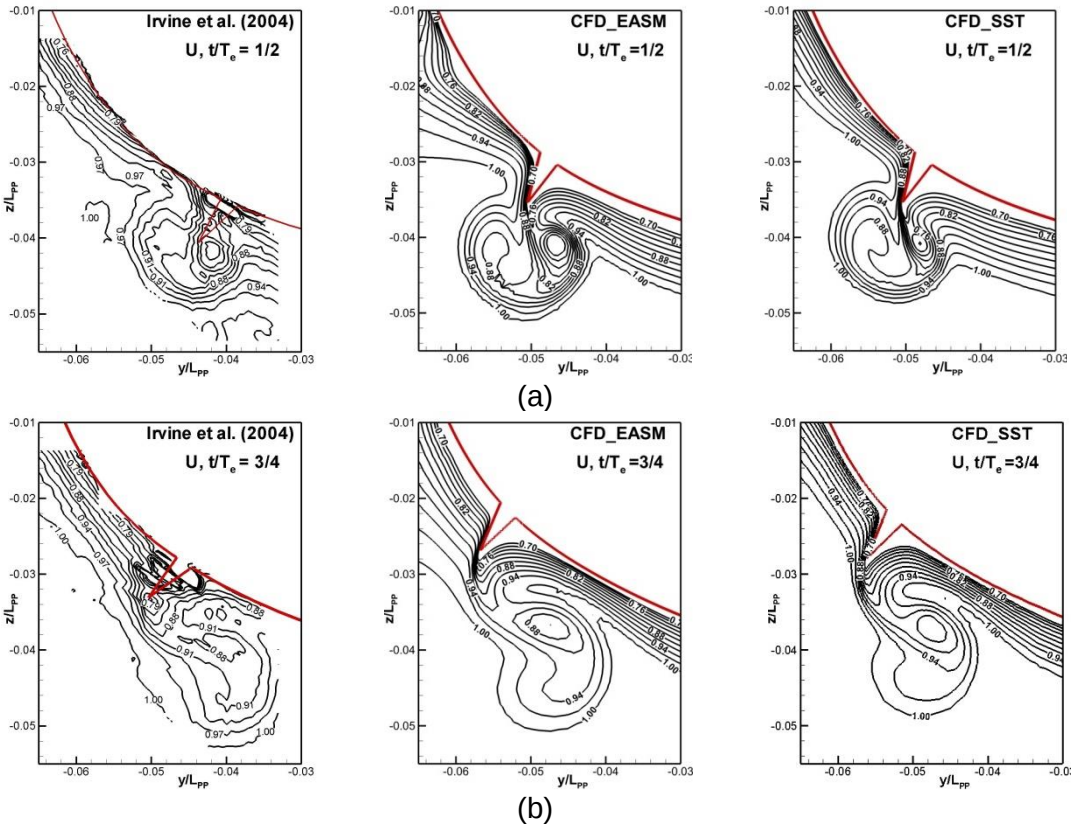

Figure 6.32 Computed and measured velocity contours at x/L_{pp}=0.675 for the second roll period instances: (a) t/T=0.5; (b): t/T=0.75

Since the roll damping effect is significantly influenced by the viscous flow separation and the interaction between hull, flow and bilge keels, it is very important to get a closer look in the flow separation and vortices formation in the hull vicinity and specifically near the bilge keels. This is why, Fig. 6.33 shows the Q*=25 second invariant of the axial velocity computed based on the EASM turbulence models for the four roll period quarters. The ship is viewed from bottom and both, port and starboard sides, to highlight the development of the vortices throughout the various simulation moments. Similar like the vortices predicted for the bare and appended hull, three major formations of vortices still persist in this case, as it was explained in the resistance simulation for the DTMB in Chapter IV. These three vortices are the two originated at the sonar dome, FBKV and SDV, and the BKV produced by the bilge keels.

Despite the under prediction of the vortices, which resulted in a lack of predicting the vortical structures until the ship stern, the vortices formations and their behavior can be comprehended from the four instances plotted in Fig. 6.30. The SDV and FBKV are generated as usually immediately after the flow separation at the sonar dome, yet they do not have a straight pattern like in calm water. The oscillation of the ship causes the vortices to create a sinusoidal-like pattern moving laterally along with the ship rolling. Vertically, and due to the viscous effect, the vortices tubes are also fluctuating as the ship rolls. Having a closer look to the BKV generated at the bilge keel, these vortices formation differs from the ones obtained in the classic resistance simulation, since the BKV at the bilge keel seem to have two contra-rotating components; one on the suction side of the bilge keel and the other on the pressure side. The intensity of the vortices is influenced by the ship roll position, as it is emphasized in Fig. 6.31.

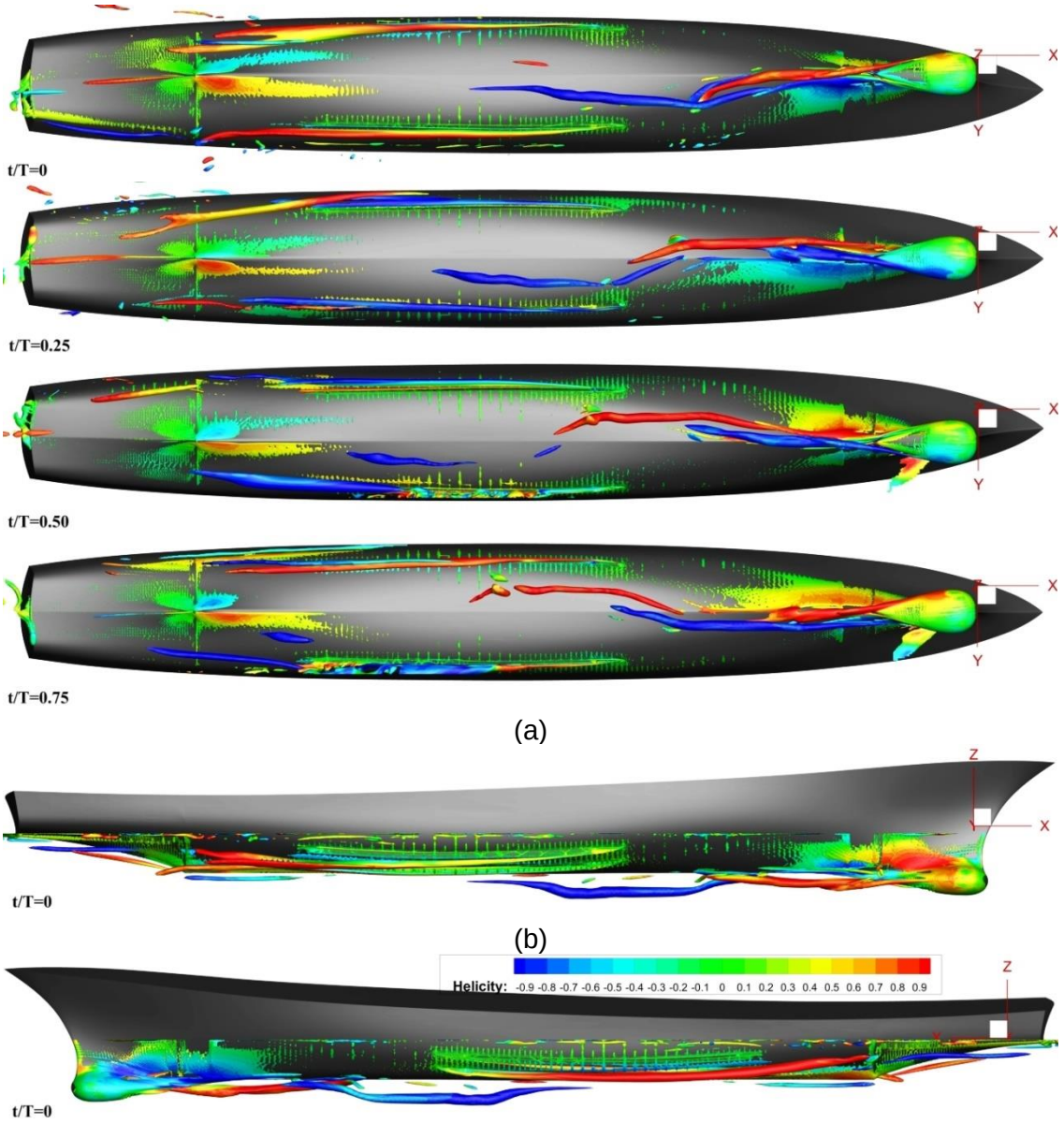

Figure 6.33 Vortices formations during the roll period quarters showing: (a) ship bottom, (b, c) starboard port sides, respectively for *t/T*=0

The vortical formations is combined with the axial velocity and the TKE contours to understand the flow configuration during the full period of roll, as illustrated in Fig. 6.34 at 8 different instances, i.e., the roll period is split into 8 segments this time. A noticeable deformation in the velocity and TKE contours exists as the high momentum flow is convected to the boundary layer causing eddies formation. When the ship is close to the peak (t/T=0 and t/T=1/8), both keel vortices are combined and located at the inward side of the keel. As the ship changes heeling heading back to the upright position, both BKV can be observed, and the boundary layer is distributed evenly on both sides. When the ship is heading to the other heeling side, a mirror effect in the boundary layer and BKV is repeated with less intense vortices, because the heeling angle is reduced by the hull flow interaction, vortex shedding and eddies formation. Eddies and vortices have a major contribution to increase the resistance in this process. This should be highly considered during ship powering estimation.

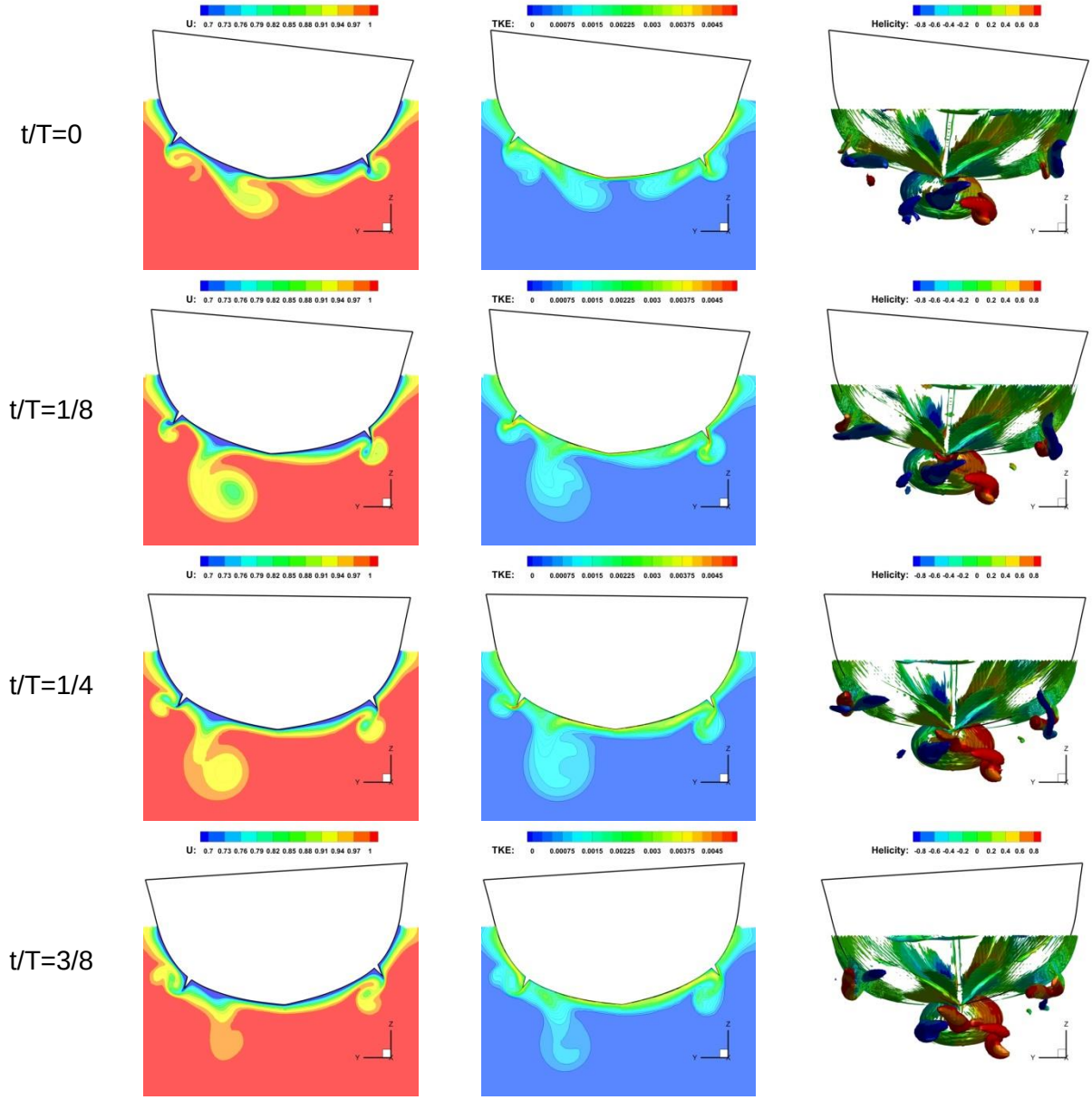

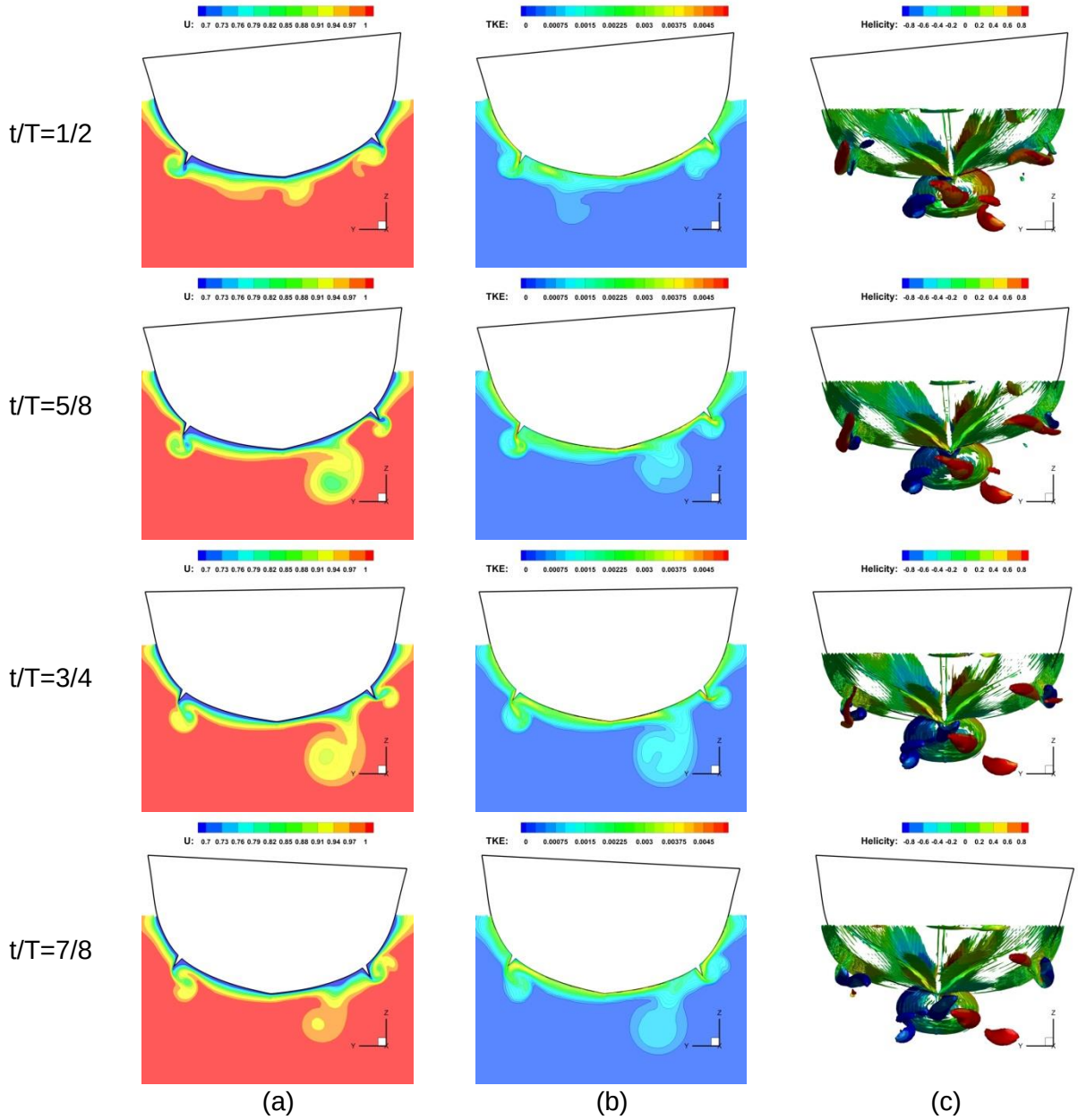

Figure 6.34 (a): U contours, (b): TKE contours and (c): Q*=25 second invariant visualized at section x/L_{pp}=0.675 at 8 segments of the roll period

Having in hand the initially expressed objectives from this study and the obtained results, it can be concluded that the CFD method can provide well representation for the roll decay performance from all the aspects of interest. Regarding the ship motions, free-surface and local flow, all were obtained successfully, and the results verification and validation confirmed this. All the results for roll damping performance were published in [154].

Generally, for the seakeeping applications, CFD can ensure a suitable, flexible and very reliable tool to predict with satisfying level of accuracy the ship performance in seakeeping simulations.

This page is intentionally left blank.

Chapter VII
Conclusions, Contributions and Recommendations

The numerical simulation of the ship hull hydrodynamic performance was presented for multiple ship hydrodynamic aspects concerning; ship resistance applications, propulsion performance or ship powering prediction, and finally, the seakeeping performance in regular head waves and roll decay analysis. The CFD method is used to represent the ship performance based on the finite volume method, using the viscous flow solver ISIS-CFD of the FINE^{TM}/Marine that is provided by NUMECA. Rigorous analyses were carried out for various ship types with different characteristics from geometry, dimensions, configuration, function and main purpose points of view. This selection was necessary to ensure that the proposed methodology is generic and can be applicable for different types of ships with different considerations.

The global objective of the presented studies is to survey the possibilities of a unique CFD code to solve different ship hydrodynamic aspects and remark its capabilities and limits of the methodology. This investigation was also aimed at providing a suitable, flexible and reliable solution tool for the recent intricate demands in ship design. Overall, it can be concluded that the global research objective has been achieved. The results obtained in the numerical simulations performed for specially selected ship hydrodynamic problems proved to be sufficiently accurate and reliable compared to other well recognized and internationally approved method, which is the tank test experiments. In the search for creating a balance between the available resources, the current capabilities and level of accuracy required for ship applications, this point was well covered, judging the level of accuracy achieved for the different CFD simulations concerning different ship hydrodynamic problems. Nevertheless, there were some limitations regarding the physical modeling of the CFD problem, which could have been enhanced by introducing more complex turbulence models, for example the use of Hybrid RANSE/LES models in complicated analysis concerning multiphase flow simulations in resistance, seakeeping and roll decay assessment. These limitations are not related to the incompatibility of using the CFD in these applications, but to the fact that these applications required significant computational resources and very long simulation time. This also does not deny the fact that these complex models were applied in this study, when possible, in mono-fluid applications concerning propulsion performance in open water and in the self-propulsion applications, showing a recognized success in predicting the main hydrodynamic aspects of the ship flow and ship fluid interactions. The contribution in this research study could provide a proper balance between accuracy and reliability within the available resources and the objectives of every study individually.

As for the local objectives in the implemented studies, it was necessary to ensure that the proposed methodology should cover and predict accurately the main variables of concern in ship applications, such as local and global forces, velocity and pressure fields, ship motions, free-surface, wake flow, vortex detection, flow separation, etc. For this purpose, all the obtained results were not just introduced to show that it can be analyzed and predicted, but also validated against experimentally measured data, showing that both numerically and experimentally obtained results were within a good agreement.

7.1 Concluding Remarks

Having a thorough review on the main objectives and the achievement is this research work research; the following general points can be concluded:

For resistance performance

1. for ship resistance applications, thorough studies were performed for three ship models; the JBC, KVLCC2 and the DTMB surface combatant. The obtained results for all the ship types compared to the available experimental data were within a very good level of accuracy, where the error range for the three ships for predicted resistance forces was within 0.45% and 7.82%, with a global average value within 3.7%. This value complies very well with the required level of accuracy for marine application for resistance studies, which was proposed in G2010 and Tokyo 2015 Workshops to be less than 4% [47, 48];

2. vertical motions prediction: i.e., sinkage and trim, in ship resistance applications have been recorded for the three ships with an error range within 0.5 and 14.1%, where the maximum error was recorded for the coarsest grid in the slowest ship speed condition that consequently result in most cases in significant discrepancy between measured and computed results. The average error of 5.4%. Again, this level is considered more than sufficient for design considerations;

3. free-surface prediction has shown a remarkable success in predicting wave configurations and profiles for the three ships with an error 2.52% in the computed wave elevation for JBC ship, 0.4% for the KVLCC2 and 1.1% for the DTMB ship model. The reason behind the discrepancy in the predicted wave profile returns to the fact that the ship speed is very small, and this requires very significant grid resolution, which can increase dramatically the simulation cost. Still, 2.52% is more than acceptable for such applications with slow speed ships;

4. local flow analysis for the three ships were performed and validated showing good agreement with the experimental data. The vortices formations in the wake region of the ship have been predicted for the three hulls with a considerably successful comparison with another research in the field;

5. the tank test data for the JBC ship model reported the influence of the ESD on the ship wake, which resulted in more enhanced uniform flow that enters to the propeller after the duct, which sequentially enhanced the propulsion efficiency. This effect has been numerically investigated and proven to be well reproduced with the CFD analysis in nominal and effective wake assessment for the JBC model;

6. since the simulation of ship performance can propose some assumptions to simplify the problem, ship resistance for the KVLCC2 with rudder was analyzed using the real rudder configuration and a simplified rudder model, to reduce the modeling and simulation effort. The simple model acted well for the resistance and vertical motion simulation, which means that some CFD assumptions can maintain the consistency of the simulation, despite the simplification performed. On the other hand, according to the author’s opinion, this can be applicable only for the resistance and forward speed

simulations, where all the lateral forces are not within the scope of the study. Once the rudder angle changes or ship heading angle is not 0˚, the exposed rudder area for the hydrodynamic forces will change, resulting in an over predicted rudder force. Which may affect the simulation accuracy in that condition;

7. an experimental approach was planned and performed in the towing tank facility available in the university with a special focus on the resistance and free-surface prediction of the DTMB ship model with the tank banking effect when the ship is sailing at medium-high speed condition. The data collected from the experiment was validated against other results from the INSEAN towing tank facility showing a reasonable agreement with an average error <5%; and also, over validated with the CFD method, with a proper prediction of the influence of the banking effect on the resistance and free-surface wave reflections at the walls of the tank. The increment in resistance with tank effect was within 2%.

For propulsion performance

8. in the open water propeller, the analysis of the thrust, torque and efficiency for both propellers, JBC and KVLCC2 resulted in an accurate prediction of the propulsion parameters in open water. For the thrust coefficient K_T, the average error for the JBC propeller model ranged between 0.68 and 2.81%, while for the torque coefficient K_Q, the error was within 1.12 and 4.96% and finally for the propulsion efficiency, the error was within 1.82 and 4.87%. This can give an indication about the accuracy of the simulation because the maximum error is < 5%. It was also concluded that the POW simulation is grid dependent and the wall modeling can significantly influence the overall errors. As for the KVLCC2 ship propeller, the results were more accurate, since the grid was enhanced to overcome the grid problems in the JBC propeller simulation. The average error for the seven simulation cases of POW, for K_T, K_Q are 0.87 and 1.42%, respectively;

9. from the local flow prediction point of view, the local flow of the propeller in POW simulation for both propellers was recorded and highlighted for different propeller analysis speeds. The obtained results for velocity, pressure, TKE, vorticity, turbulent viscosity and vortices formation have been compared to similar analysis and experiments in the same context and showed a good similarity;

10. the simplified propeller model based on the actuator disk method was tested for the two ship models for nominal and effective wake prediction, as well as, for the self-propulsion parameters. The method was successful, straight forward and less expensive compared to 3D propeller modeling. The error of the numerically obtained self-propulsion parameters compared to experimental data for the JBC ship was within 0.2 and 6.28%; while for the KVLCC2 was 1.18 and 13.7%. This significant error 13.7% was for the torque coefficient K_Q in bare hull analysis, a value that similar to the one obtained with the same conditions in research performed with different CFD code, giving a reasonable impression about the methodology. Probably the error may return to error in the EFD data representation, since the values for ship with rudder had a very good match with the experiment;

11. the self-propulsion prediction based on the 3D sliding grid ship model could capture neatly accurate results regarding the self-propulsion parameters and the propeller rotation rate for both ship models. Minimum and maximum values, respectively, of 1.57 and 3.18% are the estimated errors for the propulsion characteristics computed based on the sliding grid technique. It was also concluded that, though the 3D propeller model is more realistic and accurate, it is still very expensive and more complex compared to the actuator disk model;

12. nominal and effective wake based on both models have been put in the validation test and succeeded to resemble accurately with the EFD results;

For Seakeeping performance

13. the seakeeping has been conducted for only the DTMB ship model on 3 levels when ship is sailing in regular head waves with fixed, free condition to heave and pitch, and finally, the roll decay performance prediction. All the three aspects have been conducted and compared to the available experimental data for similar simulations, showing a good correspondence between the CFD and EFD results;

14. the results obtained for the fixed ship conditions regarding the forces and moments showed to have a good agreement for the resistance prediction with an error range of 3.25 and 9.21% for the average and first amplitude of the computed resistance in waves, on the other hand, the heave force showed a high value of the error within 18.21 and 27.55%, and 10.19 and 12.5% for pitch moment, respectively. Though the error range seems to be significant, the results were compared with the data from G2010 workshop, and it was within a close range for some results with different codes;

15. free-surface and local flow were also predicted and compared to the EFD results resulting in a well predicted free-surface and close agreement for the local flow;

16. the free ship condition was conducted with a scope to assess the numerical errors, which was conducted successfully showing that the seakeeping simulation can be grid dependent and less time dependent, especially if the time step is small enough. 250 time-steps/wave period were considered enough based on the obtained results;

17. Ship responses for heave and pitch were recorded within an average error of 2.54% and 9.83% for heave and pitch, respectively; while for the resistance, the error was within 5%. All considered acceptable, except for the pitch response which requires more investigation. Overall, results resembled well with the results obtained by other researchers;

18. the added resistance in wave was computed and compared with the calm water condition, which recorded an added resistance value that varied between 8.1 and 39.2% compared to the resistance in calm water, depending on the wavelength. These values should be taken into considerations for any powering estimations;

19. the breaking effect, and hull wave interaction was analyzed and well predicted for the ship during the free condition showing that, the flare design pushes the flow outward

during the hull-wave separation, which keeps the deck dry during the simulation. At the ship stern, a breaking roaster-tail effect waves were observed during the simulation, whose effect was increasing as the ship speed increases;

20. the analysis of local flow showed that the boundary layer of the ship is suffering a significant deformation during the wave encounter. This effect was well captured and concluded that it will have a significant impact on the propulsion performance;
21. the roll decay performance was computed and presented for different initial roll angles based on a simplified general grid approach to avoid the drawbacks from the sliding and overset grids that are usually applied in this study, which is more complex and expensive. The overall conclusion for the effect of the change in the initial roll angle reduces the accuracy of the computed roll damping, even for the finest grids;
22. the simulation was proven to be grid dependent and time independent for a time step over 300 time-steps/roll period;
23. the influence of the roll damping on the free-surface topology and profile was highlighted concluding that the pressure and viscous effect cause distortion in the free-surface, which consequently might increase the wave making resistance component;
24. the speed effect on the roll damping and free-surface was demonstrated, showing that the damping increases as the speed increases; also, the viscous and pressure influence on the free-surface is reduced as the ship speed increases;
25. the local flow of the ship during the roll period was manifested and explained based on the velocity contours, TKE and vortex formation. The results revealed the deformation in the boundary layer and the formation of eddies and significant flow separation at the bilge keel, which contributes to the increasing of the damping effect; and increases the ship resistance during the damping process.

In general, it can be concluded that the studies presented in this research work can be considered as a numerical towing tank, which succeeded in reproducing the different tank test experiments in various ship hydrodynamic aspect in a numerical representation. The obtained results are encouraging to set the base for further research in the field based on the consistent validation processes that were conducted during this research.

7.2 Personal Contributions

In the scope of analyzing the ship hydrodynamic performance, it was very important to generalize the method for multiple ship types, categories and geometries. For this purpose, three ships were chosen to achieve this goal. The first is the JBC bulk carrier ship model, while the second is the KVLCC2 ship model, and finally, the DTMB surface combatant model. To ensure that the computational simulations is not just theoretically approached, the practicality of the method were assessed based on the validation of the obtained results against experimental data, to ensure, not just the capability of the method to predict ship hydrodynamic performance, but also the accuracy of the obtained results from the numerical simulations. Rigorous CFD analysis cases have been studied with different scopes to cover the main objectives concerned in every case.

These cases are outlined in Table 7.1 showing the ship performance aspect of interest, main objectives from the study, and finally on which model the study was performed.

Table 7.1 Ship performance contribution in the present study

Ship Performance		Objective		Ship Model		
				JBC	KVLCC2	DTMB
CFD	Resistance	Drag Forces	Bare Hull	✓	✓	✓
			With Appendages	✓	✓	✓
		Motions		✓	✓	✓
		Free-surface		✓	✓	✓
		Local Flow		✓	✓	✓
		Flow Separation and Vortex detection		✓	✓	✓
		Banking Effect		x	x	✓
	Propulsion	Open Water		✓	✓	x
		Propulsion	Nominal Wake	✓	x	x
			Effective Wake	✓	x	x
			Self-propulsion Point	✓	x	x
		Local Flow & Vortex Prediction		✓	✓	x
	Seakeeping	Forces		x	✓	✓
		Motions		x	✓	✓
		Free-surface		x	✓	✓
		Local Flow & Vortex Prediction		x	x	✓
		Roll Damping		x	x	✓
Experiment	Resistance	Forces (Bare Hull)		x	x	✓
		Motions		x	x	x
		Free-surface		x	x	✓
		Tank Walls Effect		x	x	✓

Reviewing the major contributions in this research work, the following outcomes can be presented to enlighten the reader about the basic contributions achieved:

1. in the beginning of this research, a general overview was given about the motivation, principal objectives and scope of the study. This was accompanied with an executive and constructed review of the state-of-the art and recent research in ship hydrodynamics. A historical review for the conceptual initiation of the most famous ship hydrodynamic techniques were presented, highlighting the pros and cones of each method and whether it can be applicable in the current demands in ship hydrodynamics field. Principal review of the literature was introduced for the work of other researchers in the field, highlighting their achievements and how their work could be correlated to the studies performed in this research in every aspect. Ship resistance, propulsion and seakeeping research have been discussed and stated the limitations or the achievement in other research to build on or to continue the work from their standing point. The concluded achievement from the literature review stated that the early research in the field are very active and well conceded for ship resistance and propulsion; yet, an extra effort was important to be carried out in seakeeping and maneuvering applications. All these details have been illustrated in Chapter I;

2. the general ship hydrodynamic problem was presented mathematically in Chapter II focusing on the solution models and the basic process details to achieve the final solution of the problem;

3. to ensure sufficient theoretical aspects on the general representation and considerations in the CFD process in ship hydrodynamic field, Appendix A gives a brief description of the general methodologies and techniques available, with their pros and cons, capabilities and limits, in order to set the base for the main choice that can be made to reach the best quality solution possible, of course, according to the available resources;

4. since the CFD method is, in general, an approximation of a physical problem, the method must contain errors and uncertainties. Those errors and uncertainties have to be assessed to ensure that the solution is solid and does not have other influences from mathematical, numerical or physical errors. For this purpose, the understanding of sources of errors, their reason and how to avoid them was necessary to be represented in Chapter III;

5. in Chapter IV, the numerical applications were presented for predicting ship resistance performance. Three ships are investigated including the Bulk carrier JBC model, the tanker KVLLC2 model and the surface combatant DTMB ship model. For the JBC, the tank test performed and presented in the International Workshop in Tokyo 2015 was numerically replicated for ship with and without the energy saving device (ESD). Ship resistance, vertical motions, free-surface and local flow were assessed and compared to the EFD data provided from the Workshop. A combined grid and time step convergence study was conducted to estimate the numerical errors and uncertainties in the numerical solution. A special focus on the choice of the most suitable turbulence model was also included in the study, and the results were presented for 7 different turbulence models, such as the Spallart-Almaras one equation model, k-ε, k-ω and its modified forms, the Baseline and the Shear Stress Transport with its classic Menter's form and the modern 2003 form, and finally the Explicit Algebraic Stress Model EASM. The influence of the duct on the flow enhancement was covered by means of local flow analysis and duct contribution in ship drag.

   For the KVLCC2 ship model, the bare hull ship was analyzed in fixed condition with a special focus on the free-surface and the local flow to ensure the simulation capabilities in that condition. Later, the ship with rudder was analyzed with sinkage and trim free condition. The reason was to highlight the possibility of the CFD model to cover the ship with rudder performance, since the JBC ship test had no rudder included. The numerical errors were assessed based on a grid convergence study.

   For the DTMB ship model, 3 simulation levels were carried out. Two are CFD-based for bare hull and appended ship condition. In that simulation, all the hydrodynamic parameters for drag, motion free-surface and local flow were presented for both cases with a special focus on the influence of appendages on the total resistance to set the base for further investigation regarding their position and shape optimization. The third is an interactive-experimental-CFD assessment for the ship resistance and free-surface prediction with the effect of tank walls during experiment on the total resistance and free-surface configuration. The numerical errors were assessed based on a grid convergence study;

6. in Chapter V, two propeller models were analyzed, the JBC propeller model with 5 blades and the KVLCC2 propeller model with highly skewed 4 blades. The JBC propeller was analyzed to set the base for the main POW simulations, for this reason, a grid convergence study was carried out on four grids to study the influence of the grid resolution on the numerical solution. The thrust, torque and efficiency of the propeller were computed and compared with success to the EFD data. A fine grid was concerned with the propeller wake flow, where three different turbulence models were applied including SST k-ω, EASM and DES models. The wake flow was analyzed, and a special focus was made for the vortex formations.
   For the KVLCC2 propeller model, all the limitations and grid errors in the JBC propeller were enhanced in this study. This opened the way to not just predict the thrust, torque and efficiency of the propeller, but to use more complex turbulence modeling, such as DES, DDES and IDDES, to grasp more understanding of the flow separation and vortex formations in the propeller wake.
   For the propeller behind the ship, two models were used to solve the self-propulsion performance of the ship based on the actuator disk approach and sliding grid 3D propeller modeling. Nominal and effective wake for the JBC ship model were assessed and compared to the EFD data. The sliding grid also succeeded in predicting the self-propulsion point and self-propulsion parameters accurately, beside a good representation for hull propeller interaction and vortices formation in the wake. The influence of grid resolution on the simulation accuracy was also conducted based on three computational grids in each approach.
   After the rudder geometry was introduced in the Tokyo 2015 Workshop website, a dedicated study for the ship with rudder was carried out and compared to the ship without rudder condition, revealing the influence of the rudder on the propeller performance and the interaction between hull, propeller and rudder.
   Same principles were applied on the self-propulsion performance prediction for the KVLLC2 ship model in self-propulsion condition with and without rudder;

7. in Chapter VI, ship seakeeping performance was investigated for the DTMB model on three simulation levels. The first is focused on the seakeeping performance of a diffraction condition when the ship is fixed in regular head waves. The second is dedicated to the same analysis as the first case, except that the ship is free in two degrees of freedom, heave and pitch. The third is concerned with investigating the ship hydrodynamic performance in the roll decay condition for the ship appended with bilge keels only.
   In the first condition, when the ship was fixed in regular head waves, a special focus on the analysis of resistance and heave forces along with the pitch moment was predicted and compared to the EFD data for 3 wave height conditions and same wavelength. The free-surface was predicted and compared to the EFD results. The local flow was highlighted, but the main analysis of the local flow was kept for the motion condition, which was considered more critical and practical compared to the fixed ship condition.
   In the motion conditions, 12 simulation cases were carried out; the first was dedicated to the verification and validation study of the numerical errors in seakeeping simulations. The next seven cases were performed to estimate the hip responses and the added resistance in waves. The results in this case study were directly compared with a proper agreement

with the corresponding experimental data. Cases 9 and 10 were dedicated for the ship responses when the ship speed is set to zero with two different wave amplitudes and same wavelength. Results were computed for heave and pitch responses and compared to the similar experimental data.

Free-surface and local flow analysis were presented in cases 11 and 12, a special focus on the wave separation, breaking and green deck was carried out in case 11 for the free-surface prediction with a spot on the high-speed ship in waves. Separations and break were observes, while no greening effect was observed on the deck.

Local flow analysis from case 12 revealed a very important aspect regarding the flow oscillation in the ship boundary layer as a consequence for the ship interaction with wave, which may significantly affect the propulsion efficiency during sailing in waves.

Finally, the DTMB simulation in roll decay condition was carried out rigorously with multiple objectives regarding the validation of the methodology at different initial roll angles, assessment of the numerical errors based on grid and time step convergence study, studying the speed effect on the roll damping performance, free-surface analysis at different ship speeds and finally, the analysis of local flow during the roll damping process and representing the hull and bilge keels interaction with the flow to highlight the viscous flow damping effect.

Within almost five years of research in the field, since the practical start of this research work, with a special focus on studying the ship hydrodynamic performance, the scientific research effort resulted in an outcome of seventeen research papers, thirteen of which are indexed in the ISI proceedings, two are under press and expected to be indexed in ISI proceedings, one is indexed in SCOPUS and, finally, one paper indexed in the international data base IDB. One research paper is published in the Journal of Marine Science and Engineering, fiftheen are published in conference proceedings from participations in ten international conferences, four of which were held in Romania, and six in different other European countries. Three awards were accomplished in three conferences for the best presentation, one as the first place, and two as the second.

Applying the same principles from this research work in practical applications, the book author worked as a team member in a national project to study the influence of mounting a central skeg on Danube pusher tugboat between the propellers in order to enhance the propeller performance and directional stability of the tug. The author performed the numerical investigation of the problem and introduced the results for the tug separately and within the convoy.

7.3 Recommendations and Future Perspectives

The challenges in ship hydrodynamic field are endless; the new demands in the field are increasing progressively every day. The need to keep track of the continuous changes is urgent and still some problems need more analysis and thorough investigations. Though the research in this book was conducted to cover most of the ship hydrodynamic aspects, there are still some sides have not been approached; other aspects were not difficult to perform; others were incompletely analyzed; and finally, some other aspects have been analyzed and completed, yet not included in the final form of the present book manuscript.

Heading from the fact that nothing is complete and there is always a window to enhance the proposed work in this book, the following points can be expressed as a future plan to continue in the same direction in ship hydrodynamic performance research:

1. in the ship resistance simulations, the method was applied only on model scale ship with various turbulence models. In the same scope, a study with more complex turbulence model can help understanding the interaction between the flow and the hull, showing more details in the wake field of the ship, to set a proper base for ship hull performance enhancement. Further beyond the scope, the analysis of full scale ships can provide better and more realistic representation of the hull performance in real sailing conditions. Despite the fact that this requires more complex studies, advanced resources and rigorous research effort to keep the work intact, it is still a very good base for the future research plan;

2. for the propulsion performance, in the same scope, the analysis performed in the present research studies did not include the cavitation performance of the propeller. This is one of the most important aspects regarding the propeller performance prediction in both POW and behind the ship. This should be conducted soon. Beyond the scope, could also be the applications of ship propulsion at the full scale;

3. as for the seakeeping performance, the studies conducted in this research work were limited for regular head waves. To keep the problem closer to the reality, the ship seakeeping performance at different heading angles should be conducted with all the six degrees of freedom. This can provide better understanding of the ship behavior in waves, especially with the advance in predicting the viscous flow effect during seakeeping simulation, compared to the classic BEM-based methods. In addition, it should be carried out a study for the ship performance in a seaway, which will be more realistic and more accurate from the physical modeling point of view. Still, this problem is very complex and requires massive computational resources and significant research effort.

Finally, the results obtained within the current research in the scope of predicting the maneuvering performance of the ship can be published in recognized journal or conference proceedings.

References

[1] ITTC. *The Stability in Waves Committee, Final Report and Recommendations to the 28th ITTC*. Proceedings of the 28th International Towing Tank Conference, Vol. I (2017), 275–335, Wuxi, China.

[2] Tursini, L. *Leonardo da Vinci and the problems of navigation and naval design*. Transactions of the Institute of Naval Architects, 95 (2) (1953) 97–102.

[3] Gawn, R. W. L., *Historical Notes on Investigations at the Admiralty Experiment Works*, *Torquay*. Transactions of the Institute of Naval Architects, 8 (1941) 80–139.

[4] Gawn, R. W. L. *The Admiralty experiment works, Haslar*. Transactions of the Institute of Naval Architects, 97 (1) (1955) 1–35.

[5] Froude, W. *Experiments on surface friction*. British Association Reports (1872, 1874).

[6] Froude, W. *On Experiments with H.M.S. Greyhound*, Transactions of the Institute of Naval Architects, 15 (1874) 36–73.

[7] Dejhalla, R. and Prpić-Oršić J. *A Review of the state-of-the art in marine hydrodynamics*, Journal of Brodogradnja Ship Building, 57 (1) (2006) 13–22.

[8] ITTC, *The Resistance Committee, Final Report and Recommendations to the 25th ITTC*, Proceedings of the 25th International Towing Tank Conference, Vol. I (2008), 21–81, Fukouka, Japan.

[9] Taylor, D.W. *Speed and power of ships*. Press of Ransdell (1933), Washington. DC.

[10] Gertler, M. *A re-analysis of the original test data for the Taylor standard series*. TMB Report 806 (1954) DTRC.

[11] Keuning, J. A. and Sonnenberg, U. B. *Approximation of the hydrodynamic forces on sailing yacht hulls based on the Delft systematic yacht hull series*. 15th International HISWA Symposium on Yacht Design and Yacht Construction (1998) 99–152, Amsterdam, Netherlands.

[12] Doust, D. J., and O'Brien, T. P. *Resistance and propulsion of trawlers*. North East Coast Institution of Engineers and Shipbuilders Transactions, 75 (1959).

[13] Holtrop, J. and Mennen, G. G. J. A*n approximate power prediction method*. International Shipbuilding Progress, 29 (335) (1982) 166–170.

[14] Bertram V. *Practical Ship Hydrodynamics*. 2nd Edition, Butterworth Heinemann (2000), Oxford, ISBN 0-7506-4851-1.

[15] Thompson, W. (Lord Kelvin). *On ship waves transactions*. IME, 3 (1887), 409–433.

[16] Thompson, W., (Lord Kelvin). *On deep water two-dimensional waves produced by any given initiating disturbance*. Proceedings of the Royal Society of Edinburgh, 25 (1) (1904), 185–196.

[17] Havelock, T.H., *The wave-making resistance of ships: a theoretical and practical analysis*. Proceedings of the Royal Society, A. 82 (1909), Fellow of St. John's College, Cambridge, Lecturer in Applied Mathematics, Armstrong College, New east Leon-Tyne.

[18] Wigley, C. *Ship Wave Resistance*. Northeast Coast Institution of Engineers and Shipbuilders Transactions, 47 (1931).

[19] Wigley, C. *A comparison of experiment and calculated wave profiles and wave resistance for a form having parabolic waterlines*. Proceedings of the Royal Society, 144 (851) (1934), 144–159.

[20] Michell, J. H. *The wave resistance of a ship*. Philosophical Magazine, 5 (1898), 45.

[21] Havelock, T.H. *Wave resistance theory and its application to ship problems*. Transactions of the Society of Naval Architects and Marine Engineers, 59 (1951) 13–24.

[22] Hess, J.L., Smith, A.M.O. *Calculation of non-lifting potential flow about arbitrary three-dimensional bodies*. Douglas Aircraft Report, No. ES40622 (1962), Long Beach, CA: Douglas Aircraft.

[23] Baar, J. J. M., and Price, W. G. *Developments in the calculation of the wave making resistance of ships*. Proceedings of the Royal Society of London, 416 (1988) 115–147.

[24] Tuck, E. O. *The wave resistance formula of J.H. Michell (1898) and its significance to recent research in ship hydrodynamics*. Journal of the Australian Mathematical Society, Series B, 30 (1989), 365–377.

[25] Dawson, C. *A practical computer method for solving ship wave problems*. 2nd International Conference on Numerical Hydrodynamics (1977) 30–38. Berkeley, CA.

[26] Raven, H.C. *A solution method for the nonlinear ship wave resistance problem*. Ph.D. Thesis (1996), Technical University of Delft, MARIN, Holland.

[27] Larsson, L. and Raven H.C. *Ship resistance and flow*. *Principles of naval architecture series*, The Society of Naval Architects and Marine Engineers, (2010), New Jersey, ISBN 978-0-939773-76-3.

[28] Janson, C. E. *Potential flow panel methods for the calculation of free surface flows with lift*, PhD Thesis, Chalmers University of Technology, (1997).

[29] VIRTUE, NSC Members, *Best practice guidelines for marine application in computational fluid dynamics*. VIRTUE – The Virtual Tank Utility in Europe, MARNET CFD (2008).

[30] Larsson, L., Regnström, B., Broberg, L., Li, D.Q. and Janson, C.E. *Failures, fantasies, and feats in the theoretical/numerical prediction of ship performance*. The 22nd Symposium on Naval Hydrodynamics, (1999) 11-32, Washington, D.C.

[31] von Kerczek, C.H. A new generalized cross-flow momentum integral method for three-dimensional ship boundary layers. SAI Report No. 463-82-085-LJ (1982).

[32] von Kerczek, C.H., Christoph, G., and Stern, F. Further developments of the momentum integral method for ship boundary layers. SAI Report No. 8413046 (1984).

[33] Stern, F. Effects of waves on the boundary layer of a surface-piercing body, Journal of Ship Research, 30 (4) (1986) 256–274.

[34] Larsson, L. Proceedings of the 1980 SSPA-ITTC Workshop on ship boundary layers. SSPA Publication No. 90 (1981). Gothenburg: Swedish State Shipbuilding Experiment Tank, SSPA.

[35] Stern, F., Yang, J., Wang, Z., Sadat-Hosseini, H., Mousaviraad, M., Shanti, B., Xing, T. *Computational ship hydrodynamics: nowadays and way forward*. International Shipbuilding Progress, 60 (1-4) (2013), 3–105.

[36] Blazek, J. *Computational fluid dynamics: principles and applications*. 1st Edition (2001), Elsevier, Oxford, ISBN 0-08-043009-0.

[37] Larsson, L., Patel, V. C., and Dyne, G. (Eds.). *SSPA-CTH-IIHR Workshop on ship viscous flow*. Report No. 2 (1991). Gothenburg: FLOWTECH International AB.

[38] Wilson, R. V. *A review of computational ship hydrodynamics*. Technical report, SimCenter: National Center for Computational Engineering, The University of Tennessee at Chattanooga, College of Engineering and Computer Science, (2008).

[39] Tahara, Y., Stern, F., and Rosen, B. *An interactive approach for calculating ship boundary layers and wakes for nonzero Froude number*. Journal of Computational Physics, 98 (1) (1992) 33–53, IIHR Reprint No. 892.

[40] Wackers, J., Koren, B., Raven, H. C. van der Ploeg, A., Starke, A. R. Deng, G. B., Queutey, P., Visonneau, M., Hino, T. and Ohashi K. *Free-surface viscous flow solution methods for ship hydrodynamics*. Archives of Computational Methods in Engineering, 18(1) (2011) 1–41.

[41] Kodama, Y., Takeshi, H., Hinatsu, M., Hino, T., Uto, S., Hirata, N. and Murashige, S. (eds.) *Proceedings, CFD Workshop 1994*. Ship Research Institute, Tokyo, Japan.

[42] Wilcox, D.C. *Turbulence modeling for CFD*. 2nd Edition (1998) DCW Industries, La Canada, CA. ISBN: 978-0963605153.

[43] Larsson, L., Stern F. and Bertram V. (eds.) *Gothenburg 2000 a workshop on numerical ship hydrodynamics*. Chalmers University of Technology (2000), CHA/NAV/R-02/0073.

[44] Larsson, L., Stern, F. and Bertram, V. *Benchmarking of computational fluid dynamics for ship flows: the Gothenburg 2000 workshop*. Journal of Ship Research, 47 (1) (2003) 63–81.

[45] Hino, T. (editor). *CFD Workshop Tokyo 2005*, National Maritime Research Institute (2005), Tokyo, Japan.

[46] Xing, T., Carrica, P., and Stern, F. *Computational Towing Tank Procedures for Single Run Curves of Resistance and Propulsion*. ASME Journal of Fluids Engineering. 130 (2) (2008) 1–14.

[47] Larsson, L., Stern, F., Visonneau, M., (eds.). *Numerical ship hydrodynamics: an assessment of the Gothenburg 2010 Workshop*. Springer (2013). ISBN 978-94-007-7188-8.

[48] NMRI, Tokyo 2015, *A Workshop on CFD in ship hydrodynamics*, National Maritime Research institute (2015), http://www.t2015.nmri.go.jp/jbc.html.

[49] Larsson, L., *Resistance, sinkage, trim and wave pattern review*, National Maritime Research Institute, Tokyo 2015 Workshop, http://www.t2015.nmri.go.jp/Presentations/Day1-AM4-JBC-Resist_etc-Larsson.pdf.

[50] Kim, J. *Report of the results for KCS Resistance & self-propulsion*. National Maritime Research Institute, Tokyo 2015 Workshop, http://www.t2015.nmri.go.jp/Presentations/Day2-AM2-KCS-Resistance_SP-Kim.pdf.

[51] Larsson, L. *CFD in ship hydrodynamics*. Chalmers University of Technology Gothenburg (2008), Sweden.

[52] Carlton, J. S. *Marine Propellers and Propulsion*. 2nd Edition, Butterworth Heinemann (2007), Oxford, UK. ISBN 9780080549231.

[53] Rankine, W. J. M. *On the mechanical principles of the action of propellers*. Transactions of the Institution of Naval Architects, 6 (1865) 13–39.

[54] Froude, R.E. *On the part played in propulsion by differences in fluid pressure*. Transactions of the Royal Institution of Naval Architects, 30 (1889) 390–405.

[55] Froude, W. *On the elementary relation between pitch, slip and propulsive efficiency*. Transactions of the Institution of Naval Architects, 19 (1878) 47–65.

[56] Betz, A. Schraubenpropeller mit geringstem Energieverlust. K. Ges. Wiss, Gottingen Nachr. Math. -Phys., (1919) 193–217.

[57] Goldstein, S. *On the vortex theory of screw propellers*. Proceedings of the Royal Society, London Series A, 123 (1929) 440–465.

[58] Burrill, L. C. *Calculation of marine propeller performance characteristics*. North East Coast Institution of Engineers and Shipbuilders Transactions, 60 (1944).

[59] Lerbs, H. W. *Moderately loaded propellers with a finite number of blades and an arbitrary distribution of circulation*. Transactions of the Society of Naval Architects and Marine Engineers, 60 (1952) 73–123.

[60] Molland, A. F., Turnock, S. R. and Hudson D. A. Ship resistance and propulsion, practical estimation of ship propulsive power. Cambridge University Press (2011), New York, US, ISBN 978-0-521-76052-2.

[61] Sparenberg, J.A. *Application of lifting surface theory to ship screws*. Proceedings of the Koninhlijke Nederlandse Akademie van Wetenschappen, Series B, Physical Sciences, 62 (5) (1959) 286–298.

[62] Pien, P.C. *The calculation of marine propellers based on lifting surface theory*. Journal of Ship Research, 5 (2) (1961) 1–14.

[63] Kerwin, J.E. *A deformed wake model for marine propellers*. Department of Ocean Engineering Rep. 76–6, MIT (1976).

[64] Greeley, D.A. and Kerwin, J. E. *Numerical methods for propeller design and analysis in steady flow*. SNAME Transactions, 90 (1982).

[65] Kerwin, J.E., Chang-Sup Lee. *Prediction of steady and unsteady marine propeller performance by numerical lifting-surface theory*. SNAME Transactions, Paper No. 8 (1987), Annual Meeting.

[66] ITTC. *The Propulsion Committee, Final Report and Recommendations to the 24th ITTC*. Proceedings of the 24th International Towing Tank Conference, Vol. I (2005), 73–136, UK.

[67] Hess, J. L. and Valarezo, W. O. *Calculation of steady flow about propellers by means of a surface panel method*. AIAA Paper No. 85-0283 (1985).

[68] Kim, H. T. and Stern, F. *Viscous flow around a propeller-shaft configuration with infinite pitch rectangular blades*. Journal of Propulsion and Power, 6 (4) (1990) 434–444.

[69] Uto, S. *Computation of incompressible viscous flow around a marine propeller*. Journal of Society of Naval Architects of Japan, 172 (1992) 213–224.

[70] Stern, F., Kim, H. T., Patel, V. C. and Chen, H. C. *A Viscous flow approach to the computation of propeller-hull interaction*. Journal of Ship Research 32(4) (1988) 246–262.

[71] Guilmineau, E., Deng, G. B., Leroyer, A., Queutey, P., Visonneau, M. and Wackers, J. *Influence of the turbulence closures for the wake prediction of a marine propeller*. Proceedings of the 4th International Symposium on Marine Propellers, smp'15 (2015), Austin, Texas, USA.

[72] Wang, L. Z., Guo, C. Y., Su, Y. M. and Wu, T. C. *A numerical study on the correlation between the evolution of propeller trailing vortex wake and skew of propellers*. International Journal Naval Architecture & Ocean Engineering, 10 (2018) 212-224.

[73] Stern, F., Kim. H. T., Zhang, D. H., Toda, Y., Kerwin, J. and Jessup, S. *Computation of viscous flow around propeller-body configurations: series 60 CB = 0.6 ship model*. Journal of Ship Research 38 (2) (1994) 137-157.

[74] ITTC. *The Specialist Committee on Computational Fluid Dynamics, Final Report and Recommendations to the 26th ITTC*. Proceedings of the 26th International Towing Tank Conference, Vol. II (2011), 337–377, Rio de Janeiro, Brazil.

[75] Zhang Z. R., *Verification and validation for RANS simulation of KCS container ship without/with propeller*. Journal of Hydrodynamics, 22 (5) (2010) 932–939.

[76] Visonneau, M., Queutey, P., Deng, G. B., Wackers, G., Guilmineau, J., Leroyer, A. and Benoit, M. *Computation of free-surface viscous flows around self-propelled ships with the help of sliding grids*. 11th International Conference on Computer Applications and Information Technology in the Maritime Industries, COMPIT (2012), Liege, Belgium.

[77] Shen, Z. and Korpus, R. *Numerical simulations of ship self-propulsion and maneuvering using dynamic overset grids in OpenFOAM*. Tokyo 2015 Workshop on CFD in Ship Hydrodynamics, Tokyo (2015), Japan.

[78] Castro, A., Carrica, P. M. and Stern, F. *Full scale self-propulsion computations using discretized propeller for KRISO containership KCS*. Journal of Computer and Fluids, 51 (2011) 35–47.

[79] Chase, N., Carrica, P. M. *Submarine propeller computations and application to self-propulsion of DARPA Suboff*. Ocean Engineering, 60 (2012) 68-80.

[80] Mofidi, A. J. Martin, E. and Carrica. P. M. *RANS, DES and DDES simulations of self-propulsion of the Japan Bulk Carrier*. Tokyo 2015 Workshop on CFD in Ship Hydrodynamics, Tokyo (2015), Japan.

[81] International Symposiums on Marine Propulsors (SMP), http://www.marinepropulsors.com/proceedings.php.

[82] Sadat-Hossieni, H., Wu, P. C., Carrica, P. M., Kim, H., Toda, Y. and Stern, F. *CFD verification and validation of added resistance and motions of KVLCC2 with fixed and free surge in short and long head waves*. Journal of Ocean Engineering, 59 (2013) 240-273.

[83] Kim, M., Hizir, O., Turan, O. and Incecik, A. *Numerical studies on added resistance and motions of KVLCC2 in head seas for various ship speeds*. Ocean Engineering, 140 (2017) 446–476.

[84] Sato, Y., Miyata, H., and Sato, T., *CFD simulation of 3D motion of a ship in waves: application to an advancing ship in regular heading waves*. Journal of Marine Science and Technology 4(1999)108–116.

[85] Stern, F., Wilson, R., Longo, J., Carrica, P. M., Xing, T., Tahara, Y., Simonsen, C., Kim, J., Shao, J., Irvine, M., Kandysamy, M., Ghosh, S. and Weymouth, G. *Paradigm for development of simulation based design for ship hydrodynamics*. The 8th International Conference on Numerical Ship Hydrodynamics (2003), Busan, Korea.

[86] Carrica, P. M., Wilson, R. V., Noack, R. W. and Stern, F. *Ship motions using single phase level set with dynamic overset grids*. Computers and Fluids 36 (9) (2007)1415–1433.

[87] Irvine, M., Longo, J. and Stern, F., *Pitch and heave tests and uncertainty assessment for a surface combatant in regular head waves*. Journal of Ship Research 52(2) (2008) 146–163.

[88] Deng, G. B., Queutey, M. and Visonneau, M. *RANS prediction of the KVLCC2 tanker in head waves. Journal of Hydrodynamics*. 22 (5) (2010) 476–481.

[89] Queutey, P., Visonneau, M., Leroyer, A., Deng, G. and Guilmineau, E. *RANSE simulations of a naval combatant in head waves*. In Proceedings of the 11th Numerical Towing Tank Symposium (2008) 11–16, Brest, France.

[90] Shen, Z., Carrica, P. M. and Wan, *D. Ship motions of KCS in head waves with rotating propeller using overset grid method*. Paper OMAE2014-23657 (2014), San Francisco, California, USA.

[91] Mousaviraad, M. Carrica, P.M. and Stern, F. *Development and validation of harmonic wave group single-run procedure for RAO with comparison to regular wave and transient wave group procedures using URANS*. Ocean Engineering, 37 (2010) 653–666.

[92] ITTC. *The Specialist Committee on CFD in Marine Hydrodynamics - Final report and Recommendations to the 27th ITTC*. Proceedings of the 27th International Towing Tank Conference, Vol. II (2014) 522–567.

[93] Wilson, R. V., Carrica, P. M. and Stern, F. *Unsteady RANS method for ship motions with application to roll for a surface combatant*. Computers and Fluids, Vol. 35 (5) (2006) 501-524.

[94] Irkal, M. A. R., Nallayarasu, S. and Bhattacharyya, S. K. *CFD approach to roll damping of ship with bilge keel with experimental validation*. Applied Ocean Research. 55 (2016) 1–17.

[95] Gao, Q. and Vassalos, D. Numerical study of the roll decay of intact and damaged ships. The 12th International Ship Stability Workshop (2011) 277–282, Washington, USA.

[96] ITTC. *The Seakeeping Committee - Final report and Recommendations to the 28th ITTC*. Proceedings of the 28th International Towing Tank Conference, Vol. I (2017) 213–273.

[97] Morgan, W. B. and Lin, W. C. *Predicting ship hydrodynamic performance in today's world*. Naval Engineers Journal (1998) 91–98.

[98] Abkowitz, M.A., 1969. *Stability and motion control of ocean vehicles*. Ocean Engineering Series, MIT Press (1969) 348 p, ISBN: 9780262510066.

[99] Nomoto, K. *Analysis of Kempf's standard maneuver test and proposed steering quality indices*. Proceedings of 1st Symposium on Ship Maneuverability, Department Of The Navy, Maryland, United State of America (1960) 275–304.Roseman, D. P. (Editor). *The MARAD systematic series of full form ship models*. SNAME (1987) 384 p.

[100] Lewis, E. V., (Editor). *Principles of naval architecture, Vol. III - Motions in Waves and Controllability*. SNAME (1989), Jersey City, NJ, US.

[101] Clarke, D., Gedling, P. and Hine, G. *The application of maneuvering criteria in hull design using linear theory*. The Naval Architect (1983) 45–68.

[102] Stern F., Agdrup K., Kim S. Y., Hochbaum, A. C., Rhee, K. P., Quadvlieg, F., Perdon, P., Hino, T., Broglia, R. and Gorski, J. *Experience from SIMMAN 2008 – the first workshop on verification and validation of ship maneuvering simulation methods*. Journal of Ship Research 55 (2) (2011) 135–147.

[103] Toxopeus, S. *Viscous flow calculations For KVLCC2 in deep and shallow water*. 4th Int. Conference Computational Methods in Marine Engineering (2011), Lisbon, Portugal.

[104] Carrica, P. M. and Stern, F. *DES Simulations of KVLCC1 in turn and zigzag manoeuvres with moving propeller and rudder*". SIMMAN 2008, Copenhagen, Denmark.

[105] Sadat‐Hosseini, S., Kim, D. H., Taylor, G. L., Fu, T., Terril, E. and Stern, F. ***V****ortical structures and instability analysis for Athena in turning maneuver with full-scale validation*, 30th Symposium on Naval Hydrodynamics (2014) 23 p, Hobart, Australia.

[106] Sadat‐Hosseini, H., Sanada, Y. and Stern, F. *Experiments and CFD for ONRT course keeping and turning circle maneuvering in regular waves*. WMTC15 (2015), Providence, Rhode Island, USA.

[107] Liu, Y., Zou, Z. J. and Zou, L. *RANS based numerical simulation of captive model tests in shallow water for the DTC container carrier*. MASHCON (2016) 73‐82, Hamburg, Germany.

[108] ITTC. *The Maneuvering Committee - Final report and Recommendations to the 27th ITTC*. Proceedings of the 27th International Towing Tank Conference, Vol. I (2014).

[109] Queutey, P. and Visnonneau, M. *An interface capturing method for free-surface hydrodynamic flows.* Computers and Fluids, 36 (2007) 1481–11510.

[110] NUMECA, FINE™/Marine. *Theoritical manual, ISIS-CFD*. Equipe Dynamique des Systèmes Propulsifs, Marins, Laboratoire de Recherche en Hydrodynamique, Energétique, et Environnement Atmosphérique, Ecole Centrale de Nantes, Nantes Cedex 3, France (2016).

[111] AIAA, *Guide for the verification and validation of computational fluid dynamics simulations*. The American Institute of Aeronautics and Astronautics, G-077-1998.

[112] Roache P. J. *Verification and validation in computational science and engineering*. Hermosa Publishers: Albuquerque, NM, (1998). ISBN: 9780913478080.

[113] ITTC, *Recommended procedures, Guide to the expression of uncertainty in experimental hydrodynamics*. International Towing Tank Conference, ITTC Recommended Procedures and Guidelines (7.5-02-01-01), Rev. 02 (2014) 17p.

[114] ITTC, *Recommended procedures and guidelines, uncertainty analysis in CFD verification and validation methodology and procedures*. International Towing Tank Conference, ITTC Recommended Procedures and Guidelines (7.5-03-01-01), Rev. 02 (2008) 12p.

[115] Stern, F., Wilson, R. and Shao, J. *Quantitative approach to V&V of CFD simulations and certification of CFD codes*. International Journal for Numerical Methods in Fluids, 50 (2006) 1335–1355.

[116] Eça, L. and Hoekstra, M. *On the influence of the iterative error in the numerical uncertainty of ship viscous flow calculations*. Proceedings of the 26th Symposium on Naval Hydrodynamics, Rome, Italy (2006).

[117] Wilson, R. V., Shao, J. and Stern, F., *Discussion: Criticisms of the "correction factor" verification method 1*. Journal of Fluids Engineering, 126(4) (2004), 704-706.

[118] Roache, P. J. *Criticisms of the "correction factor" verification method*. Journal of Fluids Engineering, 125(4) (2003), 732–733.

[119] Wilson, R. and Stern, F. *Verification and validation for RANS simulation of a naval surface combatant*. Standards for CFD in the aerospace industry, AIAA 2002-0904 Aerospace Sciences Meeting, Reno, Nevada (2002).

[120] d'Aure, B., Mallol, B., Hirsch, C. *Resistance and seakeeping CFD simulations for the Korean container ship*, Proceedings of the Tokyo 2015: A Workshop on CFD in Ship Hydrodynamics (2015), https://numeca.com/docs/2015-tokyo_workshop-_resistance_and_seakeeping_cfd_simulations_for_the_korean_container_ship_0.pdf

[121] del Toro Lorrens, Á. *CFD verification and validation of ship hydrodynamics*. École Central de Nantes. Master Thesis (2015).

[122] Crepier, P. *Ship resistance prediction: verification and validation exercise on unstructured grids*. Proceedings of the 7th International Conference on Computational Methods in Marine Engineering, MARINE (2017), 365–376.

[123] ITTC, *Recommended procedures and guidelines, Practical guidelines for ship CFD applications*. International Towing Tank Conference, ITTC Recommended Procedures and Guidelines (7.5-03-02-03), Rev. 01 (2011), 18p.

[124] Larsson, L. *JBC, Resistance, sinkage, trim and wave pattern-review.* Power point presentation, Tokyo 2015, A Workshop on CFD in ship hydrodynamics, National Maritime Research institute (2015), https://t2015.nmri.go.jp/Presentations/Day1-AM4-JBC-Resist_etc-Larsson.pdf.

[125] Hirata, N. *JBC, Test Data in NMRI*. Power point presentation, Tokyo 2015, A Workshop on CFD in ship hydrodynamics, National Maritime Research institute (2015), https://t2015.nmri.go.jp/Presentations/Day1-AM2-JBC-TestData1-Hirata.pdff.

[126] Visonneau, M. *JBC, Local Flow Analysis*. Power point presentation, Tokyo 2015, A Workshop on CFD in ship hydrodynamics. National Maritime Research institute (2015), https://t2015.nmri.go.jp/Presentations/Day1-PM1-JBC-LocalFlow-Visonneau.pdf.

[127] Menter, F. R., Kuntz, M., Langtry, R., *Ten Years of Industrial Experience with the SST Turbulence Model*. Turbulence, Heat and Mass Transfer 4, ed: K. Hanjalic, Y. Nagano, and M. Tummers, Begell House, Inc., (2003), 625–632.

[128] Kim, W. J., Van, D. H., Kim D. H., *Measurement of flows around modern commercial ship models*. Exp. Fluid 31(2001), 567–578.

[129] Olivieri, A., Pistani, F., Avanzini A., Stern, F., *Towing Tank Experiments of Resistance and Trim, Boundary Layer, Wake, and Free-Surface Flow Around a Naval Combatant INSEAN2340 Model*. Iowa Institute of Hydraulic Research, The University of Iowa, IIHR report No.421, (2001).

[130] Longo, J., Shao, J., Irvine, M., Stern F., *Phase-averaged PIV for the nominal wake of a surface ship in regular head waves*. ASME, J. Fluids Eng. 129(5) (2007), 524–540.

[131] ITTC, *Recommended procedures and guidelines, Resistance Test*. International Towing Tank Conference, ITTC Recommended Procedures and Guidelines (7.5-02-02-01), Rev. 03 (2011), 13p.

[132] **Bekhit, A.**, Lungu, A., *Numerical Simulation of the Hydrodynamic Ship Performance*. Proceedings of the 1st International Conference on the Intelligent Transport System, INTSYS 2017, 29–30 November, Hyvinkää, Finland, published in Lecture Notes of the Institute for Computer Science, Social Informatics and Telecommunication Engineering, (2018), 120–129.

[133] **Bekhit, A.**, Popescu, F., *Local Flow Assessment of the Japan Bulk Carrier using Different Turbulence Models*, Proceedings of the 9th International Conference on Modern Technology in Industrial Engineering, MODTECH 2021, 23–26 June, online edition, Romania, IOP Conference Series: Material Science Engineering. Under press (2021).

[134] **Bekhit, A.**, Lungu, A., *Numerical Study of the* Resistance, Free-Surface and Self-Propulsion Prediction of the KVLCC2 Ship Model. Proceedings of the International Conference on Traffic and Transport Engineering, ICTTE Belgrade 2018, 27–28 September, Belgrade, Serbia. (2018), 333–340.

[135] **Bekhit, A.**, Lungu, A., *Verification and Validation Study for the Total Ship Resistance of the DTMB 5415 Ship Model*. Annals of "Dunarea de Jos" University of Galati, **Fascicle XI** – Ship Building, (2017), 53–60.

[136] **Bekhit, A.**, Lungu, A., *A Viscous Flow Simulation around a Fully Appended Ship Hull by Using a Finite Volume Technique*, Proceedings of the International Conference on Traffic and Transport Engineering, ICTTE Belgrade 2018, 27–28 September, Belgrade, Serbia. (2018), 325-332.

[137] **Bekhit, A.**, Obreja D., *Numerical and Experimental Investigation on the Free-surface Flow and Total Resistance of the DTMB Surface Combatant*. Proceedings of the 8th International Conference on Modern Technology in Industrial Engineering, MODTECH 2020, 23–27 June, online edition, Romania, IOP Conference Series: Material Science Engineering. **916**(012008) (2020).

[138] Guilmineau, E., Deng, G. B., Leroyer, A., Queutey, P., Visonneau, M., Wackers, J., *Numerical Simulations of the Cavitating and Non-Cavitating Flow around the Potsdam Propeller Test Case,* Proceedings of the 4th Int. Symposium on Marine Propellers, smp'15, (Austin, Texas, USA, June, 2015).

[139] Felli, M., Guj, G, Camussi, R., *Effect of the number of blades on propeller wake evolution*, Exp. Fluids **44** (3), (2008), 409–418.

[140] M. Felli, R. Camussi and F. Di Felice, *Mechanisms of evolution of the propeller wake in the transition and far fields*, J. Fluid Mech. 682, (2011), 5–53.

[141] Wang, L. Z., Guo, C. Y., Su, Y. M. Wu, T. C., *A numerical study on the correlation between the evolution of propeller trailing vortex wake and skew of propellers*, Int. J. Naval Architecture and Ocean Eng. 10 (2018), 212–224.

[142] **Bekhit A.**, Lungu A., *Simulation of the POW Performance of the JBC Propeller*, Proceedings of the 16th International Conference on Numerical Analysis and Applied Mathematics, ICNAAM 2018, 13–18 September, Rhodes, Greece. American Institute of Physics, AIP Conference Proceedings, **2216**, 450007, (2019).

[143] **Bekhit A.**, 2018, *Numerical Simulation of The Ship Self-propulsion Prediction using Body Force Method and Fully Discretized Propeller Model*, Proceedings of the 6th Modern Technology in Industrial Engineering Conference, MODTECH 2018, 13–16 June, Constanţa, Romania. IOP Conference Series: Materials Science and Engineering 400 (2018), 042004.

[144] **Bekhit A.**, Pacuraru F., Pacuraru S. 2019, *Hull-Propeller-Rudder Interaction of the JBC Ship Model*, Proceedings of the 17th International Conference on Numerical Analysis and Applied Mathematics, ICNAAM 2019, 23 – 28 September 2019, Rhodes, AIP Conference Proceedings 2293, 420091, (2020).

[145] Win, Y. N., *Computation of the propeller-hull and propeller-hull-rudder interaction using simple body-force distribution model*, PhD thesis, Osaka University OUKA. Japan (2014).

[146] SIMMAN, *Workshop on Verification and Validation of Ship Maneuvering Simulation Methods* (2014), https://simman2014.dk/.

[147] **Bekhit A.**, Lungu A., *URANSE Simulation for the Seakeeping of the KVLCC2 Ship Model in Short and Long Regular Head Waves*, Proceedings of the 7th Modern Technology in Industrial Engineering Conference, MODTECH 2019, 17–20 June, Iasi, Romania, IOP Conference Series: Material Science Engineering. **591(2019)** 012102.

[148] Ozdemir, Y. H., Barlas, B. *Numerical study of ship motions and added resistance in regular incident waves of KVLCC2 model*, International Journal of Naval Engineering **9**(2017), 149-159.

[149] **Bekhit A.**, Lungu A., *Numerical Simulation for Predicting Ship Resistance and Vertical Motions in Regular Head Waves*, Proceedings of the ASME 2019, 38th International Conference on Ocean, Offshore and Arctic Engineering – OMAE (2019), 9–14 June, Glasgow, Scotland, UK, OMAE2019-95237.

[150] Irvine, M., Longo, J., Stern, F. *Towing tank tests for surface combatant for free roll decay and coupled pitch and heave motions*, In Proceedings of the 25th Symposium on Naval Hydrodynamics, St Johns, Canada, 8-13 August 2004. National Academy of Sciences, the National Academies Press, (2005).

[151] ITTC. *Recommended Procedures and Guidelines: Numerical Estimation of Roll Damping*. (7.5-02 -07-04.5), Rev. 00; (2011) 32p.

[152] Begovic, E., Day, A.H., Incecik, A., Mancini, S., Pizzirusso, D., *Roll damping assessment of intact and damaged ship by CFD and EFD methods*. In Proceedings of the 12th international conference on the stability of ships and ocean vehicles (STAB2015), Glasgow, UK, 13–19 June (2015), 14–19.

[153] Atsavapranee, P., Carneal, J. B.; Grant, D., Percival, A. S., *Experimental investigation of viscous roll damping on the DTMB model 5617 hull form*, In Proceedings of the ASME 26th International Conference on Offshore Mechanics and Arctic Engineering. California, USA, 10-15 June 2007. OMAE2007-29324.

[154] **Bekhit A.**, Popescu F., *URANSE-Based Numerical Prediction for the Free Roll Decay of the DTMB Ship Model*, Journal of Marine Science and Engineering, **9**(5), (2021), 452.

[155] Piomelli, U. and Balaras, E. *Wall-layer models for large eddy simulations*. Annual Reviews of Fluid Mechanics, Vol. 34 (2002), 349–374.

[156] Bhushan, S. and Wlater, D. K. *A dynamic hybrid RANS/LES modeling framework*. Physics of Fluids, Vol. 24, 015103 (2012).

[157] Boussinesq, J. *Theorie de L'Ecoulement tourbillant. mem*, Presentes par Divers Savants Acad. Sci. Inst. Fr., Vol. 23 (1877) 46–50.

[158] Smith, A. M. O. and Cebeci, T. *Numerical solution of the turbulent boundary layer equations*. Douglas Aircraft Division report, DAC 33735 (1967).

[159] Baldwin, B. S. and Lomax, H. *Thin Layer Approximation and Algebraic Model for Separated Turbulent Flows*. American Institute of Aeronautics and Astronautics (1978), AIAA paper 78-257.

[160] Spalart, P. R. and Allmaras, S. R. *A one-equation turbulence model for aerodynamic flows*. American Institute of Aeronautics and Astronautics (1992), AIAA paper 92-0439.

[161] Baldwin, B. S. and Barth, T. J. *A one-equation turbulence transport model for high Reynolds number wall-bounded flows*. American Institute of Aeronautics and Astronautics (1991), AIAA paper 91-0610.

[162] Ferziger, J. H. and Perić, M. *Computational methods for fluid dynamics*. 3rd Edition (2002), Springer, ISBN 3-540-42074-6.

[163] Versteeg, H. K. and Malasekera W. *An introduction to computational fluid dynamics, the finite volume method*. 1st Edition, Longman Scientific and Technical, Harlow, England, ISBN 0-582-21884-5.

[164] Nichols B. D. and Hirt. C. W. *Improved Free surface boundary conditions for numerical incompressible flow calculations*. Journal of Computational Physics, Vol. 8 (1971), 434–448.

[165] Nichols B. D. and Hirt. C. W. *Calculating three-dimensional free surface flows in the vicinity of submerged and exposed structures*. Journal of Computational Physics, Vol. 12 (1973) 234–246.

[166] Donea, S., Guiliani, S. and Halleux J. P. *An arbitrary Lagrangian-Eulerian Finite Element Method for Transient Dynamic Fluid-Structure Intercations*. Computer Methods in Applied Mechanics and Engineering, Vol.33 (1982), 689–723.

[167] Harlow, F. H. and Welch, J. E. *Numerical calculation of time-dependent viscous incompressible flow of fluid with free surface*. The Physics of Fluid, Vol. 8 (1965), 2182–2189.

[168] Osher, S., Sethian J. A. *Fronts propagating with curvature-dependent speed: Algorithms based on Hamilton-Jacobi formulations*. Journal of Computational Physics. Vol. 79 (1988), 12–49.

Appendix A
Numerical Methods used in Ship Hydrodynamics Applications

The recent applications of numerical methods in ship hydrodynamics comprise mainly three important elements: physical modeling; numerical modeling and finally the computational framework. This division is very important to be taken into consideration for highlighting and understanding the CFD process and its basic levels of errors, as it is discussed in Chapter II. The physical modeling describes the basic problem and how it can be solved. Basic models in ship hydrodynamics include flow modeling, whether one- or two-phase flow, turbulence models, propulsion models, cavitation models, wave models, etc. On the other hand, the numerical modeling describes the techniques used to solve the physical models, such as solution algorithm, discretization methods, interface or free-surface modeling, grid generation, etc. Finally, the computational framework describes the computational capacity available for the simulation, which relies recently on the HPC allowing broader capabilities for using finer grids, more advanced turbulence models, parallel computing and significantly fast simulation turnaround time. The flow chart in Fig. 3.1 shows the main components of computational methods in ship hydrodynamics.

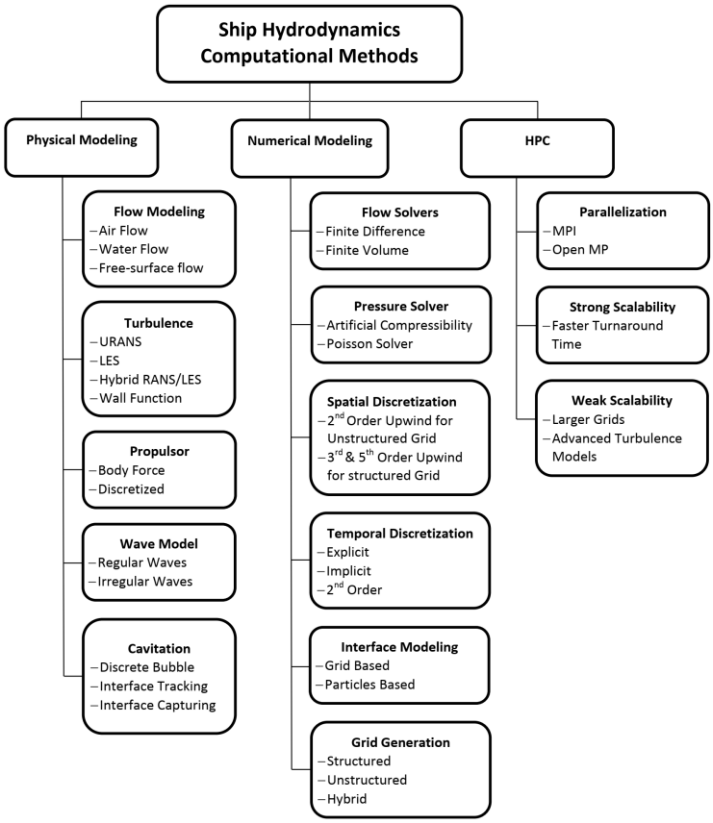

Figure A.1 Main components of the ship hydrodynamics computational methods [35, 74]

This Appendix provides in brief a general review for the basic numerical methods applied in ship hydrodynamics, summarizing the important techniques and highlights their applications and

limitations. It is worth mentioning that some of the listed models in the flow chart are not covered in the following breakdown, since they are either beyond the scope of the current research work such as the HPC or not included in the numerical simulations performed in the present research work, such as the cavitation models. In addition, the propulsion model was basically covered in Chapter I.

A.1. Physical Modeling

A.1.1 Flow Modeling

Air and water are fundamentally the two fluids involved in ship hydrodynamics. Principally, they are considered as Newtonian fluids, and the flow phenomena can be considered as incompressible due to the fact that Mach number is usually very low. Therefore, the governing equations become the incompressible NSE. Flow modeling in ship hydrodynamics accounts for the importance of the fluid that will be taken into consideration during the simulation. There are three different methods used to model the flow in ship hydrodynamics solvers: free-surface flow, air flow and two-phase flow. In free-surface flow solvers, only the water flow is modeled, and the free-surface is solved by applying an atmospheric pressure boundary condition at the free-surface. This approach is suitable for a wide range of applications, especially in ship resistance, since the largest value of resistance is mainly produced by the water component. However, this approach cannot stand for solving complicated free-surface problems, such as wave breaking and air entrainment, among others, which are becoming very important recently due to the demands of unconventional hull shapes. Air flows are showing higher interest in the recent research to analyze the air wake around the superstructures and the influence of strong winds on ship seakeeping and maneuverability. The basic principle in this approach is to simplify the ship aerodynamic problem by neglecting the free-surface deformation and velocities. Another advanced technique is to solve the water flow first and use the predicted free-surface as an unsteady boundary condition for the air flow solver; however, even with this technique, there are some limitations presented in the lack of air entrainment and wind-driven wave generation prediction [35]. In the two-phase flow solvers, both air and water are modeled, which requires special treatment for the density jump at the interface. This approach is the most common in the recent ship hydrodynamic commercial solvers, as it was presented in the last three Workshops T2005, G2010 and T2015 [45, 47 & 48]. Unlike the aforementioned approaches, this one can stand for wave breaking, air entrainment, wind-generated waves, etc. The basic principle applied in the recent years, in the vast majority of the CFD viscous flow solvers for marine applications, is to introduce a one-field formulation which identifies the phase using either a marker or indicator function in a suitable manner that will justify both kinematic and dynamic conditions of the free-surface. More details about this interface treatment will be given later in this Appendix in the numerical modeling, free-surface modeling section.

A.1.2 Turbulence Modeling

Flow is turbulent in the majority of engineering applications. In principle, the turbulent flow velocity field is decomposed into mean and fluctuating scales of motion (turbulence scales). Consequently, an additional turbulent stress term is added to the governing equation. This term stands for the energy transfer between the resolved and turbulent scales. There are two possibilities to account for these turbulent scales in the modeling process. First, is to solve the

direct NSE including all the scales of turbulence, which is known as direct numerical simulation DNS. The second is to use a filter function to solve the averaged NSE, as in case of RANSE, LES or Hybrid RANS/LES turbulence models. It is worth mentioning that the choice of a turbulence model can significantly influence the solution complexity, accuracy and computational cost as it can be observed in the hierarchical diagram plotted in Fig. A.2. A brief description of every model is giving as follows:

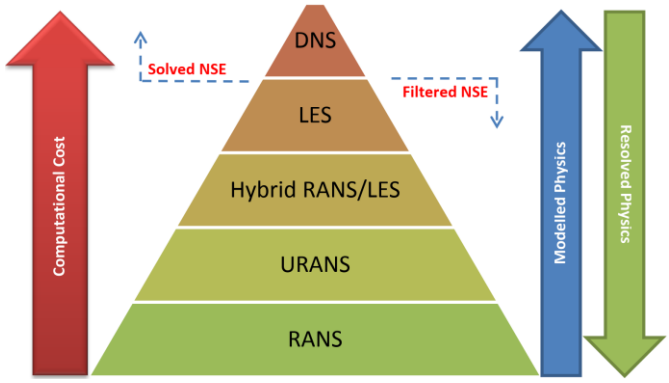

Figure A.2 Hierarchy of turbulence models based on physical modeling and computational cost

A.1.2.1 Direct Numerical Simulation (DNS)

In DNS, the unsteady NSE is completely solved including all the turbulence scales in the flow without any modeling or approximations. This means that the grid size and the time step must be as fine as possible to capture all the scales of turbulence included in the flow field. Aside of that, the computational domain size must be as large as the characteristic dimensions in length, width and height of the real physical domain, in order to include all the large scales of flow dynamics. As a consequence, resolving all the turbulent scales and frequency will require an extreme number of grid points and excessive computational effort and cost.

In order to alleviate all the associated computational problems regarding the DNS, simplified approaches were developed based on using either filtering or averaging of a certain range of the turbulent scales. This operation is known as turbulence modeling where the small-scale eddies that are less important and difficult to resolve are neglected; nevertheless, their effect is still taken into consideration during the simulation based on a statistical or theoretical averaged model known as turbulence closure model. There are two options available in this case: the first is the space averaged NSE known as LES, in which the large-scale eddies are solved, while the small scales are modeled. The second is the time averaged NSE which is known as RANS, in which the turbulence is not computed; however, its time average effect on the mean flow is considered and modeled through one of the turbulence closure models.

A.1.2.2 Large Eddy Simulation (LES)

LES can relatively overcome the associated problems with the DNS from the grid density point of view. It permits the use of relatively coarser grid compared to the DNS; however, it still requires significantly finer grids and smaller time step compared to the RANS models. Besides, it also demands a sufficiently longer simulation time to reach stable statistics of the modeled flow. Therefore, the computational cost of LES simulation is usually within an order of magnitude higher than the RANS approach.

Recently as computational facilities have become more powerful and more accessible, the LES approach is becoming more popular for marine applications especially for ships, submarines and marine propellers; yet, the application of LES in the ships inner boundary layer is still limited, because it requires a significant number of points, as previously explained, which was estimated to be relative to $Re^{1.8}$, resulting in 10^{11} points in model scale and 10^{16} for full scale ships [155]. Consequently, the very fine grid in the boundary layer results in a high aspect ratio, which inevitably has drawbacks on the solution quality, since the grid in LES has to be as cubic as possible for accuracy reasons and for high quality solutions [35]. Most recently, the effort in this scope is focusing on the development of a wall-modeled LES, or simply, the other alternative is to move towards the hybrid models.

A.1.2.3 Hybrid RANS/LES (HRL)

The hybrid RANS/LES approach is proposed to combine benefits from both models, where URANS is used in the boundary layer, while LES is used in the free-shear layer region. Two different approaches were developed based on this principle: the zonal and non-zonal approaches. In the zonal approach, a specified grid interface between the URANS and LES zones is defined, which gives flexibility in the choice of URANS and LES models. Nevertheless, there are two unresolved issues associated with the application of this principle: the first is the location of the interface, while the second is the coupling between the two models at the interface. Several studies were performed to solve the problem presented in the small-scale fluctuations that cannot be predicted based on URANS approach and are essential as an inlet condition for the LES region. Back-scatter terms, isotropic turbulence or empirical unsteady turbulent coefficient are common techniques that were proposed to combine the total stress or turbulent viscosity at the interface.

The non-zonal approach is rather simpler and more popular in marine applications, where a grid-based or physical-based approach is implemented to define the transit region. DES is the most common grid-based approach, where a single-grid system is used and the transition model between URANS and LES is done based on the ratio of the URANS to grid length scale [35]. In this approach, the transition is defined simply without a need of artificial boundary condition or any further assumptions, as in the case of the zonal approach.

DES proved in the past two decades to be a very useful model for different marine applications such as resistance, propulsion, seakeeping, maneuvering, etc., especially for applications with significant turbulence instability and vortical flows, as it was reviewed in Chapter I. However, one of the associated problems with the DES model is that it presumes the adapted dissipation at the interface to allow the development of the coherent turbulent scales to be sufficiently developed for the LES region, and the LES region contains sufficiently resolved turbulent scales to maintain the balance between the RANS and LES regions especially at the interface. These conditions are scarcely satisfied; resulting in grid and numerical sensitivity drawbacks and consequently the LES model might converge to URANS due to the lack of resolved turbulent fluctuations and stress depletion in the boundary layer. One of the proposed solutions for this problem was the Delayed DES (DDES) model and its improved form, the Improved DDES (IDDES) model, which were tested for some applications and proved their capabilities in reducing the stress depletion in the boundary layer. Yet, the proper identification of the transition region from the grid scale point of view is still uncertain, which imposes some limitations for the easy implementation of the models.

On a very different hand, another advanced approach was introduced by Bushan and Walter in [156] blending the URANS and LES models in a dynamic manner. The approach is called the Dynamic HRL (DRHL) model in which, the model switches from LES to URANS and vice versa dynamically based on a blending function controlled by the turbulent kinetic energy such that: when the resolved turbulent scales are larger than the predicted URANS produced scales, the model will work in a pure LES mode; otherwise, the model switches to the transition mode. This result in good flexibility for merging smoothly between URANS and LES models and the coupling between the regions is now based on the turbulent variation and not subjected to the previously described complications of the DES models regarding the predefined interface.

The various models included under the HRL category showed their ability to trigger resolved turbulence, improve the understanding of turbulence and vortical structure formations and predict more details within the two-phase flow models such as air entrainment. However, the grid verification techniques that were proposed and tested for RANS models are not straightforwardly applicable for the HRL because of the coupling between the models, which might result in numerical errors as previously explained. For this reason, new verification methods are required to be developed especially for these models taking into consideration the coupling process and its possible numerical problems.

A.1.2.4 Reynolds-Averaged Navier Stokes (RANS)

In RANS, the entire turbulence is modeled, and the resolved turbulence scales are assumed to be above the inertial subrange. An ensemble of the mean or phase-average of the periodic flows and the mean of the fluctuation are introduced in the NSE. This results in nine additional stress components known as the turbulent Reynolds stress components. The additional nine turbulent stress tensor components depend on many factors beside the fluid properties such as geometry, flow velocity, surface roughness and the upstream conditions, and basically expressed based on the structure of the turbulence which is also required to be defined. It is quite complicated to express the Reynolds stress tensors in the conditions of mean flow. This can be handled using one of the two different approaches: the first is based on the Boussinesq hypothesis-based models, while the second is based on the Reynolds stress transport models. A great research effort was paid in the scope of developing reliable and effective turbulence models based one of these approaches or a combination of both. One may consider this research topic to be within the list of top chart research topics in the 20th century. This continuous effort resulted in various types of turbulence models that showed their capabilities for different engineering applications and more specific in the ship hydrodynamics field, as it was highlighted in Chapter I.

The most common turbulence models are the ones based on the Boussinesq assumption, also known as eddy viscosity models, which states that the Reynolds stresses can be computed from the rate of strain tensor in the same way as the viscous stresses, the only difference is that the molecular viscosity is replaced with a turbulent equivalent viscosity [157]. This hypothesis resulted in the so-called “n-equation” turbulence model which can be summarized as follows:

- ***Zero-equation or Algebraic Model***

An algebraic approach is used to solve the turbulent quantities where the eddy viscosity is expressed in terms of the mean flow variables and mean flow gradients without solving any additional equations [74]. This model was successfully used to predict test cases with relatively accurate results in aerodynamics. The model is simple, robust and requires less computational

effort; however, for the complex ship flow problems, it is insufficient, and another advanced model is required. Examples for the most popular algebraic models are the mixing length model, Cebeci-Smith model [158] and Baldwin-Lomax model [159].

- ***One-equation Model***

An additional equation for the eddy viscosity is added to solve the kinematic eddy viscosity from the transport equation. The model allows for reasonably accurate predictions of turbulent flows with adverse pressure gradients that made it applicable in the aerodynamic filed with a recognized success. Different models based on one equation include Spalart-Allmaras [160] and Baldwin-Barth [161]. The most common one-equation model used in ship hydrodynamics applications is the Spalart-Allmaras model, which has several favorable numerical features, for example, it is “local” which means that the equation at one point does not depend on the solution at other points. Therefore, it can be easily implemented on structured multi-block or on unstructured grids [32]. Nevertheless, to improve the wake field prediction, sometimes the one-equation models are usually extended with a correction for vortical flows [74].

- ***Two-equation models***

Two additional equations for the eddy viscosity are added; the first is for the turbulent kinetic energy k, while the second is for turbulent dissipation or its dissipation rate, consecutively, ε or ω, which resulted in tow models, the k–ε and the k–ω models. In ship hydrodynamics problems, these two are considered the most popular among all the others turbulence models.

The k–ε turbulence model requires addition of the so-called damping functions to stay valid through the viscous sub-layer close to the wall. k–ε showed a rapid popularity and good results for the past three decades. However, it showed to be not suitable for flows with strong streamwise vorticity, generated at the aft bilges especially for the full-bodied ships [27]. A continuous development for this model resulted in diverse types of including the Realizable k–ε model, k–ε Renormalization Group (RNG) turbulence model, k–ε Quadratic Reynolds turbulence model, among others.

On the other hand, k–ω showed a better performance for predicting ship flows than the k–ε model. However, it is difficult to define robust boundary conditions on the outer edge. For this reason, some approaches were developed to avoid this problem by merging k–ω and k–ε, the first on the solid surface and the latter on the outside. This modification was called the baseline k–ω BSL model; while another approach was proposed to enhance the shear stress tensors obtained in adverse pressure gradients known as the shear stress tensors k–ω SST model.

Another well recognized category of turbulence models which are not based on the Boussinesq hypothesis are the Reynolds stress models (RSM). Unlike the n-equation models described previously, the eddy viscosity is not introduced in this approach; however, the transport equations of the six Reynolds stress components are solved directly, together with an additional equation to model the terms in these equations. This results in five additional transport equations in 2D flows and seven additional transport equations in 3D that must be solved. Consequently, the computational cost increases dramatically; besides, other problems related to instability and iterative solution divergences were recorded in many cases. On the other hand, Reynolds stress model has proven to provide superior wake results compared to the eddy viscosity models.

The continuous improvement of the nonlinear turbulence models resulted in the algebraic stress models (ASM), which maintains the same principle of relating algebraically the Reynolds

stresses and their partial derivatives with the rate of strain. It can be said that these models combine both benefits of Reynolds stress models and eddy viscosity models, since they involve the same number of equations as the two equation models with higher order quadratic and cubic terms, and the obtained wake results are within the same quality of Reynolds stress models; yet, with less computational effort. One example for these models is the Explicit Algebraic Stress Model (EASM); where the equation for Reynolds stress anisotropy tensor is derived from the Reynolds stress transport equation [29]. This model started to gain popularity since its remarkable results obtained for wake flow in Tokyo 2005 Workshop. In addition, it demands a relatively less computational cost compared to the RSM [45].

In ship flows with large Reynolds number, such as in full-scale simulations, the normal gradients of the flow near-wall become extremely significant as the distance to the wall tends to zero. In addition, the near-wall turbulent fluctuations and the viscous effects are of a paramount importance to be considered. A very dense grid resolution is required in the near-wall region to solve these gradients and turbulences. However, increasing the grid density near-wall can have some drawbacks on the numerical errors for the computed mass and momentum fluxes because of the high aspect ratio cells. Therefore, the wall-functions were proposed to overcome this problem and they are widely used for industrial and practical purposes.

In wall-function approach, the flow of the inner boundary layer, known as viscous sub-layer, is governed by the pressure gradients outside the viscous layer, while the velocity profile complies with the sub- and log-layer law. The boundary condition in this case is applied on the first point from the wall, known as matching point. One of the difficulties associated with the implementation of the wall-function is to place this matching point in the log-layer. Different approaches were proposed to avoid this problem, such as using multiple layer models to provide flexibility for the velocity and turbulence to switch smoothly between layers based on y^+ distance or implementing pressure gradients effect in the wall-function to account for flow separation. It is worth mentioning that the implementation of wall function significantly reduces the computational effort. Recently it is considered as an optimum solution for full-scale ship simulation with roughness effect. However, it includes some recognized limitations presented in the inaccurate prediction of highly separated 3D boundary layer with significant crossflow.

In general, turbulence modeling can be considered as the most important research topic in the last decades of the 20th century. Adverse varieties of models were proposed, and all showed their capabilities in ship hydrodynamic viscous flows, as it was discussed in Chapter I. No ‘generic’ model was developed for viscous flow problems; yet some prove their reliability in ship wake prediction. Fig. A.3 gives a breakdown chart for the most popular turbulence models in CFD applications. More details about turbulence models can be found in the remarkable review by Wilcox presented in his well-recognized book turbulence modeling for CFD [42].

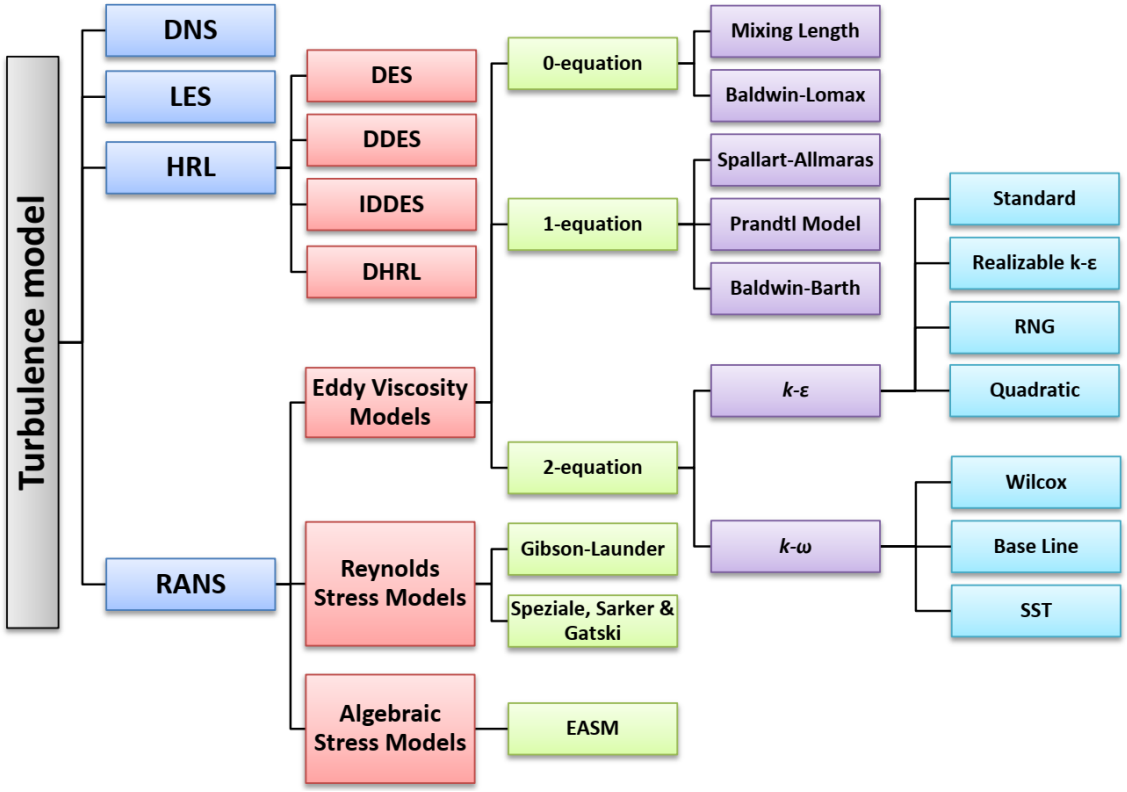

Figure A.3 Most popular turbulence models used in CFD applications

A.2 Numerical Modeling

A.2.1 Reference Frames

Choosing the frame of references for numerical simulation in ship hydrodynamics mainly depends on the type of simulation performed. As the incompressible NSE are the governing equations that describe the flow field in marine hydrodynamics, they are usually solved in an inertial earth-fixed reference frame for general problems such as resistance, propulsion and seakeeping, especially when heave, pitch and roll are the only motions taken into consideration. On the other hand, in maneuvering applications when surge, sway and yaw motions are considered, it is general to use non-inertia ship-fixed reference frame to predict ship motions.

A.2.2 Spatial Discretization

The spatial discretization of the governing equation in ship hydrodynamic problems is generally performed using either finite difference or finite volume methods; finite element method is rarely involved in ship hydrodynamic applications. The review of the state-of-the-art in ship hydrodynamic shows that finite volume method is the most popular approach used recently because it provides flexibility of choosing arbitrary polyhedral control volumes to build the spatial discretization, rather than curvilinear structured grid used in finite difference method.

In the finite difference method, the derivatives in the governing equations are replaced with a finite difference approximation derived from Taylor expansions of the unknown function. This technique was originally developed by Euler in 1768 and used for solving differential equations

using hand calculations. A consistent review for this approach can be found in [162]. Generally, finite difference method is simple, effective and easy to obtain higher-order scheme due to the use of structured grid. Nevertheless, it requires complex transformed governing equations and high-quality structured grids, which are sometimes very difficult to generate for complex geometries. Recently, Cartesian multi-block grids are used to overcome this problem.

The finite volume method is applicable for both structured and unstructured grids. Unlike the finite difference, the approximation of derivatives, surface and volume integrals are applied on the grid nodes, rather than cell centers. In Tokyo 2005, Gothenburg 2010 and Tokyo 2015 workshops, approximately two-thirds or more of the solution methods were based on the finite volume [45, 47 & 48]. More details about finite volume method can be found in the particularly devoted book of Versteeg and Malalasekera [163].

The diffusion terms in the governing equations are generally discretized using second-order central differencing scheme for both finite difference and finite volume flow solvers. On the other hand, there are varieties of discretization schemes used for the convection terms. The most popular recently for finite volume RANS solvers is the second-order upwind-biased scheme, which might differ in terms of flux-limiter or slope-limiter used to suppress the unphysical oscillations in the numerical solutions [74]. In case of finite difference, a third- or fifth-order upwind scheme is usually used; however, it incurs extra computational cost. For LES and DNS solvers, a second-order central differencing scheme is usually used to account for small-scale turbulence for its low-dissipation quality. Nonetheless, it is supposed to be used with a great care, because it is well known that central differencing scheme suffers some instability problems when the Reynolds number based on the cell size becomes larger [74].

A.2.3 Temporal Discretization

Two approaches are used in the modern ship hydrodynamic solvers, the implicit and the explicit time-marching scheme. The implicit time-marching scheme is the most popular because it allows the use of a larger time step size compared to the explicit scheme, which definitely reduces the computational effort. On the other hand, implicit time-marching implies the solution of a coupled non-linear system of equations, which involves extra computational costs. The explicit time-marching schemes require smaller time step size and are not popular for RANS computations. It is used usually for LES and DNS simulations, where the small-time step size is compulsory to resolve the small scales of turbulent eddies.

The discretization of the time derivatives is done based on a first-order backward Euler scheme, especially for steady state solutions. However, it is known that the Euler scheme introduces a substantial numerical diffusion. A considerably more accurate approach is applying a second-order schemes such as Crank-Nicolson and three-level backward schemes [74]. The fourth order Runge-Kutta schemes have been presented in some studies; however, the second-order schemes are the most popular, similarly as in case of second-order spatial discretization schemes. The choice of discretization scheme is crucially important for the stability and accuracy of the numerical solution. For example, in seakeeping problems, the most sensitive factor in the simulation is related to the free-surface wave propagation. As previously described, the schemes that use first order discretization in space will be too artificially diffusive regardless of the grid resolution, while the first order time discretization tends to lose wave energy as the numerical simulation progresses [35].

A.2.4 Grid Generation

The fluid domain surrounding the ship geometry is subdivided into a large number of grid cells to be used to obtain the fluid flow parameters. The size and shape of these grid cells can have a significant influence on the accuracy and efficiency of the flow solution. Computational grid with higher resolutions gives better numerical results than coarser grid; however, it requires more computational resources. On the other hand, this should be treated with a very good care, because in some cases, coarser grids can give closer agreement with the experiment than the finer ones. This is simply because some various errors may cancel each other [162].

The grid types in CFD in general can be either Cartesian structured or unstructured grids. As previously explained, most of ship hydrodynamic solvers use unstructured grid because it can simply define complex geometries. The benefit of using structure grid is related to its bounded matrix, which increases the computation efficiency and simplicity. The computational ship hydrodynamic solvers used for research purposes apply structured multi-block grid because it provides flexibility in grid generation and has a high level of accuracy. Elliptical smoothing algorithms are usually used to improve the quality of the grids, while a topological inter-connection approach is implemented to connect the faces of the multi-blocks [35].

In ship hydrodynamic flows, geometry motions are treated using deforming, regenerated, sliding and/or overset grid techniques. Deforming and regenerated are usually used for confined motions as in case of free-surface deformation. Sliding grid is usually used to represent the propeller rotation, while overset grid can provide a good compromise of applicability and efficiency for most marine applications; yet it is sometimes difficult to maintain the convergence between background and overset grids.

A.2.5 Interface Modeling

There are essentially two methods that can be used to model the interface in viscous ship hydrodynamics flow solvers. The first and most popular is the Eulerian grid-based method and the second is the Lagrangian particles (mesh-less) method. In the Eulerian methods, a function is used to define the free-surface shape. This can be subdivided in two different categories: the interface fitting and interface capturing.

In the interface fitting, which is also known as interface tracking, the numerical grid is generated only for the liquid domain and aligned to a deformed free-surface shape then updated iteratively in each time step. The kinematic and dynamic boundary conditions are applied only on the free-surface, which is considered as a boundary of the grid in this case. A partial differential equation is derived from the kinematic boundary condition and solved in the same approach as in the bulk flow solution. The advantage of using this technique is that it provides a high accuracy in predicting the free-surface, because the exact location of the interface can be obtained easily from the applied boundary conditions. Nevertheless, it is difficult to be used when the free-surface is subjected to large deformation, such as in case of very steep and breaking waves.

Three methods in the literature can be considered as surface tracking-based methods: the height function, line segment and the arbitrary Lagrangian-Eulerian methods.

In the height function which was proposed by Nichols and Hirt [164, 165], the free-surface is treated as a moving boundary whose position can be tracked based on its height h with respect to a reference line or surface, for 2D and 3-D flows, respectively. The method is very simple to apply, robust, straightforward, computationally efficient, and less expensive. However, it works

well for simple free-surface problems, and it cannot handle complex wave problems such as breaking or overturning waves, wave spraying and bubbles; since those cases can produce multiple free-surface heights at the same level, as it is illustrated in Fig. A.4.

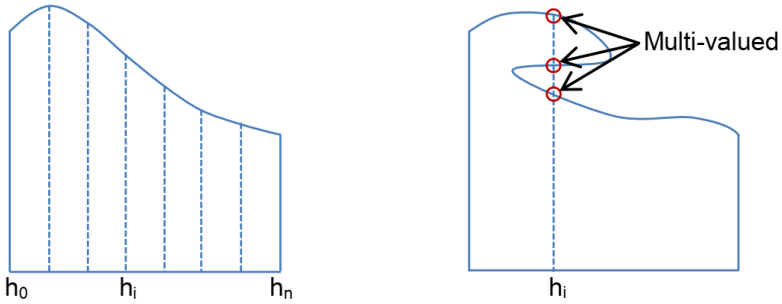

Figure A.4 Height function for a 2D open interface

The line segment method is a generalized method for the height function which is working similarly like the height function except that the free-surface is presented based on using a chain of short line segments defined by two points for the two ends of the line. Consequently, the storage capacity requires for this method is increased compared to the height function resulting in a higher computational time. This technique was exclusively limited for only 2D problems.

Finally, the arbitrary Lagrangian-Eulerian (ALE) method was proposed to combine the benefits from both approaches and overcome their weaknesses. The computational mesh in this case is represented as a moving frame with an arbitrary velocity. Linking this arbitrary velocity to the flow velocity, the interface condition can be recognized such that: when the arbitrary velocity is zero, the reference frame is fixed and the Eulerian condition is applicable; when the arbitrary velocity is equivalent to the flow velocity, the reference frame is moving corresponding to a Lagrangian condition; otherwise the reference frame is moving in space with different velocity than that of the flow. More details about this approach can be found in [166].

In the interface capturing, the flow is computed in both air and water, without imposing boundary conditions on the free-surface. Instead, a marker or a scalar indicator function is used to define the position of the interface based on three different approaches: marker-and-cell, level set and volume of fluid. In general, the interface capturing approach can be used in computational cases when the free-surface deformation is large, such as steep, breaking, and overturning waves. It is also very attractive for unstructured grid solvers because it does not require regridding for the free-surface movement, as in case of free-surface fitting techniques.

The marker-and-cell (MAC) [167] uses tracing mass-less particles introduced nearby the free-surface. In each time step, the particles are tracked during the simulation. This approach showed good results for nonlinear problems, such as in case of breaking waves. Nonetheless, it is computationally expensive, since the large-scale 3-D applications require a significantly large number of particles in order to capture accurately the free-surface. A typical example for MAC interface representation is plotted in Fig. A.5.

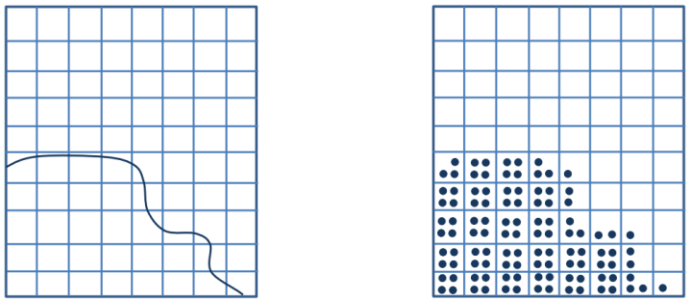

Figure A.5 Interface representation using MAC method

The volume of fluid (VOF), as originally introduced by Harlow and Welch in [167], uses the volume fraction of the water in each cell as a marker function. This scalar function is stating the condition of each cell if it contains water or air such that, if the scalar function is 1, it means that the cell is filled with water, 0 means that it is filled with air, 0.5 is corresponding to the free-surface location. The convection equation for the whole domain is solved in the same manner as in case of level set method to capture the interface. VOF method is gaining a significant popularity in the past two decades because of the promising results obtained in various research.

The level set, which first introduced by Osher and Sethian in [168], uses a scalar function defined in each cell. At the beginning of simulation, this function is defined for the whole domain based on the distance from the interface, positive in one direction and negative in the other. The free-surface location can be obtained based on the derivatives of the scalar function since its total derivatives with respect to time at the interface must be equal to zero. The surface is obtained in both air and water, but a smoothing layer needs to be introduced at the interface where the density and viscosity exhibit large jumps [29].

A consistent review supported with some practical examples for the free-surface viscous flow solution methods for ship hydrodynamics, including free-surface fitting and capturing methods, along with their implementations in CFD solvers especially dedicated for marine applications can be found in [40].

More recently, for some applications, such as seakeeping, green water, wave overturning and sloshing, the mesh-less Lagrangian, which is also known as the particle method approach, is becoming more popular. In this technique, no computational grid is used, but an infinite number of particles are used instead and distributed in the domain. Each particle moves in the domain according to its own local velocity. The free-surface shape and position can simply be determined from the motion of the particles and particles distribution. There are several schemes that were proposed in the past decade for the particle approach including the smooth particles hydrodynamics (SPH) and moving particles semi-implicit (MPS). The advantage of using these methods over the previously described grid-based methods is that it requires no computational grid. Besides, it guarantees the conservation of mass without extra computations, since the particles themselves represent the mass. Another benefit is that the particles methods compute the pressure accumulatively from the neighbor particles, unlike the grid method which involves a solution of a linear system of equations. Finally, there is no need to use an extra tracking or capturing functions due to the fact that particles represent the dense fluid (water) in domain, while the empty space represents air [29]. On the other hand, in particles method, the boundary condition on the solid wall needs a very special care. Besides, it is very difficult to solve the boundary layer near the wall using particles [74].

A.2.6 Velocity-Pressure Coupling

The velocity and pressure terms in the incompressible NSE used in ship hydrodynamic flows require a special treatment due to the absence of the flow density in the continuity equation, which results in some complications to carry out the solution directly. For this reason, the solution algorithm must be conducted in a suitable manner to retain the continuity of the flow. One of the possible approaches is to treat the continuity equation in a similar way as in case of compressible flows, by involving a term with a first-order time derivative for the pressure combined with the compressibility parameters and adding it to the continuity equation. This results in a system of hyperbolic equations; thus, the same solution algorithm used in aerodynamics can simply be applicable. The resulting equations can be solved in an implicit coupled manner, which may enhance the convergence and stability of the solution. This approach is basically known as the artificial compressibility method, which is implemented in many flow solvers, especially for steady flows.

Another method is to solve the continuity and momentum equations in a fully coupled form. This approach is basically called the pressure-based methods, since the pressure is used as a constraint to impose a divergence-free velocity field. The approach is also called projection method, since the momentum equation is projected onto a divergent-free velocity field vector in space. This projection results in a Poisson equation as the pressure governing (correction) equation. This method can be used to solve unsteady compressible flows. The most popular methods adopted this principle are the PISO method and the SIMPLE-family, which includes: SIMPLE, SIMPLER and SIMPLEC. SIMPLE-family is the predominant method used in commercial steady flow solvers, while the PISO method is more appropriate for unsteady problems. In both methods, iterative time-steps are used to advance the solution, solving the momentum first without pressure or with the pressure from the previous iteration. The Poisson equation then is solved to predict the pressure, while the velocity is later corrected based on the new pressure. These methods are considered robust; nevertheless, they produce large systems of linear equations, which consequently require a significant computation effort and cost. Despite the fact that pressure-based methods converge much slower than the artificial compressibility methods, the majority of the solutions presented in the last two workshops: G2010 and T2015 were based on the pressure-based methods [47-48]. For the time-dependent solutions, such as in case of DES and LES, another projection-based method called fractional-step method is usually used.